

**PHOTOPHYSICS OF BIS(DIARYLAMINO)BIPHENYL DYES
ADSORBED ON SILVER NANOPARTICLES**

A Dissertation
Presented to
The Academic Faculty

by

Wojciech Haske

In Partial Fulfillment
of the Requirements for the Degree
Doctor of Philosophy in the
School of Chemistry and Biochemistry

Georgia Institute of Technology
August 2010

**PHOTOPHYSICS OF BIS(DIARYLAMINO)BIPHENYL DYES
ADSORBED ON SILVER NANOPARTICLES**

Approved by:

Dr. Joseph W. Perry, Advisor
School of Chemistry and Biochemistry
Georgia Institute of Technology

Dr. Seth R. Marder
School of Chemistry and Biochemistry
Georgia Institute of Technology

Dr. Jean-Luc Brédas
School of Chemistry and Biochemistry
Georgia Institute of Technology

Dr. Mostafa A. El-Sayed
School of Chemistry and Biochemistry
Georgia Institute of Technology

Dr. Mohan Srinivasarao
School of Polymer Textile and Fiber
Georgia Institute of Technology

Date Approved:

Pracę tę Dedykuję Moim Rodzicom
Oraz Mojej Siostrze Iwonie
i Mojemu Bratu Andrzejowi

ACKNOWLEDGEMENTS

I wish to thank Prof. Joseph Perry, for his support over these years, his guidance and patience. I also thank him for providing the necessary instrumentations for conducting my research.

I want to thank Dr. Joel Hales for sharing his knowledge, providing advice when I needed it the most and help with the laser systems and for his friendship.

I want to thank Dr. Mariacristina Rumi for her help in understanding physical phenomena throughout these years, especially in the earlier years of my graduate program, her supervision during the two lab moves and help with setting up most of the instruments.

I must thank Dr. Michal Malicki who kept me motivated in the difficult times, for his help and the TPD ligands that he synthesized and shared with me. I also have to thank him for his friendship.

I want to thank Mr. Vincent Chen for the collaboration on microfabrication and his friendship.

I also thank my friends from the research group Sarah Chi for her help with the Helios system, Matteo Cozzuol and Mat Sartin for help with the nanosecond system, and Philseok Kim for valuable scientific discussions.

I also thank Will Boyd for his great work during his undergraduate research program and his friendship.

Finally, I want to thank my dear friend Maryam Doroudi for her support, help and enthusiasm.

TABLE OF CONTENTS

	Page
ACKNOWLEDGEMENTS	i v
LIST OF TABLES	x
LIST OF FIGURES	x i
LIST OF SYMBOLS AND ABBREVIATIONS	xviii
SUMMARY	xix
CHAPTER 1: INTRODUCTION.....	1
1.1. Overview of Metal Nanoparticles.....	3
1.2. Optical Properties of Metal Nanoparticles.....	6
1.3. Dynamics of Electrons in Metal Nanoparticles.....	8
1.4. Electric Field Enhancements.....	11
1.5. Chromophores near Metal Nanoparticles.....	13
1.5.1. Energy transfer from the Excited Chromophores to the Metal Nanoparticle.....	14
1.5.2. Electron Transfer from the Excited Chromophores to the Metal Nanoparticle.....	16
1.5.3. Inter-chromophore Interactions.....	17
1.6. Self-Assembled Monolayers.....	17
1.6.1. Monolayers on Gold and Silver Substrates.....	19
1.7. Thesis Objectives.....	20
1.8. References.....	22

CHAPTER 2: MATERIALS AND METHODS.....	32
2.1. Materials.....	32
2.2. Preparation of Silver Nanoparticles in The Presence of Oleylamine.....	34
2.3. Reacting OA-Coated Silver Nanoparticles with Thiols.....	35
2.4. Nomenclature of the Prepared AgNP / Thiol Systems.....	38
2.5. Stability of the AgNP / Dye Systems – Choice of Solvents.....	38
2.6. Experimental Methodology.....	39
2.6.1. FT-IR.....	39
2.6.2. UV-Vis-NIR Absorption and Fluorescence Spectroscopy.....	39
2.6.3. NMR Experiments.....	39
2.6.4. Transmission Electron Microscopy (TEM).....	40
2.6.5. Inductively Coupled Plasma – Emission Spectroscopy.....	40
2.6.6. Time-Correlated Single Photon Counting (TCSPC).....	40
2.6.7. Nanosecond Transient Absorption (TA).....	43
2.6.8. Femtosecond Broad-Band Transient Absorption.....	45
2.7. References.....	50
CHAPTER 3: CHARACTERIZATION OF SILVER NANOPARTICLES	
FUNCTIONALIZED WITH TPD LIGANDS.....	51
3.1. Introduction.....	51
3.2. TEM Analysis.....	54
3.3. UV-Vis Absorption Spectroscopy.....	60
3.4. FT-IR Spectroscopy.....	64
3.5. NMR Spectroscopy.....	72

3.5.1. The Source of Line Broadening	77
3.6. Determination of Surface Coverage of the TPD Ligands	
Adsorbed on the AgNP.....	84
3.6.1. Procedure of Etching of Silver Nanoparticles.....	86
3.6.2. Determination of the Concentration of TPD Ligands	
in the NP Samples.....	88
3.6.3. Determination of Extinction Coefficient of the AgNP.....	95
3.6.4. Determination of Average Area of The TPD ligand per AgNP....	98
3.6.5. Thermogravimetric Analysis.....	100
3.7. Conclusions.....	103
3.8. References.....	105
CHAPTER 4: PHOTOPHYSICS OF TPD CHRMOPHORES IN SOLUTION	
AND IN SOLID FILMS.....	110
4.1. Introduction.....	110
4.2. Photophysics of TPD-based Compounds in Solution and	
in Solid Films.....	111
4.3. Characterization of Oxidized TPD and TPDC12 Species in Solution	119
4.4. Femtosecond Transient Absorption	122
4.4.1. Global Fitting Analysis – Liquid Solution	127
4.4.2. Global Fitting Analysis – TPDC12 in PS.....	130
4.4.3. Global Fitting Analysis – TPDC12 Neat Film.....	132
4.4.3.1. Proposed Kinetic Model.....	136
4.4.3.2. Identification of the New Species.....	140

4.5.	Anisotropy of the TPDC12 in Solid Films	141
4.6.	Conclusions.....	144
4.7.	References.....	145
CHAPTER 5: ULTRAFAST SPECTROSCOPY OF SILVER NANOPARTICLES		
FUNCTIONALIZED WITH BIS(DIARYLAMINO)BIPHENYL		
	LIGANDS.....	147
5.1.	Introduction.....	147
5.2.	Femtosecond Transient Absorption Spectroscopy in the NIR.....	148
5.3.	Analysis of AgTPDC3 systems.....	158
5.3.1.	Excitation Energy Dependence	158
5.3.1.1.	Two-photon absorption	164
5.3.1.2.	Sequential One-Photon Absorption	165
5.3.1.2.	Exciton-Exciton Annihilation.....	166
5.3.2.	Coverage Dependence – AgTPDC3 Systems.....	169
5.4.	Analysis of AgTPDC4, AgTPDC8 and AgTPDC12 Systems.....	173
5.4.1.	Excitation energy dependence.....	173
5.4.2.	Coverage Dependence.....	181
5.5.	Anisotropy.....	187
5.6.	Conclusions.....	192
5.7.	References.....	193
CHAPTER 6: CONCLUSIONS.....		
APPENDIX A: HIGH RESOLUTION 3-D MULTIPHOTON LITHOGRAPHY		
A.1.	Introduction.....	202

A.2.	Experimental Details.....	204
A.2.1.	Materials.....	204
A.2.2.	Dose-Dependent Photoinduced Polymerization Studies.....	205
A.2.3.	PC Fabrication and Stop-Band Characterization.....	208
A.3.	Results and Discussion.....	208
A.3.1.	Feature Sizes and Thresholds.....	208
A.3.2.	Dosimetry and Order of Multiphoton Absorption Process.....	212
A.3.3.	PC Structures and Stop-Band Spectra.....	218
A.4.	Conclusion.....	221
A.5.	References.....	222

LIST OF TABLES

Table 2.1.	Nomenclature of the nanoparticles with the composition of their organic monolayers.....	38
Table 3.1.	Samples of silver nanoparticles functionalized with TPD ligands and TPD ligand / DDT mixtures expressed in percentage of TPD ligand used in the reaction mixture.....	58
Table 3.2.	Frequency of the symmetric (ν_s) and asymmetric (ν_{as}) methylene C-H stretching modes for the systems studied herein as well as for crystalline polyethylene (PE) and for a polyethylene solution in CCl_4	70
Table 3.3.	Values of the integrated 1H NMR signal in the aliphatic-proton band region normalized to the integrated aromatic-proton band.....	76
Table 3.4.	Summary of results of FWHM of the aromatic-proton band and of T_2 relaxation times found from 1H NMR spectra of Ag NPs coated exclusively with TPD-thiols.....	81
Table 3.5.	Summary of the measurements results used for the evaluation of the average number of TPD ligands per AgNP in the systems.....	99
Table 3.6.	Fraction of the organic component in the samples AgTPDCx-I, where $x = 3, 4, 8$ and 12 , expressed in percentages. The results obtained from thermogravimetric analysis are compared with the analysis based on optical absorption and ICP-ES.....	102

LIST OF FIGURES

Figure 1.1.	Lycurgus chalice.....	4
Figure 1.2.	Schematic drawing of plasmon oscillation of a metal sphere.....	7
Figure 2.1.	UV-vis spectra of supernatants after a small scale place exchange reaction of OA - AgNP with TPDC4SH.....	36
Figure 2.2.	Scheme of the optical layout of TC-SPC experiment.....	43
Figure 2.3.	Scheme of the optical layout of the nanosecond TA experiment.....	45
Figure 2.4.	Schematics representing optical layout of the femtosecond transient absorption setup.....	46
Figure 2.5.	Normalized OKE signal as a function of pump-probe delay measured at different wavelengths.....	48
Figure 3.1.	Schematic drawing of two spheres characterized by different diameters with cones representing solid angles.....	53
Figure 3.2.	TEM images of silver nanoparticles.....	55
Figure 3.3.	Histograms of diameters of silver nanoparticles measured from TEM images.....	56
Figure 3.4.	UV-vis absorption spectra of AgNP functionalized with TPD ligands in 5:1 mixture of toluene and DMF.....	61
Figure 3.5.	Position of plasmon absorption maxima (λ_{\max}) plotted as a function of number of carbon atoms in the linker of the TPD ligands.....	63
Figure 3.6.	S-H stretching mode at 2566 cm^{-1} of neat films of TPDC3SH and TPDC12SH, compared with the same spectral region of AgTPDC3-I and AgTPDC12-I.....	66
Figure 3.7.	FT-IR spectra of neat films of NP samples studied herein cast onto a KBr disc.....	67
Figure 3.8.	a) FT-IR spectra of TPDC3SH, AgTPDC3-I, and of TPD, normalized at 3030 cm^{-1} . b) Normalized FT-IR spectra of TPDC12SH and AgTPDC12-I.....	68
Figure 3.9.	FT-IR spectra of the NP systems studied herein.....	68

Figure 3.10.	FT-IR spectra, normalized to the aromatic C-H stretching mode, of neat films of the NP systems drop-cast onto a KBr disc.....	71
Figure 3.11.	^1H NMR spectra of CD_2Cl_2 solutions of silver nanoparticles.....	73
Figure 3.12.	^1H NMR spectra of CD_2Cl_2 solutions of silver nanoparticles.....	74
Figure 3.13.	^1H NMR spectral changes during T_1 experiment performed for AgTPDC3-I in CD_2Cl_2	78
Figure 3.14.	Selected spectra acquired at different delays during a CPMG-pulse-sequence experiment performed on CD_2Cl_2 solutions of AgTPDC3-I, AgTPDC4-I, AgTPDC8-I and AgTPDC12-I.....	80
Figure 3.15.	a) UV-Vis absorption spectra of TPD solution in DCM recorded after sequential addition of two volumes of SbCl_5 and of a portion of AgNP. b) UV-Vis absorption spectra of TPD in DCM – black line, and of the final product of the oxidation/reduction.....	87
Figure 3.16.	a) UV-vis absorption spectra of AgTPDC3-I – top graph, AgTPDC3-II – middle, AgTPDC3-III – bottom at varying concentrations obtained by dilution of different volumes of the stock solution in a mixture of toluene and DMF (5:1). Column b) shows spectra of these systems in DCM after the reaction with SbCl_5	89
Figure 3.17.	a) UV-vis absorption spectra of AgTPDC4-I – top graph, AgTPDC4-II – bottom at varying concentrations obtained by dilution of different volumes of the stock solution in a mixture of toluene and DMF (5:1). Column b) shows spectra of these systems in DCM after the reaction with SbCl_5	90
Figure 3.18.	a) UV-vis absorption spectra of AgTPDC8-I – top graph, AgTPDC8-II – middle, AgTPDC8-III – bottom at varying concentrations obtained by dilution of different volumes of the stock solution in a mixture of toluene and DMF (5:1) . Column b) shows spectra of these systems in DCM after the reaction with SbCl_5	91
Figure 3.19.	a) UV-vis absorption spectra of AgTPDC12-I – top graph, AgTPDC12-II – middle, AgTPDC12-III – bottom at varying concentrations obtained by dilution of different volumes of the stock solution in a mixture of toluene and DMF (5:1) . Column b) shows spectra of these systems in DCM after the reaction with SbCl_5	92
Figure 3.20.	Concentration of silver atoms measured by ICP-ES as a function of volume of the stock solutions of the samples of a) AgTPDC3-I – top	

	graph, AgTPDC3-II – middle, AgTPDC3-III – bottom and b) AgTPDC4-I – top, AgTPDC4-II – bottom.....	93
Figure 3.21.	Concentration of silver atoms measured by ICP-ES as a function of volume of the stock solutions of the samples of a) AgTPDC8-I – top graph, AgTPDC8-II – middle, AgTPDC8-III – bottom and b) AgTPDC12- I – top, AgTPDC12-II – middle and AgTPDC12-III – bottom.....	94
Figure 3.22.	Values of the extinction coefficient of silver nanoparticles at the maximum of the surface plasmon resonance in the investigated samples as a function of nanoparticles.....	97
Figure 3.23.	Thermogravimetric scans for samples AgTPDCx-I, where x = 3, 4, 8 and 12.....	101
Figure 4.1.	UV-vis absorption and fluorescence spectra of TPDC12SH in toluene / DMF (5:1).....	113
Figure 4.2.	Fluorescence decays of deoxygenated solutions of TPDC12SH in toluene and in 5:1 toluene / DMF (5:1) measured with TCSPC technique.....	114
Figure 4.3.	Fluorescence spectra of TPDC12 model compound in a neat film (black line), 0.67% wt. (red line) and 3.4% wt. (blue line) of TPDC12 model compound in polystyrene film and a solution of TPDC3SH in 5:1 mixture of toluene and DMF (doted black line).....	115
Figure 4.4.	Fluorescence decay of neat film of TPDC12 measured with TCSPC technique.....	116
Figure 4.5.	Nanosecond TA spectra recorded at several delay times of TPD solutions a) in toluene and b) in DMF.....	118
Figure 4.6.	UV-Vis-NIR absorption spectra of TPDC12 in DCM recorded before and after successive additions of 0.05 M DCM solution of SbCl ₅	119
Figure 4.7.	UV-Vis-NIR absorption spectra of DCM solutions of TPDC12, TPDC12 ^{•+} and TPDC12 ⁺⁺ in comparison with spectra of TPD, TPD ^{•+} and TPD ⁺⁺	121
Figure 4.8.	Evolution of transient absorption spectra in the visible and the NIR regions measured for: a) ca. 0.1 M TPDC12SH in toluene / DMF (5:1), b) TPDC12 in polystyrene matrix, and c) a neat film of TPDC12.....	123

Figure 4.9.	Normalized decay traces at 525 nm, 600 nm, 1050 nm and 1500 nm of a) TPDC12SH in toluene / DMF (5:1), b) TPDC12 in polystyrene matrix (3.4%), and c) neat film of TPDC12.....	125
Figure 4.10.	Transient absorption decays of TPDC12SH in toluene / DMF (5:1) solution at selected wavelengths plotted together with fitting curves.....	128
Figure 4.11.	Spectral distributions of pre-exponential amplitudes obtained from fitting the data acquired for TPDC12SH solution in toluene / DMF (5:1) with a sum of three exponentials.....	129
Figure 4.12.	Transient decays of TPDC12 in a polystyrene film at different wavelengths.....	130
Figure 4.13.	Spectral distribution, in the visible and NIR, of preexponential amplitudes obtained from fitting the TA data acquired for TPDC12 in a PS matrix (3.4 % of TPDC12 by weight) with a sum of three exponential functions.....	130
Figure 4.14.	Transient decays of the neat film of TPDC12 at multiple wavelengths a) in the visible region, and b) in the NIR region.....	132
Figure 4.15.	Spectral distribution in the visible (left) and in the NIR (right) of preexponential amplitudes obtained from fitting of the TA traces measured for a photoexcited neat film of TPDC12 with a sum of three exponential functions.....	133
Figure 4.16.	A simplified energy level diagram for TPDC12 in neat film showing excitation and assumed relaxation pathways for both cases: a) without and b) with forming the new species.....	134
Figure 4.17.	Transient absorption spectra in: a) visible and b) NIR of TPDC12 neat film at early time $\Delta OD(0.6 \text{ ps})$ and after 480 ps $\Delta OD(480 \text{ ps})$, plotted together with a spectrum obtained by subtraction: $\Delta OD(0.6 \text{ ps}) - \Delta OD(480 \text{ ps})$ and spectral amplitudes A_I	138
Figure 4.18.	UV-Vis-NIR absorption spectrum of TPDC12 ^{•+} in DCM, and amplitudes of the long living component A_0 obtained from global fitting of transient absorption kinetics of neat film of TPDC12.....	140
Figure 4.19.	Anisotropy spectra at selected decay times and anisotropy decay kinetics at selected wavelengths of TPDC12 in polystyrene films doping ratios of a) 3.4% by weight and b) 0.67% by weight.....	143

Figure 5.1.	Time evolution of transient absorption spectra of: a) AgTPDC12-I, b) AgTPDC8-I, c) AgTPDC4-I and d) AgTPDC3-I in a mixture of 5:1 toluene:DMF.....	150
Figure 5.2.	Normalized transient decay traces of AgTPDC _x -I (where x = 3, 4, 8 and 12) recorded at: a) 1050 nm and b) at 1520 nm.....	151
Figure 5.3.	Spectral distribution of pre-exponential amplitudes from global fitting analysis of: a) AgTPDC12-I, b) AgTPDC8-I, c) AgTPDC4-I and d) AgTPDC3-I in a mixture of 5:1 toluene:DMF.....	153
Figure 5.4.	NIR absorption spectrum of radical cation of TPDC12 in DCM overlaid with spectral profiles of the offset ($A_0(\lambda)$) component obtained from global fitting analysis of neat film of TPDC12 and spectral profiles of pre-exponential amplitudes associated with time constant of 5 ps of the sample AgTPDC3-I.....	155
Figure 5.5.	Normalized decay curves of transient absorption of AgTPDC3-I and the neat film of TPDC12, recorded at 1050 nm and 1520 nm.....	156
Figure 5.6.	Spectral distribution of pre-exponential amplitudes obtained from fitting with sum of two exponentials of the decay traces of AgTPDC3-I in a mixture of 5:1 toluene:DMF at different excitation energies.....	159
Figure 5.7.	a) Pulse energy dependence of amplitudes A_1 at 1050 nm and A_2 at 1520 nm for AgTPDC3-I, b) ratio of amplitudes A_2 at 1520 nm to A_1 at 1050 nm plotted as a function of excitation energy.....	161
Figure 5.8.	Schematic diagram describing energy levels of TPD and cation-like TPD ($\text{TPD}^{\bullet+}$) and possible pathways for photoinduced charge separation.....	163
Figure 5.9.	Fraction of TPD ligands in excited state to the molecules in ground state as a function of distance from the front wall of the cuvette calculated for AgTPDC3-I for five excitation energies.....	167
Figure 5.10.	Spectral distribution of pre-exponential amplitudes for a) AgTPDC3-I, b) AgTPDC3-II and c) AgTPDC3-III in a mixture of 5:1 toluene:DMF.....	170
Figure 5.11.	Ratio of pre-exponential amplitudes A_2 at 1500 nm to the amplitudes A_1 at 1050 nm as a function of the area per TPD ligand on the AgNP surface.....	172
Figure 5.12.	Spectral distribution of pre-exponential amplitudes for AgTPDC4-I in a mixture of 5:1 toluene:DMF at varied excitation energies.....	174

Figure 5.13.	Changes in the amplitudes A_1 at 1050 nm and A_2 at 1520 nm plotted as a function of excitation energy in the sample AgTPDC4-I.....	176
Figure 5.14.	Spectral distribution of pre-exponential amplitudes for AgTPDC8-I and AgTPDC12-I in a mixture of 5:1 toluene:DMF at highest and lowest excitation energies.....	178
Figure 5.15.	Peak spectral amplitude A_1 at 1050 nm plotted as a function of excitation energy for samples AgTPDC8-I and AgTPDC12-I.....	180
Figure 5.16.	Spectral distribution of pre-exponential amplitudes of: a) AgTPDC4-I, b) AgTPDC4-II, c) AgTPDC8-I, d) AgTPDC8-III, e) AgTPDC12-I and f) AgTPDC12-III in a mixture of 5:1 toluene:DMF.....	182
Figure 5.17.	Pre-exponential amplitudes A_2 at 1500 nm normalized to the values of amplitudes A_1 at 1050 nm plotted as a function of the area available to a TPD ligand on the AgNP surface. The data is presented for systems AgTPDC3-x and AgTPDC4-y.....	184
Figure 5.18.	a) Anisotropy decay of AgTPDC3-I in solution of 5:1 mixture of toluene and DMF at 1211 nm plotted together with transient decay at the same wavelength for sample, b) anisotropy decay at three different wavelengths.....	189
Figure 5.19.	Anisotropy decays at 1056 nm, 1211 nm and 1521 nm measured for solutions in 5:1 mixture of toluene and DMF of AgTPDCx-I (where x = 3, 4, 8, 12).....	191
Figure A.1.	Molecular structures of photoinitiators used in this work, DABP and DABSB.....	205
Figure A.2.	Schematic illustrations of both types of support structures used for dosimetry studies: (a) rectangular solid walls and (b) rectangular “stack of logs” structure.....	207
Figure A.3.	SEM overview images of lines fabricated at threshold powers with (a) 730 nm excitation using DABSB-triacrylate resin and with (b) 520 nm excitation using DABP-triacrylate resin.....	211
Figure A.4.	Dosimetry studies on lines fabricated with 730 nm excitation using DABSB-triacrylate resin. Measured (a) line widths and (b) calculated voxel volumes as a function of inverse scan speed for different excitation powers.....	214
Figure A.5.	Polymer growth rates (as determined in text) derived from the dosimetry studies shown in Figure A.4b as a function of excitation power.....	216

Figure A.6.	Dosimetry studies on lines fabricated with 520 nm excitation using the DABP-triacrylate resin.....	218
Figure A.7.	SEM overview images of woodpile-type PC structures fabricated with 520 nm excitation at (a) 0.60 μ W and at (b) 0.45 μ W using the DABP-triacrylate resin.....	219
Figure A.8.	Transmission spectra of PBG structure fabricated with 520 nm excitation at 0.60 μ W using the DABP-triacrylate resin.....	221

LIST OF ABBREVIATIONS

2PA	Two-Photon Absorption
AgNP	Silver Nanoparticles
C12	12 carbon atoms
C3	3 carbon atoms
C4	4 carbon atoms
C8	8 carbon atoms
EEA	Exciton-Exciton Annihilation
ICP-ES	Inductively Coupled Plasma – Emission Spectroscopy
MPL	Multi-Photon Lithography
NIR	Near Infrared
NMR	Nuclear Magnetic Resonance
PBG	Photonic Band-Gap
PS	Polystyrene
SAM	Self-Assembled Monolayer
SEM	Scanning Electron Microscopy
TA	Transient Absorption
TCSPC	Time Correlated single photon counting
TEM	Transmission Electron Microscopy
TGA	Thermogravimetric Analysis
TPD	Bis(diarylamino)biphenyl
UV-VIS	Ultraviolet – Visible

SUMMARY

Understanding of the photophysical and optical properties of organic-inorganic hybrid systems, such as those composed of chromophores attached to the surface of metal nanoparticles is of current interest. This dissertation investigates the photophysics of bis(diarylamino) biphenyl (TPD) and silver nanoparticles (AgNP). A main goal of this work was to develop an understanding of the relaxation pathways involved in the deactivation of photoexcited TPD chromophores in close proximity to silver nanoparticles. The TPD chromophores were attached to the silver nanoparticle core via an alkylthiol group. The TPD-AgNP systems were synthesized and characterized using Transmission Electron Microscopy (TEM), UV-visible absorption, infrared spectroscopy, and Nuclear Magnetic Resonance (NMR) spectroscopy, Inductively Coupled Plasma – Emission Spectroscopy (ICP-ES) and Thermogravimetric Analysis (TGA). Time-resolved photophysical processes in these systems were studied using femtosecond transient absorption spectroscopy.

Initial studies of the interaction of the TPD and AgNP addressed the linker length dependence of the dye excited state decay kinetics, wherein alkyl linker chains of 3, 4, 8 and 12 carbon atoms were used. These results showed that an ultrafast deactivation of the excited state of the TPD chromophore, which is three orders of magnitude faster than that of the free chromophore in solution, occurred in all of the systems. However, an unexpected new transient species was observed for the systems with three and four carbon linker chains. Further studies showed this species to be spectroscopically very similar to the TPD radical cation, suggesting a charge separation pathway in the excited

state relaxation. Possible pathways for formation of the cation-like state included 1) direct two-photon photoionization of TPD, 2) photoinduced electron transfer from the excited TPD to the metal nanoparticle, or 3) a bimolecular mechanism that involves a pair of excited TPD molecules undergoing exciton-exciton annihilation and producing the cation like species from an intermolecular charge separation from the higher excited state formed via annihilation. These possibilities were examined through comparisons to the photophysics of alkyl substituted TPD in solution and in solid films, investigation of the pulse energy and TPD surface coverage dependence of the yield of the cation-like TPD species, transient absorption anisotropy decay dynamics, and kinetic modeling studies. Taken together, these investigations provide support for exciton-exciton annihilation being responsible for the formation of cation-like species. The packing of the TPD chromophores is concluded to be of critical importance in the generation of the cation like species but it is also possible that proximity to the silver nanoparticle plays a role in facilitating charge separation as well.

CHAPTER 1

INTRODUCTION

Ligand coated nanoparticles have gained great interest, due to the ability to couple functional ligands with the inorganic nanoparticles.¹ The adsorption of ligands to the nanoparticle surfaces allows for incorporating inorganic materials in organic media or attaching functional organic ligands to the inorganic cores. Such hybrid systems can exhibit properties that take advantage of both organics and inorganics resulting in a material with intermediate properties, e.g. high dielectric constant flexible films² or having a uniquely new behavior, e.g. enhanced Raman³ or fluorescence⁴ intensity. Metal nanoparticles are the most interesting from the optical stand point, due to free electrons of the metal, which are confined in sub-wavelength scale particles.^{5, 6} Functionalization of such nanoparticles with chromophoric ligands offers opportunity to prepare systems with high local concentrations of chromophores⁷, which can have potential light harvesting properties.^{8, 9} Additionally, the effects associated with close proximity of chromophores to metal surfaces can result in enhanced emission such as in surface enhanced Raman scattering (SERS)¹⁰ or metal enhanced fluorescence (MEF).¹¹⁻¹³ Functionalized metal nanoparticles have been found to be very promising in areas such as: medicine,^{14, 15} sensing^{4, 16, 17} and nonlinear optical materials^{18, 19}.

This thesis in substantial part is concerned with studying organic chromophores adsorbed onto the surface of silver nanoparticles using variety of analytical methods. The

main goal of this thesis is associated with studying the photophysical properties of N,N'-diphenyl-bis(3-methylphenyl)-biphenyl-4,4'-diamine (TPD) attached to silver nanoparticles via a thiol group, which strongly binds to the silver surface, with an alkyl linker between the TPD and the thiol. The photophysical properties are examined in the context of the distance from the silver surface, controlled by the length of the alkyl linkers, as well as interactions between the chromophores.

The thesis consists of five chapters. Chapter 1 contains an introduction and background information about development of monolayers, their importance and properties, followed by background about photophysical properties of metal nanoparticles and metal nanoparticle – organic dye systems, and the thesis objectives. Materials and methodologies used in this work are described in Chapter 2. Synthesis and some properties of synthesized nanoparticles are also included in this chapter. Chapter 3 contains a description of the nanoparticle characterization using analytical methods such as transmission electron microscopy (TEM), UV-visible (UV-vis) absorption spectroscopy, infrared (IR) spectroscopy, nuclear magnetic resonance spectroscopy (NMR), inductively coupled plasma – emission spectroscopy (ICP-ES) and thermogravimetric analysis (TGA). Here, the footprints of the chromophoric ligands are also determined. Chapter 4 deals with photophysical studies of the TPD chromophores, without the presence of silver nanoparticles, in liquid solution and in solid films. Chapter 5 describes photophysics of the silver nanoparticle / TPD systems. Conclusions are given in Chapter 6. Appendix A is a copy of a publication on multiphoton lithography, which is not discussed in the main body of the thesis.

1.1. Overview of Metal Nanoparticles

The concept of nanotechnology or nanoscience has been introduced quite recently but in fact this field has a long history. The history of gold and silver nanoparticles can be traced back to the Roman times, where nanoparticles of these two metals were used as colorants. Perhaps the oldest and the most famous artifact incorporating metal nanoparticles is the fifth century Lycurgus chalice^{20,21} (Figure 1.1). The chalice contains about 5-70 nm silver and gold nanoparticles incorporated in a glass matrix.²² The color of the glass from which it is made is green in reflected light and translucent red in transmission. The process of coloring glass with small amounts of “dissolved gold” was widely used in middle ages for staining window glass.²¹ Johann Kunckel, the seventeenth century glassmaker and alchemist, is very often credited by many sources as the first one to develop procedures for incorporating gold into molten silica, to produce well-known “ruby glass”.²² The source of these brilliant colors was not known until Faraday’s time. Michael Faraday had postulated that the color of ruby glass and aqueous solution of gold are due to small gold particles.²³ However, the physical model of such behavior of small gold particles was only intuitive at that time. Small silver particulates also played an important role with a worldwide impact on science and technology. In the mid-nineteenth century Fox-Talbot and Daguerre introduced photochemistry of silver halide, which resulted in the beginning of the era of photography.²⁴



Figure 1.1. Lycurgus chalice. The glass of the chalice contains small amounts of colloidal gold and silver, which give it these unusual optical properties. The opaque green cup (left) turns to a glowing translucent red when light is shone through it. Source: www.britishmuseum.org

Theoretical models describing the color of small dielectric particles did not exist until the beginning of twentieth century. The first quantitative theoretical model describing interaction of small metal particles emerged in 1904. In this model J. C. Maxwell-Garnett^{25, 26} used expressions for the polarizability of a spherical particle derived by Rayleigh and Lorentz in order to define optical constants. Maxwell-Garnett's model applies only to a description of particles, whose dimensions were negligible with respect to the incident wavelength of light, in a medium. The model does not treat particles individually and the differences of color seen in the systems of the particles were assigned to different interparticle distances in the medium. The model, for example, does not address the effects of different particles sizes.^{25, 26} The first rigorous theoretical model, which could predict optical properties of metal particles, in fact, any dielectric

particles, was introduced by Gustav Mie in 1908.²⁷ The model deals with individual spherical nanoparticles with known sizes interacting with light. His approach has been later extended to particles of other shapes, such as cylinders and ellipsoids.^{28, 29}

In the 1950's, anodization of aluminum was discovered and named integral coloring of aluminum surfaces.²² The process leading to this phenomenon was not understood until 1970s when Goad and Moskovits³⁰ demonstrated that the “integral coloring” phenomenon was due to plasmon absorption of aluminum nanoparticles embedded in a layer of alumina. Also, in the 1970's nano-porous silver and gold gained interest due to their applications in surface enhanced Raman spectroscopy (SERS).^{31, 32} The electromagnetic enhancing properties of these metals lead to development of theoretical models, which would provide insights into fundamental optical properties of metal particles of various shapes.^{29, 33-35}

The research on the metal nanoparticles revived in 1990s with the development of synthetic methods, which allowed for preparation of gold nanoparticles coated with thiolated ligands. In 1994 Brust et al.³⁶ published the successful preparation of gold nanoparticles stabilized with alkylthiols. The importance of this method lies in synthetic accessibility of the nanoparticles as well as flexibility in choice of protecting ligands.³⁷⁻⁴⁰ Moreover, such nanoparticles can be manipulated in a similar way to regular organic compounds: e.g. they can be precipitated, filtered or re-dispersed in an appropriate solvent.³⁹ These new properties of the nanoparticles allowed for the study of nanoparticles modified with different ligands, as well as studies of monolayers on the nanoparticles surfaces.⁴⁰⁻⁴² Self-assembled monolayers (SAMs) on the surfaces of metal nanoparticles opened a new opportunity for investigating such systems, using techniques

that were not suitable for studying SAMs on flat surfaces, or required specialized equipment.⁴³ That includes techniques such as UV-vis absorption and IR spectroscopies or NMR.^{39, 43-45}

1.2. Optical Properties of Metal Nanoparticles

Metal nanoparticles have interesting optical properties due to the presence of conduction electrons. When nanoparticles are exposed to light, the electron cloud is displaced by the oscillating electric field. Figure 1.2 shows schematic of such a process. The electron cloud is displaced relative to nuclei by the electric field, creating a restoring force due to coulombic attraction of the displaced electrons and the nuclei. These systems can be treated as classical harmonic oscillators, characterized by their resonance frequency. The resonant, collective oscillation of electrons in metals is called plasmon resonance. The depiction given here describes dipolar plasmon resonance, which is a dominant mode for small nanoparticles (< 20 nm in diameter for silver), however higher modes are also present in larger nanoparticles. The frequency of plasmon resonance in metal nanoparticles is dependent on: the density of electrons, the effective electron mass, and the size and shape of the particle. However, this description does not include the effects associated with interband transitions of bound electrons.⁴⁶ The electronic properties that also include such transitions however, are included in complex dielectric function of the metal.⁴⁷

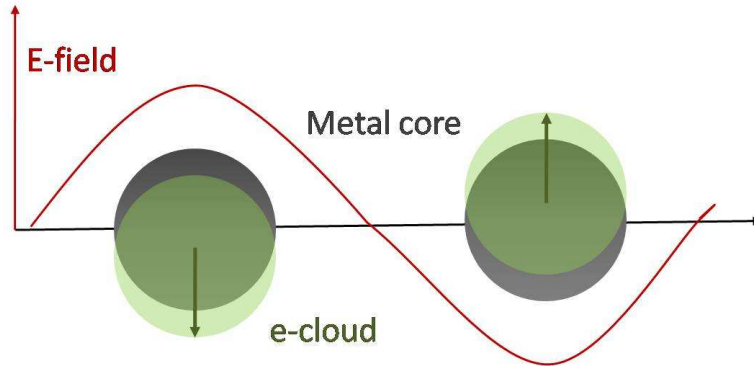


Figure 1.2. Schematic drawing of plasmon oscillation of a metal sphere. Metal spheres are in dark gray color, the displaced electron cloud in green, and electric field in red. Drawing adopted from: Kelly et al. *J. Phys. Chem. B* 2003, 17, 668-677

In 1908 Gustav Mie²⁷ solved Maxwell equations for electromagnetic waves interacting with small metal particles, using the frequency dependent dielectric function of a bulk metal. For a spherical particle the solution of these electrodynamic calculations with appropriate boundary conditions leads to the extinction cross-section of the nanoparticles. For spheres much smaller than the wavelength of excitation light only the dipolar contribution is significant and Mie theory is reduced to the dipole approximation form:⁵

$$\sigma_{ext}(\omega) = 9 \frac{\omega}{c} \epsilon_m^{3/2} V \frac{\epsilon_2(\omega)}{[\epsilon_1(\omega) + 2\epsilon_m]^2 + \epsilon_2(\omega)^2} \quad (1.1)$$

where V is the particle volume, ω is angular frequency of incident light, c is speed of light, ϵ_m is dielectric constant of dielectric material and $\epsilon(\omega) = \epsilon_1(\omega) + i\epsilon_2(\omega)$ is dielectric function of the sphere. It is evident from the above equation that the position of the plasmon resonance is not affected by the nanoparticle size in the dipolar approximation.

When the particle becomes big enough (usually larger than 20 nm for gold) the contribution from quadrupolar and higher order modes become significant and the plasmon resonance shifts. The resonance condition is met when the denominator in equation (1.1) becomes very small. This occurs when $\epsilon_l(\omega_p) = -2\epsilon_m$ and when the imaginary part of the metal's dielectric function is small, where ω_p is frequency of plasmon resonance.⁵ It is clear from this resonance condition that the position of the plasmon resonance depends on the dielectric constant of the medium.⁴⁸ The plasmon resonance occurs at lower frequency when nanoparticles are embedded in a material with higher dielectric constant.⁴⁸

1.3. *Dynamics of Electrons in Metal Nanoparticles*

The development of femtosecond lasers has enabled studies of ultrafast processes such as spectral evolution of excited metal nanoparticles. The interaction of the electrons with the lattice vibrations in thin metal films has been studied by means of time-resolved transmission and reflection spectroscopy.⁴⁹⁻⁵³ Femtosecond transient absorption has been also employed for studying metal nanoparticles dispersed in solvents.^{5, 54-57} The interaction of conduction electrons with light leads to the excitation of the conduction electrons, which then dissipate acquired energy through the following processes: electron-electron, electron-phonon and phonon-phonon relaxations.⁵

Before arrival of the laser pulse the energy distribution of conduction electrons can be described according to Fermi-Dirac statistics that has the following mathematical formula:

$$f = \frac{1}{1 + \exp\left(E - \frac{E_f}{kT}\right)} \quad (1.2)$$

where k , T , E_F and E are the Boltzmann constant, the temperature, the Fermi energy and the energy of the electronic energy levels respectively. The Fermi-Dirac statistics describe the energetic distribution of electrons at given temperature - also known as Fermi distribution. After pump pulse induced heating the electron distribution is non-thermal with regard to Fermi-Dirac statistics.⁵ The energy of these excited electrons is then rapidly redistributed between electrons by electron-electron scattering to achieve Fermi distribution. This process is called electron thermalization; it is very fast as the electrons undergo thermalization within a few femtoseconds.⁵⁸ Kreibig et al.³⁵ determined dephasing time for 2 nm silver nanoparticles to be 2 fs when the particles are embedded in a matrix and 7 fs for the same particles in vacuum. Based on nonlinear studies Peuch et al.⁵⁹ concluded that dephasing time of the coherent plasmon oscillation is shorter than 20 fs. This process is due to the elastic interactions between the hot electrons, where the energy of all the electrons in the nanoparticle is preserved. In the following step the energy from the now thermalized electrons (having Fermi distribution of energies) is transferred to the atomic lattice of the metal particle by electron-phonon coupling. The electron-phonon interaction times are typically on the order of a few picoseconds for thin gold films.⁴⁹⁻⁵³ In the case of metal nanoparticles, an additional mechanism of relaxation of hot electronsⁱ is introduced due to the spatial confinement of the electrons, where the oscillating electrons undergo scattering at the nanoparticle surface.^{35, 60} Measurements performed for silver nanoparticles from 5 to 15 nm radius, show the electron-phonon relaxation times are comparable with value obtained for a silver film (~0.85 ps).⁶¹ The

ⁱ Hot electrons are not in thermal equilibrium with the atomic lattice.

relaxation time of silver nanoparticles, with size of 2.1 nm in radius, was reduced to ~ 0.6 ps.⁶¹ In the next step the temperature of the particle is dissipated to the surrounding medium through phonon-phonon interactions. The phonons of the atomic lattice of the metal particle couple to the phonons of the surrounding medium, where surrounding medium serves as heat sink. The phonon-phonon relaxation is usually on the order of 100-200 ps.⁶² After the full cycle the system returns to its original state. This description does not take into account interband transition and only conduction electrons are considered. This is a reasonable approximation for silver, since the plasmon resonance of silver nanoparticles has only very little overlap with interband transition.⁵

It is also important to discuss dependence of the relaxation times on excitation pump power. The experimentally measured electron-phonon relaxation time increases with increasing pump power.^{55, 56} The energy relaxation in metal nanoparticles can be modeled with two-temperature model (TTM).⁶³ The TTM model shows that the electronic heat capacity depends on the electron temperature, hence pump power. According to the model the effective rate constant of the thermal relaxation of the electron gas becomes temperature dependent.⁵

Typical transient absorption spectra of metal nanoparticles consist of the bleaching of the plasmon absorption, which is a negative absorption change and a dominating feature in the spectrum, and two much weaker, positive absorption change satellite bands.^{56, 62} The two positive features are due to broadening of the plasmon resonance band at higher electronic temperatures, followed absorption of the laser pulse by the nanoparticles.⁶⁴ The plasmon band broadening is associated with faster de-phasing time of the coherent plasmon oscillation as a result of increased electron scattering rate.

Due to the electron-phonon coupling the energy is transferred to the atomic lattice, which causes expansion of the nanoparticle volume and a decrease in the density of the electrons. The electron density is correlated with dielectric function of the metal and lowering of the density of electrons caused by thermal expansion of the nanoparticle shifts resonance towards lower frequency.^{5, 65}

1.4. Electric Field Enhancements

The collective oscillation of conduction electrons in metal nanoparticles, induced by incident light, produces its own electric field close to the nanoparticle surface. The induced electric field can be larger than the incident electric field by many orders of magnitude, depending on the distance from the metal surface and the nanoparticle size, shape and the dielectric function of the metal.^{29, 34, 66} Silver is one of the most desirable materials for strong electric field enhancements.⁶⁷ One of the first techniques exploiting this phenomenon was surface enhanced Raman spectroscopy (SERS).⁶⁸ Silver and gold are the most frequently used materials as substrates for this technique,⁶⁹ since they provide large electric field enhancements and at the same time are stable in ambient conditions. Electromagnetic enhancements as large as 10^6 were reported for systems incorporating isolated silver colloids^{67, 68, 70} Much stronger enhancements were reported for metal islands or well defined nanostructures with sharp features, such as nanoprisms,^{71, 72} nanorods⁷³⁻⁷⁵ and nanocages.⁷⁶

Optical properties of molecules near metal surfaces have been widely studied in the past three decades starting with the discovery of Raman enhancements of pyridine adsorbed on roughened silver surface.⁷⁷ Raman spectroscopy provides high structural

information, but suffers extremely small cross-sections,³² up to 12-14 orders of magnitude lower than fluorescence cross-sections, rendering it a technique of very low sensitivity.³² Thanks to SERS, the signal intensities near roughened silver surfaces can be up to 11 orders of magnitude higher than in normal Raman spectroscopy⁷⁸ bringing its sensitivity close to the detection limits of fluorescence, allowing even for single molecule detection.^{79, 80}

Fluorescence enhancements of chromophores at silver islands have been also reported.^{12, 13, 81} The enhancements are not as large as the ones observed in SERS, partially due to very efficient quenching of the excited states of the dyes. However, fluorescence can be enhanced when the chromophores are appropriately distant from the metal nanostructures.^{4, 82, 83}

Wenseleers et al.⁸⁴ reported enhancements of two-photon induced fluorescence of organic dyes in close proximity to the silver fractal structures. Theoretical studies have predicted very large electric field enhancements near random fractals.⁸⁵ Due to lack of symmetry, the random fractals provide localized plasmon modes, which produce giant local fields in sub-wavelength size, so-called hot spots. The studies of two photon induced fluorescence microscopy showed that the enhancements of the fluorescence of the chromophores deposited on silver fractals are spatially inhomogeneous.⁸⁴ The peak enhancements of fluorescence reported are as high as 160,000.⁸⁴ Two-photon absorption enhancements have also been reported for chromophores in activatedⁱⁱ gold colloid solution.⁸⁶ Using the Z-scan technique the two-photon absorption cross-section of the dye was increased by a factor of 480.

ⁱⁱ Activation of colloids is a process of aggregation of the nanoparticles.

1.5. *Chromophores near Metal Nanoparticles*

Studies of photo-physical properties of systems composed of organic dyes and metal nanoparticles are focused predominantly on radiative and nonradiative decay rates of the chromophores, and the influence of metal nanoparticles on these rates. Due to its very good stability and photo-physical properties, gold is used most of the time as a metal of choice. Silver, on the other hand, is more interesting from the aspect of optical properties,⁶⁷ but due to higher desorption rates of the ligands from silver surface⁴⁵ than from gold, it is not as frequently studied as gold. The most frequently used techniques for measuring deactivation rates of the chromophore-metal nanoparticle systems are based on fluorescence decays.^{16, 83, 87, 88} However, due to the usually large differences between fluorescence efficiencies of the chromophores attached to metal nanoparticle and free chromophores in solution, the fluorescence signals can be dominated by the desorbed chromophores.^{82, 88} The presence of free chromophoric ligands in the studied nanoparticle solutions can lead to misinterpretation of the results.

There are three main pathways that can lead to deactivation of excited chromophores in the proximity of metal nanoparticles. The first one is associated with efficient energy transfer from excited dye to the metal, where oscillating dipole strongly interacts with conduction electrons of the metal. The second possibility that needs to be considered is electron transfer from the excited dye to the metal. The third deactivation process is due to dye-dye interactions, if the chromophores are densely packed at the nanoparticle surface, which can lead, for example, to the formation of an excimer.⁸

1.5.1. Energy Transfer from the Excited Chromophores to the Metal Nanoparticle

Sparked by the fast development of SERS, several theoretical models have been developed to describe, and predict, electric field enhancements in the proximity of metal nanostructures.⁸⁹⁻⁹¹ The phenomenon of fluorescence quenching of chromophores in the proximity to a metal surface has been known for a long time. The first quantitative model was proposed by R. R. Chance and R. Silbey in the late seventies.⁹² They proposed a classical description of a dipole antenna near a flat metal surface. A more general, quasi-static model was developed in the early eighties by Gersten and Nitzan (GN).⁹³ It describes radiative and nonradiative lifetimes and the corresponding emission quantum yield of a fluorophore near or inside a small dielectric particle, and shows that its photophysical properties strongly depend on the particle size and shape.⁹³ Shortly after, an “exact” electrodynamic theory emerged,⁹⁴ which similarly to the GN model considers a chromophore close to a metal sphere. The limitation of the exact electrodynamic theory is that it can only be applied to spherical dielectric particles, whereas the GN model can be extended to spheroids, which allows for taking into account the shape-induced change of the plasmon resonance frequency and electric field intensities.⁹³ The GN model is in qualitative agreement with experimental data; however it fails when the particle approaches the limit of a flat surface.⁹¹ The model has been corrected by taking into account radiation damping and dynamic depolarization, as suggested by Wokaun and co-workers^{89, 90} and later implemented in the model by Mertens et al..⁹⁵ The authors have shown that the improved GN model is applicable over larger particle sizes than the original GN model. The authors suggested that the original GN model substantially

overestimates the radiative decay rates and to lesser extend the nonradiative decay rates, leading as a consequence, to overestimations of the quantum yields.⁹⁵

The development of a model describing the decay rates of a molecule at small distances from the nanoparticle surface is certainly more complex, since quantum effects cannot be neglected.⁹⁶ Quantum mechanical calculations of such big systems however, are very computationally demanding. This has led to the development of another classical approach, which accounts for nonlocal (NL) optical response of the metal particles and replaces the frequency dependent dielectric function $\epsilon(\omega)$ with dielectric function that is frequency and wave vector dependent $\epsilon(\mathbf{k}, \omega)$.⁹⁶ For particles smaller than 10 nm the NL model predicts greater radiative rates and smaller nonradiative rates than the original GN model. The rates are also very much dependent on the orientation of the molecule with respect to the metal surface.

Despite its computational cost, a quantum mechanical model has been proposed by Corni and Tomasi⁹⁷⁻¹⁰⁰. The chromophore in this model is treated quantum chemically using either Hartree-Fock (HF) or density-functional theory (DFT), whereas metal and solvent are considered as continuous bodies characterized by their dielectric functions.^{98, 99} The models were tested using lissamine molecule, which is located 1 nm away from the surface of gold nanoparticles of varying sizes.¹⁰¹ The results of the quantum mechanical models have been directly compared to the original GN model and experimental data.¹⁰¹ Interestingly, the radiative decays obtained from both models, quantum and GN, are in good agreement with each other, however there is an order of magnitude discrepancy with the experimental data.¹⁰¹

1.5.2. Electron Transfer from Excited Chromophores to Metal Nanoparticle

The process of electron transfer from excited-state chromophores to the metal nanoparticles is not very well established and there are relatively few reports of such deactivation mechanisms. The expectation of such electron transfer process often comes from the electrochemical reports demonstrating reversible multi-electron reduction of gold nanoparticles stabilized with alkylthiolates.^{102, 103}

Glomm et al.¹⁰⁴ studied fluorescence decay rates of ruthenium (II) tris(bipyridine) and osmium (II) tris(bipyridine) in presence of silver and gold nanoparticles. The nanoparticles, both gold and silver were electrostatically stabilized with citrate.¹⁰⁴ The results were also compared with that of gold nanoparticles coated with mercaptooctanoic acid. The authors suggested that the electron transfer from the dyes to the metal is the dominant mechanism of fluorescence quenching in all of the above cases, with some contribution from energy transfer in the case of the chromophores in the presence of the gold nanoparticles coated with mercaptooctanoic.¹⁰⁴

Nanosecond transient absorption spectroscopy has been also used to study pyrene attached to small gold nanoparticles via alkylthiolate linker.¹⁰⁵ Electron transfer from excited dye to the gold nanoparticle was suggested as the main deactivation mechanism.¹⁰⁵ However, the argument is only based on very subtle changes in the transient absorption spectra with respect to the spectra of the free chromophore in solution.

1.5.3. Inter-chromophore Interactions

A high local density of chromophores attached to metal nanoparticles can facilitate additional deactivation pathway due to interactions between the chromophores upon photo-excitation. Excimer formation between pyrene ligands attached to gold nanoparticles via alkylthiolate linker has been recently reported.¹⁰⁶ The effects of linker length and coverage dependence, by dilution of the chromophoric ligands with dodecanethiol, have been addressed. These systems were studied by fluorescence spectroscopy. Based on the correlation between coverage and relative intensity of the excimer emission with respect to monomer emission, the authors concluded that the emission comes from the excimers of pyrene moieties attached to gold nanoparticles.¹⁰⁶ Surprisingly, the fluorescence lifetime of these systems was similar to the lifetimes of the free chromophores in solution.¹⁰⁶

In another study, contradicting results were reported, where disulfides with alkyl spacers and pyrene end groups are attached to the gold nanoparticles, while fluorescence changes were recorded during this process.¹⁰⁷ The authors reported decreasing excimer emission of the disulfide-pyrene moiety upon binding to the gold nanoparticles.¹⁰⁷

1.6. Self-Assembled Monolayers

This thesis is devoted to studying chromophoric ligands adsorbed on silver nanoparticles via silver-thiol bonding. The ligands can be described by their three parts: the functional end group (the chromophore), the alkyl linker and the binding thiol group.

Due to the fact that the chromophores are attached to the silver nanoparticles through alkyl thiol it is relevant to recall literature reports on self-assembled monolayers.

Understanding and control of the properties of interfaces is extremely important in technology and is scientifically fascinating. Inorganic particles mixed in an organic medium can provide new properties of the composite material, e.g. by mixing metal oxide nanoparticles, which have a high dielectric permittivity, with an organic polymer, one can substantially increase the effective dielectric constant of the film while preserving the polymer's ease of solution processability.² The properties of interfaces are also very important in medicine, where e.g. proper treatment of titanium surfaces promotes cell adhesion and better bone-implant assimilation. Compatibility of materials that are not miscible can be obtained by introduction of a thin layer, which can compatibilize the two very different interfaces.^{2, 108} One of the most studied and extremely interesting is a single molecule layer, a monolayer.

The importance of ultrathin films at surfaces on properties such as friction and lubrication has been recognized at the beginning of the 20th century. Irvin Langmuir proposed the concept of monolayers in 1917 while studying properties of amphiphiles on water¹⁰⁹. An ordered monolayer could be produced by applying lateral pressure to a floating film and subsequently transferring it onto a solid surface, as demonstrated by Katherine Blodgett¹¹⁰. Films prepared using this technique are now known as Langmuir – Blodgett films. The technique became very popular and has found lots of applications.¹¹¹ These films however are thermodynamically unstable and their formation requires specialized apparatus.¹¹² In 1946 Ziman and coworkers¹¹³ have observed a spontaneous formation of monolayers of alkylamines on a platinum surface. This type of monolayer

formation is known as self-assembled monolayer (SAM), the name being due to the spontaneous formation without applying external pressure. The importance of the SAMs was not been recognized until 1980, when the studies of monolayers of alkanethiols on surfaces of coinage metals started dominating the emerging field. The strong Au-S bond, the inertness of gold and the stability of the thiol monolayers have made gold the substrate of choice for many research groups^{114, 115}. SAMs have been studied for potential applications in sensors,¹¹⁶ molecular recognition,¹¹⁷ growth of molecular crystals¹¹⁸ and corrosion inhibition.¹¹⁹

1.6.1. Monolayers on Gold and Silver Substrates

Fenter et. al¹²⁰ have shown that octadecylthiol on silver (111) forms a dense and well ordered monolayer with lattice spacing ~ 4.7 Å. The molecular spacing between the alkyl chains is nearly identical to the bulk hydrocarbon spacing, which appears to be constrained by molecular size of the alkyl chains.¹²¹ This finding is also consistent with studies of Langmuir-Blodgett monolayers of long *n*-alkyl chain alcohol ($\text{CH}_3(\text{CH}_2)_{20}\text{OH}$) on the surface of water¹¹². At the highest surface pressure the distance between the nearest neighbors is very similar to that found on Ag (111) for octyldecaneethiols. This is very different for *n*-alkylthiol monolayers on gold,^{111,122} where the distance between the sulfur atoms determines the packing and orientation of the ligands in the monolayers.

The differences in arrangement of SAMs between silver and gold surfaces are striking considering similarities in their atomic lattices. The distance between the nearest neighbors in Au(111) and Ag(111) are 2.88 Å and 2.89 Å respectively.¹²³ However, they differ substantially in their oxidation (by 1.7 eV) potentials and work functions (by 0.6

eV).¹²⁴ Moreover, the surface binding energies for thiolates on Au(111) show more variation for the peak-to-valley values than Ag(111), 6.0 kcal/mole for Au and 3.3 kcal/mole for Ag.¹²⁴ Thiolates on Au(111) occupy every sixth hollow site, which correspond energy minimum and to the most energetically favorable binding sites. On the other hand, the thiolates on Ag(111) can be adsorbed at less favorable sites, since the interaction between alkyl groups can provide enough stabilization energy to compete with the lower binding energy.¹²³ As a result, the packing density of alkylthiolates on gold surfaces is limited by the atomic lattice of gold, whereas on silver it is limited by the steric interactions of the alkyl chains.¹²³ Such differences in packing density result in different orientations of alkyl chains with respect to the surface, since Van der Waals interactions minimize the energy of the alkyl chains by reduction of the free volume. The most efficient means of reducing the free volume of alkyl chains attached at their binding sites is to tilt all the chains in one direction. As a result, alkyl chains on gold are oriented at $\sim 30^\circ$ to the surface normal, whereas the tilt angle of the alkyl chains on silver is below 10° .¹²³

1.7. Thesis objectives

The goal of this thesis is to understand the photophysical processes of organic chromophores in the proximity of silver nanoparticles. Such chromophore/silver nanoparticle systems can offer potential advantages in e.g. sensing^{4, 16} or light harvesting for photovoltaics,^{8, 9} however the photophysical properties of these systems are still not well understood. Moreover, in order to study such systems in the context of photophysics, they should be first thoroughly characterized for their structural properties.

The objectives of this thesis were to: 1) prepare silver nanoparticles functionalized with the organic dye, bis(diarylamino)biphenyl (TPD), covalently attached to the metal surface via alkyl linkers with varying lengths. Similar systems with mixed-ligand monolayers were also prepared, where dodecanethiol was used as a spectroscopically inert ligand, in order to decrease coverage of the TPD ligands on the nanoparticles. The coverage dependent studies address the question of the influence of intermolecular interaction on the photophysical properties of the dyes adsorbed on silver nanoparticles. 2) Characterize the silver nanoparticle/dye systems in order to determine whether the distance of the TPD chromophores from the nanoparticle surface can be controlled by the length of the alkyl linker and how the TPD ligands are packed on the silver nanoparticles. 3) Study the photophysics of the TPD dyes alone at high and low concentrations in order to understand the intrinsic photophysical decay pathways for isolated and densely packed TPD molecules. 4) Understand the mechanism of excited state relaxation of the TPD dyes on silver nanoparticle surfaces through, transient absorption spectroscopy, pulse energy, coverage and linker length dependent investigations.

The choice of the TPD moiety was motivated by its photophysical characteristics, such as high fluorescence efficiency, relatively simple photophysics and large spectral overlap of the fluorescence emission with the plasmon absorption of the silver nanoparticles. Additionally, TPD has a large two-photon cross-section at relatively short wavelengths (*ca.* 540 nm).¹²⁵ TPD is also known to be quite emissive in the solid state, although the yield is significantly lower than in solutions suggesting that there are photophysical pathways for excited state decay involving of TPD molecules. An

interesting question is whether the photophysics of TPD attached to spherical AgNP will exhibit coverage dependent relaxation or will depend on the length of the linker attaching it to the surface. Moreover, the two-photon cross-section of the chromophores, when spectrally overlapped with the plasmon absorption, might provide significant enhancements of the two-photon absorption cross-section.⁸⁴ The last argument is more relevant to gold rather than silver nanoparticles, as the gold plasmon resonance is around 520 nm and overlaps with TPD two photon absorption. However, the plasmon resonance of AgNP may be tuned to this spectral region by, e.g., aggregation of the nanoparticles or by using silver nanorods or nanoprisms instead.

1.8. References

1. Love, J. C.; Estroff, L. A.; Kriebel, J. K.; Nuzzo, R. G.; Whitesides, G. M., Self-Assembled Monolayers of Thiolates on Metals as a Form of Nanotechnology. *Chem. Rev.* **2005**, *105* (4), 1103-1170.
2. Kim, P.; Jones, S. C.; Hotchkiss, P. J.; Haddock, J. N.; Kippelen, B.; Marder, S. R.; Perry, J. W., Phosphonic Acid-Modified Barium Titanate Polymer Nanocomposites with High Permittivity and Dielectric Strength. *Adv. Mater.* **2007**, *19* (7), 1001-1005.
3. Pustovit, V. N.; Shahbazyan, T. V., Microscopic theory of surface-enhanced Raman scattering in noble-metal nanoparticles. *Phys. Rev. B* **2006**, *73* (8), 085408.
4. Lakowicz, J. R.; Fu, Y., Modification of single molecule fluorescence near metallic nanostructures. *Laser Photonics Rev.* **2009**, *3* (1-2), 221-232.
5. Link, S.; El-Sayed, M. A., Shape and size dependence of radiative, non-radiative and photothermal properties of gold nanocrystals. *Int. Rev. Phys. Chem.* **2000**, *19*, 409-453.
6. Daniel, M.-C.; Astruc, D., Gold Nanoparticles: Assembly, Supramolecular Chemistry, Quantum-Size-Related Properties, and Applications toward Biology, Catalysis, and Nanotechnology. *Chem. Rev.* **2003**, *104* (1), 293-346.

7. Stellacci, F.; Bauer, C. A.; Meyer-Friedrichsen, T.; Wenseleers, W.; Marder, S. R.; Perry, J. W., Ultrabright Supramolecular Beacons Based on the Self-Assembly of Two-Photon Chromophores on Metal Nanoparticles. *J. Am. Chem. Soc.* **2002**, *125* (2), 328-329.
8. Thomas, K. G.; Kamat, P. V., Chromophore-Functionalized Gold Nanoparticles. *Acc. Chem. Res.* **2003**, *36* (12), 888-898.
9. Barazzouk, S.; Kamat, P. V.; Hotchandani, S., Photoinduced Electron Transfer between Chlorophyll a and Gold Nanoparticles. *J. Phys. Chem. B* **2005**, *109* (2), 716-723.
10. Johansson, P.; Xu, H.; Käll, M., Surface-enhanced Raman scattering and fluorescence near metal nanoparticles. *Phys. Rev. B* **2005**, *72* (3), 035427.
11. Malicka, J.; Gryczynski, I.; Lakowicz, J. R., Fluorescence spectral properties of labeled thiolated oligonucleotides bound to silver particles. *Biopolymers* **2004**, *74* (3), 263-271.
12. Kuhn, S.; Hakanson, U.; Rogobete, L.; Sandoghdar, V., Enhancement of Single-Molecule Fluorescence Using a Gold Nanoparticle as an Optical Nanoantenna. *Phys. Rev. Lett.* **2006**, *97* (1), 017402.
13. Fort, E.; Gresillon, S., Surface enhanced fluorescence. *J. Phys. D: Appl. Phys.* **2008**, (1), 013001.
14. Huang, X.; Jain, P. K.; El-Sayed, I. H.; El-Sayed, M. A., Gold nanoparticles: interesting optical properties and recent applications in cancer diagnostics and therapy. *Nanomedicine* **2007**, *2* (5), 681-693.
15. Huang, X.; Neretina, S.; El-Sayed, M. A., Gold Nanorods: From Synthesis and Properties to Biological and Biomedical Applications. *Adv. Mater.* **2009**, *21*, 1-31.
16. Shang, L.; Qin, C.; Wang, T.; Wang, M.; Wang, L.; Dong, S., Fluorescent Conjugated Polymer-Stabilized Gold Nanoparticles for Sensitive and Selective Detection of Cysteine. *J. Phys. Chem. C* **2007**, *111* (36), 13414-13417.
17. Griffin, J.; Singh, Anant K.; Senapati, D.; Rhodes, P.; Mitchell, K.; Robinson, B.; Yu, E.; Ray, Paresh C., Size- and Distance-Dependent Nanoparticle Surface-Energy Transfer (NSET) Method for Selective Sensing of Hepatitis C Virus RNA. *Chem. - Eur. J.* **2009**, *15* (2), 342-351.
18. Cohanoschi, I.; Hernandez, F. E., Surface Plasmon Enhancement of Two- and Three-Photon Absorption of Hoechst 33 258 Dye in Activated Gold Colloid Solution. *J. Phys. Chem. B* **2005**, *109* (30), 14506-14512.
19. Li, J.; Guo, L.; Zhang, L.; Yu, C.; Yu, L.; Jiang, P.; Wei, C.; Qin, F.; Shi, J., Donor-[small pi]-acceptor structure between Ag nanoparticles and azobenzene chromophore and its enhanced third-order optical non-linearity. *Dalton Trans.* **2009**, (5), 823-831.

20. Wagner, F. E.; Haslbeck, S.; Stievano, L.; Calogero, S.; Pankhurst, Q. A.; Martinek, K. P., Before striking gold in gold-ruby glass. *Nature* **2000**, 407 (6805), 691-692.
21. Ruivo, A.; Gomes, C.; Lima, A.; Botelho, M. L.; Melo, R.; Belchior, A.; Pires de Matos, A., Gold nanoparticles in ancient and contemporary ruby glass. *Journal of Cultural Heritage* **2008**, 9 (Supplement 1), e134-e137.
22. Feldheim, D., L.; Foss, J. C. A., *Metal Nanoparticles Synthesis, Characterization, and Applications*. Marcel Dekker: New York, 2002.
23. Faraday, M., Experimental Relations of Gold (and Other Metals) to Light. *Philos. Trans. R. Soc. London, A* **1857**, 147, 331-366.
24. Newhall, B., *The History of Photography from 1839 to the Present Day*. The Museum of Modern Art New York, NY 1964.
25. Garnett, J. C. M., Colours in Metal Glasses and in Metallic Films. *Philos. Trans. R. Soc. London, A* **1904**, 203, 385-420.
26. Garnett, J. C. M., Colours in Metal Glasses, in Metallic Films, and in Metallic Solutions. II. *Philos. Trans. R. Soc. London, A* **1906**, 205, 237-288.
27. Mie, G., Beiträge zur Optik trüber Medien, speziell kolloidaler Metallosungen. *Ann. Physik* **1904**, 25, 377-445.
28. Asano, S.; Sato, M., Light scattering by randomly oriented spheroidal particles. *Appl. Opt.* **1980**, 19 (6), 962-974.
29. Kelly, K. L.; Coronado, E.; Zhao, L. L.; Schatz, G. C., The Optical Properties of Metal Nanoparticles: The Influence of Size, Shape, and Dielectric Constant. *J. Phys. Chem. B* **2003**, 17, 668-677.
30. Goad, D. G. W.; Moskovits, M., Colloidal metal in aluminum-oxide. *J. Appl. Phys.* **1978**, 49 (5), 2929-2934.
31. Lu, H. P., Site-specific Raman spectroscopy and chemical dynamics of nanoscale interstitial systems. *J. Phys.: Condens. Matter* **2005**, (7), R333.
32. Kneipp, K.; Kneipp, H.; Itzkan, I.; Dasari, R. R.; Feld, M. S., Surface-enhanced Raman scattering and biophysics. *J. Phys.: Condens. Matter* **2002**, (18), R597.
33. Dressel, M.; Gruner, G., *Electrodynamics of Solids - Optical Properties of Electrons in Matter*. CAMBRIDGE UNIVERSITY PRESS (VIRTUAL PUBLISHING): Cambridge, 2003; p 474.
34. Jensen, T.; Kelly, L.; Lazarides, A.; Schatz, G. C., Electrodynamics of Noble Metal Nanoparticles and Nanoparticle Clusters. *J. Cluster Sci.* **1999**, 10 (2), 295-317.

35. Kreibig, U.; Bour, G.; Hilger, A.; Gartz, M., Optical Properties of Cluster-Matter: Influences of Interfaces. *Physica Statatus Sololidi (a)* **1999**, *175* (1), 351-366.
36. Brust, M.; Walker, M.; Bethell, D.; Schiffrin, D. J.; Whyman, R., Synthesis of thiol-derivatised gold nanoparticles in a two-phase Liquid-Liquid system. *J. Chem. Soc., Chem. Commun.* **1995**.
37. Badia, A.; Cuccia, L.; Demers, L.; Morin, F.; Lennox, R. B., Structure and Dynamics in Alkanethiolate Monolayers Self-Assembled on Gold Nanoparticles: A DSC, FT-IR, and Deuterium NMR Study. *J. Am. Chem. Soc.* **1997**, *119* (11), 2682-2692.
38. Brust, M.; Schiffrin, D. J.; Bethell, D.; Kiely, C. J., Novel gold-dithiol nano-networks with non-metallic electronic properties. *Adv. Mater.* **1995**, *7* (9), 795-797.
39. Kohlmann, O.; Steinmetz, W. E.; Mao, X.-A.; Wuelfing, W. P.; Templeton, A. C.; Murray, R. W.; Johnson, C. S., NMR Diffusion, Relaxation, and Spectroscopic Studies of Water Soluble, Monolayer-Protected Gold Nanoclusters. *J. Phys. Chem. B* **2001**, *105* (37), 8801-8809.
40. Kira, A.; Kim, H.; Yasuda, K., Contribution of Nanoscale Curvature to Number Density of Immobilized DNA on Gold Nanoparticles. *Langmuir* **2009**, *25* (3), 1285-1288.
41. Laaksonen, T.; Pelliniemi, O.; Quinn, B. M., Ion Permeability of SAMs on Nanoparticle Surfaces. *J. Am. Chem. Soc.* **2006**, *128* (44).
42. Lazarides, A. A.; Schatz, G. C., DNA-Linked Metal Nanosphere Materials: Structural Basis for the Optical Properties. *J. Phys. Chem. B* **2000**, *104* (3), 460-467.
43. Lica, G. C.; Zelakiewicz, B. S.; Tong, Y. Y., Electrochemical and NMR characterization of octanethiol-protected Au nanoparticles. *J. Electroanal. Chem.* **2003**, *554-555*, 127-132.
44. Terrill, R. H.; Postlethwaite, T. A.; Chen, C.-h.; Poon, C.-D.; Terzis, A.; Chen, A.; Hutchison, J. E.; Clark, M. R.; Wignall, G., Monolayers in Three Dimensions: NMR, SAXS, Thermal, and Electron Hopping Studies of Alkanethiol Stabilized Gold Clusters. *J. Am. Chem. Soc.* **1995**, *117* (50), 12537-12548.
45. Bauer, C. A. Synthesis and structure-assembly realtionships of metal nanoparticles and their coupling with two-photon organic dyes. University of Arizona, Tucson, 2005.
46. Alvarez, M. M.; Khoury, J. T.; Schaaff, T. G.; Shafigullin, M. N.; Vezmar, I.; Whetten, R. L., Optical Absorption Spectra of Nanocrystal Gold Molecules. *J. Phys. Chem. B* **1997**, *101* (19), 3706-3712.
47. Mulvaney, P., Surface Plasmon Spectroscopy of Nanosized Metal Particles. *Langmuir* **1996**, *12* (3), 788-800.

48. Underwood, S.; Mulvaney, P., Effect of the Solution Refractive Index on the Color of Gold Colloids. *Langmuir* **1994**, *10* (10), 3427-3430.
49. Eesley, G. L., Generation of nonequilibrium electron and lattice temperatures in copper by picosecond laser pulses. *Phys. Rev. B* **1986**, *33* (4), 2144.
50. Eesley, G. L., Observation of Nonequilibrium Electron Heating in Copper. *Phys. Rev. Lett.* **1983**, *51* (23), 2140.
51. Groeneveld, R. H. M.; Sprik, R.; Lagendijk, A., Effect of a nonthermal electron distribution on the electron-phonon energy relaxation process in noble metals. *Phys. Rev. B* **1992**, *45* (9), 5079.
52. Groeneveld, R. H. M.; Sprik, R.; Lagendijk, A., Femtosecond spectroscopy of electron-electron and electron-phonon energy relaxation in Ag and Au. *Phys. Rev. B* **1995**, *51* (17), 11433.
53. Del Fatti, N.; Bouffanais, R.; Vallée, F.; Flytzanis, C., Nonequilibrium Electron Interactions in Metal Films. *Phys. Rev. Lett.* **1998**, *81* (4), 922.
54. Hodak, J. H.; Henglein, A.; Hartland, G. V., Photophysics of Nanometer Sized Metal Particles: Electron-Phonon Coupling and Coherent Excitation of Breathing Vibrational Modes. *J. Phys. Chem. B* **2000**, *104* (43), 9954-9965.
55. Hodak, J. H.; Martini, I.; Hartland, G. V., Spectroscopy and Dynamics of Nanometer-Sized Noble Metal Particles. *J. Phys. Chem. B* **1998**, *102* (36), 6958-6967.
56. Link, S.; Burda, C.; Wang, Z. L.; El-Sayed, M. A., Electron dynamics in gold and gold-silver alloy nanoparticles: The influence of a nonequilibrium electron distribution and the size dependence of the electron-phonon relaxation. *J. Chem. Phys.* **1999**, *111* (3), 1255-1264.
57. Link, S.; El-Sayed, M. A., Spectral Properties and Relaxation Dynamics of Surface Plasmon Electronic Oscillations in Gold and Silver Nanodots and Nanorods. *J. Phys. Chem. B* **1999**, *103* (40), 8410-8426.
58. Lamprecht, B.; Krenn, J. R.; Leitner, A.; Aussenegg, F. R., Particle-plasmon decay-time determination by measuring the optical near-field's autocorrelation: influence of inhomogeneous line broadening. *Appl. Phys. B: Lasers Opt.* **1999**, *69* (3), 223-227.
59. Puech, K.; Henari, F. Z.; Blau, W. J.; Duff, D.; Schmid, G., Investigation of the ultrafast dephasing time of gold nanoparticles using incoherent light. *Chem. Phys. Lett.* **1995**, *247* (1-2), 13-17.
60. Voisin, C.; Del Fatti, N.; Christofilos, D.; Vallee, F., Ultrafast Electron Dynamics and Optical Nonlinearities in Metal Nanoparticles. *J. Phys. Chem. B* **2001**, *105* (12), 2264-2280.

61. Del Fatti, N.; Flytzanis, C.; Vallée, F., Ultrafast induced electron–surface scattering in a confined metallic system. *Appl. Phys. B: Lasers Opt.* **1999**, 68 (3), 433-437.
62. Ahmadi, T. S.; Logunov, S. L.; El-Sayed, M. A., Picosecond Dynamics of Colloidal Gold Nanoparticles. *J. Phys. Chem.* **1996**, 100 (20), 8053-8056.
63. Rosei, R.; Antonangeli, F.; Grassano, U. M., d bands position and width in gold from very low temperature thermomodulation measurements. *Surf. Sci.* **1973**, 37, 689-699.
64. Perner, M.; Bost, P.; Lemmer, U.; von Plessen, G.; Feldmann, J.; Becker, U.; Mennig, M.; Schmitt, M.; Schmidt, H., Optically Induced Damping of the Surface Plasmon Resonance in Gold Colloids. *Phys. Rev. Lett.* **1997**, 78 (11), 2192.
65. Perner, M.; Klar, T.; Grosse, S.; Lemmer, U.; von Plessen, G.; Spirkel, W.; Feldmann, J., Homogeneous line widths of surface plasmons in gold nanoparticles measured by femtosecond pump-and-probe and near-field optical spectroscopy. *J. Lumin.* **1998**, 76-77, 181-184.
66. Shuford, K. L.; Gray, S. K.; Ratner, M. A.; Schatz, G. C., Substrate effects on surface plasmons in single nanoholes. *Chem. Phys. Lett.* **2007**, 435 (1-3), 123-126.
67. Zeman, E. J.; Schatz, G. C., An accurate electromagnetic theory study of surface enhancement factors for silver, gold, copper, lithium, sodium, aluminum, gallium, indium, zinc, and cadmium. *J. Phys. Chem.* **1987**, 91 (3), 634-643.
68. Kerker, M.; Siiman, O.; Bumm, L. A.; Wang, D. S., Surface enhanced Raman scattering (SERS) of citrate ion adsorbed on colloidal silver. *Appl. Opt.* **1980**, 19 (19), 3253-3255.
69. Kneipp, K.; Kneipp, H.; Itzkan, I.; Dasari, R. R.; Feld, M. S., Ultrasensitive Chemical Analysis by Raman Spectroscopy. *Chem. Rev.* **1999**, 99 (10), 2957-2976.
70. Wang, D. S.; Kerker, M., Enhanced Raman scattering by molecules adsorbed at the surface of colloidal spheroids. *Phys. Rev. B* **1981**, 24 (4), 1777.
71. Ciou, S.-H.; Cao, Y.-W.; Huang, H.-C.; Su, D.-Y.; Huang, C.-L., SERS Enhancement Factors Studies of Silver Nanoprism and Spherical Nanoparticle Colloids in The Presence of Bromide Ions. *J. Phys. Chem. C* **2009**, 113 (22), 9520-9525.
72. Cui, B.; Clime, L.; Li, K.; Veres, T., Fabrication of large area nanoprism arrays and their application for surface enhanced Raman spectroscopy. *Nanotechnology* **2008**, (14), 145302.
73. Nikoobakht, B.; Wang, J.; El-Sayed, M. A., Surface-enhanced Raman scattering of molecules adsorbed on gold nanorods: off-surface plasmon resonance condition. *Chem. Phys. Lett.* **2002**, 366 (1-2), 17-23.

74. Jana, N. R.; Pal, T., Anisotropic Metal Nanoparticles for Use as Surface-Enhanced Raman Substrates. *Adv. Mater.* **2007**, *19* (13), 1761-1765.
75. Oyelere, A. K.; Chen, P. C.; Huang, X.; El-Sayed, I. H.; El-Sayed, M. A., Peptide-Conjugated Gold Nanorods for Nuclear Targeting. *Bioconjugate Chem.* **2007**, *18* (5), 1490-1497.
76. Skrabalak, S. E.; Chen, J.; Au, L.; Lu, X.; Li, X.; Xia, Y., Gold Nanocages for Biomedical Applications. *Adv. Mater.* **2007**, *19* (20), 3177-3184.
77. Fleischmann, M.; Hendra, P. J.; McQuillan, A. J., Raman spectra of pyridine adsorbed at a silver electrode. *Chem. Phys. Lett.* **1974**, *26* (2), 163-166.
78. Xu, H.; Aizpurua, J.; Käll, M.; Apell, P., Electromagnetic contributions to single-molecule sensitivity in surface-enhanced Raman scattering. *Phys. Rev. E* **2000**, *62* (3), 4318.
79. Kneipp, K.; Wang, Y.; Kneipp, H.; Perelman, L. T.; Itzkan, I.; Dasari, R. R.; Feld, M. S., Single Molecule Detection Using Surface-Enhanced Raman Scattering (SERS). *Phys. Rev. Lett.* **1997**, *78* (9), 1667.
80. Kneipp, K.; Kneipp, H.; Kartha, V. B.; Manoharan, R.; Deinum, G.; Itzkan, I.; Dasari, R. R.; Feld, M. S., Detection and identification of a single DNA base molecule using surface-enhanced Raman scattering (SERS). *Phys. Rev. E* **1998**, *57* (6), R6281.
81. Yongdong, L.; Mahdavi, F.; Blair, S., Enhanced fluorescence transduction properties of metallic nanocavity arrays. *IEEE J. Sel. Top. Quantum Electron.* **2005**, *11* (4), 778-784.
82. Anger, P.; Bharadwaj, P.; Novotny, L., Enhancement and Quenching of Single-Molecule Fluorescence. *Phys. Rev. Lett.* **2006**, *96* (11), 113002.
83. Horimoto, N. N.; Imura, K.; Okamoto, H., Dye fluorescence enhancement and quenching by gold nanoparticles: Direct near-field microscopic observation of shape dependence. *Chem. Phys. Lett.* **2008**, *467* (1-3), 105-109.
84. Wenseleers, W.; Stellacci, F.; Meyer-Friedrichsen, T.; Mangel, T.; Bauer, C. A.; Pond, S. J. K.; Marder, S. R.; Perry, J. W., Five Orders-of-Magnitude Enhancement of Two-Photon Absorption for Dyes on Silver Nanoparticle Fractal Clusters. *J. Phys. Chem. B* **2002**, *106* (27), 6853-6863.
85. Drachev, V. P.; Bragg, W. D.; Podolskiy, V. A.; Safonov, V. P.; Kim, W.-T.; Ying, Z. C.; Armstrong, R. L.; Shalaev, V. M., Large local optical activity in fractal aggregates of nanoparticles. *J. Opt. Soc. Am. B* **2001**, *18* (12), 1896-1903.
86. Cohanoschi, I.; Hernandez, F. E., Surface Plasmon Enhancement of Two- and Three-Photon Absorption of Hoechst 33 258 Dye in Activated Gold Colloid Solution. *J. Phys. Chem. B* **2005**, *109* (30), 14506-14512.

87. Issa, N. A.; Guckenberger, R., Fluorescence near metal tips: The roles of energy transfer and surface plasmon polaritons. *Opt. Express* **2007**, *15* (19), 12131-12144.
88. Jennings, T. L.; Singh, M. P.; Strouse, G. F., Fluorescent Lifetime Quenching near $d = 1.5$ nm Gold Nanoparticles: Probing NSET Validity. *J. Am. Chem. Soc.* **2006**, *128* (16), 5462-5467.
89. Wokaun, A.; Gordon, J. P.; Liao, P. F., Radiation Damping in Surface-Enhanced Raman Scattering. *Phys. Rev. Lett.* **1982**, *48* (14), 957.
90. Meier, M.; Wokaun, A., Enhanced fields on large metal particles: dynamic depolarization. *Opt. Lett.* **1983**, *8* (11), 581-583.
91. Kim, Y. S.; Leung, P. T.; George, T. F., Classical decay rates for molecules in the presence of a spherical surface: A complete treatment. *Surf. Sci.* **1988**, *195* (1-2), 1-14.
92. Chance, R. R.; Prock, A.; Silbey, R., Molecular Fluorescence and Energy Transfer Near Interfaces. *Adv. Chem. Phys.* **1978**, *37*, 1-65.
93. Gersten, J.; Nitzan, A., Spectroscopic properties of molecules interacting with small dielectric particles. *J. Chem. Phys.* **1981**, *75* (3), 1139-1152.
94. Ruppin, R., Decay of an excited molecule near a small metal sphere. *J. Chem. Phys.* **1982**, *76* (4), 1681-1684.
95. Mertens, H.; Koenderink, A. F.; Polman, A., Plasmon-enhanced luminescence near noble-metal nanospheres: Comparison of exact theory and an improved Gersten and Nitzan model. *Phys. Rev. B* **2007**, *76* (11), 115123.
96. Vielma, J.; Leung, P. T., Nonlocal optical effects on the fluorescence and decay rates for ad molecules at a metallic nanoparticle. *J. Chem. Phys.* **2007**, *126* (19), 194704.
97. Corni, S.; Tomasi, J., Theoretical evaluation of Raman spectra and enhancement factors for a molecule adsorbed on a complex-shaped metal particle. *Chem. Phys. Lett.* **2001**, *342* (1-2), 135-140.
98. Corni, S.; Tomasi, J., Enhanced response properties of a chromophore physisorbed on a metal particle. *J. Chem. Phys.* **2001**, *114* (8), 3739-3751.
99. Corni, S.; Tomasi, J., Excitation energies of a molecule close to a metal surface. *J. Chem. Phys.* **2002**, *117* (15), 7266-7278.
100. Andreussi, O.; Corni, S.; Mennucci, B.; Tomasi, J., Radiative and nonradiative decay rates of a molecule close to a metal particle of complex shape. *J. Chem. Phys.* **2004**, *121* (20), 10190-10202.
101. Dulkeith, E.; Morteaux, A. C.; Niedereichholz, T.; Klar, T. A.; Feldmann, J.; Levi, S. A.; van Veggel, F. C. J. M.; Reinhoudt, D. N.; Möller, M.; Gittins, D. I., Fluorescence

Quenching of Dye Molecules near Gold Nanoparticles: Radiative and Nonradiative Effects. *Phys. Rev. Lett.* **2002**, 89 (20), 203002.

102. Hicks, J. F.; Miles, D. T.; Murray, R. W., Quantized Double-Layer Charging of Highly Monodisperse Metal Nanoparticles. *J. Am. Chem. Soc.* **2002**, 124 (44), 13322-13328.

103. Hicks, J. F.; Templeton, A. C.; Chen, S.; Sheran, K. M.; Jasti, R.; Murray, R. W.; Debord, J.; Schaaff, T. G.; Whetten, R. L., The Monolayer Thickness Dependence of Quantized Double-Layer Capacitances of Monolayer-Protected Gold Clusters. *Anal. Chem.* **1999**, 71 (17), 3703-3711.

104. Glomm, W. R.; Moses, S. J.; Brennaman, M. K.; Papanikolas, J. M.; Franzen, S., Detection of Adsorption of Ru(II) and Os(II) Polypyridyl Complexes on Gold and Silver Nanoparticles by Single-Photon Counting Emission Measurements. *J. Phys. Chem. B* **2004**, 109 (2), 804-810.

105. Ipe, B. I.; Thomas, K. G.; Barazzouk, S.; Hotchandani, S.; Kamat, P. V., Photoinduced Charge Separation in a Fluorophor Gold Nanoassembly. *J. Phys. Chem. B* **2001**, 106 (1), 18-21.

106. Ipe, B. I.; Thomas, K. G., Investigations on Nanoparticle-Chromophore and Interchromophore Interactions in Pyrene-Capped Gold Nanoparticles. *J. Phys. Chem. B* **2004**, 108 (35), 13265-13272.

107. Werts, M. H. V.; Zaim, H.; Blanchard-Desce, M., Excimer probe of the binding of alkyl disulfides to gold nanoparticles and subsequent monolayer dynamics. *Photochem. Photobiol. Sci.* **2004**, 3 (1), 29-32.

108. Nuzzo, R. G.; Dubois, L. H.; Allara, D. L., Fundamental studies of microscopic wetting on organic surfaces. 1. Formation and structural characterization of a self-consistent series of polyfunctional organic monolayers. *J. Am. Chem. Soc.* **1990**, 112 (2), 558-569.

109. Langmuir, I., The constitution and fundamental properties of solids and liquids. Liquids.1. *J. Am. Chem. Soc.* **1917**, 39 (9), 1848-1906.

110. Blodgett, K. B., Films Built by Depositing Successive Monomolecular Layers on a Solid Surface. *J. Am. Chem. Soc.* **1935**, 57 (6), 1007-1022.

111. Chidsey, C. E. D.; Liu, G.-Y.; Rowntree, P.; Scoles, G., Molecular order at the surface of an organic monolayer studied by low energy helium diffraction. *J. Chem. Phys.* **1989**, 91 (7), 4421-4423.

112. Barton, S. W.; Thomas, B. N.; Flom, E. B.; Rice, S. A.; Lin, B.; Peng, J. B.; Ketterson, J. B.; Dutta, P., X-ray diffraction study of a Langmuir monolayer of C₂₁H₄₃OH. *J. Chem. Phys.* **1988**, 89, 2257.

113. Bigelow, W. C.; Picket, D. L.; Zisman, W. P., Oleophobic monolayers I. Films adsorbed from solution in nonpolar liquids. *J. Colloid Interface Sci.* **1946**, *1*, 513.
114. Barfield, M., Nuclear spin-spin coupling via nonbonded interactions. 1. Conformational and substituent effects on vicinal carbon-13-proton and carbon-13-carbon-13 coupling constants. *J. Am. Chem. Soc.* **1980**, *102* (1), 1-7.
115. Nuzzo, R. G.; Allara, D. L., Adsorption of bifunctional organic disulfides on gold surfaces. *J. Am. Chem. Soc.* **1983**, *105* (13), 4481-4483.
116. Kepley, L. J.; Crooks, R. M.; Ricco, A. J., A selective SAW-based organophosphonate chemical sensor employing a self-assembled, composite monolayer: a new paradigm for sensor design. *Anal. Chem.* **1992**, *64* (24), 3191-3193.
117. Lukas Häussling, B. M., Helmut Ringsdorf, Heinrich Rohrer., Direct Observation of Streptavidin Specifically Adsorbed on Biotin-Functionalized Self-Assembled Monolayers with the Scanning Tunneling Microscope. *Angew. Chem., Int. Ed. Engl.* **1991**, *30* (5), 569-572.
118. Frostman, L. M.; Bader, M. M.; Ward, M. D., Nucleation and Growth of Molecular Crystals on Self-Assembled Monolayers. *Langmuir* **1994**, *10* (2), 576-582.
119. Yamamoto, Y.; Nishihara, H.; Aramaki, K., Self-Assembled Layers of Alkanethiols on Copper for Protection Against Corrosion. *J. Electrochem. Soc.* **1993**, *140* (2), 436-443.
120. Fenter, P.; Eisenberger, P.; Li, J.; Camillone, N.; Bernasek, S.; Scoles, G.; Ramanarayanan, T. A.; Liang, K. S., Structure of octadecyl thiol self-assembled on the silver(111) surface: an incommensurate monolayer. *Langmuir* **1991**, *7* (10), 2013-2016.
121. Doucet, J.; Denicolo, I.; Craievich, A., X-ray study of the "rotator" phase of the odd-numbered paraffins C₁₇H₃₆, C₁₉H₄₀, and C₂₁H₄₄. *J. Chem. Phys.* **1981**, *75* (3), 1523-1529.
122. Strong, L.; Whitesides, G. M., Structures of self-assembled monolayer films of organosulfur compounds adsorbed on gold single crystals: electron diffraction studies. *Langmuir* **1988**, *4* (3), 546-558.
123. Ulman, A., Formation and Structure of Self-Assembled Monolayers. *Chem. Rev.* **1996**, *96* (4), 1533-1554.
124. Sellers, H.; Ulman, A.; Shnidman, Y.; Eilers, J. E., Structure and binding of alkanethiolates on gold and silver surfaces: implications for self-assembled monolayers. *J. Am. Chem. Soc.* **1993**, *115* (21), 9389-9401.
125. Paci, B.; Andraud, C.; Anemian, R.; Nunzi, J.-M., One- and two-photon picosecond excitation dynamics of the singlet states of a tetraphenyl-diamine derivative in solution. *J. Phys. B: At., Mol. Opt. Phys.* **2004**, (8), 1581.

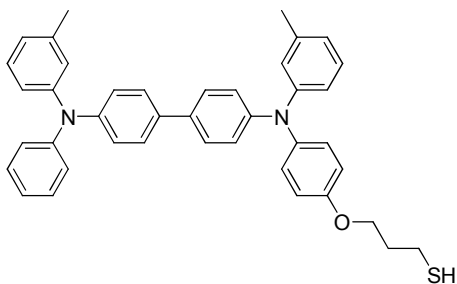
CHAPTER 2

MATERIALS AND METHODS

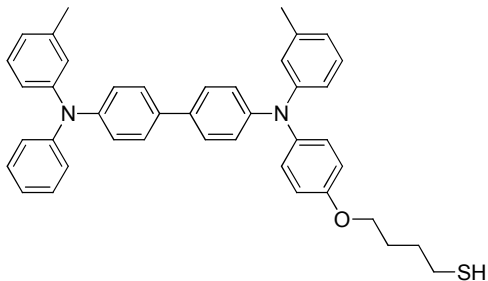
2.1. Materials

All solvents, other than ethanol, were purchased from Aldrich and used as received. Reagent grade solvents were used in all syntheses and spectrophotometric grade solvents were used in all optical measurements. Ethanol (200 proof) was supplied by VWR stockroom. All reagents were used as received: silver acetate (99.99 %) and dodecylthiol were supplied by Aldrich except for oleylamine (supplied by Acros), which was distilled and stored under nitrogen.

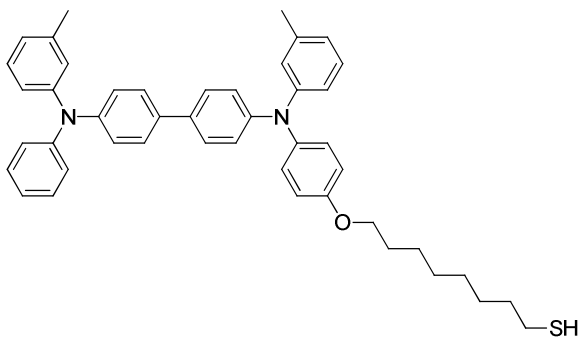
The following ligands used in this dissertation were synthesized by Dr. Michal Malicki:



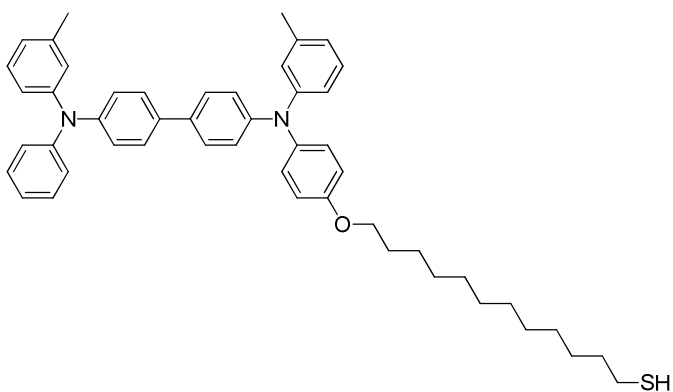
3-(4-{[4'-(Phenyl-m-tolyl-amino)-biphenyl-4-yl]-m-tolyl-amino}-phenoxy)-propane-1-thiol (TPDC3SH)



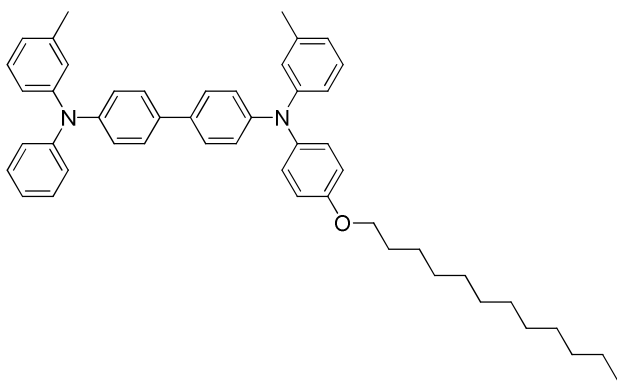
N-[4-(12-Mercaptobutyloxy)phenyl]-*N'*-phenyl-*N,N'*-di(*m*-tolyl)-biphenyl-4,4'-diamine
(TPDC4SH)



N-[4-(12-Mercaptooctyloxy)phenyl]-*N'*-phenyl-*N,N'*-di(*m*-tolyl)-biphenyl-4,4'-diamine
(TPDC8SH)



N-[4-(12-Mercaptododecyloxy)phenyl]-*N'*-phenyl-*N,N'*-di(*m*-tolyl)-biphenyl-4,4'-diamine
(TPDC12SH)



N-[4-(Dodecyloxy)phenyl]-*N'*-phenyl-*N,N'*-di(*m*-tolyl)-biphenyl-4,4'-diamine (**TPDC12**)

2.2. Preparation of Silver Nanoparticles in the Presence of Oleylamine (OA)

The silver nanoparticles were synthesized according to a modified method reported by Hiramatsu et al.¹ Silver acetate (0.83 g, 5.0 mmol) was dissolved in a mixture of 12 mL of freshly distilled oleylamine (OA) and 8 mL of toluene. The solution was then added into 100 mL of boiling o-xylene. The mixture was stirred with a Teflon coated magnetic stir bar. The progress of the reaction was monitored by UV-vis absorption, where 10 μ L of the reaction mixture was diluted in 3 mL of toluene in 1 cm glass cuvette. The reaction was stopped after about 23 hours, when the intensity of plasmon absorption did not increase within 1 hour. The reaction mixture was then cooled to about 80°C and excess solvent was removed using nitrogen flow until the volume of the mixture was about 20 mL. The mixture was then cooled to room temperature. Subsequently, the nanoparticles were precipitated by addition of ~80 mL of ethanol. The precipitated nanoparticles were centrifuged at 3500 rcf for 3 min and washed 3 times with ethanol. The nanoparticles were dried in vacuum oven at room temperature over night and then transferred to a glove box under nitrogen. Subsequently, the nanoparticles were dissolved

in 5 mL of deoxygenated toluene. From this moment all the nanoparticles were handled under nitrogen. The final weight (273 mg) was determined based on the amount of silver only, by measuring the concentration of silver using inductively coupled plasma – emission spectrometry (ICP-ES).ⁱⁱⁱ The size of the nanoparticles measured with TEM was 4.3 ± 1.5 nm.

2.3. *Reacting OA-Coated Silver Nanoparticles with Thiols – Place Exchange Reaction*

The thiol of choice or mixture of thiols, with 33% or 66% of dodecanethiol (DDT) by mole in the mixture of two thiols, was added to the known volume of the stock solution of OA-coated silver nanoparticles (concentration 54.6 mg / mL) in 1.5 times excess,^{iv} and the mixture was stirred for about 2 h. After that the particles were then precipitated with addition of about 3mL of hexane. The resulting precipitate was repetitively washed with hexane until only weak fluorescence was observed in the supernatant upon UV-irradiation (usually about 5 washes). The fluorescence could not be completely eliminated.

The choice of 1.5 times excess in the place exchange reaction described above was determined based on small scale test. Small volumes of the AgNP stock solution were mixed with specific volumes of prepared stock solutions of the thiols. The volumes of the thiols used were based on the calculation of the stoichiometry in the footnote,^{iv} the

ⁱⁱⁱ The procedure for the sample preparation for ICP-ES is described in the instrumental section devoted to this technique

^{iv} The stoichiometry of the reaction was calculated assuming the thiol footprint² (F_{thiol}) of 18 \AA^2 and the total mass of starting NP's (m_{NP}) coming from metallic silver with density³ $d_{Ag} = 10.5 \text{ g/cm}^3$. The total surface of particles (S) was computed according to $S = \frac{3m_{NP}}{rd_{Au}}$ where r is particle radius (2.13 nm). The

needed amount of moles of the thiol (n_{thiol}) was calculated according to $n_{thiol} = \frac{S}{N_A F_{thiol}}$.

thiols would be in 1, 1.5, 2 and 3 times excess.^v Also an equivalent of the TPDC4SH was used without AgNP as a reference sample. After 2h the particles were precipitated with the same volume of hexane for each sample and centrifuged at 3500 rcf; the same volume was also added to the reference sample. The supernatants were collected and their UV-vis absorption spectra were recorded. Figure 2.1 shows the spectra of the supernatants after reaction of the AgNP with TPDC4SH, and the reference solution.

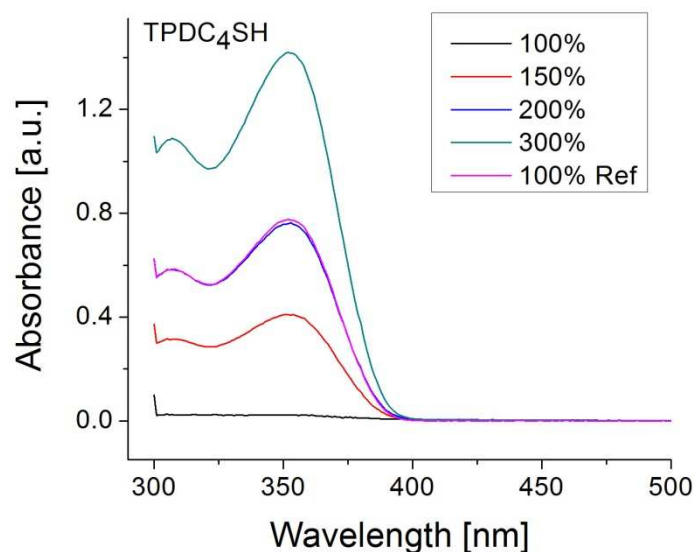


Figure 2.1. UV-vis spectra of supernatants after a small scale place exchange reaction of OA - AgNP with TPDC4SH. The legend shows molar percentages of the thiols with respect to the available binding sites, which were determined according to the calculation provided in footnote iv. 100% Ref is a reference spectrum of a solution with the molar amount of the TPD-thiol equivalent to 100% of available binding sites that was not exposed to silver nanoparticles. All the supernatants and the reference solution had the same volumes.

^v The values of excess are equivalent to the molar percentages of the thiols with respect to the available binding sites shown in the Figure 2.1.

The reference solution has the molar equivalent of the TPD-thiol to 100% of the available binding sites of the AgNP used in this experiment.

The spectrum of the supernatant after place exchange reaction for the sample with 100% of the calculated coverage (or equivalent number of TPDC4SH to the number of available binding sites) is not distinguishable from baseline. The spectrum with 200% of the calculated coverage (or 2 times excess) has the same intensity as the reference sample. The spectra of the rest of the samples scale quantitatively with the amount of thiols used. This suggests stoichiometric reaction of thiols with the AgNP. Thus, 1.5 times excess value was chosen for the large scale synthesis in order to ensure full coverage of AgNP with the thiols.

2.4. Nomenclature of the Prepared AgNP / Thiol Systems

The AgNP / thiol systems are named in the following way: AgTPDC_{x-z}, where x = 3, 4, 8 or 12, and z = I, II or III. Number x represents number of carbon atoms in the alkyl linker of the TPD ligand and roman number z is larger for larger fraction of dodecanethiol used during the exchange of ligands. The nomenclature is summarized in the Table 2.1.

Table 2.1. Nomenclature of the nanoparticles with the composition of their organic monolayers.

Sample name	Molar %	Sample name	Molar %
AgTPDC3-I	100%	AgTPDC8-I	100%
AgTPDC3-II	66%	AgTPDC8-II	66%
AgTPDC3-III	33%	AgTPDC8-III	33%
AgTPDC4-I	100%	AgTPDC12-I	100%
AgTPDC4-II	50%	AgTPDC12-II	66%
		AgTPDC12-III	33%

2.5. Stability of the AgNP / Dye Systems – Choice of Solvents

UV-vis absorption spectra of silver nanoparticles dissolved in toluene decay over time and nanoparticles stain walls of the cuvette. Stability of AgNP in solution can be significantly improved by mixing toluene with small amount of DMF. Mixture of 5:1 toluene and DMF was chosen, since the AgTPDC_{x-I} do not stain glass over a very long time, at least 48 h; AgNP with mixed ligands stain glass sooner and the observed trend is that the higher fraction of DDT the faster glass staining was observed.

2.6. *Experimental Methodology*

2.6.1. *FT-IR*

A nitrogen-purged Digilab FTS-600 FT-IR instrument equipped with an MCT detector was used for measuring IR absorption spectra of films. A KBr disc was used as a substrate for the films in the measurements. 126 scans were collected for each spectrum with 2 cm^{-1} resolution. Each solution transmission spectrum was referenced to the transmission spectrum of clean KBr disc and the baseline was corrected manually using the spline function approach.

2.6.2. *UV-Vis-NIR Absorption and Fluorescence Spectroscopy*

Absorption spectra of solutions in quartz cuvettes were recorded on a Shimadzu UV-3600 UV-Vis-NIR spectrometer. Fluorescence spectra of solutions in quartz cuvettes were acquired on a Fluorolog 2 spectrofluorimeter from Horiba Jobin Yvon and were corrected for instrument response.

2.6.3. *NMR Experiments*

^1H NMR spectra were recorded using Bruker DRX-500 or Varian Gemini-300 spectrometers. Measurements of T_1 and T_2 relaxation times of CD_2Cl_2 solutions of Ag NPs were performed with the use of a Bruker DRX-500. T_1 relaxation time measurements were performed using the conventional population-inversion recovery method, and the Carr-Purcell-Meiboom-Gill (CPMG) pulse sequence was employed in T_2 relaxation time measurements.

2.6.4. *Transmission Electron Microscopy (TEM)*

A toluene solution of each NP sample was drop casted onto a holey carbon-coated copper grid substrate. The analysis was performed using a JEOL 100 CX-II system at 100 kV acceleration voltage. The instrument is equipped with a calibrated CCD camera that was used to acquire the images. More than 400 particles were analyzed for each sample using the freeware ImageJ to obtain particle size distribution.

2.6.5. *Inductively Coupled Plasma – Emission Spectroscopy (ICP-ES)*

The ICP-ES analysis was performed by the Chemical Analysis Laboratory at the Institute of Paper Science and Technology at Georgia Institute of Technology. The aqueous solutions for ICP-ES analysis were prepared by oxidizing small volumes, 20 – 160 μ L, of the stock solutions of nanoparticles with 0.5 mL HNO_3 followed by dilution with 10 mL of distilled water.

2.6.6. *Time-Correlated Single Photon Counting (TCSPC)*

Fluorescence lifetimes of solutions were measured using the time-correlated single-photon counting technique. A schematic representation of the optical setup is shown in Figure 2.2. A femtosecond mode-locked Ti:Sapphire laser (Tsunami, Spectra-Physics) pumped by a 5W diode laser (Millennia, Spectra-Physics) was used as the excitation source. The laser generated pulses of mean power ~ 0.5 W with the repetition rate of ~ 81 MHz at 730 nm. The laser beam was split (BS2) and a small fraction of the light was directed to a spectrum analyzer. The rest of the beam was split again (BS2) and

ca. 5% of the beam was focused onto the timing photodiode (Newport 818-BB-21A, PD1). The photodiode signal was used to drive a constant-fraction discriminator (Tennelec TC455 Quad, CFD2). The rate of the discriminator output pulses was reduced sixteen times with the use of a frequency divider (FD, Pulse Research Lab, PRL-256N). The divided signal was sent through another constant fraction discriminator (CFD4) to the stop input of a time to amplitude converter (Ortec 457, TAC). The majority of the laser beam was focused onto a BBO crystal and frequency doubled. The resulting second harmonic (365 nm) and the fundamental beams were separated after passing a quartz prism and a half-wave plate. The fundamental beam was blocked and the frequency doubled beam was sent through a pinhole to a Glan-Thompson polarizer (POL1) with the transmitted polarization direction oriented perpendicularly to the surface of the table. The power at the sample was controlled by rotating the polarization plane of the half-wave plate. The beam was passed through a beam splitter (BS3) and the reflected light was focused onto a DC-coupled photodiode (Thorlabs DET210, PD2) connected to a series RC circuit with a time constant of 0.22 sec. The output of the RC circuit was connected to an input of a DAQ board (National Instruments, USB-6221 BNC) connected via a USB port to a PC. This electronic setup was used as the “signal integrator”, effectively measuring the relative energy dose at the sample. The transmitted beam was focused on the sample by a quartz lens with a 30 cm focal length. The sample holder was masked so only a small portion of the fluorescence light was collected. The fluorescence was detected at 90° with respect to the excitation beam. The fluorescence light was collimated by a quartz lens and sent through a sheet polarizer (POL2) with its polarization plane at the magic angle (54.7°) to the normal of the surface of the table. The light was then sent

through a depolarizer (DEPOL) and focused onto the entrance slit of a monochromator (Instruments SA H10, 1200 grooves/mm, 100 mm path length, Mono). The monochromatic light was then sent to a photomultiplier tube (Hamamatsu R1564U-01, PMT) biased at 3250 V. The pulses from the photomultiplier were amplified by a 1 GHz amplifier (Ortec 9306, Amp) and sent to a constant fraction discriminator (CFD3) and then to the start input of the time-to-amplitude converter (TAC). The output of the time-to-amplitude converter was directed to a pulse height analyzer (Ortec-Norland 5600 Multichannel Analyzer, PHA), and transferred to a personal computer (PC). The PHA channel width was determined for each experiment from the distance between two consecutive laser pulses and the repetition rate of the laser (measured by the timing photodiode PD2 and a pulse counter (Protek B-808)). The Instrument Response Function (IRF) was measured before each decay experiment using silica particles suspended in water (Ludox, Aldrich). The full width at half maximum (FWHM) of the response function was between 50 and 70 ps. The system was optimized by checking the goodness of the fit (χ^2 , randomness of residual function) and the extracted value of the fluorescence lifetime of the fitted decay function of 1,4-bis(5-phenyloxazol-2-yl) benzene (POPOP) in degassed cyclohexane.^{17,18} Generally values of χ^2 lower than 1.20 indicated good fits. In order to ensure operation in the linear regime of the electronics, the count rate at the Start input of TAC was kept below 10 kcps. Both IRFs and decays were collected until the number of counts at maximum reached 10,000, although for unstable NP samples only 5,000 counts at maximum were collected. The experimental data were fitted using the FAST software from Edinburgh Instruments.

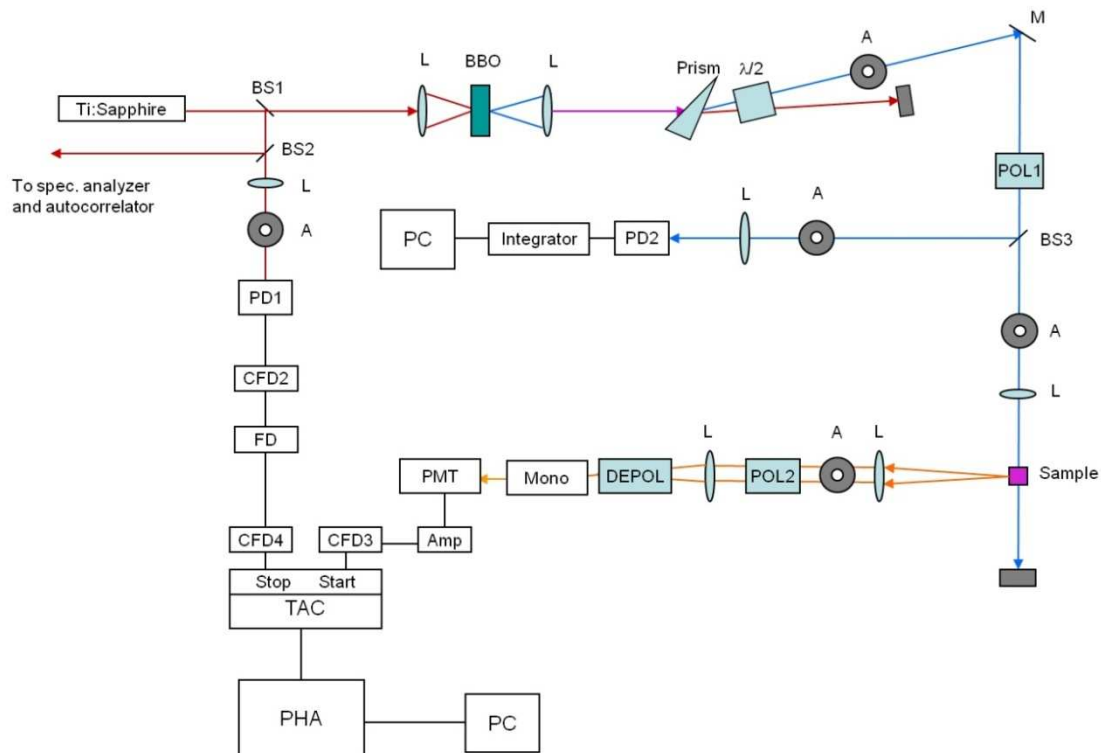


Figure 2.2. Scheme of the optical layout of TC-SPC experiment; L = lens, A = aperture, $\lambda/2$ = Half-wave plate. See text for the details. Schematics provided by Dr. Michal Malicki.

2.6.7. Nanosecond Transient Absorption (TA)

The measurement of the visible transient absorption spectrum of ca. 1×10^{-5} M toluene solution of TPDC12 was performed with the help of Mr. Matteo Cozzuol (the Perry group). The solution was degassed by the freeze-pump-thaw technique and kept in a sealed quartz cuvette with a 1 cm optical path. Figure 2.3 shows a schematic of the optical setup for the TA measurement. The 355 nm excitation beam in the nanosecond transient absorption setup was generated by a nanosecond Q-switched laser (Newport Spectra Physics Quanta-Ray PRO-250-10) with 8 ns pulse duration. The energy of the

pulse was measured using a PE25BB pyroelectric head connected to an Ophir Nova II power meter and the power stability was constantly monitored during the measurement. This was done by placing a glass slide along the propagation path of the excitation beam and redirecting ca. 4 % of the excitation beam to an amplified silicon PIN detector (Newport 818-BB-21A). The collected signal was converted to a DC output in the range from 0 to 10 Volts by a gated integrator (SRS SR250). A National Instrument BNC-2110 data acquisition interface was used to save the data into a personal computer. A white-light source (Newport, 250 W tungsten lamp, driven by a 300 W radiometric power supply, model 69931) was used as the probe. The angle between the pump and the probe light was about 15° and it was kept as small as possible to maximize the pump-probe spatial overlap. After passing through the sample, the probe light was sent to a monochromator (PI SP150) and then to an PIN detector (HCA-S-200M-Si). The electric signal from the photodiode was detected with an oscilloscope (Tektronix TDS 3034b), triggered by the Quanta-Ray Q-switch pulse, and recorded into a personal computer memory via a GPIB interface. Changes in optical density as a function of time, $\Delta OD(t)$, were calculated according to: $\Delta OD(t) = -\log (I(t) / I_0)$, where I_0 is an averaged signal from the photodiode measured before the laser pulse, and $I(t)$ is the photodiode signal measured at a delay t from the excitation pulse.

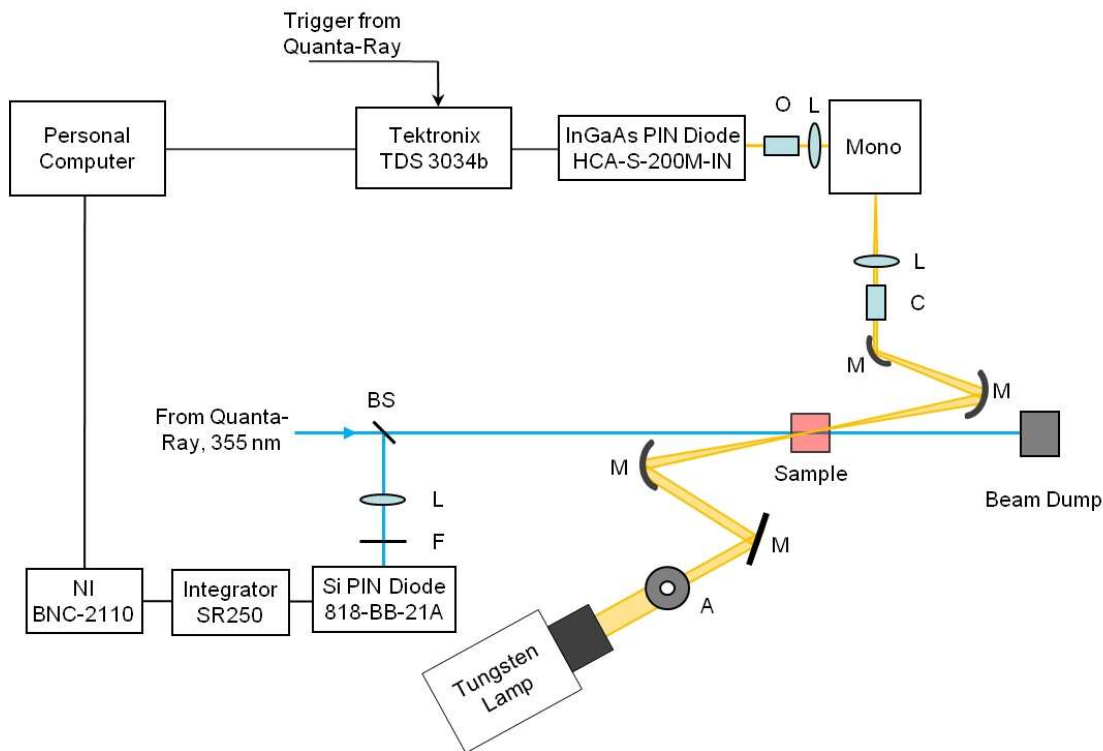


Figure 2.3. Scheme of the optical layout of the nanosecond TA experiment; BS = beam splitter, L = lens, F = filter, M = mirror, A = aperture, C = collimator, O = microscope objective, Mono = monochromator. See text for the details. Schematics provided by Mr. Matteo Cozzuol.

2.6.8. Femtosecond Broad-Band Transient Absorption

Femtosecond transient absorption spectra were acquired using a commercially available transient absorption spectroscopy system (Newport, Helios). The optical layout is shown in Figure 2.4. This system accepts two input laser beams, one of variable wavelength used as the pump beam and one of a fixed wavelength (800 nm) used to generate the probe beam in a proprietary nonlinear optical crystal. For the pump beam, the light source was an ultrafast optical parametric amplifier (Newport, TOPAS) running

at a repetition rate of 1 kHz, pumped by a Ti:Sapphire regenerative amplifier (Newport, Spitfire). The TOPAS output was set to 700 nm with a pulse width of approximately 120 fs (FWHM) and frequency doubled using a BBO crystal, resulting in the excitation wavelength of 350 nm. Approximately 5% of the Spitfire fundamental at 800 nm was used for NIR white-light continuum (WLC) generation (400 – 750 or 850 – 1650 nm) in the Helios nonlinear crystal to provide the experimental probe beam. The polarization of the excitation beam was set to the magic angle with respect to the polarization of the probe beam in order to sample pure depopulation dynamics. With these specifications, the instrument response function (IRF) was approximately 300 – 400 fs (FWHM).^{vi} The temporal window that can be studied is 3200 ps wide. At each temporal delay point, data were averaged for 2 s. The Helios pump beam was chopped at 500 Hz to obtain pumped (signal) and non-pumped (reference) absorption spectra of the sample. The data were stored as 3-D Wavelength-Time-Absorbance matrices that were exported for use with the fitting software.

^{vi} IRF was assumed to have a Gaussian profile and its width (FWHM) was estimated based on fitting of time resolved data of various samples in the software provided by the manufacturer of Helios (Surface Explorer Pro from Newport, Spectra Physics). The fitting procedure takes into account IRF with its width as one of the parameters. Allowing IRF width to be a floating parameter returned values between 300 and 400 fs for transient absorption data in the NIR range.

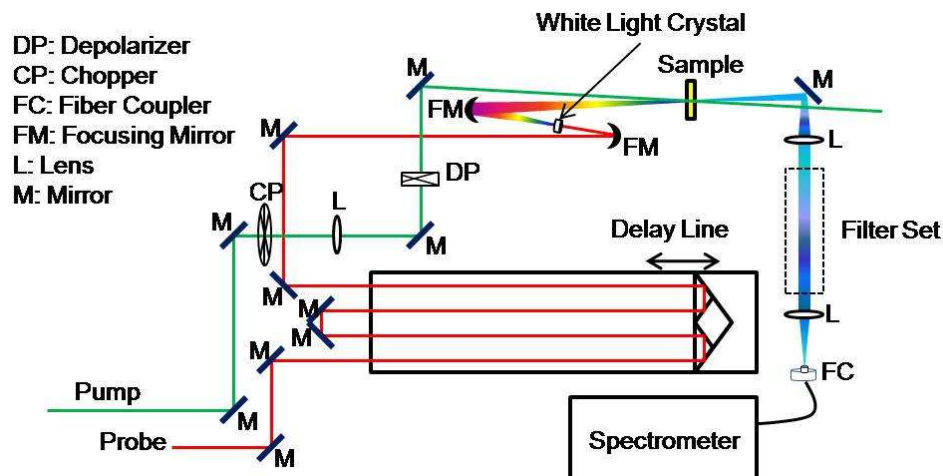


Figure 2.4. Schematics representing optical layout of the femtosecond transient absorption setup. Schematics provided by Dr. San-Chui Chi.

An optical Kerr effect (OKE) experiment on a sample of CCl_4 was performed in order to measure the temporal chirp of the signal. Briefly, the sample was pumped with a 350 nm light with polarization vertical to the optical table surface. The WLC probe light was also vertically polarized and passed through the irradiated sample. The probe beam was sent to the detector through a polarizer which was set to horizontal polarization. The OKE signal was then collected for different pump-probe delay time. As can be seen in Figure 2.5, the normalized OKE signals at different wavelengths do not show significant temporal shift with respect to each other. This illustrates no appreciable temporal chirp of the WLC probe in the NIR region and therefore chirp correction of the acquired transient spectra was unnecessary.

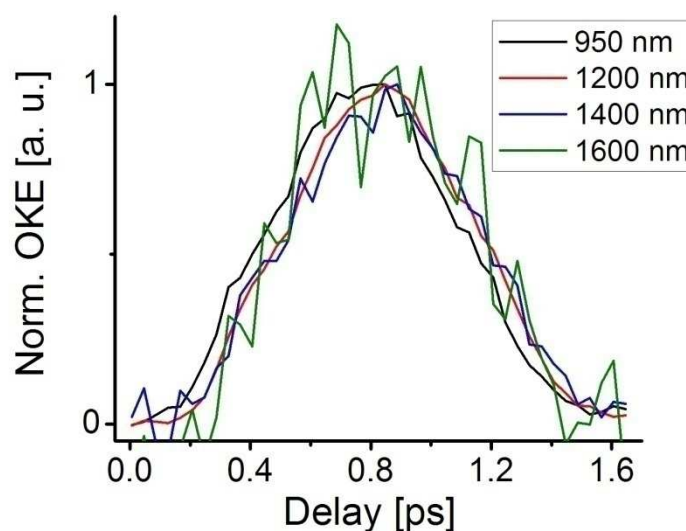


Figure 2.5. Normalized OKE signal as a function of pump-probe delay measured at different wavelengths. The OKE measurements were performed by Dr. Michal Malicki.

The studied solutions of NPs had OD_{350} of between 1.8 and 2.5 in a 2 mm path length quartz cuvette, and were stirred continuously throughout the data acquisition. A neat film of TPDC12 was prepared by drop casting from a toluene solution. Slow solvent evaporation resulted in a film of very good optical quality. All samples were photostable under the applied excitation conditions (subsequent measurements showed no change of the transient signal after ca. 10 minutes of signal acquisition). Excitation pulse energy values of 0.48 μJ , 0.96 μJ , 1.44 μJ and 2.4 μJ at the sample were used for the measurements of the NP solutions, a solution of TPDC12SH in 5:1 mixture of toluene and DMF, and the neat film of TPDC12, respectively. The excitation beam spot size at the sample was determined to be 315 μm (HW1/e).

The excitation beam with photon fluence $\Phi_0 = 3.4 \times 10^{14}$ photons/cm² at the front face of the sample^{vii} was propagated through the 2 mm path length of a sample containing known concentrations of AgNP metallic cores and TPD moieties (as estimated from the absorbance of the samples), describing the system as a series of thin slabs with planes perpendicular to the direction of beam propagation.^{viii} In the calculation the sample was divided into 1000 slabs. Excitation beam attenuation and ground-state population depletion of both the metallic core and the TPD moiety in each slab were computed according to the following equations and then used as input for the following slab:

$$\Phi_i = \Phi_{i-1} e^{-[(N_{Ag}^0 - N_{Ag}^*(i))\sigma_{Ag} + (N_{TPD}^0 - N_{TPD}^*(i))\sigma_{TPD}]\Delta l} \quad (2.1)$$

$$N_{Ag}^*(i) = N_{Ag}^0 (1 - e^{-\sigma_{Ag}\Phi_i}) \quad (2.2)$$

$$N_{TPD}^*(i) = N_{TPD}^0 (1 - e^{-\sigma_{TPD}\Phi_i}) \quad (2.3)$$

where Φ_i, Φ_{i-1} are the excitation beam fluence values at the i 'th slab and in the slab immediately before respectively, N_{Ag}^0, N_{TPD}^0 are the ground-state populations of the AgNP metallic core and the TPD moiety respectively, $N_{Ag}^*(i), N_{TPD}^*(i)$ are the excited-state populations of the AgNP metallic core and the TPD moiety in the i 'th slab respectively, $\sigma_{Ag}, \sigma_{TPD}$ are the ground-state cross sections at 350 nm for the AgNP metallic core and the TPD moiety respectively, and Δl is the path length of the slab. Such

^{vii} The fluence was calculated using the measured power of the excitation (pump) beam at the front face of the sample (2.4 mW), repetition rate of the laser (1 kHz), the photon energy (5.7×10^{-19} J), and the overlap of the pump and probe beams, both of which were measured to have a Gaussian function spatial distribution with parameters $\sigma_{\text{pump}} = 315 \mu\text{m}$ (HW1/e) and $\sigma_{\text{probe}} = 170 \mu\text{m}$ (HW1/e). For further calculations the intensity profiles of the overlapped beams were assumed to be constant over the overlap region.

^{viii} This approach was taken in order to account for both the ground-state depletion of the two-component system (TPD moiety and AgNP metallic core) and the excitation beam attenuation through the sample as the studied solutions had high absorbance values at the excitation wavelength.

computation was repeated for each slab until the end of the path length was reached ($i = 1000$). The output of the calculation was the value of fluence of the excitation beam after passing through the sample, and the total initial excited-state populations of both the Ag NP metallic core ($N_{Ag}^* = \sum_{i=0}^{1000} N_{Ag}^*(i)$) and the TPD moiety ($N_{TPD}^* = \sum_{n=0}^{1000} N_{TPD}^*(i)$).

2.7. References

1. Hiramatsu, H.; Osterloh, F. E., A Simple Large-Scale Synthesis of Nearly Monodisperse Gold and Silver Nanoparticles with Adjustable Sizes and with Exchangeable Surfactants. *Chem. Mater.* **2004**, *16* (13), 2509-2511.
2. Ulman, A., Formation and Structure of Self-Assembled Monolayers. *Chem. Rev.* **1996**, *96* (4), 1533-1554.
3. Lide, D. R., *CRC Handbook of Chemistry and Physics*. 86th Edition ed.; American Chemical Society: Boca Raton, FL, 2006; Vol. 128, p 2544.

CHAPTER 3

CHARACTERIZATION OF SILVER NANOPARTICLES FUNCTIONALIZED WITH TPD LIGANDS

3.1. Introduction

Adsorption of ligands onto metal nanoparticles has been extensively studied in the last decade.¹⁻⁴ In particular, research activities addressing chemistry and physics of alkyl thiolates-coated gold nanoparticles have sprouted after the development of the synthetic method reported by Brust et al.,⁶ which allows for the synthesis of large quantities of gold nanoparticles (ca. 5 nm in diameter) protected with thiolate ligands. Due to the ease of functionalization with a variety functional groups and often good solubility of such nanoparticles in many organic solvents, a wide range of analytical techniques could be used for the characterization of such nanoparticles. These systems have been extensively studied with TEM,⁷ absorption spectroscopy,⁸ FT-IR⁹ and Raman¹⁰ spectroscopies, NMR spectroscopy,^{3, 11} XRD,^{4, 12} XPS¹³ and other techniques.^{13, 14} The properties of monolayers on surfaces with high curvatures are often different from those on flat surfaces, e.g., the interaction between ligands or the degree of packing have been shown to be affected by the surface curvature.¹⁵ This can be rationalized by invoking the concept of free volume¹⁶ and its dependence on the distance from the curved surface, as presented in Figure 3.1. Parts of molecules, such as alkylthiols, close to the particle surface experience less freedom of movement (dashed line ellipse b) than the parts located further away from the

surface (dashed line ellipse c), assuming that the lines representing the solid angle in Figure 3.1 represent boundaries for the molecule movements. The angle is determined by the footprint of the molecule on the surface. The gradient of free volume as a function of distance from the surface decreases (dashed line ellipse b' and c') for larger particles, i.e., for less curved surfaces, and eventually goes to zero in the case of flat surfaces. As a consequence molecules attached to small spherical nanoparticles can experience more freedom of movement than further away from the surface.

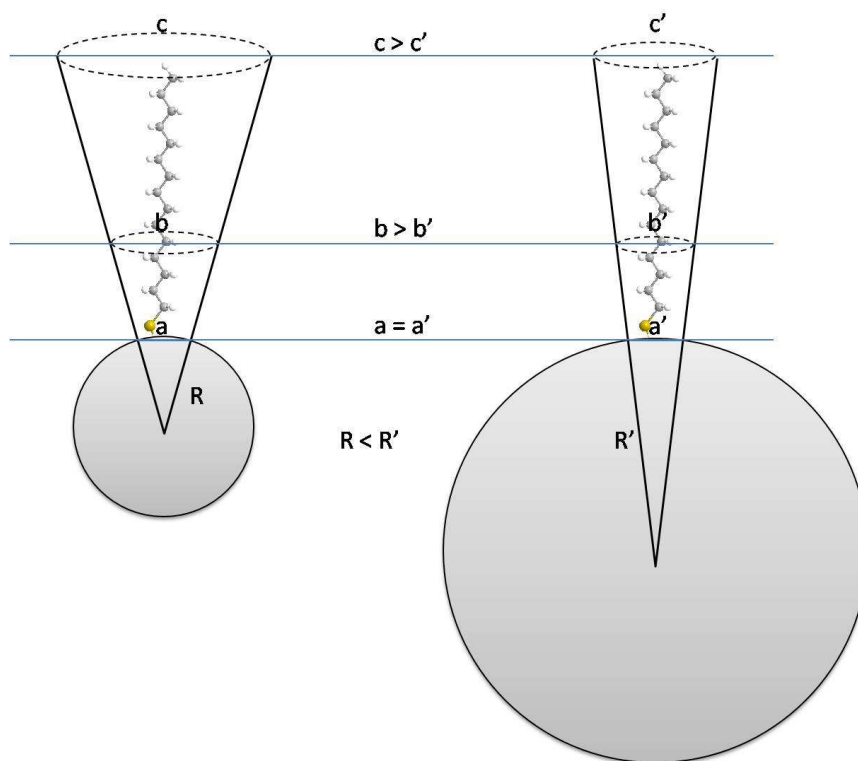


Figure 3.1. Schematic drawing of two spheres characterized by different diameters with cones representing solid angles. The angles were chosen such that their cross-section at the surface is the same as the molecular footprint on the surface ($a = a'$). The horizontal lines visualize various distances from the surface of the spheres and the dashed ellipsis b , b' , c and c' define values of the free volume within the cones at those distances.

This chapter deals with chemical characterization of silver nanoparticles (AgNP) functionalized with N,N'-Bis(3-methylphenyl)-N,N'-diphenylbenzidine (TPD) ligands or mixtures of TPD ligands and dodecylthiol (DDT). TPD is a chromophore whose photophysical properties are presented in Chapter 4 and DDT is an optically inert ligand, which is used to vary the concentration of the TPD ligands on the surface of the nanoparticles. The concentration of TPD ligands – an important parameter that

characterizes the studied systems – is lower in the mixed-ligand systems than in the nanoparticles coated only with TPD ligands. The composition of the systems AgNP – organic ligands is summarized in Table 3.1. A variety of analytical techniques was utilized to analyze these systems. TEM was used to determine the size distribution of the metallic cores of the Ag nanoparticles. UV-Vis absorption, IR absorption and NMR spectroscopies were used to investigate the chemical character and structure of the organic ligands. Molar extinction coefficients of silver nanoparticles as well as the footprints of the TPD-ligands have been determined from absorption spectroscopy and compared with the results obtained from TGA studies. Understanding of the structure of the TPD / AgNP systems studied herein is crucial for the discussion regarding the photophysics of these systems presented in the Chapter 5.

3.2. *TEM Analysis*

TEM allows for imaging of metallic cores of nanoparticles with sizes down to ca. 1 nm.^{17, 18} Apart from establishing the size distribution of the metallic cores, TEM imaging allows for the measurement of the spacing between metallic cores, which often form well ordered 2D arrays on the surface of TEM substrates. This, in principle, makes it possible to establish the thickness of the shell of organic ligands attached to the surface of metal nanoparticles.^{4, 19}

TEM results are presented in Figures 3.2 and 3.3 and the summary of the data analysis is given in Table 3.1. As can be seen from the images shown in Figure 3.2 most of the particles are spherical or close to spherical with average diameters being rather similar from sample to sample, as evidenced by the histograms shown in Figure 3.3.

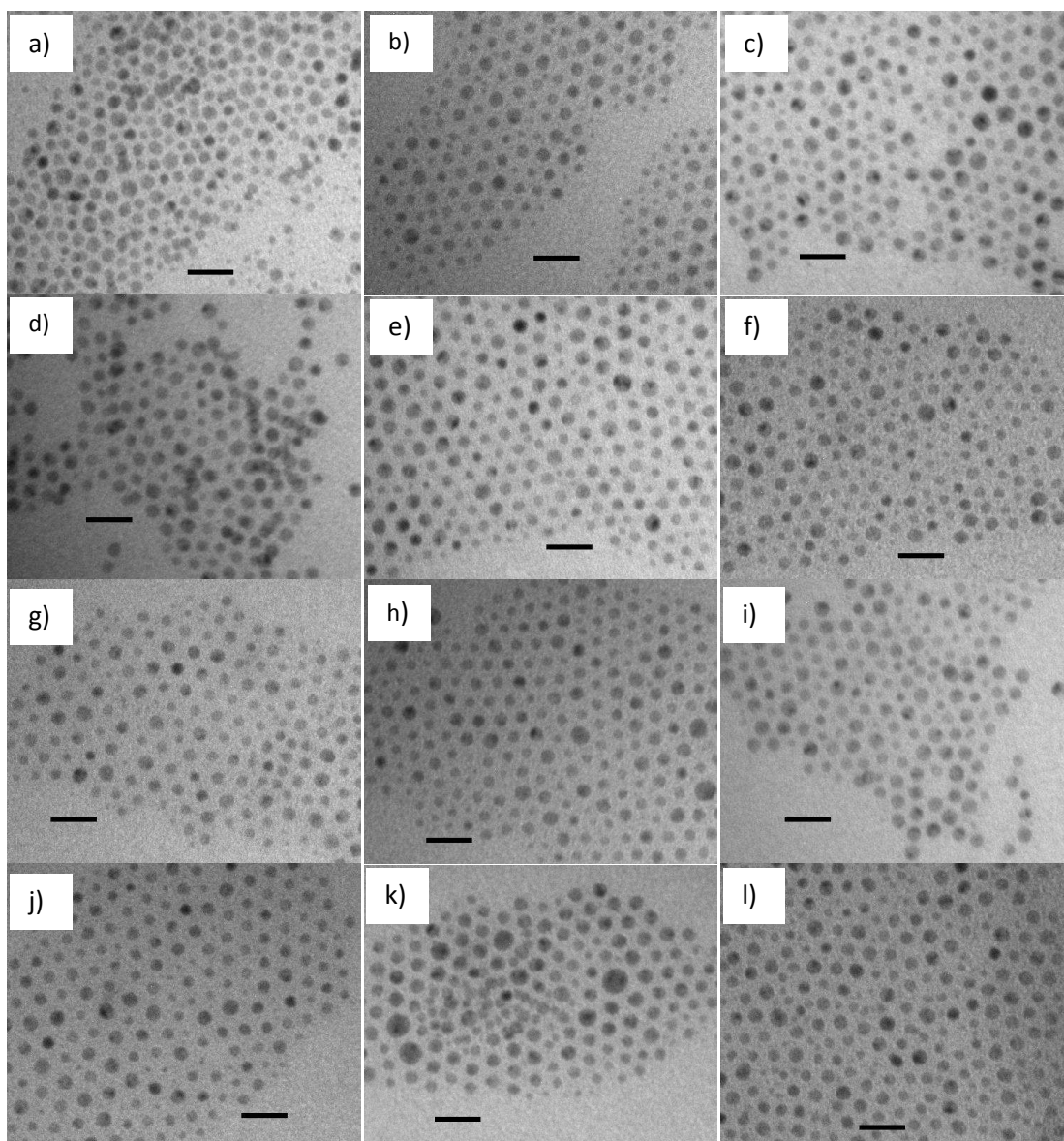


Figure 3.2. TEM images of silver nanoparticles a) Ag NPs protected with oleylamine before the place-exchange reaction, b) AgTPDC3-I, c) AgTPDC3-II, d) AgTPDC3-III, e) AgTPDC4-I, f) AgTPDC4-II, g) AgTPDC8-I, h) AgTPDC8-II, i) AgTPDC8-III, j) AgTPDC12-I, k) AgTPDC12-II and m) AgTPDC12-III. (scale bar = 20 nm).

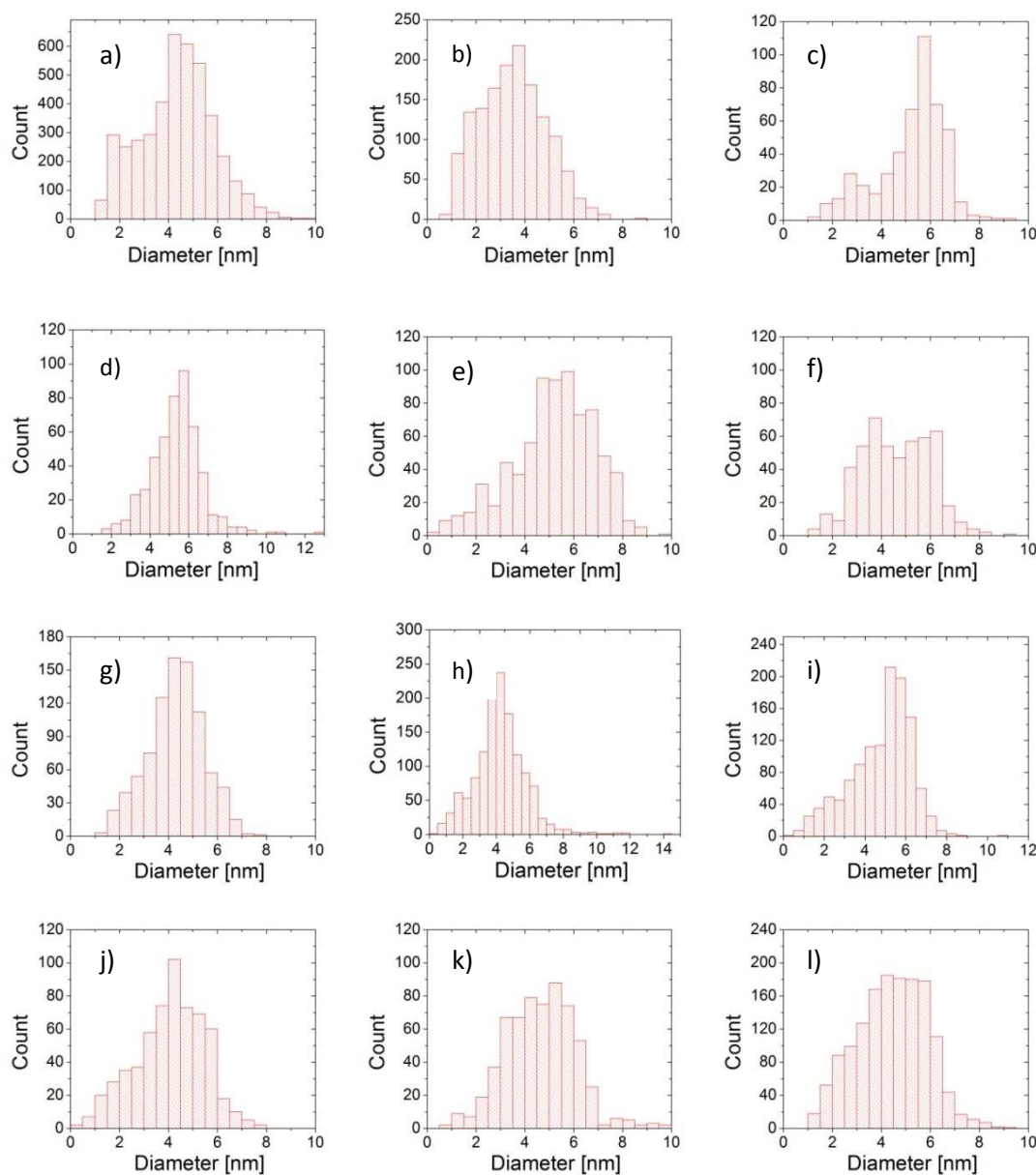


Figure 3.3. Histograms of diameters of silver nanoparticles measured from TEM images for a) Ag NPs protected with oleylamine before the place-exchange reaction, b) AgTPDC3-I, c) AgTPDC3-II, d) AgTPDC3-III, e) AgTPDC4-I, f) AgTPDC4-II, g) AgTPDC8-I, h) AgTPDC8-II, i) AgTPDC8-III, j) AgTPDC12-I, k) AgTPDC12-II and m) AgTPDC12-III.

As mentioned before, additional information that can be obtained from TEM images is related to the distance between nanoparticles in an ordered array formed on the surface of the TEM substrate.⁴ The measurements of the distance between the surfaces of adjacent nanoparticles can provide insight about shell thickness that the ligands form around the nanoparticles, or whether the ligands from one particle can penetrate the ligand shell of the other particle, process known as interdigitation.²⁰ This type of information from TEM images is an approximation due to the fact that micrograph only shows the projection of the particles onto horizontal plane (XY), which means that the distance between nanoparticles recorded is inaccurate if the particles are vertically displaced. These instances contribute to underestimation of the measurement. The other possibility of an error comes from the fact that a shell composed of organic ligands is invisible under TEM, thus making it impossible to determine whether the shells are in contact with each other. This overestimates the results. However, from the areas of the image where particles form ordered 2D arrays, it is possible to do statistical analysis in order to estimate the inter-particle spacing or at least do comparative studies of the nanoparticles protected with different ligands or mixture of ligands. A summary of such measurements performed on the TEM images acquired for the NPs studied herein are presented in Table 3.1.

Table 3.1. Samples of silver nanoparticles functionalized with TPD ligands and TPD ligand / DDT mixtures expressed in percentage of TPD ligand used in the reaction mixture. Average diameters and errors were established from the analysis of TEM images. L is the length of a fully extended ligand. The bolded font corresponds to the systems without DDT.

Sample	Molar %	Ave. Diameter [nm]	Interparticle distance [nm]	Estimated 2×L [nm]
AgTPDC3-I	100%	3.5 ± 1.3	3.4 ± 0.6	4.0
AgTPDC3-II	66%	5.2 ± 1.4	2.7 ± 0.4	
AgTPDC3-III	33%	5.4 ± 1.3	2.4 ± 0.5	
AgTPDC4-I	100%	5.2 ± 1.5	3.6 ± 0.5	4.3
AgTPDC4-II	50%	4.6 ± 1.4	2.9 ± 0.6	
AgTPDC8-I	100%	4.3 ± 1.2	3.8 ± 0.6	5.3
AgTPDC8-II	66%	4.2 ± 1.6	3.4 ± 0.5	
AgTPDC8-III	33%	4.8 ± 1.5	2.6 ± 0.5	
AgTPDC12-I	100%	4.1 ± 1.4	4.5 ± 0.5	6.3
AgTPDC12-II	66%	4.6 ± 1.4	3.1 ± 0.6	
AgTPDC12-III	33%	4.4 ± 1.4	3.1 ± 0.6	

A fully extended TPDC3SH molecule is about 2.0 nm long.^{ix} Lengths of the other ligands were obtained by adding 1.26 Å per additional CH₂ group^x in the alkyl chain to the length of TPDC3SH ligand. The measured values of the average inter-particle distance are found to be slightly lower than twice the length of fully extended TPDC3SH

^{ix} The length, L, of fully extended TPDC3SH ligand was estimated based on the optimized geometry of the molecular structure of the ligand, by measuring the distance from the sulfur atom to the further most methyl group on aromatic end group of the ligand. The geometry of the molecule was optimized using the molecular mechanics 2 (MM2) option in ChemBio3D Ultra 11.0.

^x The added length to the alkyl chain was calculated based on bond length between carbon atoms of 1.54 Å and a bond angle of 109.5°.

and TPDC4SH molecules. This suggests a rather small degree of interlocking between the adjacent shells. As can be seen from Table 3.1, the values of the interparticle distance found for systems AgTPDC8-I and AgTPDC12-I are significantly smaller than the estimated double length of the corresponding ligands. The length difference between the studied ligands originates from the number of methylene groups in the alkyl spacer between the TPD moiety and the thiol group. The measured differences in the interparticle-distance values between AgTPDC3-I and AgTPDC4-I (theoretically a difference of 2 C-C bonds that is 0.2 nm), AgTPDC3-I and AgTPDC8-I (10 C-C bonds; 1.2 nm), and between AgTPDC3-I and AgTPDC12-I (18 C-C bonds; 2.1 nm) are 0.2 nm, 0.4 nm, and 1.1 nm, respectively. This disparity between the theoretical and the measured difference in the average interparticle distance between different systems indicate that while the degree of interdigitation⁴ in AgTPDC4-I is similar to that in AgTPDC3-I, AgTPDC8-I and to a larger extent AgTPDC12-I show significantly higher degree of ligand interdigitation than AgTPDC3-I. These results are consistent with the bulky TPD end groups being placed at larger distances from the curved surface in the systems incorporating TPD-thiols with longer alkyl spacers, where larger TPD-TPD distance allows for higher degree of interdigitation. This is entirely consistent with the increased density of the end groups in the ligand shell in systems incorporating shorter alkyl spacers between the TPD end group and the thiol group.

The results of the measurements of interparticle distances for the nanoparticles in which TPD-thiols are diluted with dodecylthiol show smaller values of distance between metallic cores than for the particles coated with TPD-thiols only (Table 3.1). Furthermore, the average interparticle distance decreases with the higher degree of dilution. As

expected, the smaller number of the bulky TPD moieties on the surface allow for higher degree of interdigitation.⁴

3.3. *UV-Vis Absorption Spectroscopy*

Metal nanoparticles have interesting optical properties due to plasmon resonance absorption. The position of the plasmon absorption band depends on the particle size, shape, dielectric function of the metal and dielectric constant of the surrounding medium. In the case of spherical particles, in the size range of interest in this study, the position of the plasmon absorption band is only weakly dependent on the particle size. Thus, the most significant changes in the plasmon absorption band are expected to come from the changes in the dielectric properties of the nanoparticles' immediate surroundings. These changes, in the discussed systems, are due to different composition of the organic shells.

UV-Vis absorption spectra of the nanoparticles functionalized with TPD-thiols and TPD-thiols / DDT ligand mixtures in the toluene / DMF solvent mixture are shown in the Figure 3.4. Each spectrum shows two peaks: one maximum in the range 430 - 465 nm and a weaker maximum or shoulder at ca. 365 nm. The first band is due to the plasmon resonance of silver nanoparticles, while the latter originates from the absorption of the TPD moieties. Analysis of the data reveals an interesting trend. The position of the plasmon absorption band is red shifted for the NP systems prepared with higher fractions of TPD-thiols when compared to the systems the smallest fraction of TPD ligands. Additionally, the intensity of the band at 365 nm in the normalized absorption spectra is higher for the samples synthesized with the use of higher fractions of TPD-thiols.

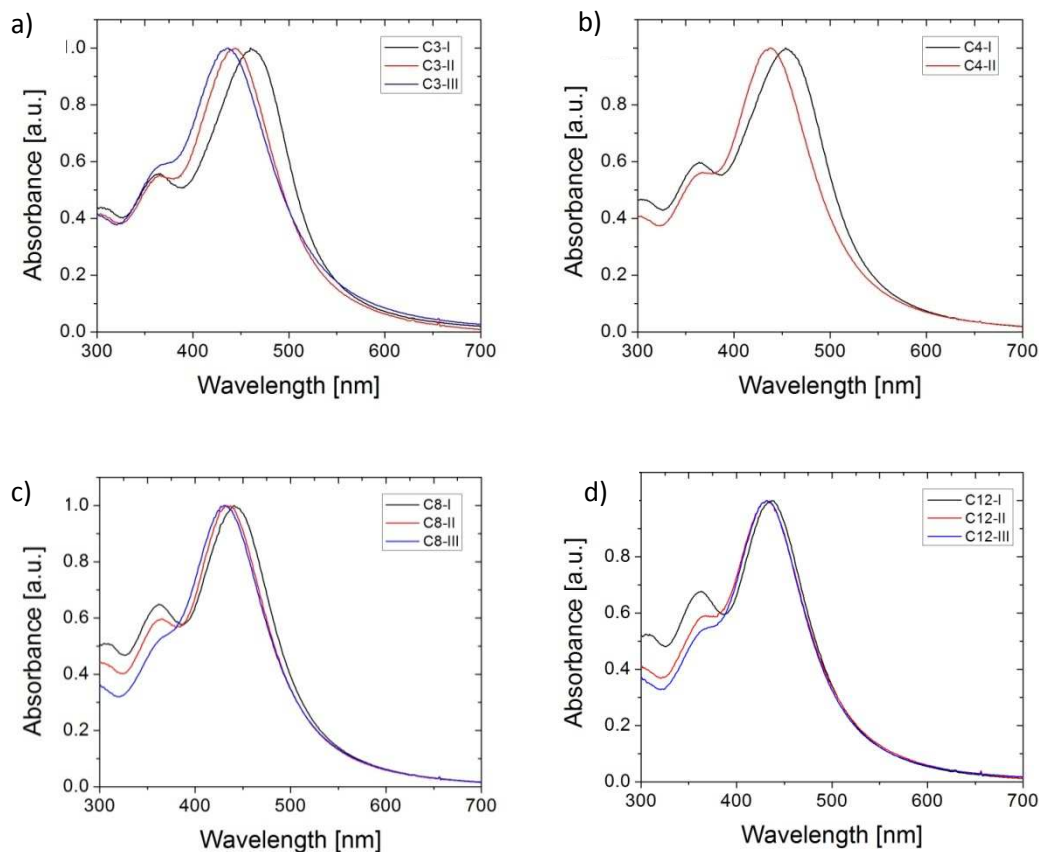


Figure 3.4. UV-vis absorption spectra of AgNP functionalized with TPD ligands in 5:1 mixture of toluene and DMF of: a) AgTPDC3-I, II, III; b) AgTPDC4-I, II; c) AgTPDC8-I, II, III; d) AgTPDC12-I, II, III. The spectra are normalized at the maximum of plasmon absorption.

These observations are consistent with TPD-thiols being attached to the surface of Ag nanoparticles. In accordance to Beer's law, the increased absorbance due to the TPD-moiety in the systems prepared with higher fractions of TPD-thiols suggests that more chromophores have been attached to the surface of NPs, with respect to the AgNP with a lower fraction of the TPD-thiols. The abovementioned red shift of the surface plasmon resonance band is a consequence of Mie theory, according to which the position of the maximum of plasmon resonance red-shifts with increase of the dielectric constant of the

surrounding medium.⁸ The dielectric constant of bulk TPD $\epsilon(418 \text{ nm}) = 3.46$,²¹ is considerably higher than the dielectric constant of toluene ($\epsilon \approx 2.2$ in the visible spectral range)²² and that of dodecanethiol ($\epsilon \approx 2.1$).²³ Consequently, the overall dielectric constant of the ligand shell is larger and the position of the plasmon absorption band red shifts for AgNP coated with a denser monolayer of TPD ligands. The largest shifts of the surface plasmon resonance band as a function of TPD-thiol fraction used in the synthesis are observed for the samples incorporating TPDC3SH. As can be seen from Figure 3.4a the surface plasmon resonance maximum shifts from 437 nm for AgTPDC3-III to 461 nm for the particles coated exclusively with TPDC3-thiol (AgTPDC3-I).^{xi} A summary of the observed surface plasmon resonance band position as a function of the composition of the nanoparticle stabilizing ligands, i.e., as a function of the methylene units in the spacer between the TPD moiety and the thiol group for different mixtures of TPD-thiols and dodecanethiol, is presented in Figure 3.5. Clearly, the largest differences in the position of the surface plasmon resonance band as a function of the alkyl-spacer length can be seen for NPs coated exclusively with TPD-thiols. The systems incorporating mixtures of ligands show a similar trend but to a smaller extent. This phenomenon can be explained by the effective dielectric constant of the surrounding medium. The effective dielectric constant that is used in the Mie theory is largest for TPDC3SH due to its high polarizability and its proximity to the surface. This is consistent with the data shown in Figure 3.5. Diluting the polarizable TPD thiol on the surface of AgNPs with DDT decreases the effective dielectric constant around each NP resulting in surface plasmon

^{xi} Mie theory predicts that if the dielectric constant of the medium changes from 2.2 to 3.46 the plasmon of silver nanoparticles shifts towards red by more than 50 nm.

resonant bands that are blue shifted with respect to those measured for NPs coated exclusively with TPD-thiols. The introduction of a longer linker between the polarizable TPD moiety and the metal surface lowers the effective dielectric constant around each NP and, as can be seen in Figure 3.5, results in surface plasmon resonance band positions that shift towards the blue for systems with longer alkyl spacers. Dilution of the chromophoric ligands with the longest alkyl spacer results in much smaller plasmon shifts than for the TPD chromophores with shorter alkyl spacer. In fact in the case of AgTPDC12-I and AgTPDC12-II the surface plasmon resonance band is the same (431 nm) for both of them.

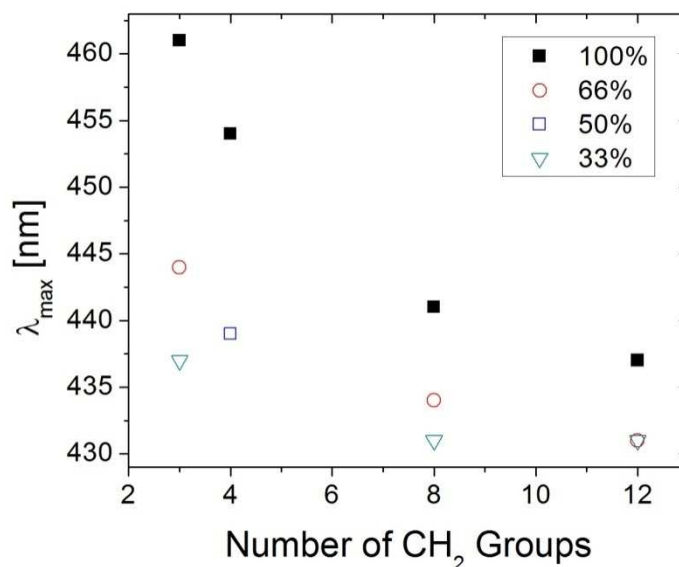


Figure 3.5. Position of plasmon absorption maxima (λ_{\max}) plotted as a function of number of carbon atoms in the linker of the TPD ligands. Percentage of TPD ligands used during synthesis: 100% – black squares, 66% – red circles, 50% - blue hallow square, 33% – turquoise triangle.

UV-vis spectra of AgTPDCx (where x = 3, 4, 8 and 12) support the conclusion that the TPD ligands are adsorbed onto the surface of silver nanoparticles. Moreover, the above observations are consistent with the TPD end group of the ligands being at different distances from the metal surface. The extent of plasmon resonance shifts is qualitatively consistent with the relative lengths of the linkers in the ligands and also with the degree of dilution of the chromophoric shell with dodecanethiol.

3.4. *FT-IR Spectroscopy*

Infrared spectroscopy has been used for studying the degree of ordering of self assembled monolayers (SAMs) on both flat surfaces^{23, 24} and on the surface of nanoparticles,⁹ often referred to as 2D-SAMs and 3D-SAMs, respectively.¹³ It has also been used to establish presence of chemical groups in the samples of nanoparticle / organic ligand systems.^{9, 25-27} IR spectroscopy is particularly useful for establishing the degree of order of alkyl chains.^{28,29} Fully extended, i.e., all-*trans*, alkyl chains show the highest degree of order, while gauche conformation within chains introduce disorder. This information was obtained from the FT-IR studies of crystalline solids and melts or solutions of n-alkyl chains⁵ and polyethylene.³⁰ For example, in FT-IR studies of polyethylene the symmetric (ν_s) and asymmetric (ν_{as}) methylene C-H stretching modes were observed at 2856 cm⁻¹ and 2928 cm⁻¹, respectively, for the polymer in solution.³⁰ On the other hand, in crystalline polyethylene these vibrations were observed at 2850 cm⁻¹ and 2920 cm⁻¹.^{5, 30} This shift of the frequency of the modes to higher energies for polyethylene in solution when compared to crystalline polyethylene is thought to be due to a greater number of gauche defects in the former system.³⁰ The information about the

frequencies of the modes for *gauche* and *trans* conformations were also applied to the monolayers. Studies of 2D-SAMs of alkyl thiols on gold have shown that the positions of the bands originating from these vibrational modes change from *gauche*-defect rich, liquid-like for submonolayers (low density of ligands on the surface) to all-*trans*, crystalline-like of dense monolayers for alkyl thiols with chains longer than six carbon atoms.^{23, 24, 31} Shorter chain lengths show liquid-like behavior regardless of the density of ligands on the surface.⁹ Murray and coworkers used infrared spectroscopy to study ordering of alkyl thiols on the surface of small gold nanoparticles.⁹ The authors showed that, despite the large surface curvature, the IR spectra of alkyl thiolate ligands attached to gold NPs were similar to those measured for the corresponding 2D-SAMs, which can be justified by the higher density of ligands^{15, 16, 32} on the nanoparticles than on a flat surface.

Infrared spectra of the silver nanoparticles functionalized with TPD ligands were collected in the range 700-3200 cm^{-1} . Here we focus mainly here is only on the region 2800-3200 cm^{-1} . In fact, the spectral region from 1200 to 1600 cm^{-1} is dominated by the TPD moiety itself and changes very little between the samples. It is also important to mention that the weak signal originating from the S-H stretching mode at 2566 cm^{-1} observed for TPDC3SH and TPDC12SH is not present in the corresponding NP samples (Figure 3.6). This suggests that the S-H bond is broken⁹ upon adsorption of the thiols on the silver surface, consistent with previous studies of thiol monolayers³³ adsorbed on noble metal surfaces.

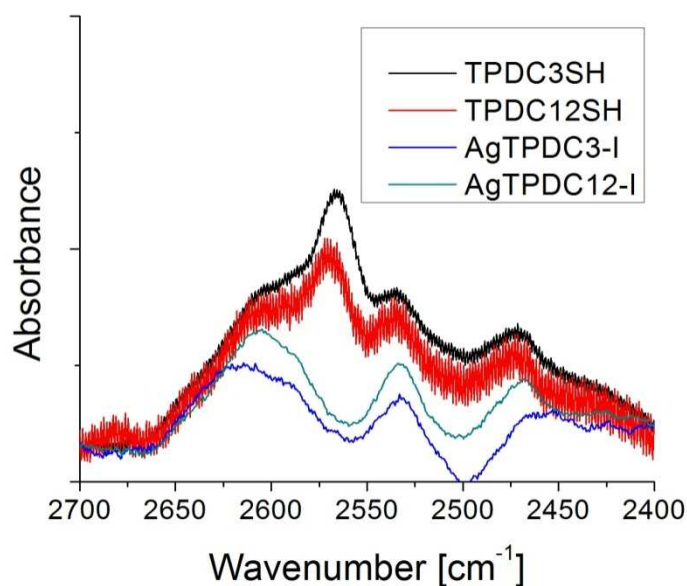


Figure 3.6. S-H stretching mode at 2566 cm^{-1} of neat films of TPDC3SH and TPDC12SH, compared with the same spectral region of AgTPDC3-I and AgTPDC12-I. The films were cast onto a KBr disc and normalized at 3030 cm^{-1} .

FT-IR spectra acquired for silver nanoparticles coated with TPD-thiols show the presence of IR modes characteristic to the free dye (TPDC12SH), thus confirming presence of the ligands in the samples of nanoparticles (Figure 3.7). Furthermore, the intensity of the aliphatic C-H stretching bands ($3000\text{--}2800\text{ cm}^{-1}$) increases with respect to the aromatic C-H stretching modes, with the number of carbon atoms in the linker chain, which is consistent with the structure of the ligands.

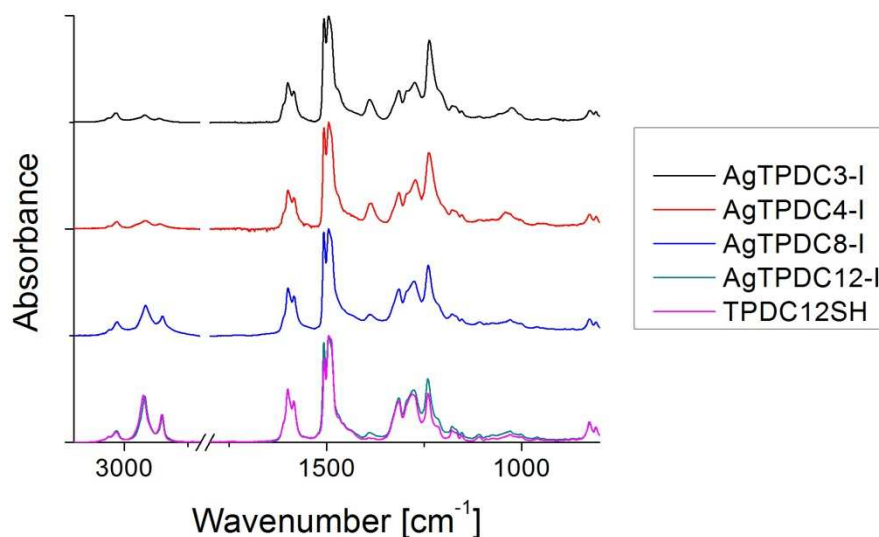


Figure 3.7. FT-IR spectra of neat films of NP samples studied herein cast onto a KBr disc. The spectra were normalized at 3030 cm^{-1} and displaced vertically for clarity.

As described before, the position of the bands originating from the methylene C-H stretching modes can bring insights into the degree of ordering of the alkyl spacers on the nanoparticles surface. Figure 3.8a shows IR absorption spectra of the unbound TPDC3SH, AgTPDC3-I, and N,N'-diphenyl-bis(3-methylphenyl)-biphenyl-4,4'-diamine (commercially available TPD without any linker). Looking at the region of interest 3000 cm^{-1} , one can see that the position of the methylene C-H vibrations overlaps with the position of the methyl groups of TPD. However, the intensities of the peaks from the methyl groups are weak compared to the intensity of the peaks from C-H vibrations of the methylene groups, even for the TPD ligand with the shortest aliphatic chain. It can be assumed, based on this evidence that the positions of the maxima are predominantly due to bands corresponding to $-\text{CH}_2-$ stretching modes.

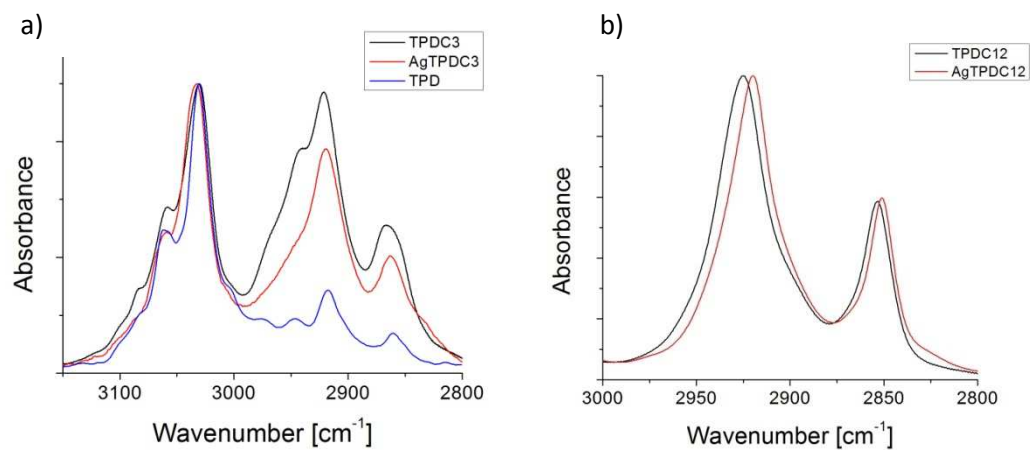


Figure 3.8. a) FT-IR spectra of TPDC3SH, AgTPDC3-I, and of TPD, normalized at 3030 cm^{-1} . b) Normalized FT-IR spectra of TPDC12SH and AgTPDC12-I.

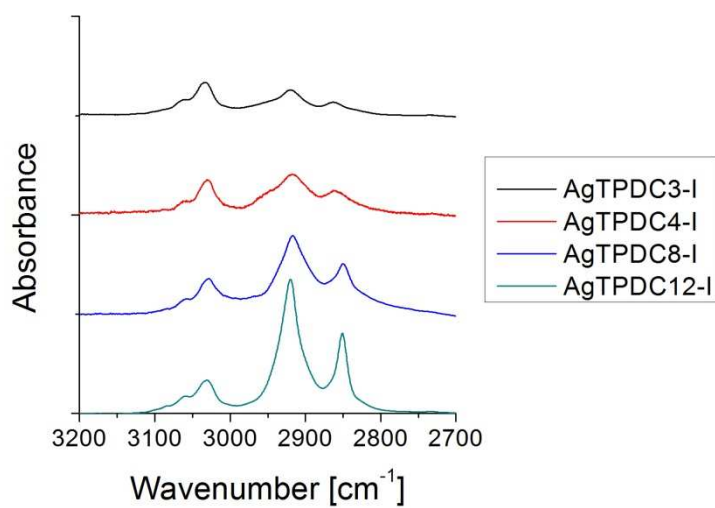


Figure 3.9. FT-IR spectra of the NP systems studied herein. The spectra were normalized at 3030 cm^{-1} and displaced vertically for clarity.

The positions of ν_s and ν_{as} bands for TPDC3SH and AgTPDC3-I are somewhat unusual, as $\nu_s = 2863 \text{ cm}^{-1}$ suggests a gauche-rich and $\nu_{as} = 2920 \text{ cm}^{-1}$, on the other hand, a *trans*-rich conformation. A similar behavior, however, has been observed⁹ for butanethiol-coated gold nanoparticles and it was attributed to highly disordered, liquid-like conformation of the ligands. AgTPDC4-I bands are shifted towards lower energies (Figure 3.9, Table 3.2) with respect to AgTPDC3, $\nu_s = 2860 \text{ cm}^{-1}$ and $\nu_{as} = 2917 \text{ cm}^{-1}$, indicating fewer gauche defects⁹ than in AgTPDC3-I. A predominantly all-*trans* conformation is instead seen for AgTPDC8 ($\nu_s = 2850 \text{ cm}^{-1}$ and $\nu_{as} = 2917 \text{ cm}^{-1}$) and AgTPDC12-I ($\nu_s = 2850 \text{ cm}^{-1}$ and $\nu_{as} = 2920 \text{ cm}^{-1}$). A comparison of AgTPDC12-I and TPDC12 ($\nu_s = 2853 \text{ cm}^{-1}$ and $\nu_{as} = 2923 \text{ cm}^{-1}$) is presented in Figure 3.8b and suggests that the unbound ligand in the neat film shows more gauche defects, i.e., more liquid-like behavior, than the same molecule bound to the nanoparticle.

Table 3.2. Frequency of the symmetric (ν_s) and asymmetric (ν_{as}) methylene C-H stretching modes for the systems studied herein as well as for crystalline polyethylene³⁰ (PE) and for a polyethylene solution⁵ in CCl₄.

Sample	ν_{as} [cm ⁻¹]	ν_s [cm ⁻¹]
AgTPDC3-I	2920	2863
AgTPDC4-I	2917	2860
AgTPDC8-I	2917	2850
AgTPDC12-I	2920	2851
Crystalline PE	2920	2850
Solution PE	2928	2856
TPDC12SH	2925	2853

FT-IR spectra of the nanoparticles modified with mixture of ligands - TPDCxSH (x = 3, 4, 8, 12) and DDT - are shown in Figure 3.10 and compared to the spectra of the nanoparticles functionalized exclusively with TPD ligands. It is clear that the signal intensity in the 2800 - 3000 cm⁻¹ region of the normalized spectra, to the aromatic C-H mode, is higher for the mixed-ligand systems than for the nanoparticles coated exclusively with TPD-thiols. This confirms the presence of different amounts of DDT in the systems that were prepared in the presence of mixture of TPD-thiols and DDT.

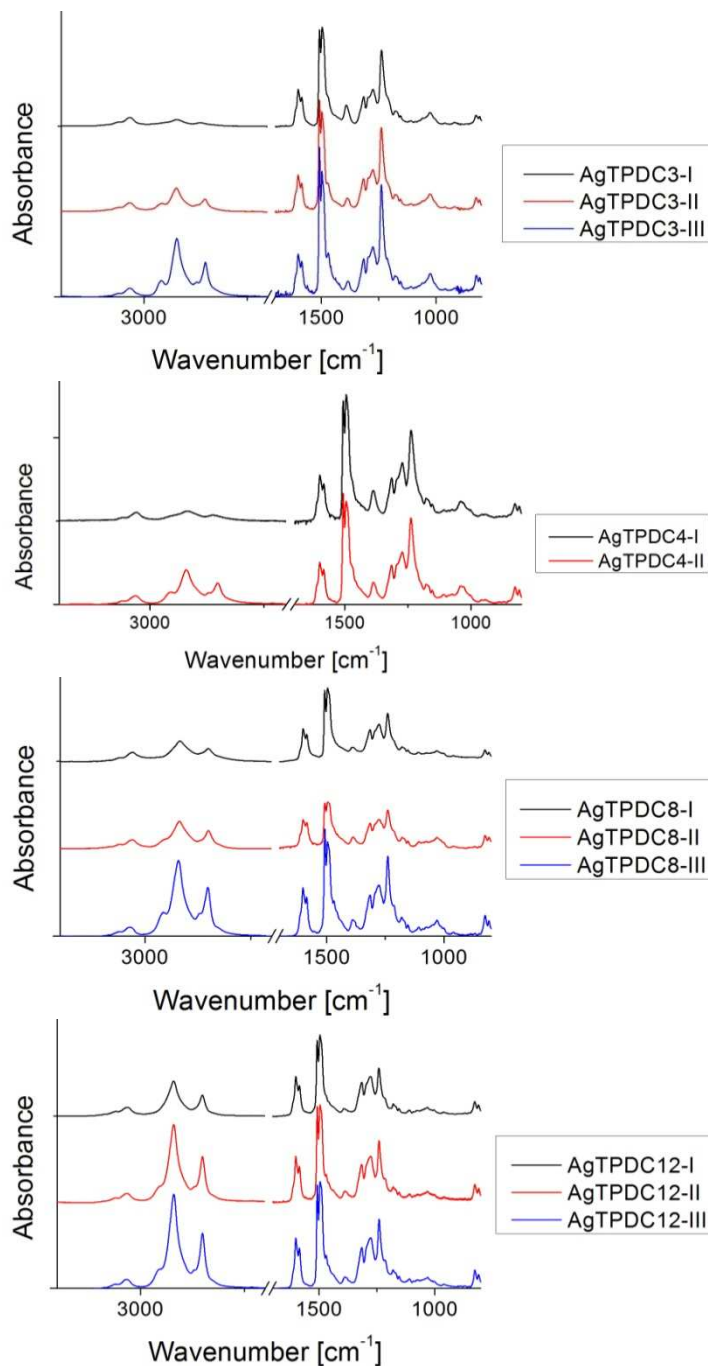


Figure 3.10. FT-IR spectra, normalized to the aromatic C-H stretching mode, of neat films of the NP systems drop-cast onto a KBr disc.

3.5. *NMR Spectroscopy*

^1H NMR spectroscopy is a commonly used technique for studying organic ligands adsorbed onto metal nanoparticles.^{3, 34} A considerable number of literature reports involve NMR investigations of gold nanoparticles functionalized with alkylthiolate ligands.^{3, 11, 34, 35} At the same time only few reports deal with NMR studies of organic monolayers adsorbed onto silver nanoparticles.² The ^1H NMR data acquired for the silver nanoparticles systems described in this thesis was used to provide further insights into the composition and structure of the studied systems. In particular, spin-spin relaxation time (T_2) measurements were performed in order to address structural aspects of the TPD-thiol monolayers,^{3, 36} from which the relative degree of packing of the aromatic end groups (TPD) can be determined.

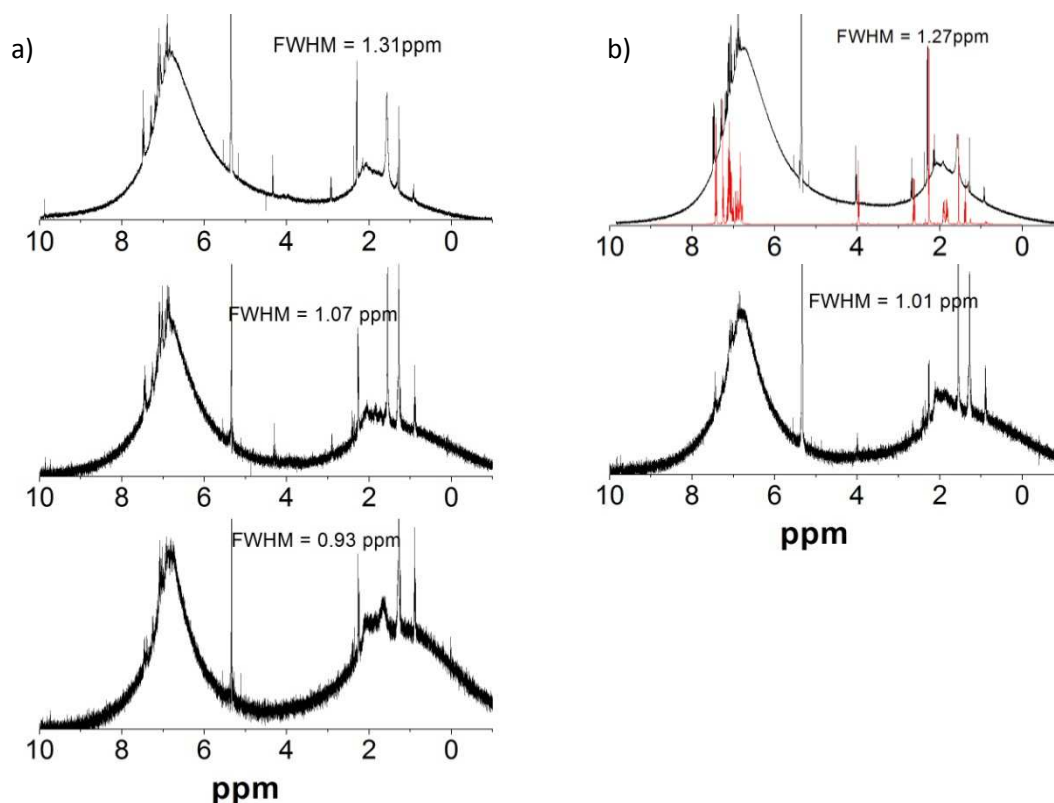


Figure 3.11. ^1H NMR spectra of CD_2Cl_2 solutions of silver nanoparticles: a) AgTPDC3-I – top spectrum, AgTPDC3-II – middle spectrum, AgTPDC3-III – bottom spectrum; b) AgTPDC4-I – top spectrum, AgTPDC4-II – bottom spectrum. ^1H NMR spectrum of TPDC4SH in CDCl_3 (provided by Dr. Michal Malicki) is included in the uppermost graph for comparison (red line). The full width at half-maximum (FWHM) measured for the broad band in the aromatic-proton region is given for each spectrum.

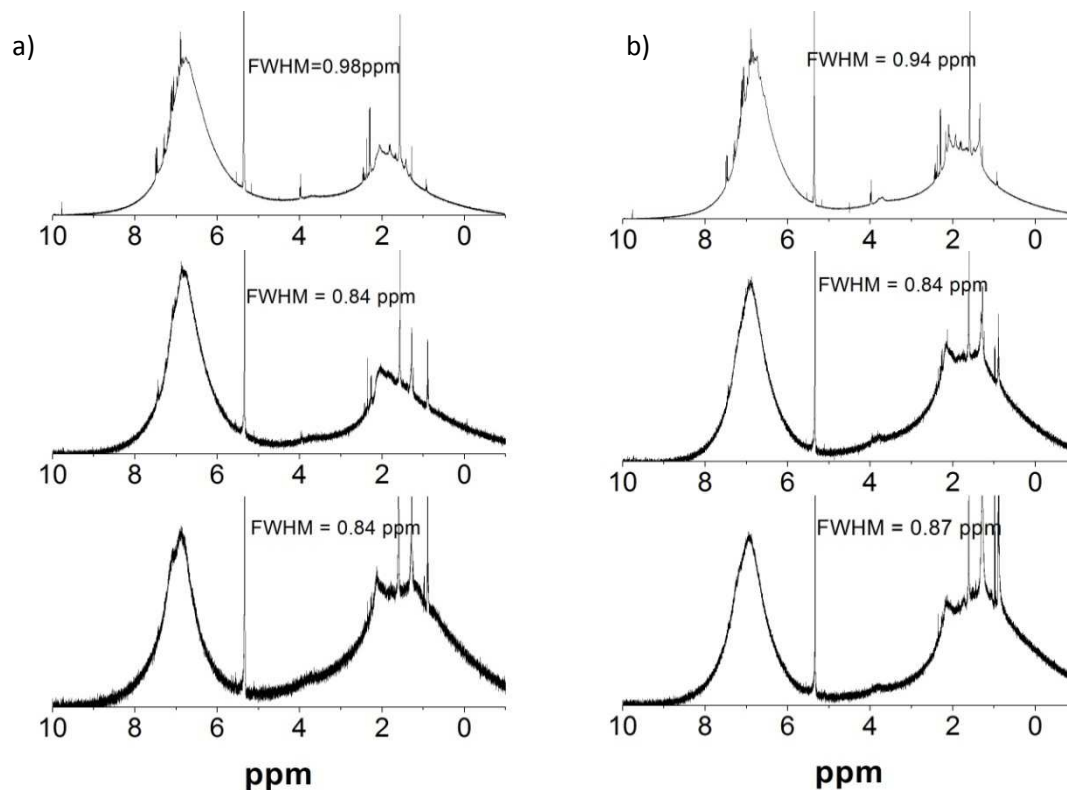


Figure 3.12. ^1H NMR spectra of CD_2Cl_2 solutions of silver nanoparticles: a) AgTPDC8-I – top spectrum, AgTPDC8-II – middle spectrum, AgTPDC8-III – bottom spectrum; b) AgTPDC12-I – top spectrum, AgTPDC12-II – middle spectrum, AgTPDC12-III – bottom spectrum. The full width at half-maximum (FWHM) measured for the broad band in the aromatic-proton region is given for each spectrum.

Figure 3.11 and 3.12 show the ^1H NMR spectra of CD_2Cl_2 solutions of silver nanoparticles studied herein. Each spectrum exhibits two broad bands: one around 6.8 ppm (aromatic protons) and another at ca. 2 ppm (aliphatic protons). The broad bands in most cases are also accompanied by sharp lines on top of them. In order to help identify the origin of these bands and the sharp lines, the spectrum of the sample AgTPDC4-I is

plotted together with spectrum of TPDC4SH ligand. The spectral lines of the TPDC4SH ligand are positioned on the lower field side of the band maximum at around 6.8 ppm. The spectrum of AgTPDC4-I shows sharp peaks on the lower field side of the band, and the peak positions agree well with the positions of the peaks of TPDC4SH. The broad band at 6.8 ppm is a result of broadening of the ^1H NMR lines of the aromatic protons of the TPDC3SH ligands due to homogenous and inhomogeneous broadening.^{3, 37} More detailed discussion about the broadening mechanisms will be provided later in this section. The sharp features, on the other hand, can be assigned to free ligands, which are present in the solution together with the adsorbed ligands.^{xii} The presence of a broad band and sharp features in the aliphatic-proton region can be explained analogously to the description of the aromatic-proton signals.

The relative intensities of the aliphatic and the aromatic bands should be also indicative of DDT present in the samples. Table 3.3 summarizes the integrated signals of the aliphatic band normalized to the aromatic one.^{xiii} The increasing values of the aliphatic-proton signal integral for the systems incorporating higher fractions of DDT in the mixed-ligand monolayers are in agreement with the larger amounts of alkyl chains in these systems.^{xiv}

The measured values of the integrated aliphatic-proton signal are most likely underestimated in all cases. Lica et al. demonstrated that ^1H NMR peaks of protons on the methylene group in the α -position to the thiol group in octylthiol adsorbed on gold

^{xii} It is shown in this section below that T_2 is much longer for the sharp peaks than the broad band.

^{xiii} The signal was integrated in the range from -2.5 to 4.5 ppm and from 4.5 to 10.0 ppm for the aliphatic- and the aromatic-proton bands, respectively. The obtained integral values were multiplied by a factor such that the integral of the aromatic-proton band was equal to unity for each spectrum.

^{xiv} Due to multiple sources of error the values in Table 3.3 can be considered only qualitatively.

nanoparticles do not show any signal, while the remaining protons show signals that are significantly broaden and shifted downfield.³⁴ The lack of signal from protons on the methylene group in the α -position to the thiol group is thought to be caused by the effect of their proximity to the metal surface.³⁴ If this is also the case for the systems studied herein, this effect leads to an underestimation of the aliphatic-proton band integral values. The possible mechanisms of broadening and shifts of the peaks are discussed bellow.

Table 3.3. Values of the integrated ^1H NMR signal in the aliphatic-proton band region normalized to the integrated aromatic-proton band.^v The numbers in parenthesis represent the expected values, for the systems with TPD ligands only.

Sample	Aliphatic-proton Band Integral	Sample	Aliphatic-proton Band Integral
AgTPDC3-I	0.4 (0.5)	AgTPDC4-I	0.4 (0.6)
AgTPDC3-II	0.7	AgTPDC4-II	0.9
AgTPDC3-III	1.4		
AgTPDC8-I	0.6 (0.9)	AgTPDC12-I	0.9 (1.2)
AgTPDC8-II	0.9	AgTPDC12-II	1.5
AgTPDC8-III	1.7	AgTPDC12-III	1.7

The fraction of desorbed chromophoric ligands can be estimated by comparing integration values of the sharp features present in the spectra with the integral of the

whole band.^{xv} The integrated NMR signal of the sharp features that are present in the aromatic-proton region was found to be less than 2% of the broad band for all samples. Such comparison can be justified based on the observation that the spin-lattice relaxation time (T_1) is comparable for free and bound ligands, as discussed below.

3.5.1. *The Source of Line Broadening*

There are two major mechanisms contributing to broadening of NMR lines of organic ligand coated metal nanoparticles: inhomogeneous and homogenous broadening.^{1, 3, 11, 35, 36} Inhomogeneous broadening originates from the distribution of chemical shifts caused by different environments the molecules experience on the surface of a NP. It has been proposed that different binding sites, i.e., terraces, edges, and vertices, lead to different chemical shifts thus contributing to the broadening of the ^1H NMR signals.¹ Peaks of α - and β -CH₂ groups in thiolates adsorbed on Au nanoparticles experience the most severe broadening and this effect falls off sharply with the distance from the metal surface.²⁷ Homogenous broadening, on the other hand, is associated with proton relaxation times. The half-width of an NMR signal is inversely proportional to the relaxation time of the species giving rise to the signal. The line width is therefore dependent on the fastest type of relaxation.³⁷ Normally the spin-spin relaxation time, T_2 , is much shorter than the spin-lattice relaxation, T_1 , thus:

$$\nu_{1/2} \sim \frac{1}{T_2} \quad (3.1)$$

^{xv} Integration of the sharp peaks was performed after subtracting the underlying broad band by baseline correction.

The NMR relaxation times (T_1 and T_2) are influenced by temperature, viscosity of the medium and size of the molecules, e.g., in crystalline solids where both translational and rotational movements of the molecules are stopped, T_1 values are exceptionally large, while T_2 values are remarkably small.³⁷

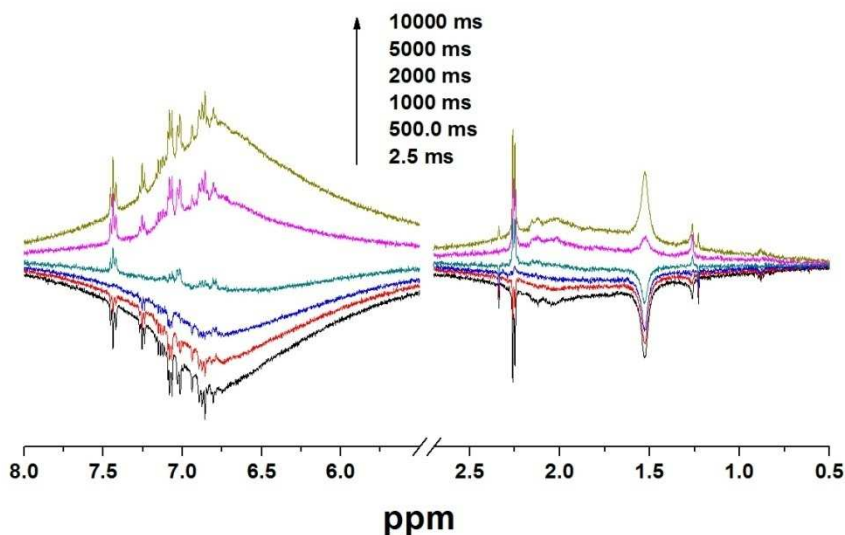


Figure 3.13. ^1H NMR spectral changes during T_1 experiment performed for AgTPDC3-I in CD_2Cl_2 .

The AgNP systems under investigation show T_1 values of ca. 3 seconds, only slightly larger than T_1 measured for free ligands in solution (Figure 3.13). The sharp peaks in Figure 3.13 are due to the presence of unbound ligands. This actually provides us with a means for the direct comparison of spin-lattice relaxation times of the chromophores attached to the nanoparticles and of the unbound ligands in solution. It is evident from Figure 3.13 that the spectral evolution of both the broad aromatic-proton band as well as that of the sharp features is very similar. This is consistent with the TPD

ligands, attached or not to the nanoparticles, being dissolved in a solvent. The inhomogeneity of the magnetic field introduced by a random movement of the solvent molecules (lattice) should be similar for both free ligands and the ligands anchored to the nanoparticles.

Spin-spin relaxation, T_2 , on the other hand, is affected by nuclei precessing with the same frequency very close to each other, where energy can be exchanged between the nuclei, leading to dephasing of the magnetization in the sample. The exchange of the energy between nuclei is more efficient when the nuclei are close to each other for a long time, such as in concentrated solutions or a crystalline material, than in dilute solutions. This process certainly should decrease spin-spin relaxation time of the systems of tightly packed ligands on nanoparticle surface and in principle should be indicative of the degree of packing of the chromophores in the monolayers on the nanoparticles.

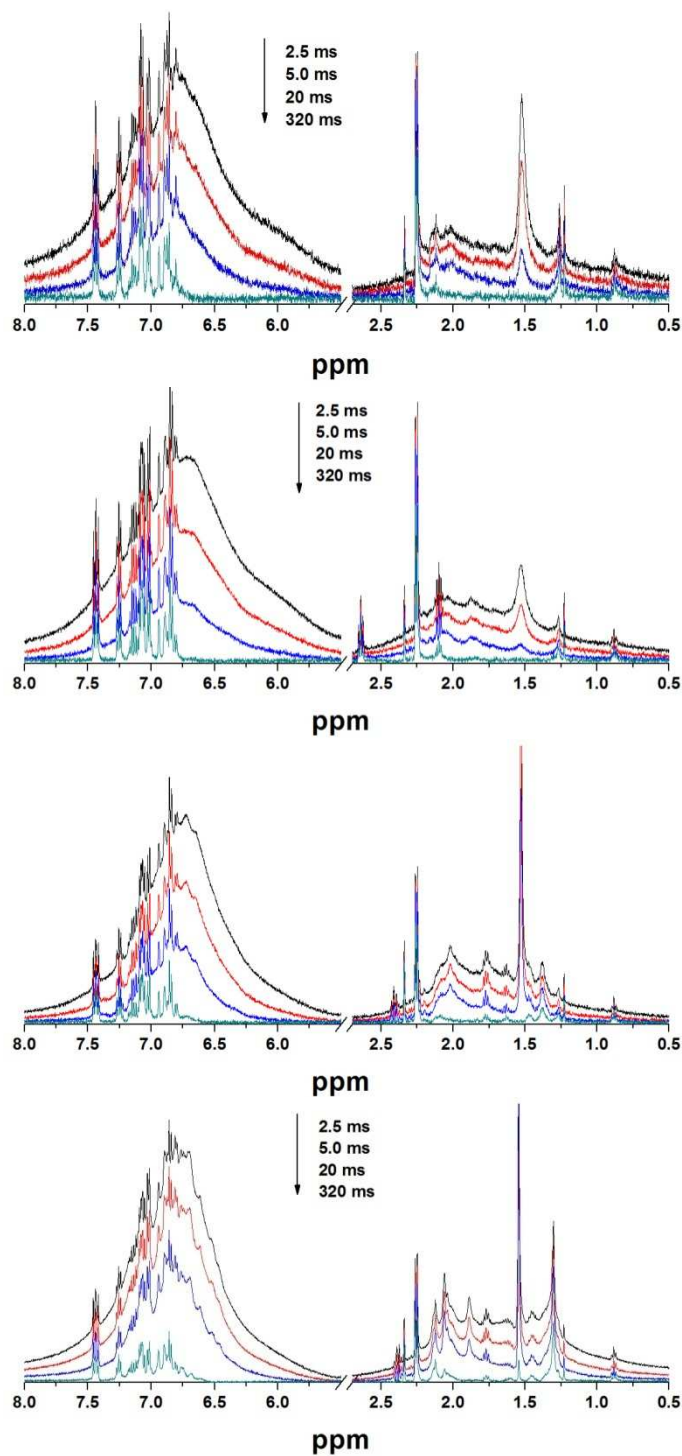


Figure 3.14. Selected spectra acquired at different delays during a CPMG-pulse-sequence experiment performed on CD_2Cl_2 solutions of AgTPDC3-I, AgTPDC4-I, AgTPDC8-I and AgTPDC12-I, from top to bottom.

Spin-spin relaxation times were measured using the CPMG-pulse-sequence technique. The spectral evolutions throughout the CPMG-pulse-sequence measurements are shown in Figure 3.14. It is evident that the broad features decay much faster than the sharp peaks, which means that T_2 values of the protons in TPD moieties attached to the surface of nanoparticles are much smaller than those of free ligands.^{xvi} The values of T_2 at 6.8 ppm and at 2.0 ppm extracted from these measurements^{xvii} are summarized in Table 3.4 together with the values of the FWHM measured for the aromatic-proton bands Figure 3.11 and Figure 3.12).^{xviii} According to equation (3.1), FWHM should be correlated with the T_2 values, if the broadening is solely due to homogenous broadening.

Table 3.4. Summary of results of FWHM of the aromatic-proton band and of T_2 relaxation times found from ^1H NMR spectra of Ag NPs coated exclusively with TPD-thiols.

Sample	FWHM [ppm]	T_2 at 6.8 ppm [ms]	T_2 at 2.0 ppm [ms]
AgTPDC3	1.31	14.4	35
AgTPDC4	1.27	11.0	20.7
AgTPDC8	0.98	17.2	25
AgTPDC12	0.94	25.8	52

^{xvi} T_2 measured for the sharp peaks is about 2 seconds, which is typical for dilute solutions.

^{xvii} T_2 relaxation time is defined as a time after which the signal decays to 1/e of its original intensity.

^{xviii} The positions, at which T_2 relaxation times are reported, have been chosen to be close to the maxima and centers of the bands and at the same time not to overlap with the sharp peaks.

The values of FWHM of the aromatic band show a consistent trend with the length of the linker of the TPD ligand. The largest half-width is observed for AgTPDC3-I and then it systematically gets smaller for the chromophores with longer linkers. If the broadening is solely due to the decrease in T_2 , an opposite trend should be observed for the spin-spin relaxation values of the aromatic band. However, the smallest value for T_2 at 6.8 ppm is measured for AgTPDC4 and for the ligands with longer linkers it gets systematically longer, which is in agreement with the corresponding FWHM values. This systematic behavior, for the C4, C8 and C12 alkyl linker systems, correlates well with the alkyl chain length and is consistent with the concept of larger free volume for the TPD being further away from a sphere. The larger free volume for the TPD end group means larger distance between the chromophores and slower T_2 relaxation time. The AgTPDC3-I system, however, does not fit to this trend, since both the FWHM and T_2 are larger than for AgTPDC4-I, which clearly indicates that homogenous broadening is not the only mechanism contributing to the peak broadening. Significant amount of broadening should also be due to inhomogeneity of the chemical environment. As mentioned above, different binding sites and proximity to the metal surface can lead to different chemical shifts, thus contributing to the broadening of the ^1H NMR signals.¹ The effects of the inhomogeneous broadening can be also seen in all systems, since the maxima of the broad aromatic bands are down field from the signals of the free TPD ligands. Moreover, the inhomogeneous broadening is significantly larger in C3 linker system than in C4 linker system as both FWHM and T_2 are larger for the first one.

A possible reason for smaller T_2 values measured for sample AgTPDC3-I can be due to the significantly smaller average size of the nanoparticles, 3.5 nm for C3 vs. 5.2

nm for C4 system, which should result in a larger free volume for the TPD end groups. A smaller sphere has larger curvature than a bigger particle, which provides more free volume for the end group (Figure 3.1). This suggests that the degree of packing^{xix} only partially contributes to the broadening of the aromatic band and that significant broadening is most likely due to environmental inhomogeneity.³⁵ Moreover, IR absorption data for the alkyl C-H stretching modes suggests that the degree of order is higher for the chromophores with longer alkyl linkers than in the chromophores with short chains, at least along the alkyl chains as discussed in section 3.4. The IR data is also supported by the fact that larger value of T_2 at 2.0 ppm for the C3 system than for C4 and C8 is also consistent with more disorder in the alkyl linker.^{xx} A lesser degree of order would also introduce more inhomogeneity. It should be also pointed out that the AgTPDC3-I sample is the only sample with an odd number of carbon atoms in the ligand linker, which could induce different orientation of the chromophoric end groups with respect to each other and/or the silver core than in the case of even number of methylene groups, and this could affect the degree of packing.³⁸ The effect of odd or even number of carbon atoms in the alkyl linker on the geometry of the end group is known as the odd-even effect³⁸ and is described in more detail in Chapter 5.

In conclusion, the results of the measurements of T_1 and T_2 relaxation times are consistent with the notion of a densely packed layer of ligands attached to the AgNP and are consistent with the IR results on these systems. Spin-spin relaxation and inhomogeneous broadening seem to be the main source of severe broadening of the

^{xix} Lower degree of packing of ligands in the sample AgTPDC3-I is also supported by footprint calculations shown below in Table 3.5.

^{xx} Smaller degree of packing or longer T_2 can also be a result of a larger distance between the alkyl chains if the limiting factors for packing are the bulky TPD end groups.

proton NMR lines. Moreover, T_2 measurements provide very useful information about the degree of packing of the TPD end groups attached to the nanoparticles via thiolated alkyl chain. The values of T_2 , which are related to the degree of packing of the TPD ligands, are consistent with the concept of free volume as a function of distance from a spherical nanoparticle for the systems C4, C8 and C12. On the other hand, the lesser degree of packing of the monolayer in the C3 system can be assigned either to the smaller average size of the nanoparticles, a higher degree of disorder in the monolayer, or a particular geometry of the bulky TPD end groups.

3.6. *Determination of Surface Coverage of the TPD Ligands Adsorbed on the AgNP.*

The goals of this section are to determine the average number of TPD ligands per nanoparticle and the average footprint^{xxi} of the TPD ligands on the nanoparticle surface, which characterize the coverage of the AgNP with the TPD ligands. The information about the coverage is crucial in the photophysical studies of the TPD / AgNP systems. The average number of TPD ligands per nanoparticle and the average footprint of the TPD ligands on the nanoparticle surface can be determined if the number of TPD ligands and the surface area of the nanoparticles are known in the corresponding TPD / AgNP systems, which can be calculated from known molar concentrations of TPD and AgNP.

One method of performing such analysis invokes Beer's law, since both TPD and AgNP show strong absorption in the UV-visible range. In order to utilize this method the extinction coefficients and absorbance of the TPD ligands and the AgNP must be known. The extinction coefficient of TPD ligands can be readily determined from Beer's law

^{xxi} Footprint refers to an area per TPD ligand in systems of AgNP functionalized with TPD ligands only.

using unbound TPD ligands. The absorbance of TPD in the TPD / AgNP systems, on the other hand, is more difficult to measure, since there is a substantial overlap of the TPD absorption band with the plasmon absorption from AgNP, where the absorption originating from the TPD moiety is seen as a small peak or a shoulder, depending on the TPD / AgNP system, on the high-energy slope of the surface plasmon resonance band (Figure 3.4). Apart from this complication, the position of the surface plasmon resonance band depends substantially on the TPD-thiol coverage as well as on the length of the alkyl linker between the TPD end group and the nanoparticle surface. Additionally, there are reports indicating alteration of the extinction coefficient of dyes in the proximity of metal nanoparticles.³⁹ The above obstacles do not allow for accurate determination of the TPD absorbance in the TPD / AgNP systems from their UV-vis absorption spectra. The absorbance of TPD in the studied systems was measured after eliminating the plasmon absorption by etching the AgNP with an oxidizing agent⁴⁰. The absorbance of the AgNP, on the other hand, can be readily measured, since there is no interference from the TPD absorption to the plasmon resonance absorption band at its maximum (Figure 3.4). Finally, in order to determine the extinction coefficient of the AgNP in the studied systems the formula weights of the nanoparticles and their concentrations need to be known. The formula weights are determined for the measured nanoparticle diameters and known density of metallic silver, whereas the concentrations are determined using inductively coupled plasma emission spectroscopy (ICP-ES).

3.6.1. Procedure of Etching of Silver Nanoparticles

The plasmon absorption of AgNPs can be eliminated, as mentioned above, by etching silver metal electrochemically. However, the possible effects of the oxidizing agent used for this purpose on the TPD chromophores need to be addressed. Figure 3.15a shows effects of a strongly oxidizing agent, SbCl_5 , on a solution of TPD in dichloromethane (DCM). The radical monocation of TPD ($\text{TPD}^{\bullet+}$)⁴¹ is formed upon addition of a substoichiometric amount of SbCl_5 (red line), followed by spectral changes that can be attributed to the formation of the TPD dication (TPD^{++}) upon addition of an excess of the oxidizing agent⁴¹ (blue line). Interestingly, addition of a small amount of dodecanethiol (DDT) coated AgNP to the solution of TPD^{++} results in a complete disappearance of the silver nanoparticles with spectral changes that also suggest a reduction of the dication to the neutral form of TPD. Figure 3.15b shows TPD spectrum in DCM (black line) together with the spectrum of the same solution of TPD after adding the DDT coated AgNP and subsequent addition of SbCl_5 . There is no sign of $\text{TPD}^{\bullet+}$ and the surface plasmon resonance band of AgNP clearly disappears leaving only the spectrum of neutral TPD, which very well matches the original spectrum of the TPD solution.

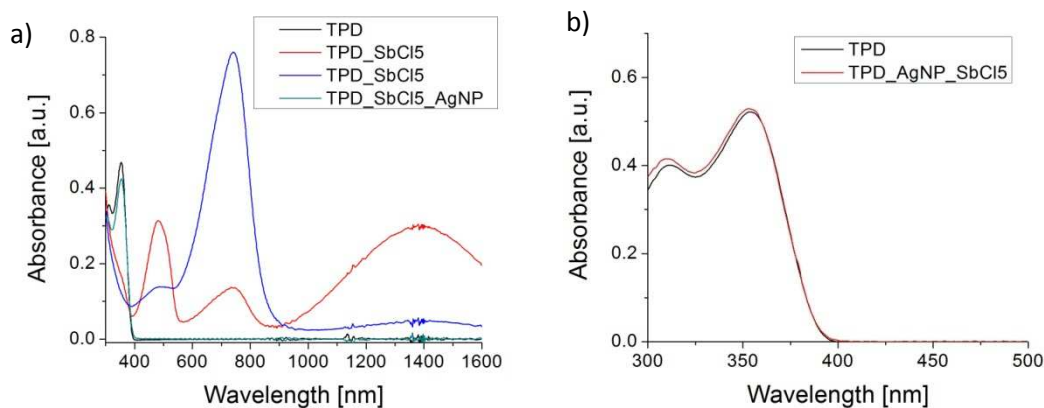


Figure 3.15. a) UV-Vis absorption spectra of TPD solution in DCM recorded after sequential addition of two volumes of SbCl_5 and of a portion of AgNP. TPD in DCM – black line, TPD^{*+} formed by oxidation of TPD with substoichiometric amount of SbCl_5 – red line, TPD^{*+} formed after addition of excess of SbCl_5 – blue line, TPD spectrum after addition of DDT coated AgNP to the solution of TPD^{*+} . b) UV-Vis absorption spectra of TPD in DCM – black line, and of the final product of the oxidation/reduction processes depicted in the next chapter. The absorbance was scaled to account for dilution caused by addition of solutions of AgNP and SbCl_5 .

As can be seen from Figure 3.15b, the spectrum of the mixture of TPD, AgNP and SbCl_5 not only looks almost exactly like the spectrum of TPD, but also the value of absorbance is almost identical to the absorbance of the original TPD solution. This shows that SbCl_5 can be utilized as an agent for the oxidation of AgNP functionalized with TPD ligands in order to determine the concentration of the TPD moieties in these samples.

3.6.2. Determination of the Concentration of TPD Ligands in the NP Samples

The concentration of TPD ligands was calculated from Beer's law. Five different volumes of a stock solution of AgTPDC_{x-z} (where $x = 3, 4, 8, 12$, $z = \text{I, II, III}$) were diluted with 3 mL of DCM in a 1 cm cuvette followed by addition of 10 μL of 10^{-3} M DCM solution of SbCl_5 resulting in a colorless solution. In the column b) of Figure 3.16, Figure 3.17, Figure 3.18 and Figure 3.19 are shown spectra of TPD ligands after oxidation of the silver cores with the insets showing values of absorbance at 355 nm as a function of the volume of the stock solutions. The data points shown in the insets were fitted with a linear function ($y = Ax$). The molar concentrations C_{TPD} of TPD in the stock solutions were calculated from modified Beer's equation:

$$C_{\text{TPD}} = \frac{A \cdot V_1}{\epsilon_{\text{TPD}} \cdot l} \quad (3.2)$$

where A is a slope obtained from the fitting, $V_1 = 3000 \mu\text{L}$, $l = 1 \text{ cm}$ and $\epsilon_{\text{TPD}} = 4.04 \times 10^4 \text{ M}^{-1} \text{ cm}^{-1}$.^{xxii} The results are summarized in Table 3.5.

^{xxii} The measurement of extinction coefficient of TPD ligands is described in experimental section.

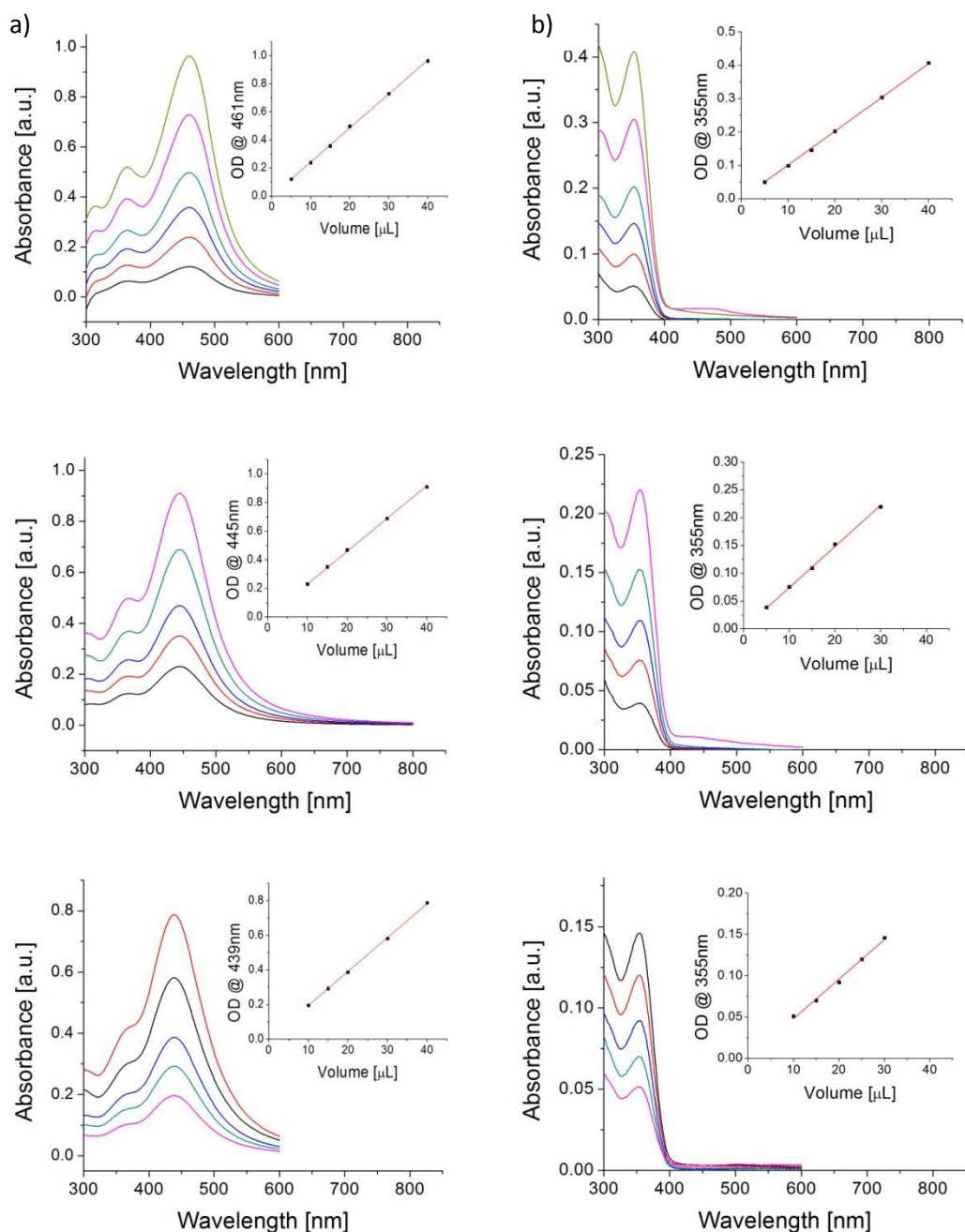


Figure 3.16. a) UV-vis absorption spectra of AgTPDC3-I – top graph, AgTPDC3-II – middle, AgTPDC3-III – bottom at varying concentrations obtained by dilution of different volumes of the stock solution in a mixture of toluene and DMF (5:1). The insets show the OD at λ_{max} as a function of the volumes of the stock solutions used. Column b) shows spectra of these systems in DCM after the reaction with SbCl_5 .

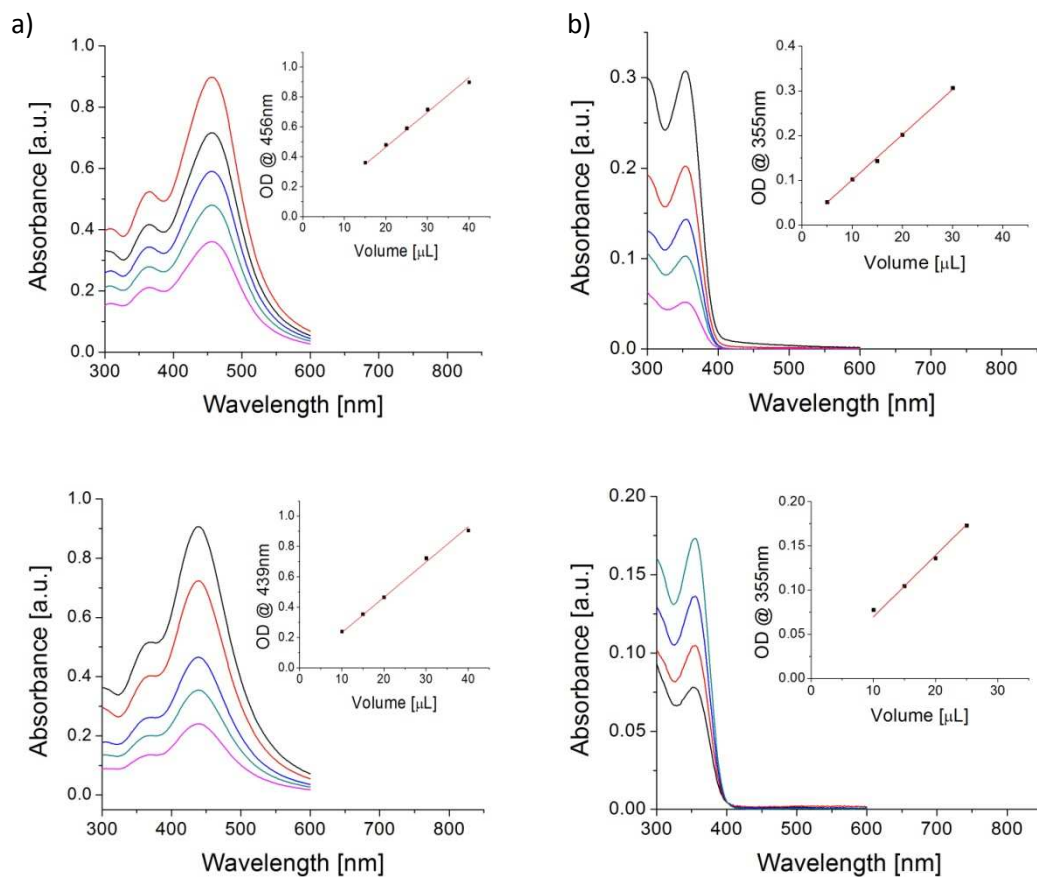


Figure 3.17. a) UV-vis absorption spectra of AgTPDC4-I – top graph, AgTPDC4-II – bottom at varying concentrations obtained by dilution of different volumes of the stock solution in a mixture of toluene and DMF (5:1). The insets show the OD at λ_{max} as a function of the volumes of the stock solutions used. Column b) shows spectra of these systems in DCM after the reaction with SbCl_5 .

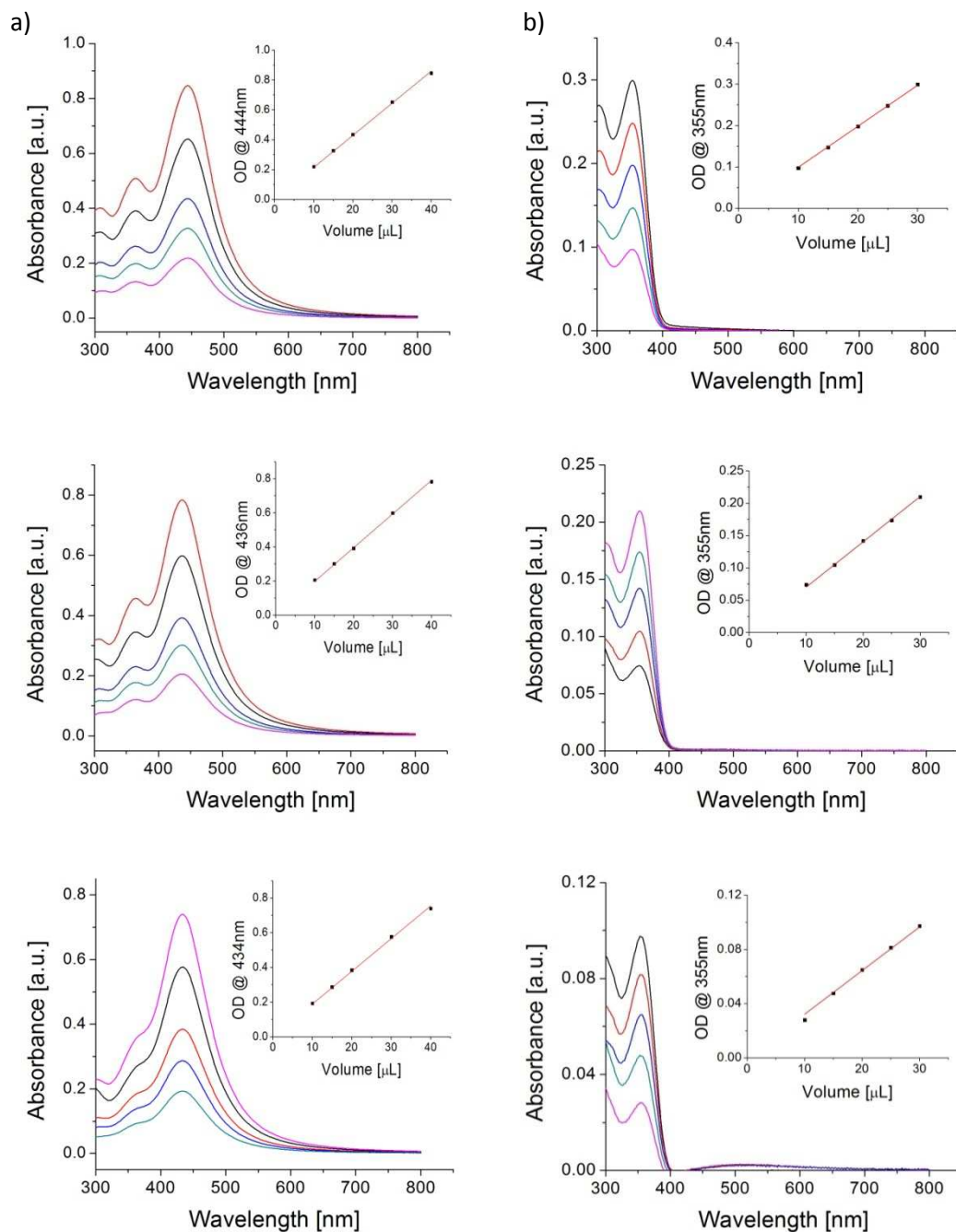


Figure 3.18. a) UV-vis absorption spectra of AgTPDC8-I – top graph, AgTPDC8-II – middle, AgTPDC8-III – bottom at varying concentrations obtained by dilution of different volumes of the stock solution in a mixture of toluene and DMF (5:1). The insets show the OD at λ_{\max} as a function of the volumes of the stock solutions used. Column b) shows spectra of these systems in DCM after the reaction with SbCl_5 .

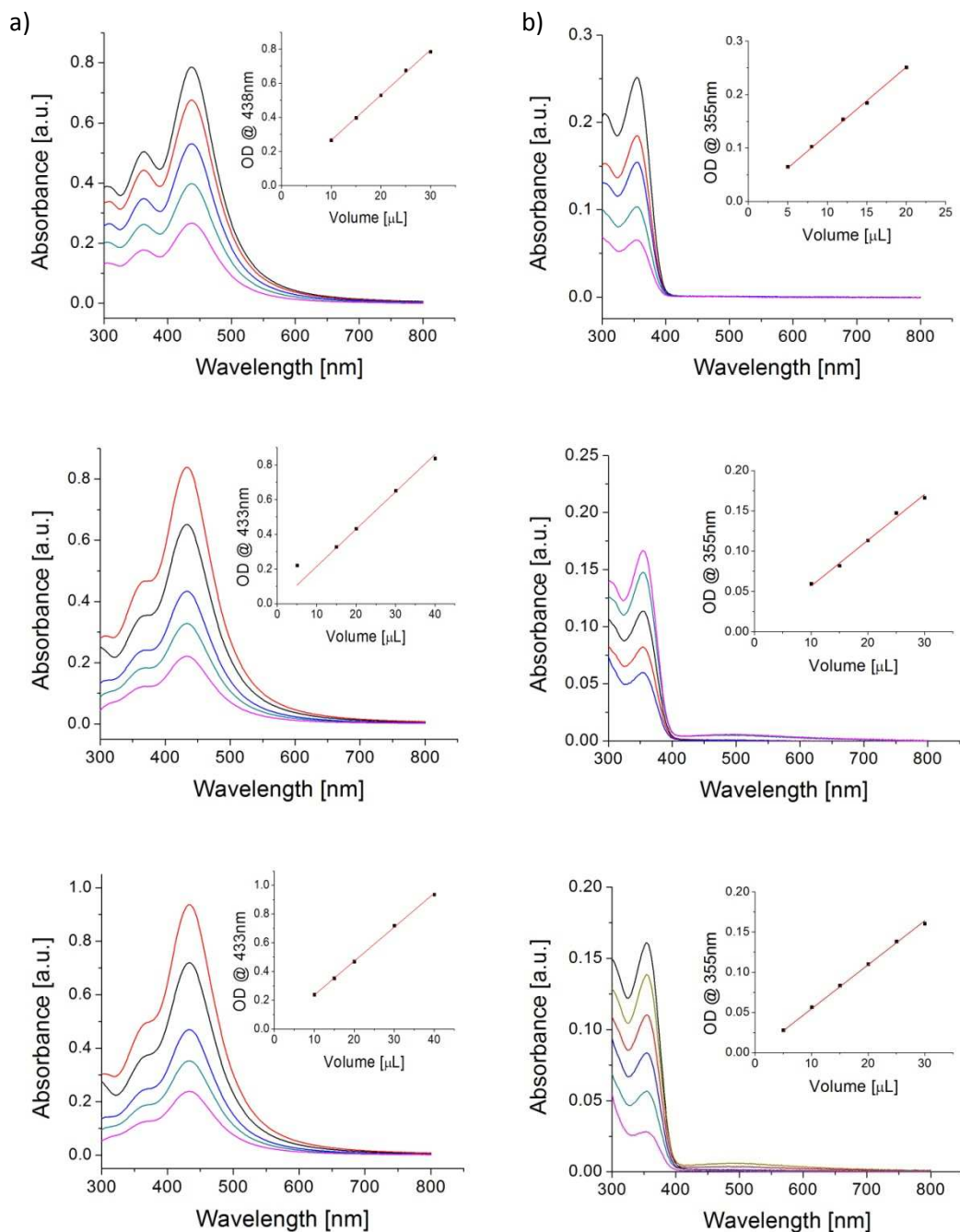


Figure 3.19. a) UV-vis absorption spectra of AgTPDC12-I – top graph, AgTPDC12-II – middle, AgTPDC12-III – bottom at varying concentrations obtained by dilution of different volumes of the stock solution in a mixture of toluene and DMF (5:1). The insets show the OD at λ_{max} as a function of the volumes of the stock solutions used. Column b) shows spectra of these systems in DCM after the reaction with SbCl_5 .

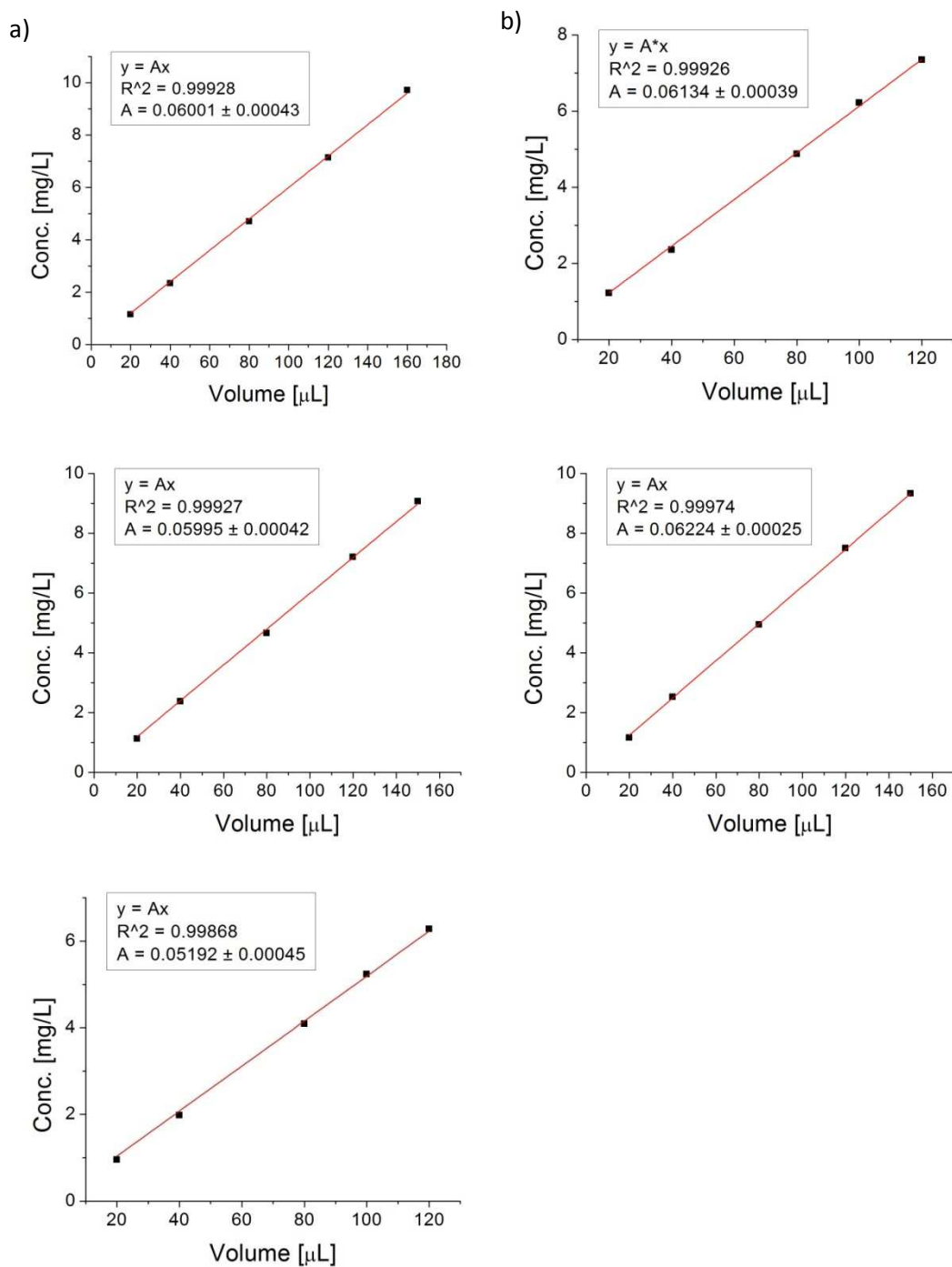


Figure 3.20. Concentration of silver atoms measured by ICP-ES as a function of volume of the stock solutions of the samples of a) AgTPDC3-I – top graph, AgTPDC3-II – middle, AgTPDC3-III – bottom and b) AgTPDC4-I – top, AgTPDC4-II – bottom. Each sample was reacted with 0.5 mL of HNO_3 and further diluted with 10 mL of water.

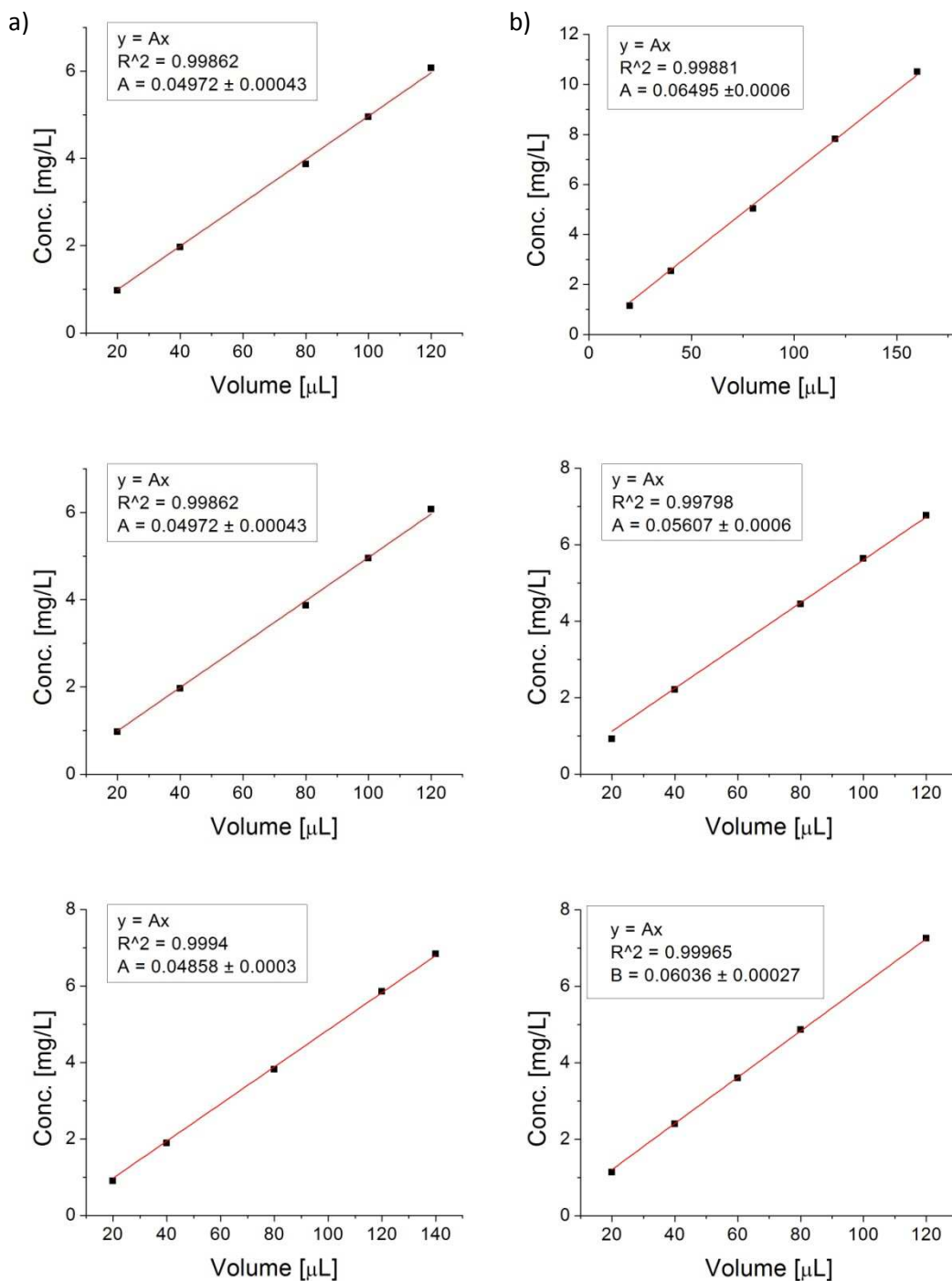


Figure 3.21. Concentration of silver atoms measured by ICP-ES as a function of volume of the stock solutions of the samples of a) AgTPDC8-I – top graph, AgTPDC8-II – middle, AgTPDC8-III – bottom and b) AgTPDC12-I – top, AgTPDC12-II – middle and AgTPDC12-III – bottom. Each sample was reacted with 0.5 mL of HNO_3 and further diluted with 10 mL of water.

3.6.3. Determination of Extinction Coefficient of the Silver Nanoparticles

The molar concentration of the silver nanoparticles can be calculated from the concentration of silver in the stock solutions, expressed in g / L, the size of the nanoparticles measured from TEM images, and a known density of bulk silver. The concentration, in g / L, of silver in the stock solutions of the TPD / AgNP systems were measured with inductively coupled plasma emission spectroscopy (ICP-ES). In order to obtain statistically reliable data the concentrations were measured at 5 different dilutions^{xxiii} for each of the TPD / AgNP systems. The measured values of concentration of silver are plotted as a function of the stock solution volumes used (Figure 3.20 and Figure 3.21). The data were then fitted with a linear function and the slope was used to calculate the concentrations of silver in the corresponding stock solutions – C . Assuming a perfectly spherical shape of the nanoparticles, the molar concentration – C_{AgNP} was calculated according to the equation (3.3) from the concentration C and average formula weight – FW , which was obtained from the TEM analysis, using equation (3.4).

$$C_{AgNP} = \frac{C}{FW} \quad (3.3)$$

$$FW = \frac{\sum_i^n \left(\frac{4}{3}\right) \pi r_i^3 \cdot d \cdot N_A}{n} \quad (3.4)$$

where: C is the concentration of silver in g / L, r is the measured from TEM images radius of the nanoparticles, $d = 10.5 \text{ g / cm}^3$ represents the density of bulk silver,^{42, 43} and N_A is Avogadro is number. The averaging of the FW is obtained by summing the calculated weight of n nanoparticles (where $n > 500$) and dividing by n according to

^{xxiii} The solutions for ICP-ES were prepared oxidizing small volumes, 20 – 160 μL , (Figure 3.20 and Figure 3.21) of the stock solutions of nanoparticles with 0.5 mL HNO_3 followed by dilution with 10 mL of distilled water.

equation (3.4). This type of summation in averaging accounts more appropriately for the particle size distribution than calculation the *FW* based on average radius of the nanoparticles. The calculated molar concentration of AgNP in each studied systems is used to determine the extinction coefficient of the AgNP from the Beer's law;

$$Abs = \epsilon_{AgNP} \frac{C_{AgNP} \cdot l}{V_1} \cdot V_0 \quad (3.5)$$

where: ϵ_{AgNP} is the extinction coefficient of silver nanoparticles at the maximum of the surface plasmon resonance band (λ_{max}), C_{AgNP} is the concentration of AgNP, l is the path length (1 cm), V_0 is the volume of the stock solution, $V_l = 3$ mL and Abs is the absorbance at λ_{max} whose values measured for 5 different stock solution volumes, V_0 , are plotted in Figure 3.16, Figure 3.17, Figure 3.18 and Figure 3.19. The plotted data points were fitted with a linear function ($y = Ax$). Using the slope of the fitting function A ;

$$A = \epsilon_{AgNP} \frac{C_0 \cdot l}{V_1} \quad (3.6)$$

the extinction coefficients were calculated from the equation (3.7).

$$\epsilon_{AgNP} = \frac{A \cdot V_1}{C_0 \cdot l} \quad (3.7)$$

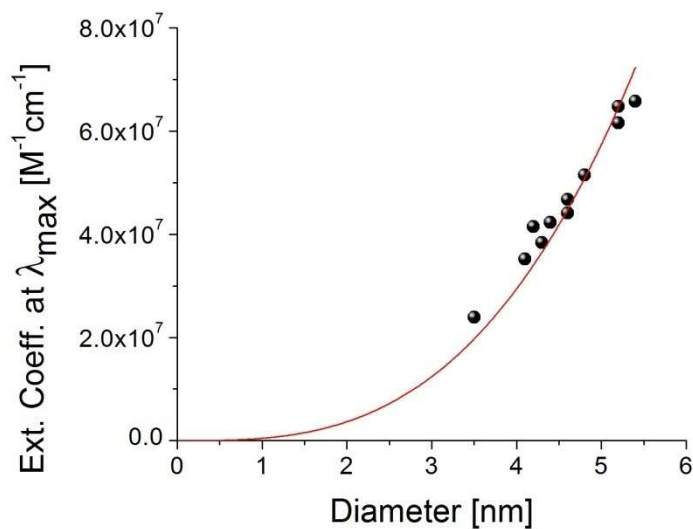


Figure 3.22. Values of the extinction coefficient of silver nanoparticles at the maximum of the surface plasmon resonance in the investigated samples as a function of nanoparticles (black spheres). The red line represents a fit of the data with a function $y = ax^3$.

The values of ϵ_{AgNP} for the studied nanoparticles are summarized in Figure 3.22 where they are plotted as a function of the average diameter of AgNP. According to Mie theory the relationship between the extinction coefficient and particle size can be described by⁴⁴: $\epsilon_{AgNP} \sim R^3$, where R is the radius of the particle. Red line in Figure 3.22 is a fit of the experimentally measured values of the molar extinction coefficient with a function $y = ax^3$. Observed dependence of the extinction coefficient of silver nanoparticles on their size is in a good agreement with theoretical prediction.

3.6.4. Determination of Average Area of The TPD ligand per AgNP

The average number of TPD ligands per AgNP, $Area_{TPD}$, was found by calculating the total surface area of all the measured nanoparticles in TEM analysis, divided by the number of TPD ligands corresponding to the number of measured nanoparticles, according to the equation (3.8).

$$Area_{TPD} = \frac{\sum_i^n 4\pi r_i^2}{nN} \quad (3.8)$$

where n is the number of nanoparticles the size of which was measured, r_i is the radius of the i -th particle, and N is the average number of TPD ligands per AgNP, which was determined from the ratios of average molar concentrations of TPD and AgNP. This calculation accounts for statistical distribution of the nanoparticle sizes, thus reducing error associated with nanoparticle size dispersion, but does not take into account possible footprint changes of the adsorbed ligands due to different curvatures of the nanoparticles. The errors were propagated to throughout all calculations. The errors associated with the measurements of nanoparticle sizes were determined by measuring 5 particles 20 times. The summary of the analysis described above is presented in Table 3.5.

Table 3.5. Summary of the measurements results used for the evaluation of the average number of TPD ligands per AgNP in the systems shown in the first column from the left. Subsequent columns show: average diameter, average formula weight of AgNP cores, concentration of silver atoms in the stock solutions, molar concentration of AgNP, extinction coefficient of AgNP, molar concentration of TPD ligands in stock solutions, ratio of TPD ligands per AgNP, and the average area per one TPD ligand on AgNP surface. The bolded font corresponds to the nanoparticles modified with TPD ligands only.

Sample	Avg. 2R [nm]	Avg. FW of AgNP [g / mole]	Conc. of Ag is stock solutions [mg / L]	Avg. molar concentration of AgNP [M]	Extinction coefficient of AgNP [$M^{-1}cm^{-1}$]	Molar concentration of TPD [M]	Avg. # of TPD ligands / AgNP	Avg. Area per TPD [\AA^2]
AgTPDC3-I	3.5 ± 1.3	2.1×10^5	630.1	3.0×10^{-6}	2.4×10^7	7.6×10^{-4}	250 ± 6	17.9 ± 0.4
AgTPDC3-II	5.2 ± 1.4	5.6×10^5	629.5	1.1×10^{-6}	6.2×10^7	5.6×10^{-4}	498 ± 13	18.5 ± 0.5
AgTPDC3-III	5.4 ± 1.3	6.1×10^5	545.2	0.9×10^{-6}	6.6×10^7	3.6×10^{-4}	403 ± 11	24.0 ± 0.7
AgTPDC4-I	5.2 ± 1.5	6.0×10^5	644.1	1.1×10^{-6}	6.5×10^7	7.6×10^{-4}	704 ± 18	13.3 ± 0.3
AgTPDC4-II	4.6 ± 1.4	4.1×10^5	643.5	1.6×10^{-6}	4.4×10^7	5.2×10^{-4}	330 ± 10	22.2 ± 0.7
AgTPDC8-I	4.3 ± 1.2	3.2×10^5	540.6	1.7×10^{-6}	3.8×10^7	7.4×10^{-4}	443 ± 11	14.2 ± 0.4
AgTPDC8-II	4.2 ± 1.6	3.7×10^5	522.1	1.4×10^{-6}	4.2×10^7	5.3×10^{-4}	368 ± 10	17.4 ± 0.5
AgTPDC8-III	4.8 ± 1.5	4.6×10^5	510.1	1.1×10^{-6}	5.2×10^7	2.4×10^{-4}	220 ± 6	36.2 ± 1.0
AgTPDC12-I	4.1 ± 1.4	3.0×10^5	682.0	2.3×10^{-6}	3.5×10^7	9.4×10^{-4}	417 ± 11	14.1 ± 0.4
AgTPDC12-II	4.6 ± 1.4	4.3×10^5	588.7	1.4×10^{-6}	4.7×10^7	4.3×10^{-4}	308 ± 9	24.1 ± 0.7
AgTPDC12-III	4.4 ± 1.4	3.8×10^5	633.8	1.7×10^{-6}	4.2×10^7	4.1×10^{-4}	245 ± 6	28.0 ± 0.7

The values of molecular footprint^{xxiv} for the different TPD-thiols are slightly smaller than, and in the case of TPDC3SH almost the same as, the footprint of alkylthiol molecules adsorbed on flat silver surface in densely packed monolayers. There the value of the footprint has been reported to be ca. 18 Å².⁴⁵ The smaller values of the footprint in the case of TPD-thiol coated AgNP can be explained by the fact that curved surfaces (which is the case for the small particles studied herein) provide more free volume than flat surfaces, allowing for higher density of the ligands in the monolayers.¹⁵

The slightly larger footprint calculated for AgTPDC3-I despite the smaller average size of the AgNP cores is consistent with a lower degree of order or conformational difference from the other samples, as suggested by FT-IR results. AgTPDC3-I is the only sample with TPD ligands having an odd number of carbon linkers, which could introduce an energetically favorable orientation of the chromophores with respect to the nanoparticle surface that is different from the orientation assumed in the case of even numbers of carbon atoms. The different orientation could hinder the degree of packing, leading to larger areas occupied by ligand on the surface of AgNP. Both the degree of order and the different orientation of the chromophores with respect to the metal surface could lead to the same effects and cannot be distinguished at this point.

3.6.5. Thermogravimetric Analysis

Thermogravimetric analysis (TGA) is often used in determining the amount of organics in hybrid materials containing organic and inorganic components.^{11, 46, 47} The

^{xxiv} In case of AgNP functionalized with TPD ligands only the average area occupied by one TPD ligand defines the TPD ligand footprint.

studied AgTPDCx-I systems ($x = 3, 4, 8$ and 12) are composed of a silver core and organic TPD ligands. Samples with mixed ligands are not considered in this analysis. Before the TGA measurements the samples were washed at least 3 times with hexane and dried in vacuum over at room temperature for 2 days. About 5 mg of each sample was used for the measurements. The mass loss was determined based on mass difference of each sample at room temperature and $900\text{ }^{\circ}\text{C}$, after which point no significant loss is observed as shown in Figure 3.23.

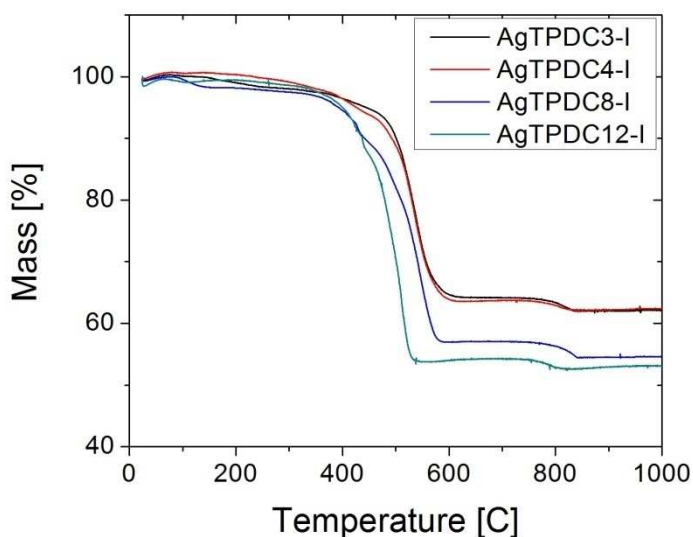


Figure 3.23. Thermogravimetric scans for samples AgTPDCx-I, where $x = 3, 4, 8$ and 12 . The measurements were performed by Mr. Chun Huang.

The TGA results are presented in Table 3.6, as a percentage of the mass loss, together with the percentage of the organic fraction in the AgTPDCx-I systems determined from the data presented in Table 3.5.

Table 3.6. Fraction of the organic component in the samples AgTPDCx-I, where x = 3, 4, 8 and 12, expressed in percentages. The results obtained from thermogravimetric analysis are compared with the analysis based on optical absorption and ICP-ES.

Sample	% of organics from TGA	% of organics from results in Table 3.5
AgTPDC3-I	38	42
AgTPDC4-I	38	42
AgTPDC8-I	45	48
AgTPDC12-I	47	50

The fractions obtained by TGA are consistently lower than the results obtained from the other method, by about 10% for samples TPDC3-I and AgTPDC4-I, and by about 6% for samples AgTPDC8-I and AgTPDC12-I. One of the possibilities for this discrepancy can be due to partial oxidation of silver during TGA measurement, since the atmosphere was air^{xxv}. Assuming the same conditions for oxidation in all samples, it should have smaller effect on samples with larger loss as there is smaller weight contribution from silver. This is indeed the case. Overall, the values of the organic fractions obtained with these two methods are in a good agreement with each other.

^{xxv} TGA measurements were initially performed in nitrogen atmosphere but no complete decomposition of the organics could be observed up to 1100°C. This was evident by lack of a plateau at the end of the scans.

3.7. Conclusions

The results of the TEM measurements show that the silver nanoparticles coated with different TPD-thiol and dodecanethiol ligands are spherical or close to spherical with their diameters ranging from 3.5 – 5.4 nm. The TEM-based interparticle spacing indicates that the short-linker TPD-thiols tend to form denser shells around the Ag core, which does not allow for substantial interdigitation of the ligands. A larger degree of interdigitation can be observed for AgTPDC8-I and the largest for AgTPDC12-I.

The presence of the TPD containing organic shells around silver nanoparticles is also confirmed by UV-Vis, FT-IR and ^1H NMR spectroscopies. UV-Vis absorption spectra show a clear dependence of the position of the surface plasmon resonance band on the length of the alkyl linker between the TPD end group and the nanoparticle surface, indicating a close proximity of the polarizable chromophores to the nanoparticle surface, which is in agreement with Mie theory. FT-IR spectra of the AgNP confirm the presence of TPD moieties and allow for determination of the conformation of alkyl chains. The positions of the methylene C-H stretching modes indicate predominantly fully extended C8 and C12 linkers, with C3 and C4 linkers showing gauche defects. ^1H NMR spectroscopy provides insights into the density of the TPD end groups in the AgNP systems. T_2 relaxation time values indicate an increase in the density of packing for the systems with an even number of methylene groups in the alkyl linkers with a decrease in its length. This trend is consistent with the concept of the decrease in the free volume when approaching the surface of a sphere, which is also consistent with the fact that the average areas per TPD ligand at the surface of AgNP in the systems of even number of carbons in the linker are very similar to each other, $\sim 14 \text{ \AA}^2$. The system with the shortest

linker has a value of T_2 larger than for the C4 linker system, indicating lower density of packing both in the chromophoric end groups and the aliphatic linker. It is also consistent with average area per TPD ligand at the nanoparticle surface (17.9 \AA^2), despite the small size of the silver cores. Odd number of carbon atoms in the alkyl linker can introduce different orientation of the end groups of the ligands, from that for even number of carbon atoms, affecting the way the ligands pack on the surface. Alternatively, disorder in the linker conformations can also lead to similar observations. Thus, both the degree of order and the different orientation of the chromophores with respect to each other or the metal surface could lead to the same effects and cannot be at this point distinguished.

Oxidation of the silver cores of the particles was used for the determination of the concentration of TPD ligands and ICP-ES and TEM analysis allowed for the determination of the concentration and molar extinction coefficients of silver nanoparticles. The molar concentrations of TPD ligands and AgNP were then used for the determination of the average surface area per TPD ligand. Moreover, TGA results are in good agreement with the results obtained with the method described above.

3.8. References

1. Badia, A.; Gao, W.; Singh, S.; Demers, L.; Cuccia, L.; Reven, L., Structure and Chain Dynamics of Alkanethiol-Capped Gold Colloids. *Langmuir* **1996**, *12* (5), 1262-1269.
2. Porter, L. A.; Ji, D.; Westcott, S. L.; Graupe, M.; Czernuszewicz, R. S.; Halas, N. J.; Lee, T. R., Gold and Silver Nanoparticles Functionalized by the Adsorption of Dialkyl Disulfides. *Langmuir* **1998**, *14* (26), 7378-7386.
3. Kohlmann, O.; Steinmetz, W. E.; Mao, X.-A.; Wuelfing, W. P.; Templeton, A. C.; Murray, R. W.; Johnson, C. S., NMR Diffusion, Relaxation, and Spectroscopic Studies of Water Soluble, Monolayer-Protected Gold Nanoclusters. *J. Phys. Chem. B* **2001**, *105* (37), 8801-8809.
4. Bauer, C.; Stellacci, F.; Perry, J., Relationship Between Structure and Solubility of Thiol-Protected Silver Nanoparticles and Assemblies. *Top. Catal.* **2008**, *47* (1), 32-41.
5. Snyder, R. G.; Strauss, H. L.; Elliger, C. A., Carbon-Hydrogen Stretching Modes and the Structure of n-alkyl Chains. 1. Long, Disordered Chains. *J. Phys. Chem.* **1982**, *86* (26), 5145-5150.
6. Brust, M.; Walker, M.; Bethell, D.; Schiffrin, D. J.; Whyman, R., Synthesis of Thiol-Derivatised Gold Nanoparticles in a Two-Phase Liquid-Liquid System. *J. Chem. Soc., Chem. Commun.* **1994**, 801.
7. Lin, X. M.; Sorensen, C. M.; Klabunde, K. J., Digestive Ripening, Nanophase Segregation and Superlattice Formation in Gold Nanocrystal Colloids. *J. Nanopart. Res.* **2000**, *2*, 157-164.
8. Kelly, K. L.; Coronado, E.; Zhao, L. L.; Schatz, G. C., The Optical Properties of Metal Nanoparticles: The Influence of Size, Shape, and Dielectric Constant. *J. Phys. Chem. B* **2003**, *17*, 668-677.
9. Hostetler, M. J.; Stokes, J. J.; Murray, R. W., Infrared Spectroscopy of Three-Dimensional Self-Assembled Monolayers: n-Alkanethiolate Monolayers on Gold Cluster Compounds. *Langmuir* **1996**, *12* (15), 3604-3612.

10. Price, R. C.; Whetten, R. L., Raman Spectroscopy of Benzenethiolates on Nanometer-Scale Gold Clusters. *J. Phys. Chem. B* **2006**, *110* (44), 22166-22171.
11. Terrill, R. H.; Postlethwaite, T. A.; Chen, C.-h.; Poon, C.-D.; Terzis, A.; Chen, A.; Hutchison, J. E.; Clark, M. R.; Wignall, G., Monolayers in Three Dimensions: NMR, SAXS, Thermal, and Electron Hopping Studies of Alkanethiol Stabilized Gold Clusters. *J. Am. Chem. Soc.* **1995**, *117* (50), 12537-12548.
12. Yamamoto, M.; Nakamoto, M., Novel Preparation of Monodispersed Silver Nanoparticles via Amine Adducts Derived from Insoluble Silver Myristate in Tertiary Alkylamine. *J. Mater. Chem.* **2003**, *13*, 2064-2065.
13. Sandhyarani, N.; Pradeep, T., Current Understanding of the Structure, Phase Transitions and Dynamics of Self-Assembled Monolayers on Two- and Three-Dimensional Surfaces. *Int. Rev. Phys. Chem.* **2003**, *22* (2), 221 - 262.
14. Bunge, S. D.; Boyle, T. J.; Headley, T. J., Synthesis of Coinage-Metal Nanoparticles from Mesityl Precursors. *Nano Lett.* **2003**, *3* (7), 901-905.
15. Cederquist, K. B.; Keating, C. D., Curvature Effects in DNA: Au Nanoparticle Conjugates. *ACS Nano* **2009**, *3* (2), 256-260.
16. Hill, H. D.; Millstone, J. E.; Banholzer, M. J.; Mirkin, C. A., The Role Radius of Curvature Plays in Thiolated Oligonucleotide Loading on Gold Nanoparticles. *ACS Nano* **2009**, *3* (2), 418-424.
17. Jiang, P.; Xie, S.; Yao, J.; Pang, S.; Gao, H., The Stability of Self-Organized 1-Nonanethiol-Capped Gold Nanoparticle Monolayer. *J. Phys. D: Appl. Phys.* **2001**, *34*, 2255-2259.
18. Shimizu, T.; Teranishi, T.; Hasegawa, S.; Miyake, M., Size Evolution of Alkanethiol-Protected Gold Nanoparticles by Heat Treatment in the Solid State. *J. Phys. Chem. B* **2003**, *107*, 2719-2724.
19. Kim, B.; Tripp, S. L.; Wei, A., Self-Organization of Large Gold Nanoparticle Arrays. *J. Am. Chem. Soc.* **2001**, *123* (32), 7955-7956.

20. Li, M.; Schnablegger, H.; Mann, S., Coupled Synthesis and Self-Assembly of Nanoparticles to Give Structures with Controlled Organization. *Nature* **1999**, *402* (6760), 393-395.
21. Holzer, W.; Penzkofer, A.; Hörhold, H. H., Travelling-Wave Lasing of TPD Solutions and Neat Films. *Synth. Met.* **2000**, *113* (3), 281-287.
22. Debenham, M.; Dew, G. D., The refractive index of toluene in the visible spectral region. *J. Phys. E: Sci. Instr.* **1981**, *14* (5), 544-545.
23. Porter, M. D.; Bright, T. B.; Allara, D. L.; Chidsey, C. E. D., Spontaneously Organized Molecular Assemblies. 4. Structural Characterization of n-Alkyl Thiol Monolayers on Gold by Optical Ellipsometry, Infrared Spectroscopy, and Electrochemistry. *J. Am. Chem. Soc.* **1987**, *109* (12), 3559-3568.
24. Nuzzo, R. G.; Fusco, F. A.; Allara, D. L., Spontaneously Organized Molecular Assemblies. 3. Preparation and Properties of Solution Adsorbed Monolayers of Organic Disulfides on Gold Surfaces. *J. Am. Chem. Soc.* **1987**, *109* (8), 2358-2368.
25. Kim, P.; Jones, S. C.; Hotchkiss, P. J.; Haddock, J. N.; Kippelen, B.; Marder, S. R.; Perry, J. W., Phosphonic Acid-Modified Barium Titanate Polymer Nanocomposites with High Permittivity and Dielectric Strength. *Adv. Mater.* **2007**, *19* (7), 1001-1005.
26. Hiramatsu, H.; Osterloh, F. E., A Simple Large-Scale Synthesis of Nearly Monodisperse Gold and Silver Nanoparticles with Adjustable Sizes and with Exchangeable Surfactants. *Chem. Mater.* **2004**, *16* (13), 2509-2511.
27. Badia, A.; Cuccia, L.; Demers, L.; Morin, F.; Lennox, R. B., Structure and Dynamics in Alkanethiolate Monolayers Self-Assembled on Gold Nanoparticles: A DSC, FT-IR, and Deuterium NMR Study. *J. Am. Chem. Soc.* **1997**, *119* (11), 2682-2692.
28. Bain, C. D.; Whitesides, G. M., Modeling Organic Surfaces with Self-Assembled Monolayers. *Angew. Chem., Int. Ed. Engl.* **1989**, *28* (4), 506-512.
29. Dubois, L. H.; Nuzzo, R. G., Synthesis, Structure, and Properties of Model Organic Surfaces. *Annu. Rev. Phys. Chem.* **1992**, *43* (1), 437-463.

30. Snyder, R. G.; Maroncelli, M.; Strauss, H. L.; Hallmark, V. M., Temperature and Phase Behavior of Infrared Intensities: the Poly(methylene) Chain. *J. Phys. Chem.* **1986**, *90* (22), 5623-5630.
31. Nuzzo, R. G.; Dubois, L. H.; Allara, D. L., Fundamental Studies of Microscopic Wetting on Organic Surfaces. 1. Formation and Structural Characterization of a Self-Consistent Series of Polyfunctional Organic Monolayers. *J. Am. Chem. Soc.* **1990**, *112* (2), 558-569.
32. Kira, A.; Kim, H.; Yasuda, K., Contribution of Nanoscale Curvature to Number Density of Immobilized DNA on Gold Nanoparticles. *Langmuir* **2009**, *25* (3), 1285-1288.
33. Zharnikov, M.; Grunze, M., Spectroscopic Characterization of Thiol-Derived Self-Assembling Monolayers. *J. Phys.: Condens. Matter* **2001**, *13* (49), 11333-11365.
34. Lica, G. C.; Zelakiewicz, B. S.; Tong, Y. Y., Electrochemical and NMR characterization of octanethiol-protected Au nanoparticles. *J. Electroanal. Chem.* **2003**, *554-555*, 127-132.
35. Hostetler, M. J.; Wingate, J. E.; Zhong, C.-J.; Harris, J. E.; Vachet, R. W.; Clark, M. R.; Londono, J. D.; Green, S. J.; Stokes, J. J.; Wignall, G. D.; Glish, G. L.; Porter, M. D.; Evans, N. D.; Murray, R. W., Alkanethiolate Gold Cluster Molecules with Core Diameters from 1.5 to 5.2 nm: Core and Monolayer Properties as a Function of Core Size. *Langmuir* **1998**, *14* (1), 17-30.
36. Badia, A.; Demers, L.; Dickinson, L.; Morin, F. G.; Lennox, R. B.; Reven, L., Gold-Sulfur Interactions in Alkylthiol Self-Assembled Monolayers Formed on Gold Nanoparticles Studied by Solid-State NMR. *J. Am. Chem. Soc.* **1997**, *119* (45), 11104-11105.
37. Macomber, R. S., *A complete introduction to modern NMR spectroscopy*. John Wiley and Sons, Inc.: New York, 1997.
38. Barriet, D.; Lee, T. R., Fluorinated Self-Assembled Monolayers: Composition, Structure and Interfacial Properties. *Curr. Opin. Colloid Interface Sci.* **2003**, *8* (3), 236-242.
39. Malicki, M. Electronic and Optical Properties of Hybrid Gold - Organic Dye Systems. Ph.D. Thesis, Georgia Institute of Technology, Atlanta, 2009.

40. Viger, M.; Live, L.; Therrien, O.; Boudreau, D., Reduction of Self-Quenching in Fluorescent Silica-Coated Silver Nanoparticles. *Plasmonics* **2008**, 3 (1), 33-40.
41. Low, P. J.; Paterson, M. A. J.; Puschmann, H.; Goeta, A. E.; Howard, J. A. K.; Lambert, C.; Cherryman, J. C.; Tackley, D. R.; Leeming, S.; Brown, B., Crystal, Molecular and Electronic Structure of N,N'-Diphenyl-N,N'-bis(2,4-dimethylphenyl)-(1,1'-biphenyl)-4,4'-diamine and the corresponding Radical Cation. *Chem. - Eur. J.* **2004**, 10 (1), 83-91.
42. Lide, D. R., *CRC Handbook of Chemistry and Physics*. 86th Edition ed.; American Chemical Society: Boca Raton, FL, 2006; Vol. 128, p 2544.
43. Bielanski, A., *Podstawy Chemii Nieorganicznej*. Wydawnictwo Naukowe PWN: Warszawa, 1987.
44. Link, S.; El-Sayed, M. A., Shape and Size Dependence of Radiative, Non-Radiative and Photothermal Properties of Gold Nanocrystals. *Int. Rev. Phys. Chem.* **2000**, 19, 409-453.
45. Heath, J. R.; Knobler, C. M.; Leff, D. V., Pressure/Temperature Phase Diagrams and Superlattices of Organically Functionalized Metal Nanocrystal Monolayers: The Influence of Particle Size, Size Distribution, and Surface Passivant. *J. Phys. Chem. B* **1997**, 101 (2), 189-197.
46. Pang, L. S. K.; Saxby, J. D.; Chatfield, S. P., Thermogravimetric analysis of carbon nanotubes and nanoparticles. *J. Phys. Chem.* **1993**, 97 (27), 6941-6942.
47. Wu, S.-H.; Chen, D.-H., Synthesis of high-concentration Cu nanoparticles in aqueous CTAB solutions. *J. Colloid Interface Sci.* **2004**, 273 (1), 165-169.

CHAPTER 4

PHOTOPHYSICS OF TPD CHROMOPHORES IN SOLUTION AND IN SOLID FILMS

4.1. Introduction

Optical and electronic properties of N,N'-diphenyl-bis(3-methylphenyl)-biphenyl-4,4'-diamine (TPD) are of great interest in the field of organic electronics due to the molecule's exceptional hole transporting ability in bulk.¹⁻³ In particular, TPD thin films are widely used as hole transport layers in organic light emitting diodes (OLEDs)^{1, 3-5}. TPD has also been demonstrated to possess interesting nonlinear optical characteristics^{6, 7} and to be an active laser material, both in solution as well as in the solid state.^{6, 8} It has also been used as a host for phosphorescent molecules for OLED applications⁹; in this case Förster energy transfer¹⁰ as well as Dexter energy transfer¹¹ from photoexcited TPD to the phosphors, e.g., Ir(ppy)₃ or PtOEP, were observed.^{9, 12} Due to the particular interest in the charge separation and mobility in systems incorporating TPD for their potential use in organic electronics applications, spectroscopic studies of TPD in the solid state are usually performed under electronic bias.¹³ In these studies, the authors demonstrated that fluorescence efficiencies of TPD in neat films were lower than fluorescence efficiencies of TPD in polymer matrices. It was suggested that this effect was caused by an electron transfer process from a photoinduced TPD molecule to a neighboring ground-state TPD

molecule followed by nonradiative charge recombination. This suggested electron transfer should be greatly dependent on distance between the chromophores and should be observed only at high chromophore concentration e.g. in neat films of TPD.

The main focus of this dissertation is to understand the photophysics of TPD ligands adsorbed on silver nanoparticles (AgNP). In order to be able to investigate these systems, the photophysical behavior of the organic chromophores themselves must be understood. TPD chromophores form an organic shell around the metallic core of each nanoparticle and, depending on their density of packing, they could exhibit either solution-like behavior (when they are loosely packed) or solid-like behavior (when the ligands are densely packed). Thus both solution- and solid-like characteristics of TPD-based chromophores may be relevant for the behavior of the coupled nanoparticle-TPD systems. An indication of the solid-like characteristics of the organic ligands attached to AgNPs was presented in Chapter 3 where, while ^1H NMR T_1 relaxation times were almost unchanged from those of free ligands, the values of T_2 were strongly affected by the close proximity of neighboring TPD molecules, in effect exhibiting solid-like behavior.

4.2. *Photophysics of TPD-based Compounds in Solution and in Solid Films*

The lowest optically allowed electronic transition of TPDC12SH is characterized by an absorption band with a maximum at 355 nm (Figure 4.1). The molar extinction coefficients of the TPD ligands TPDC12SH has been measured for solutions in toluene, DCM,^{xxvi} and in a toluene / DMF (5:1) mixture. The measured molar extinction

^{xxvi} Extinction coefficient in DCM is used in Chapter 3 for the calculations of TPD concentration.

coefficient are very similar in all tested solvents and the value of $\epsilon(355 \text{ nm}) = 4.04 \times 10^4 \text{ M}^{-1} \text{ cm}^{-1}$ ($\pm 2\%$) was determined for the toluene / DMF (5:1) solution. The mixture of toluene and DMF was chosen due to excellent stability of AgNP in that solution.^{xxvii} The fluorescence spectrum of TPDC12SH in toluene / DMF (5:1) solution exhibits a maximum at ca. 400 nm and a shoulder at ca. 420 nm. The fluorescence quantum yield was measured using *p*-bis-*o*-methyl-styrylbenzene (BMSB) in cyclohexane as a standard and was determined to be 0.78 ± 0.04 in toluene and 0.82 ± 0.06 in toluene / DMF (5:1) solution.

Fluorescence lifetimes of deoxygenated TPDC12SH solutions were measured using the time correlated single photon counting technique (TCSPC). The samples were excited at 365 nm and the fluorescence decays were collected at 420 nm. These are shown in Figure 4.2. Each fluorescence decay kinetic was fitted with a single-exponential decay function. The time components obtained from the fitting routine are: $1.06 \text{ ns} \pm 0.01 \text{ ns}$ for TPDC12SH in toluene and $1.60 \text{ ns} \pm 0.01 \text{ ns}$ for TPDC12SH in toluene / DMF (5:1). The lifetime of TPDC12SH solution in toluene is similar to the lifetime measured for TPDC12 model compound in toluene which was reported to be 1.07 ns .¹⁴

^{xxvii} The cause of instability of the nanoparticles is not known but it results in staining of the cuvette walls and a decrease in the absorbance originating from the metallic cores of AgNP. Addition of DMF to toluene results in a stable absorption spectrum over time and no staining of the cuvette. Details are described in Chapter 3.

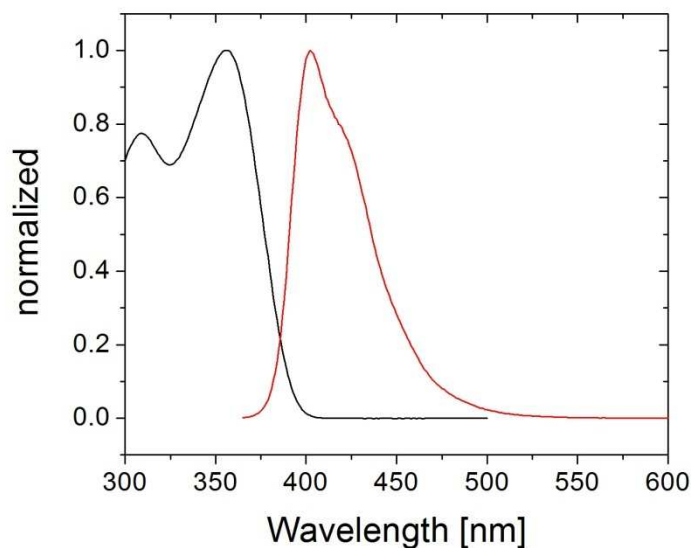


Figure 4.1. UV-vis absorption (black line) and fluorescence (red line) spectra of TPDC12SH in toluene / DMF (5:1). The spectra were normalized at the maximum peak intensity. The extinction coefficient at the maximum of absorption is $\varepsilon(\lambda_{\text{max}}) = 4.04 \times 10^4 \text{ M}^{-1} \text{ cm}^{-1} (\pm 2\%)$.

Radiative (k_r) and nonradiative (k_{nr}) decay rates can be calculated according to:

$$QY = \frac{k_r}{k_r + k_{nr}} \quad (4.1)$$

$$k_r + k_{nr} = 1/\tau \quad (4.2)$$

where QY is fluorescence quantum yield and τ is the measured lifetime. The calculated rates for the toluene solution are: $k_r = 7.6 \times 10^8 \text{ s}^{-1}$ and $k_{nr} = 1.8 \times 10^8 \text{ s}^{-1}$. The corresponding values for the toluene / DMF (5:1) solution were found to be: $k_r = 5.1 \times 10^8 \text{ s}^{-1}$ and $k_{nr} = 1.1 \times 10^8 \text{ s}^{-1}$.

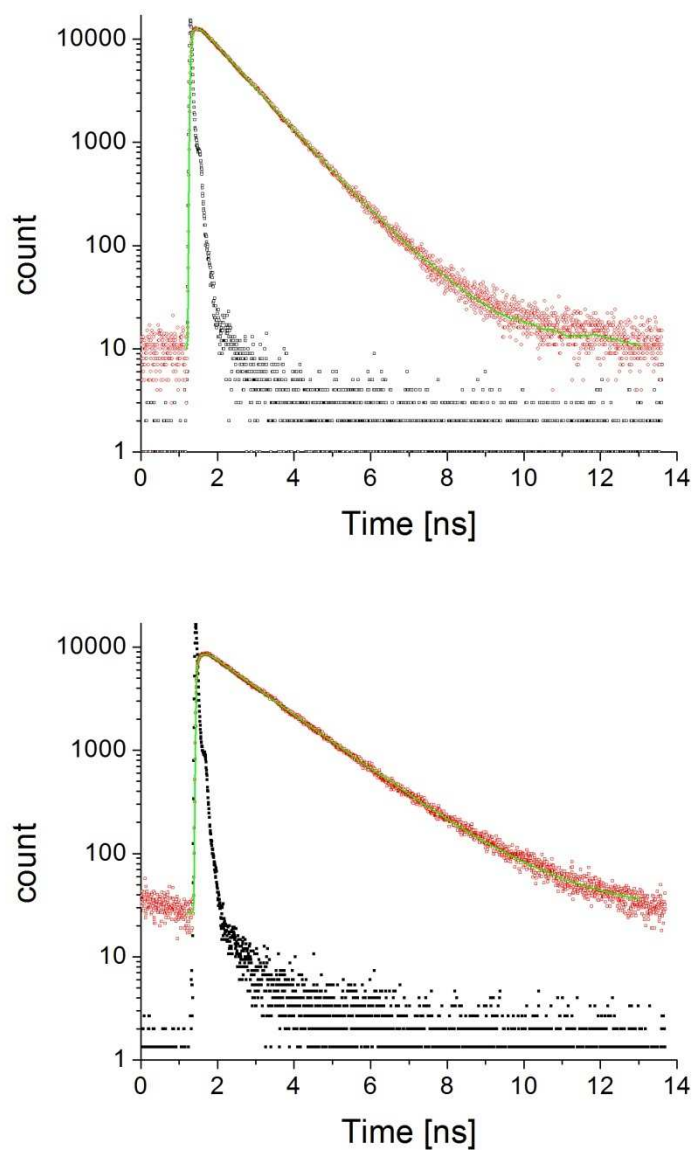


Figure 4.2. Fluorescence decays of deoxygenated solutions of TPDC12SH in toluene (top) and in 5:1 toluene / DMF (5:1) (bottom) measured with TCSPC technique. The samples were excited at 365 nm and the fluorescence signal was collected at 420 nm. Instrument response function (IRF, FWHM ca. 80 ps) is represented by black dots and the collected signals are represented by red circles. The fluorescence decay kinetics were fitted with single exponential decay functions, which are shown as the green lines. The lifetimes were found to be 1.06 ns for the sample in toluene and 1.60 ns for the sample in 5:1 toluene:DMF mixture.

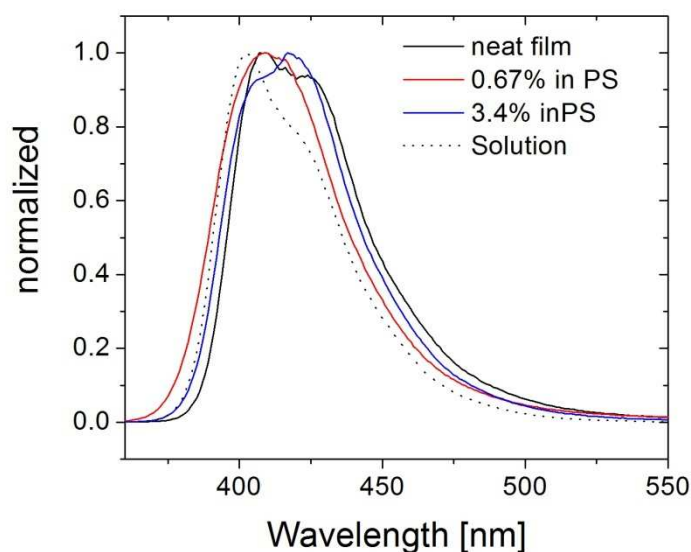


Figure 4.3. Fluorescence spectra of TPDC12 model compound in a neat film (black line), 0.67% wt. (red line) and 3.4% wt. (blue line) of TPDC12 model compound in polystyrene film and a solution of TPDC3SH in 5:1 mixture of toluene and DMF (doted black line). The spectra were normalized at the maximum peak intensity. Fluorescence spectra of the films were collected in front face geometry.

The fluorescence spectra of the TPDC12 model compound in solid films are shown in Figure 4.3. The spectrum of the neat film exhibits two vibronic bands at 410 nm and 425 nm. These two features are not clearly seen for the spectrum of the TPDC12 in polystyrene film at low concentration (0.67%) but they appear in the fluorescence spectrum of the TPDC12 in polystyrene film at 3.4% concentration. Overall, the fluorescence spectra progressively red-shift with higher concentration of TPDC12. Furthermore, the fluorescence spectra in solid films are in general broader than the spectrum of the TPD moiety in solution and the vibronic structure is not as well defined.

Fluorescence decay measurements were performed on a neat film of TPDC12. The kinetic was fitted with a triexponential decay function yielding three lifetimes: 0.030 ns, $0.280 \text{ ns} \pm 0.07 \text{ ns}$ and $0.900 \text{ ns} \pm 0.03 \text{ ns}$. The first component carries with it a large error that could be partly attributed to the presence of amplified spontaneous emission, which was reported for neat films of TPD to be at around 420 nm.⁶ With respect to the remaining two decay components, the neat film may experience self-quenching effects that could contribute to a distribution of lifetimes rather than a discrete component.¹⁵ This distribution could be due to inhomogenities in the film, which result in different domain sizes giving rise to quenching mechanisms with varying decay rates.

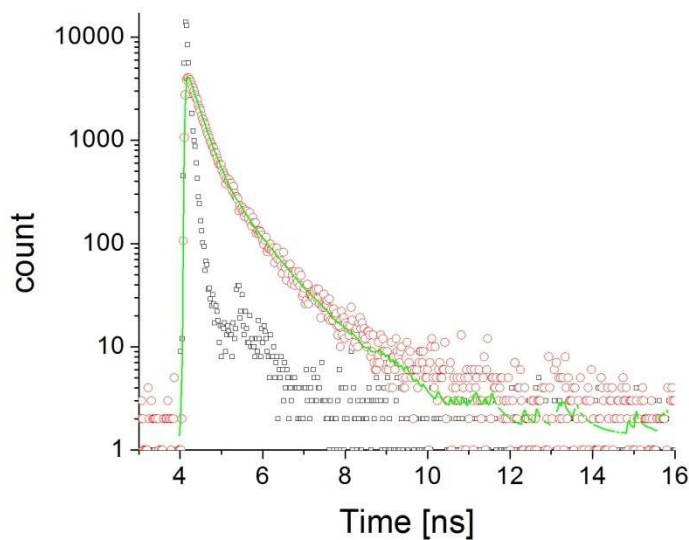


Figure 4.4. Fluorescence decay of neat film of TPDC12 measured with TCSPC technique. The samples were excited with 365 nm and the fluorescence signal was collected at 420 nm. IRF is represented by black circles and the collected fluorescence signal is represented by red circles. The decay was fitted with triexponential decay function represented with the green line.

Nanosecond transient absorption (TA) spectroscopy was employed in order to measure the spectrum of the excited triplet state of TPD in toluene and in DMF. The measurements were performed on TPD and not on the TPDC12 model compound. However, due to the structural similarity of the two molecules and their comparable linear optical properties, their triplet spectra are expected to be similar as well. The data were provided by Mr. Matteo Cozzuol and Mr. William R. D. Boyd III.

Figure 4.5 shows nanosecond TA spectra collected for deoxygenated solutions of TPD. The spectra with maxima at ca. 620 nm were assigned to absorption of the TPD triplet state; the spectra were absent in air-saturated solutions. A decay kinetic obtained for the two different samples was fitted with a monoexponential decay function yielding 10 μ s and 135 μ s for the toluene and DMF solutions, respectively. The spectral profile of absorption of TPDC12 triplet state in the near IR has been reported by Dr. Michal Malicki.¹⁴ The spectrum shows a broad feature with steadily decreasing intensity from the maximum value at 1000 nm down to a fifth of the maximum value at 1600 nm. The NIR decay kinetics were also found to be very similar to those observed in the visible portion of the spectrum. Ultrafast excited-state dynamics of TPD in both solution- and solid-state have been addressed by fs TA spectroscopy and will be discussed later in this chapter.

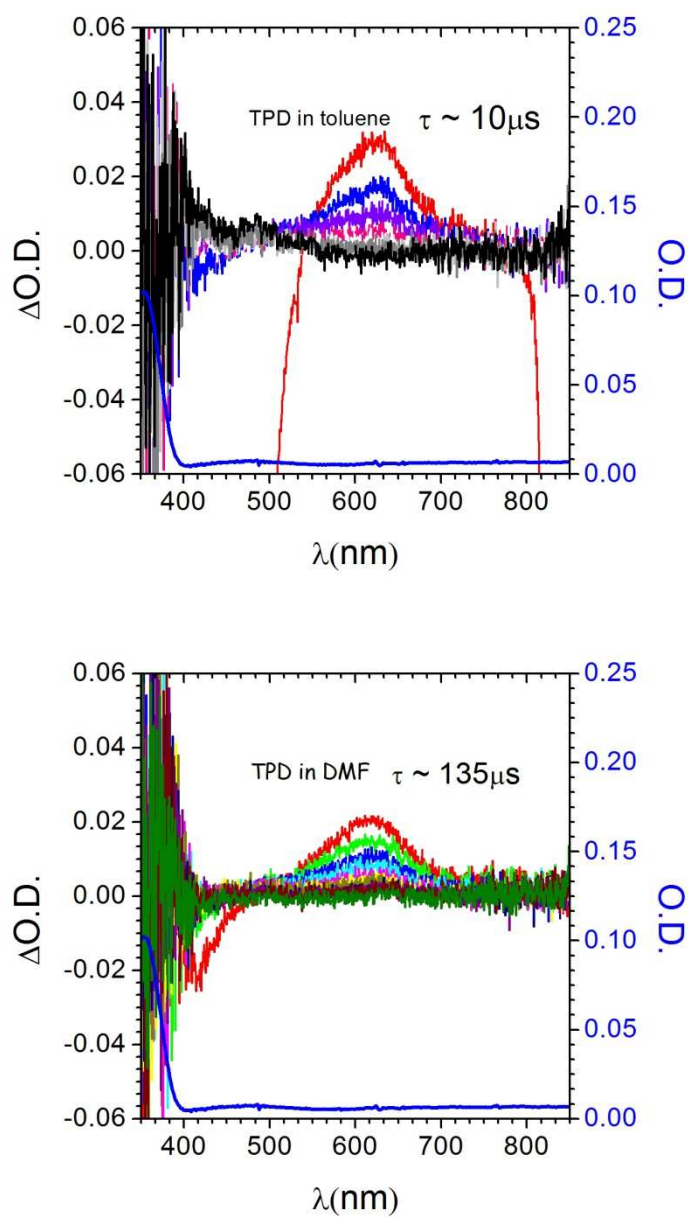


Figure 4.5. Nanosecond TA spectra recorded at several delay times (scale on the left) of TPD solutions a) in toluene and b) in DMF. Concentration of solutions was chosen such that the resulting OD at the excitation wavelength (355 nm) was around 0.1 in 1 cm cuvette. Absorption spectra of the samples are represented by the blue lines (scale on the right). Values provided in the figures are lifetimes obtained by fitting decay traces with a monoexponential decay function. Spectra provided by Mr. M. Cozzuol.

4.3. Characterization of Oxidized TPD and TPDC12 Species in Solution

Photo-generation of radical cations in TPD neat films is well known to occur under applied voltage.¹ There are also reports implying that fluorescence quenching of the TPD in such films, without applied voltage, which can be also due to photoinduced charge separation, leading to excited state deactivation.¹⁵ Such a possibility needs to be considered in the transient absorption studies addressed in the next section of this chapter, thus UV-Vis-NIR absorption studies of chemically generated radical cations of TPDC12 are discussed below.

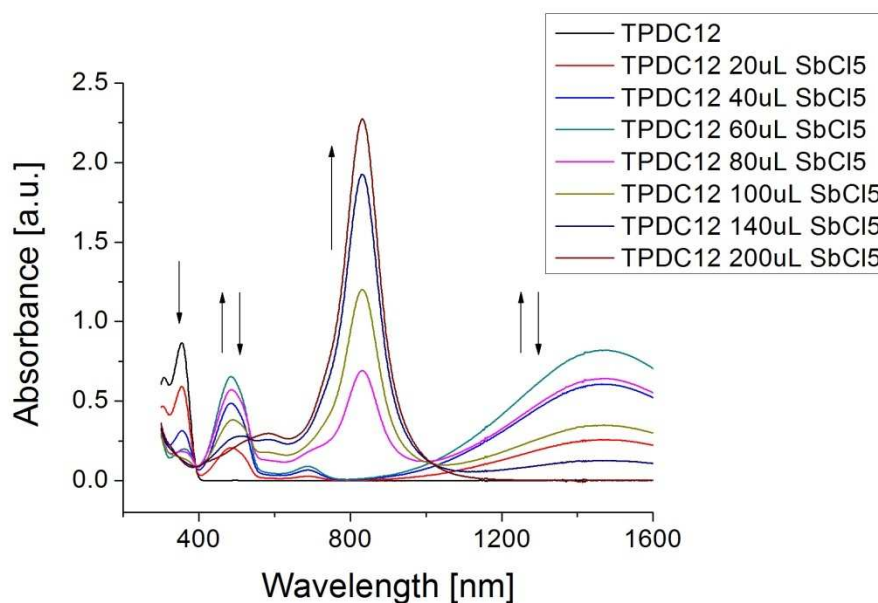


Figure 4.6. UV-Vis-NIR absorption spectra of TPDC12 in DCM recorded before and after successive additions of 0.05 M DCM solution of SbCl_5 . Arrows indicate direction of change of the peak intensities during the addition of the oxidizing agent.

Figure 4.6 shows UV-Vis absorption spectra of TPDC12 in DCM after reaction with different amounts of SbCl_5 . It can be seen that a reaction takes place after the addition of the initial aliquots of the SbCl_5 solution generating a new species with absorption bands at 480 nm, 690 nm and a broad band at 1470 nm. According to a literature report by Low et al. these absorption bands are characteristic of TPDC12 monocation (TPDC12^{*+}).¹⁶ Further addition of SbCl_5 results in a decrease of the intensity of the absorption bands originating from TPDC12^{*+} and a growth of a band around 830 nm. This band is assigned to a TPDC12 dication (TPDC12^{++}).¹⁶ Molar extinction coefficients of TPDC12 mono- and dication were estimated from the titration experiment described above, by referencing them against the known extinction coefficient of the TPDC12 absorption band at 355 nm. The estimated values of molar extinction coefficients of the following bands at the maximum of absorption in $\text{M}^{-1} \text{ cm}^{-1}$ are:

$$\varepsilon_{\text{TPDC12}}(355 \text{ nm}) = 4.0 \times 10^4 \text{ M}^{-1} \text{ cm}^{-1}, \varepsilon_{\text{TPDC12}^{*+}}(480 \text{ nm}) = 3.0 \times 10^4 \text{ M}^{-1} \text{ cm}^{-1}, \varepsilon_{\text{TPDC12}^{*+}}(1470 \text{ nm}) = 3.8 \times 10^4 \text{ M}^{-1} \text{ cm}^{-1}, \varepsilon_{\text{TPDC12}^{++}}(830 \text{ nm}) = 1.1 \times 10^5 \text{ M}^{-1} \text{ cm}^{-1}.$$

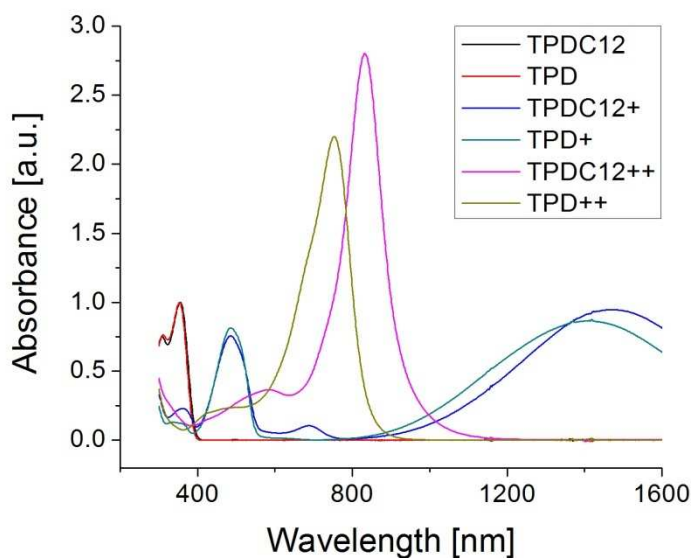


Figure 4.7. UV-Vis-NIR absorption spectra of DCM solutions of TPDC12, TPDC12⁺ and TPDC12⁺⁺ in comparison with spectra of TPD, TPD⁺ and TPD⁺⁺. The spectra of the molecules in their neutral form were normalized at the maximum of absorption; the same normalization factors were applied to the spectra of the corresponding mono- and dications.

Figure 4.7 shows UV-Vis-NIR absorption spectra of TPDC12 and TPD as well as spectra of the corresponding oxidized species in DCM. As expected, the spectra of TPD and TPDC12 are very similar. However, there are some differences in the positions of the bands of the corresponding oxidized forms of the two dyes. The only difference in the molecular structure of TPD and TPDC12 is the presence of the alkoxy group in TPDC12. Apparently the weak π -donor red-shifts the low energy bands in the mono- and dication of the TPD moiety. Moreover, only TPDC12⁺ shows a weak band at around 690 nm, most likely due to symmetry breaking.¹⁷

4.4. *Femtosecond Transient Absorption*

The ultrafast dynamics of TPDC12SH in solution and of TPDC12 in polystyrene films and in a neat film have been studied using fs TA. The concentration of the studied solution of TPDC12SH was about 0.1 M in toluene / DMF (5:1). The polystyrene films were cast onto microscope slide substrates from toluene solutions yielding films with concentrations of TPDC12 of 0.67% and 3.4% by weight. The neat film of TPDC12 was prepared by casting from a toluene solution.

Figure 4.8 shows transient absorption spectra at a few delay times between the pump (excitation at 350 nm) and the broadband probe in the visible and NIR spectral regions measured for TPDC12 and TPDC12SH. The evolution of the spectra of TPDC12SH in toluene / DMF (5:1) solution in the visible region shows clear variation of the spectral profile within the first 30 ps (Figure 4.8). These fast changes in the spectral shape are most likely related to the relaxation of the excited-state geometry in response to the solvated molecules.^{5, 18} The spectrum collected after a delay of ca. 3 ns (limitation of the instrumental setup) is dominated by a band that shows a maximum at ca. 620 nm. This long-lived signal most likely originates from the absorption of the excited triplet state of the TPD moiety as its spectral shape is similar to the excited triplet state of TPD found via ns-pulsed TA presented in Figure 4.5. In the NIR, the spectra decay without major variations in shape, essentially changing from profiles with modest peak amplitudes to broader, featureless spectra.

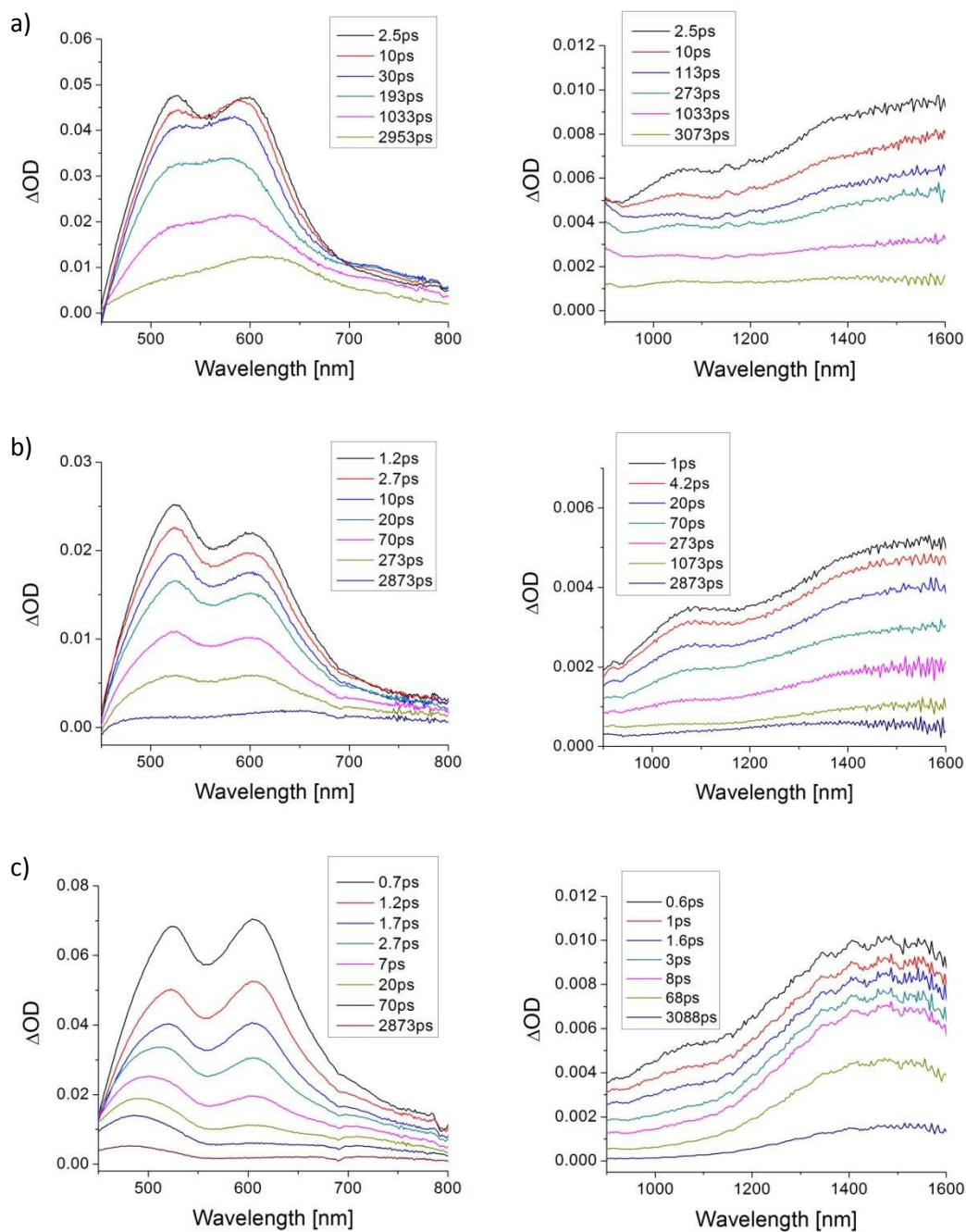


Figure 4.8. Evolution of transient absorption spectra in the visible (left) and the NIR (right) regions measured for: a) ca. 0.1 M TPDC12SH in toluene / DMF (5:1), b) TPDC12 in polystyrene matrix, and c) a neat film of TPDC12 (the NIR data were provided by Dr. Malicki). The samples were excited at 350 nm.

In the visible region, fs TA spectra of TPDC12 in the polystyrene matrix (Figure 4.8b) show minimal changes in shape after the photoexcitation, in contrast to the spectra recorded for the solution of TPDC12SH in toluene / DMF (5:1). This is likely due to restricted geometry relaxation of the photoexcited solvated molecule in the viscous polystyrene matrix.¹⁹ The neat film of TPDC12 behaves quite differently from the other two samples (Figure 4.8c), i.e. the spectra decay substantially faster than in the previously described systems. Furthermore, in the NIR, the transient spectrum shows negligible spectral amplitude at 1050 nm while exhibiting significant amplitude at 1500 nm ca. 70 ps after the excitation pulse. This is in contrast to the solution and low-concentration film NIR transient spectra that show appreciable amplitude in both spectral regions at longer delays (>70 ps). This suggests that after photoexcitation of the neat film the initially excited state of the TPD moiety decays rapidly leading to the formation of a new species which absorbs at 1500 nm. This supposition is at least consistent with the spectral evolution of the visible TA spectra, where the gradual blue shift of the 525 nm band towards 480 nm is accompanied by the faster decay of the band at 600 nm. There are reports in the literature suggesting that charge separation takes place in neat TPD films upon excitation of TPD to its first excited state, even without external bias.¹⁵ However, direct evidence has not been provided previously. The possibility of charge separation in photoexcited TPDC12 neat films is addressed later in this chapter.

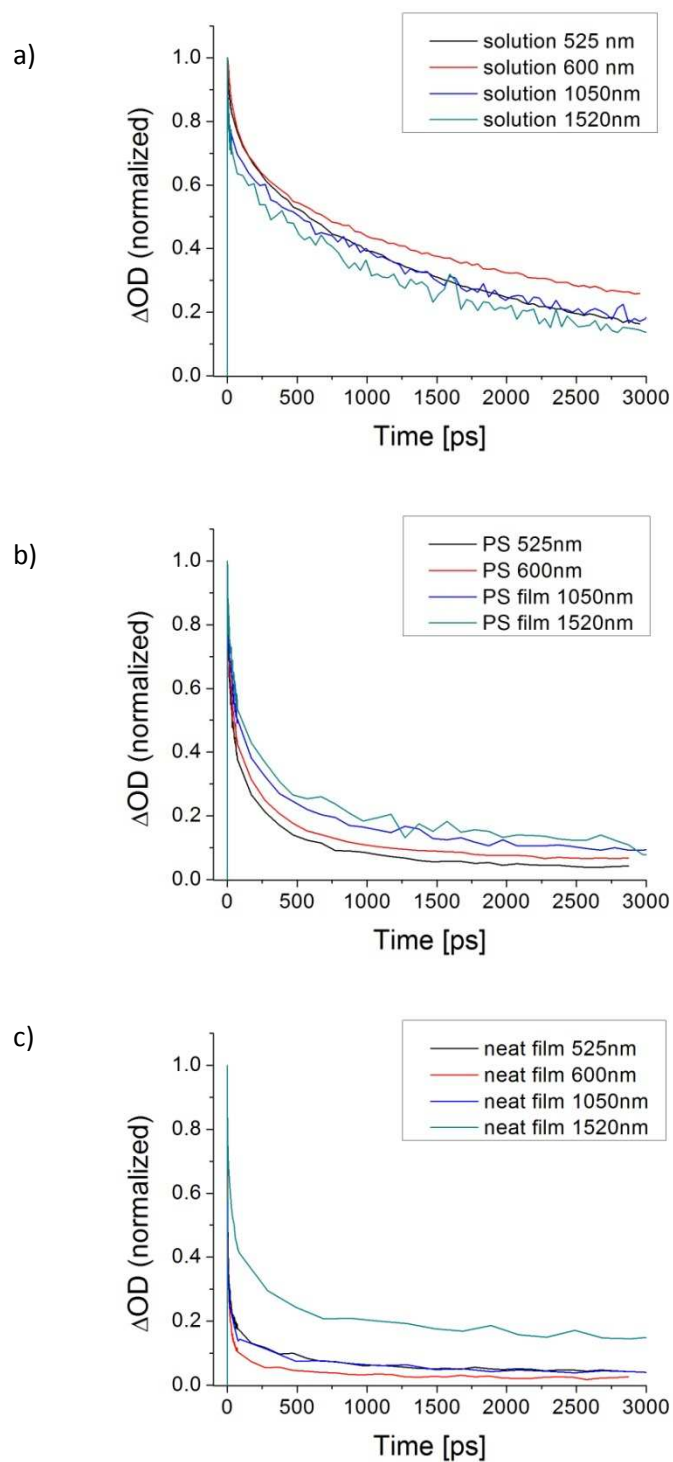


Figure 4.9. Normalized decay traces at 525 nm, 600 nm, 1050 nm and 1500 nm of a) TPDC12SH in toluene / DMF (5:1), b) TPDC12 in polystyrene matrix (3.4%), and c) neat film of TPDC12.

The temporal evolution of the above transient absorption spectra can be perhaps better visualized in the kinetic traces at selected wavelengths, which are shown in Figure 4.9. The decays are very similar at 525 nm, 1050 nm, and 1500 nm for kinetics of the TPDC12SH toluene / DMF (5:1) solution. However, the TA trace at 600 nm, the wavelength at which there is significant contribution from the excited triplet state, shows a slower rate of decay than the rates recorded at the other three wavelengths. The rates of decay of the TA traces measured for TPDC12 in polystyrene matrix (3.4 %) (Figure 4.9b) are faster than for the dynamics described above for the TPD12SH solution but still remain similar across all probe wavelengths. Figure 4.9c shows decay kinetics at a few wavelengths measured for the neat film. In this case the decays are faster than those measured for both TPDC12SH in solution and for TPDC12 in the polystyrene matrix. This is likely a consequence of the formation of the new species mentioned above. There are a few interesting observations involving the decays presented in Figure 9c. First, the trace at 600 nm shows the fastest decay suggesting a small contribution from absorption of the new species at this wavelength, effectively indicating that the trace is dominated by relaxation of the initially excited state. Secondly, the trace at 1500 nm shows a fast decay component as well as a substantial contribution from a much slower decay component. This indicates that the absorption of the new species is the strongest at 1500 nm and the weakest at 600 nm.

4.4.1. Global Fitting Analysis – Liquid Solution

Global fitting analysis of the TA decay traces was performed in order to extract components contributing to the transient absorption spectra and to better understand the dynamics of the studied systems. The decays at multiple wavelengths were fitted with a sum of three exponentials, where t_0 , τ_1 , τ_2 and τ_3 are all global fitting parameters and t is the time variable.

$$\Delta OD = A_0 + A_1 e^{-(t-t_0)/\tau_1} + A_2 e^{-(t-t_0)/\tau_2} + A_3 e^{-(t-t_0)/\tau_3} \quad (4.3)$$

The floating parameters that were not globally assigned were the pre-exponential amplitudes: A_1 , A_2 , A_3 and the offset parameter A_0 . t_0 is a time offset which was fixed at the position of the maximum of the decay curves. A_0 can be interpreted as the amplitude of the exponential lifetime which is infinitely long. Considering the maximum pump-probe delay of the fs TA setup (3 ns), any decay component with a lifetime longer than ca. 10 ns will appear to be infinitely long.

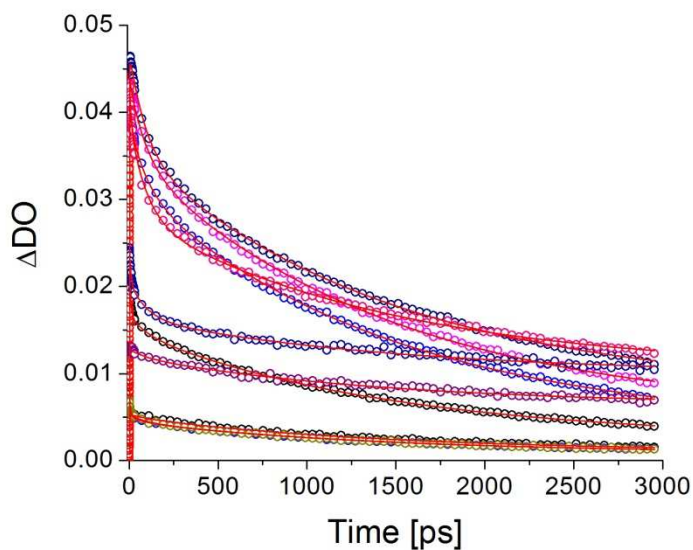


Figure 4.10. Transient absorption decays of TPDC12SH in toluene / DMF (5:1) solution at selected wavelengths plotted together with fitting curves (red lines).

Figure 4.10 shows decay curves obtained from TA measurements of the 2.5×10^{-6} M solution of TPDC12SH in toluene / DMF (5:1) at multiple probe wavelengths. The decays were fitted with the tri-exponential function and the fittings are shown as red, solid lines that overlap the data points, represented by empty circles. The values of pre-exponential amplitudes (A_1 , A_2 , A_3) and the offset parameter A_0 were plotted as a function of probe wavelength in Figure 4.11.

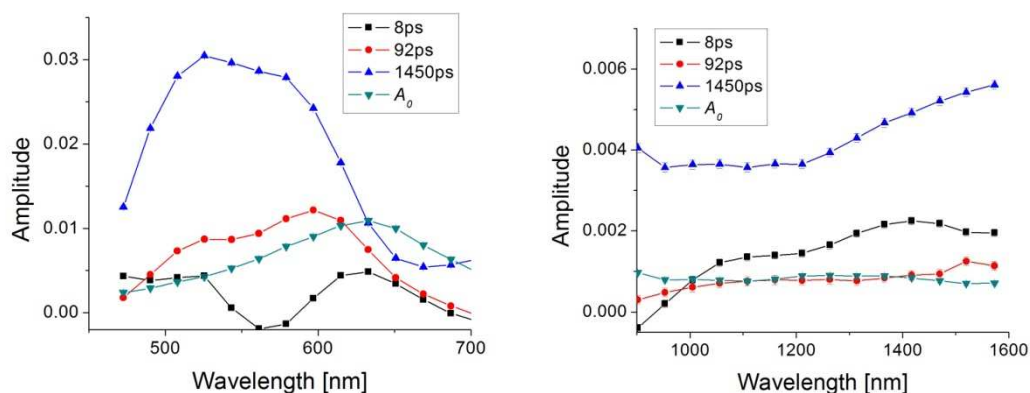


Figure 4.11. Spectral distributions of pre-exponential amplitudes (A_1 , A_2 , A_3 with corresponding lifetimes $\tau_1 = 8.0 \pm 0.2$ ps, $\tau_2 = 92 \pm 2$ ps and $\tau_3 = 1450 \pm 11$ ps) and the offset parameter A_0 obtained from fitting the data acquired for TPDC12SH solution in toluene / DMF (5:1) with a sum of three exponentials.

The results of the global fitting represented by the spectral distribution of the pre-exponential amplitudes show rather complicated dynamics of the molecules after excitation. The first two fast components, $\tau_1 = 8$ ps and $\tau_2 = 92$ ps, are most likely due to a geometry relaxation of the TPD moiety^{7, 19, 20} and a conformational relaxation¹⁸. The component with the lifetime of $\tau_3 = 1450$ ps has the largest pre-exponential amplitudes. The decay rate of this component agrees reasonably well with the excited-state lifetime of the dye measured with TCSPC (ca. 1.60 ns). The agreement between the fluorescence-based excited-state lifetime and the long-lived decay component resulting from fitting the fs TA data suggests that the spectral profiles found for the long lived component, with lifetime τ_3 , represents the absorption from the relaxed geometry of the first excited singlet state of TPDC12SH. The longest component, represented by A_0 values, shows a spectral profile in UV-vis that is consistent with the excited triplet state of TPD (Figure 4.5).

4.4.2. Global Fitting Analysis – TPDC12 in PS

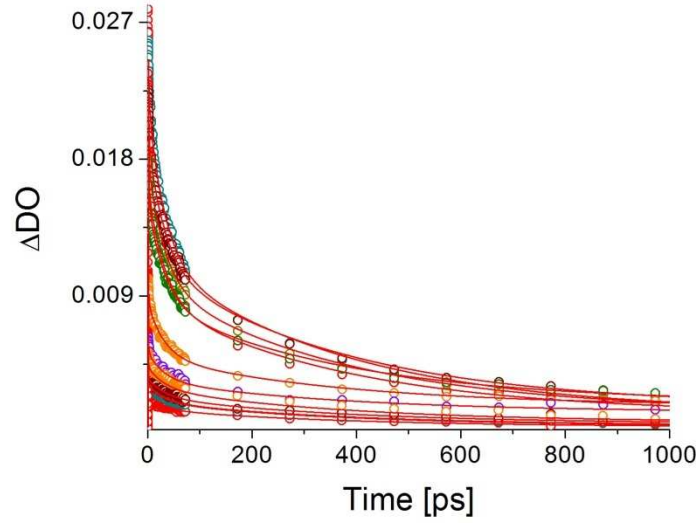


Figure 4.12. Transient decays of TPDC12 in a polystyrene film at different wavelengths. The concentration of TPDC12 in PS was 3.4 % by weight. All fitting curves are presented as red lines.

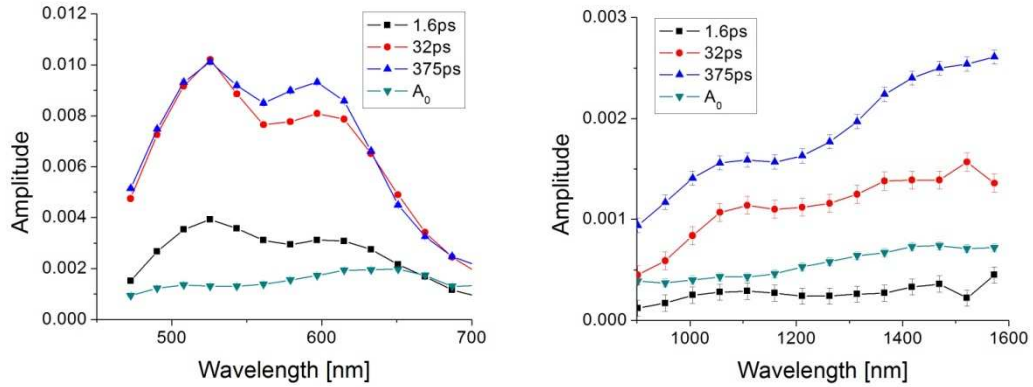


Figure 4.13. Spectral distribution, in the visible (left) and NIR (right), of pre-exponential amplitudes (A_1 , A_2 , A_3 with corresponding lifetimes $\tau_1 = 1.6 \pm 0.04$ ps, $\tau_2 = 32 \pm 0.5$ ps and $\tau_3 = 375 \pm 5$ ps) and the offset parameter, A_0 , obtained from fitting the TA data acquired for TPDC12 in a PS matrix (3.4 % of TPDC12 by weight) with a sum of three exponential functions.

Global fitting analysis of the data acquired for the films was performed in the same way as for the solution data. Figure 4.12 shows transient absorption decay traces at multiple wavelengths measured for 3.4% TPDC12 in polystyrene (PS) matrix. Figure 4.13 shows the values of the pre-exponential amplitudes in two spectral regions: in the visible (left) and in the NIR (right) as well as the lifetimes obtained from the fitting ($\tau_1 = 1.6 \pm 0.04$ ps, $\tau_2 = 32 \pm 0.5$ ps and $\tau_3 = 375 \pm 5$ ps). Contrary to the toluene / DMF (5:1) solution, the three fastest components seen in TPDC12 in the PS matrix show spectral profiles that are rather similar to each other. Moreover, these spectral profiles are similar in shape to the profile of the A_3 component found for the toluene / DMF (5:1) solution, which was associated with absorption from the lowest excited singlet state of the TPD moiety and has a lifetime of 1450 ps. In fact, one might expect the spectral evolution to be simpler for the TPD in a solid matrix compared to liquid solution due to the lack of excited state geometry relaxation while the temporal evolution might be more complex, due to a higher concentration of chromophores.¹⁷ The different distribution of lifetimes with similar spectral pre-exponential amplitudes may be due to interactions between chromophore molecules in the film in which the concentration distribution of TPDC12 might be inhomogeneous. Moreover, the overall faster decay of the TPD transient absorption signal compared to the liquid solution suggests that this intermolecular interaction may lead to some non-radiative deactivation mechanism¹⁵. It should also be noted that the spectral profile of the A_0 component in visible region coincides with the position of the triplet absorption measured for TPDC12SH in both toluene and in DMF solutions (see Figure 4.5).

4.4.3. Global Fitting Analysis – TPDC12 Neat Film

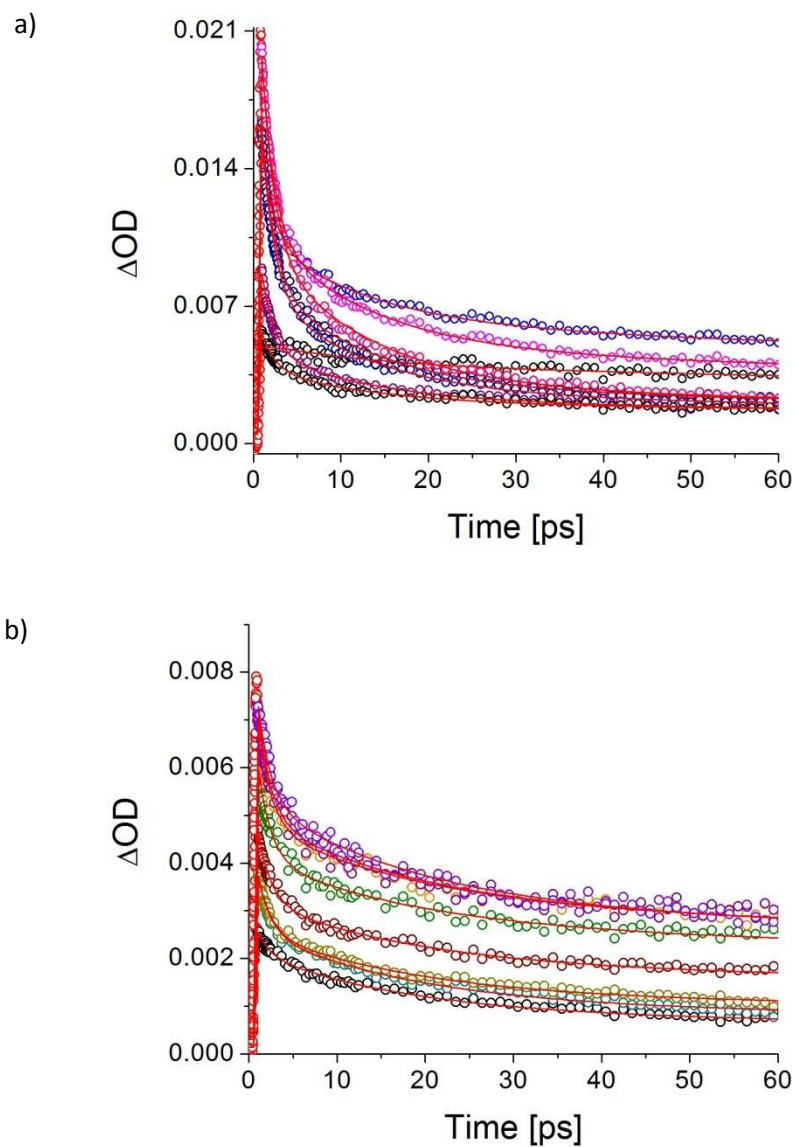


Figure 4.14. Transient decays of the neat film of TPDC12 at multiple wavelengths a) in the visible region, and b) in the NIR region. All fitting curves lines are presented with the red lines.

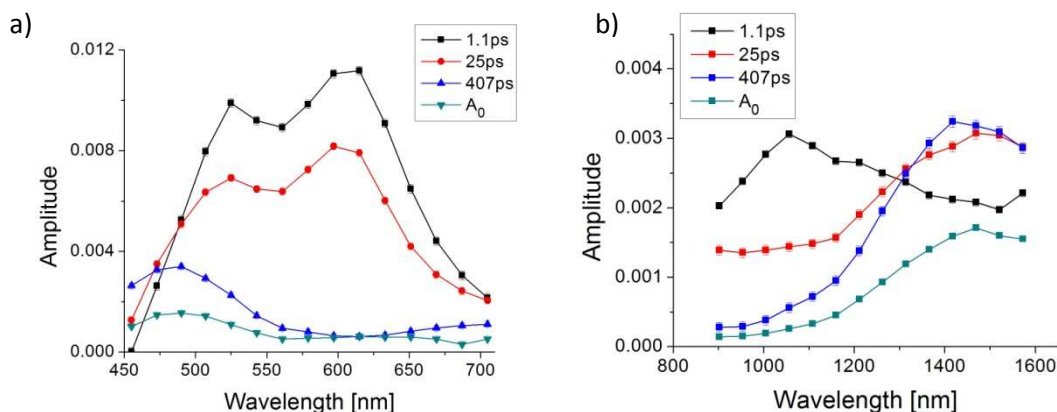


Figure 4.15. Spectral distribution in the visible (left) and in the NIR (right) of pre-exponential amplitudes (A_1 , A_2 , A_3 with corresponding lifetimes: $\tau_1 = 1.1 \pm 0.02$ ps, $\tau_2 = 25 \pm 0.1$ ps and $\tau_3 = 407 \pm 14$ ps) and the offset parameter A_0 obtained from fitting of the TA traces measured for a photoexcited neat film of TPDC12 with a sum of three exponential functions.

Figure 4.14 shows transient absorption decays at multiple wavelengths of a neat film of TPDC12 and Figure 4.15 shows spectral distributions of pre-exponential amplitudes obtained from fitting the TA data. The lifetimes found from the fitting are: $\tau_1 = 1.1 \pm 0.02$ ps, $\tau_2 = 24 \pm 0.1$ ps and $\tau_3 = 407 \pm 14$ ps. The lifetimes found for the TPDC12 neat film are shorter than the lifetimes found from fitting of TA data acquired for TPDC12SH in toluene / DMF (5:1). The spectral profiles of the pre-exponential amplitudes A_1 and A_2 are reminiscent of the first singlet excited state absorption spectrum of the TPD compounds in solution and in the polystyrene film. The amplitudes with slower time components (A_3 , A_0) have significantly different profiles than A_1 and A_2 and also possess markedly different profiles than the A_3 and A_0 components in solution and in the polystyrene matrix.

Spectral distributions of the pre-exponential amplitudes in the NIR are different from the previously discussed samples of TPD-based compounds in solution and in the polystyrene film. The fast component A_1 (black line in Figure 4.15) is clearly different from the initial transient absorption spectra (Figure 4.8c). Furthermore, this component shows a band at 1050 nm but does not show the band observed for the previous samples at 1500 nm. On the other hand, the spectral profile of the components A_2 (red line in Figure 4.15b), which actually looks similar to the spectral profile of the TPDC12SH excited state in solution, shows a distinct band at 1500 nm which becomes even more intense for the amplitudes A_3 (blue line in Figure 4.15b). The offset, A_0 , also exhibits a spectral distribution with a clear band centered about 1500 nm (green line in Figure 4.15b). This overall behavior suggests that a spectrally distinct species is being formed in conjunction with the rapid decay of the initially photoexcited TPDC12.

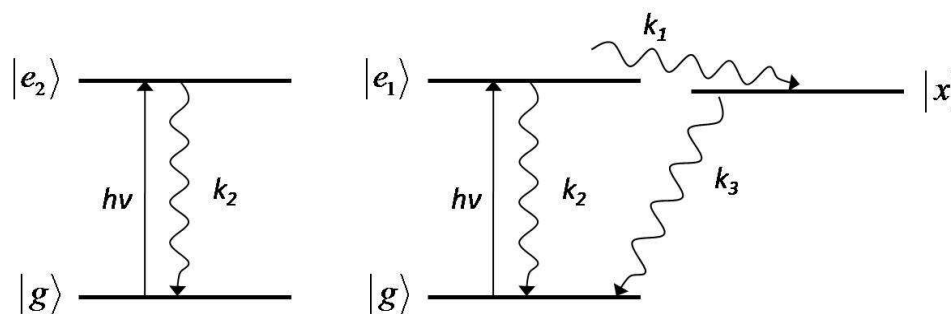


Figure 4.16. A simplified energy level diagram for TPDC12 in neat film showing excitation and assumed relaxation pathways for both cases: a) without and b) with forming the new species.

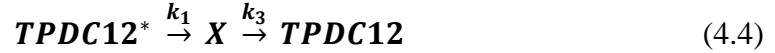
Hypothesizing that one deactivation pathway of the excited TPDC12 molecules leads to the formation of the new species, while the other one represents relaxation back

to the ground state, one could assign the amplitudes A_1 to the excited state of the molecules undergoing the transformation to the new species, $|e_1\rangle$ to $|x\rangle$, and A_2 to the transition from state $|e_2\rangle$ to $|g\rangle$. It is possible that part of the TPDC12 molecules in the neat film can be arranged in a manner, which allows forming e.g. excited state complex, an excimer, leading to the formation of the new species. The other part of the chromophores, on the other hand, may have geometry that does not allow for the new species to form. This scenario could result in the two time components with amplitudes A_1 and A_2 , respectively. The new species is evident in the distinct shape of the spectral amplitudes A_3 or A_0 . Such spectral similarity between these two amplitudes suggests that that they could be due to the same species with two different lifetimes or perhaps showing a dispersion of lifetimes, as it could be dependent on the geometry of the chromophores.^{xxviii} The shape of the spectral profile A_1 can be influenced by the spectral profile of the quickly growing new species, X , if the relaxation rates are dominated by k_1 , i.e. $k_2 \ll k_1$. A simplified kinetic model of just such a process is discussed in more detail below. The shape of the spectral profile of the A_2 , on the other hand, is consistent with the shape of the spectrum of TPD excited state, the TA spectrum shortly after the excitation pulse, as shown in Figure 4.8c.

^{xxviii} The formation of the new species is characteristic to the TPDC12 neat film only, suggesting that perhaps inter chromophore interaction is crucial to its formation. The chromophores in the amorphous film may be oriented randomly or form small crystalline domains, which may affect the lifetime of the species.

4.4.3.1. *Proposed Kinetic Model*

A simplified kinetic model describing the aforementioned process, associated with amplitudes A_1 under assumption that $k_2 \ll k_1$, was described by Dr. Michal Malicki¹⁴ in the following way:



where $TPDC12^*$ is the initially excited state of $TPDC12$ that decays with a rate constant k_1 to form a new species X which then relaxes, with a time constant k_3 , to generate $TPDC12$ in its ground state. The kinetic equations describing these processes are as follows:

$$[TPDC12^*](t) = [TPDC12^*]_0 e^{-k_1 t} \quad (4.5)$$

$$[X](t) = [TPDC12^*]_0 \frac{k_1}{k_3 - k_1} (e^{-k_1 t} - e^{-k_3 t}) \quad (4.6)$$

$[TPDC12^*]_0$ is the initial concentration of $TPDC12$ in the excited state formed after excitation with the laser pulse at 350 nm. The time dependent concentrations of the two species give rise to ΔOD according to Beer's law:

$$\Delta OD_{TPD^*}(t, \lambda) = b \varepsilon_{TPD^*}(\lambda) [TPDC12^*]_0 e^{-k_1 t} \quad (4.7)$$

$$\Delta OD_X(t, \lambda) = b \varepsilon_X(\lambda) [TPDC12^*]_0 \frac{k_1}{k_3 - k_1} (e^{-k_1 t} - e^{-k_3 t}) \quad (4.8)$$

where $\Delta OD_{TPD^*}(t, \lambda)$ and $\Delta OD_X(t, \lambda)$ are time and wavelength dependent transient absorption intensities originating from $TPDC12^*$ and from species X , respectively. ε_{TPD^*} and ε_X are the molar extinction coefficients of $TPDC12^*$ and of species X , respectively, and b is a path length. The measured signal is a sum of these two components:

$$\Delta OD(t, \lambda) = \Delta OD_{TPD^*}(t, \lambda) + \Delta OD_X(t, \lambda) \quad (4.9)$$

This sum can be rewritten by substituting equation (4.7) and equation (4.8), and grouping the terms with the same time constant:

$$\begin{aligned} \Delta OD(t, \lambda) = & b[TPDC12^*]_0 \left(\varepsilon_{TPD^*}(\lambda) + \varepsilon_X(\lambda) \frac{k_1}{k_3 - k_1} \right) e^{-k_1 t} \quad (4.10) \\ & + b\varepsilon_X(\lambda)[TPDC12^*]_0 \frac{k_1}{k_1 - k_3} e^{-k_3 t} \end{aligned}$$

The pre-exponential components in equation (4.10) describe the pre-exponential amplitudes A_1 and A_3 found from fitting the experimental data:

$$A_1(\lambda) = b[TPDC12^*]_0 \left(\varepsilon_{TPD^*}(\lambda) + \varepsilon_X(\lambda) \frac{k_1}{k_3 - k_1} \right) \quad (4.11)$$

$$A_3(\lambda) = b\varepsilon_X(\lambda)[TPDC12^*]_0 \frac{k_1}{k_1 - k_3} \quad (4.12)$$

The spectral distribution of amplitudes A_1 is a linear combination of the wavelength dependent extinction coefficients of $TPDC12^*$ and of species X . The factor determining the relative contribution of the extinction coefficients on the amplitudes A_1 is dependent on the decay rates k_1 and k_3 . The global fitting analysis of the neat film of $TPDC12$ revealed that the relationship between these decay rates corresponding to the A_1 and A_3 is: $k_3 \ll k_1$. The rate of decay of species X is assumed^{xxix} to be related to the amplitude profile of the pre-exponential components A_3 . While equation (4.11) can be simplified to take the following form:

$$A_1(\lambda) = b[TPDC12^*]_0 (\varepsilon_{TPD^*}(\lambda) - \varepsilon_X(\lambda)) \quad (4.13)$$

^{xxix} However, the spectral characteristics of the species X are present in the profiles of A_3 and A_0 . It has been argued before that most likely the multiple discrete time components are due to dispersion of lifetimes in the neat, inhomogeneous film.

revealing that the spectrum of the pre-exponential amplitudes A_I is proportional to the difference between the extinction coefficients of TPDC12* and X.

It is reasonable to assume that at the very early time, shorter than the extracted decay components, i.e. ca. 0.6 ps from the excitation pulse, the transient absorption spectrum correspond to the excited state of TPDC12 and the transient absorption spectra recorded at delays larger than the lifetime of the excited state TPDC12, e.g. 480 ps are due to the new species X. According to the equation (4.13) it should be possible to obtain a spectrum corresponding to the amplitudes A_I by subtracting $\Delta OD(480 \text{ ps})$ from $\Delta OD(0.6 \text{ ps})$.

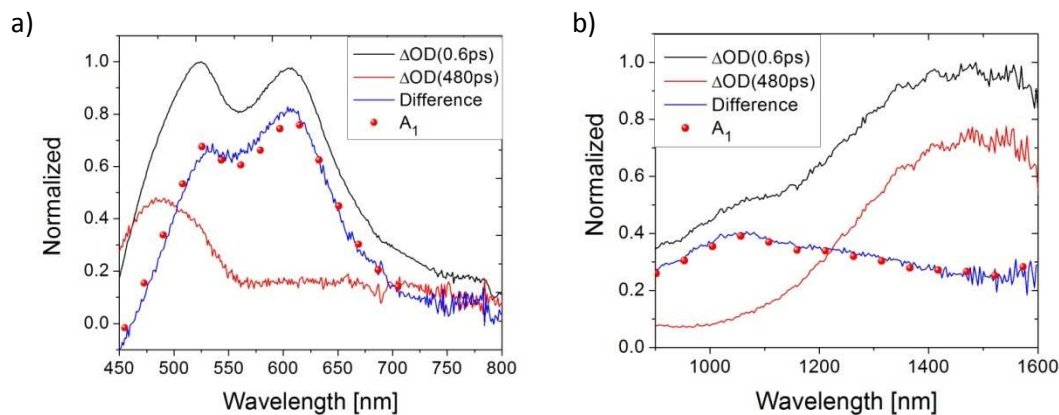


Figure 4.17. Transient absorption spectra in: a) visible and b) NIR of TPDC12 neat film at early time $\Delta OD(0.6 \text{ ps})$ and after 480 ps $\Delta OD(480 \text{ ps})$, plotted together with a spectrum obtained by subtraction: $\Delta OD(0.6 \text{ ps}) - \Delta OD(480 \text{ ps})$ and spectral amplitudes A_I obtained from global fitting. The spectrum $\Delta OD(0.6 \text{ ps})$ was normalized at its maximum, while the spectrum $\Delta OD(480 \text{ ps})$ was scaled in a way to best reconstruct the spectral profile A_I when subtracting the two transient absorption spectra.

Figure 4.17 shows transient absorption spectra in a) the visible and b) the NIR region recorded at 0.6 ps $\Delta OD(0.6 \text{ ps})$ and 480 ps $\Delta OD(480 \text{ ps})$ after the excitation pulse together with the difference between these two spectra and the spectral amplitudes A_I . The intensity of the spectrum $\Delta OD(0.6 \text{ ps})$ was normalized at its maximum and the intensity of the spectrum $\Delta OD(480 \text{ ps})$ scaled in order to best fit the amplitudes A_I upon subtraction, $\Delta OD(0.6 \text{ ps}) - \Delta OD(480 \text{ ps})$. The curve obtain from this procedure reproduces the spectral profiles very well, indicating that the evolution of the transient spectra is consistent with the presented kinetic model and supports the concept of formation of the new species upon photoexcitation of the TPDC12 neat film.

4.4.3.2. Identification of the New Species

The spectral profiles A_0 and A_3 , found for TPDC12 neat film, were assigned to the formation of the new species upon photoexcitation. The spectrum of the electrochemically generated TPDC12 radical cation is shown in Figure 4.18 together with the spectral profile of the amplitudes A_0 . The profiles of the amplitudes and UV-vis-NIR absorption spectrum of TPDC12^{•+} were normalized to the respective peaks at 480 nm and at 1470 nm. The discrepancy associated with the peak at around 650 nm in the A_0 profile is most likely due to the long-lived triplet absorption. Overall, the similarity of the two spectral shapes is quite remarkable, suggesting a formation of TPDC12 radical cation or TPDC12 cation-like species in the photoexcited neat film of TPDC12.

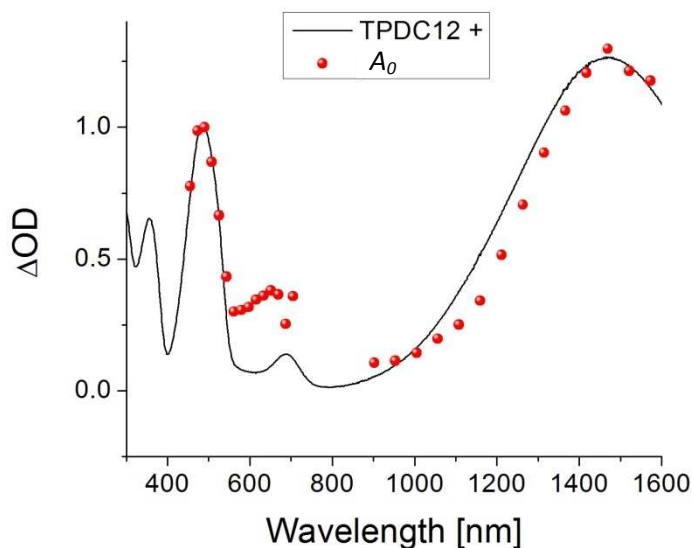


Figure 4.18. UV-Vis-NIR absorption spectrum of TPDC12^{•+} in DCM solution – black line, and amplitudes of the long living component A_0 obtained from global fitting of transient absorption kinetics of neat film of TPDC12 – red spheres. The spectra were normalized at 480 nm.

The results above support the formation of TPDC12 cation-like species upon photoexcitation of the neat TPDC12 film. Other samples that were studied, i.e. TPDC12SH in toluene / DMF (5:1) solution and TPDC12 in the PS matrix, do not exhibit such behavior, suggesting that the process of formation of the cation-like species takes place only at high concentration of TPD moieties. This further suggests that the most likely mechanism leading to cation formation involves intermolecular charge transfer between two TPD molecules. This is also consistent with the fluorescence quenching in a neat film of TPD reported by Tsuboi and Penzkofer.¹⁵

4.5. *Anisotropy of the TPDC12 in Solid Films*

The temporal evolution of anisotropy during excited state absorption measurements can be used to obtain very useful information about orientational changes of the transition dipole moments of the investigated species by rotational movement, or transfer of energy by either Forster or Dexter mechanisms between molecules.^{18, 19} When little interaction between neighboring molecules can be assumed, the decay of anisotropy of chromophores in solution is usually dependent on the local molecular environment. The rate of decay is dependent on the solvent viscosity¹⁸ and it becomes extremely slow in solid-state environments. Thus, in such environments, solid films, the mechanism of anisotropy decay via molecular reorientation can be virtually eliminated, leaving interaction between chromophores as the dominant decay mechanism.

The anisotropy measurements were done for TPDC12 in PS films at doping ratios of a) 3.4 wt. % and b) 0.67 wt. %. The anisotropy (r) of the transient absorption was calculated using the following formula:

$$r = \frac{\Delta OD_{\parallel} - \Delta OD_{\perp}}{\Delta OD_{\parallel} + 2\Delta OD_{\perp}} \quad (4.14)$$

where: ΔOD_{\parallel} and ΔOD_{\perp} are collocated transient absorption after excitation with parallel and perpendicularly polarized (with respect to the probe polarization) femtosecond laser pulses. Figure 4.19 shows the anisotropy spectra and decay kinetics at selected wavelengths for the doped films. Decay of the anisotropy kinetics of the higher concentration film is faster than for the lower TPDC12 concentration film. Moreover, the decays are not dependent on wavelength.

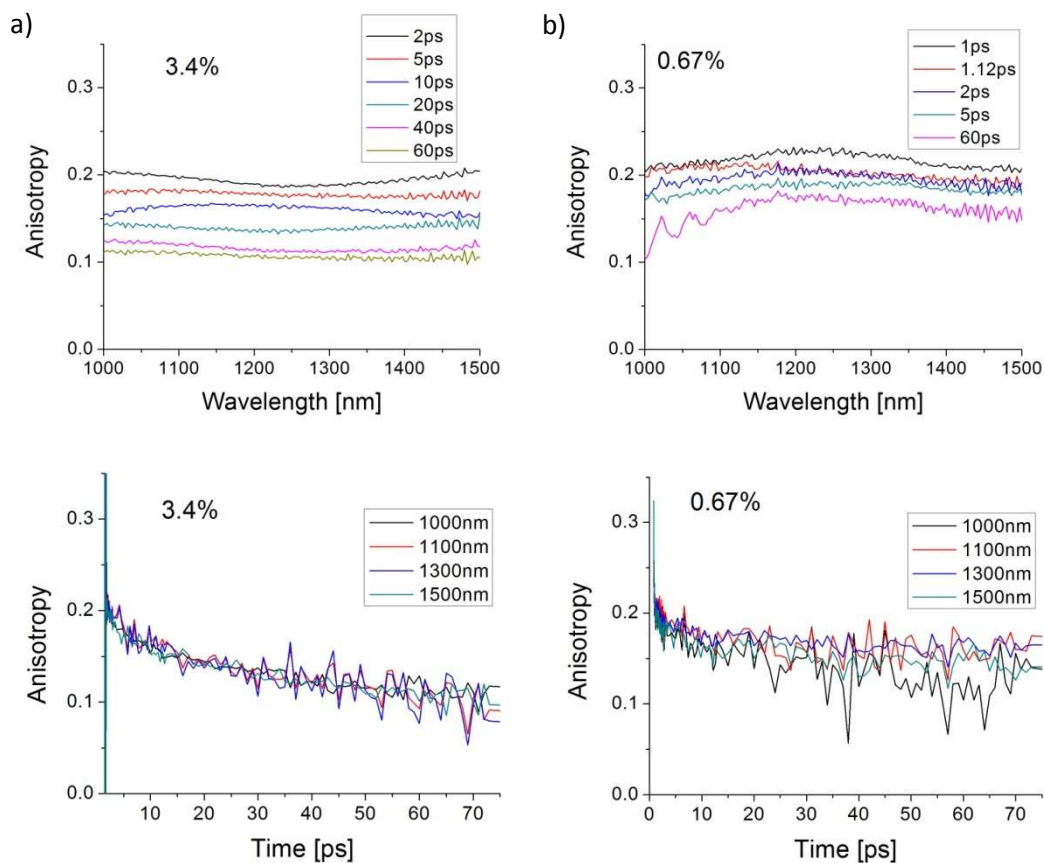


Figure 4.19. Anisotropy spectra at selected decay times (top) and anisotropy decay kinetics at selected wavelengths (bottom) of TPDC12 in polystyrene films doping ratios of a) 3.4% by weight and b) 0.67% by weight.

There seems to be some dependence of the concentration of the chromophores on the depolarization rate. Such concentration dependence is consistent with the concept of some sort of energy exchange between neighboring TPDC12 molecules, since molecules are immobilized in a solid film and molecules at higher concentration are either closer to each other or form larger domains, allowing for more efficient energy migration.

4.6. *Conclusions*

Excited state dynamics of TPD chromophores in solution, as well as TPDC12 in polystyrene and as neat films, were investigated by TCSPC and transient absorption spectroscopy. The fluorescence decay of the TPD chromophore in toluene and in 5:1 mixture of toluene and DMF are significantly slower than the fluorescence decay of the TPDC12 neat film, which is consistent with literature reports. Moreover, a global fitting analysis of the femtosecond transient absorption data shows different excited state decay dynamics between the solution of TPDC12SH, TPDC12 in PS, and the TPDC12 neat film. The spectral components assigned to the first singlet excited state absorption of the chromophore in solution have the lifetime of 1450 ps, which is consistent with the fluorescence decay observed by TCSPC. The corresponding lifetimes of TPDC12 in PS and in neat film form are significantly shorter. Global fitting analysis also reveals that the excited state absorption of the neat film of TPDC12 is accompanied by absorption of a cation-like species of TPD with significantly longer lifetime than the excited state. The spectral profiles of the extracted amplitudes are consistent with part of the excited TPDC12 decaying directly to the ground state, while the other part of the excited chromophores deactivating via an intermediate step leading to the formation of the cation-like species. The formation of the cation-like species is consistent with the proposed simplified kinetic model of a two step process. The cation-like TPD is not observed in the other samples, with lower concentration of the chromophores. This observation indicates that intermolecular interaction between the chromophores is crucial to produce the new species upon photoexcitation. The intermolecular interactions are also observed in concentration dependent anisotropy measurements of the transient absorption

of the TPDC12 in PS, where the higher concentration of chromophores results in faster anisotropy decay, which is consistent with some sort of energy migration between the adjacent chromophores.

4.7. References

1. Kalinowski, J.; Szybowska, K., Photoconduction in the archetype organic hole transporting material TPD. *Org. Electr.* **2008**, 9 (6), 1032-1039.
2. Kalinowski, J.; Stampor, W.; Cocchi, M.; Virgili, D.; Fattori, V.; Di Marco, P., Triplet energy exchange between fluorescent and phosphorescent organic molecules in a solid state matrix. *Chem. Phys.* **2004**, 297 (1-3), 39-48.
3. Coropceanu, V.; Malagoli, M.; Andre, J. M.; Bredas, J. L., Charge-Transfer Transitions in Triarylamine Mixed-Valence Systems: A Joint Density Functional Theory and Vibronic Coupling Study. *J. Am. Chem. Soc.* **2002**, 124 (35), 10519-10530.
4. Gong, X.; Ostrowski, J. C.; Moses, D.; Bazan, G. C.; Heeger, A. J., Electrophosphorescence from a Polymer Guest-Host System with an Iridium Complex as Guest: Förster Energy Transfer and Charge Trapping. *Adv. Funct. Mater.* **2003**, 13 (6), 439-444.
5. Cornil, J.; Gruhn, N. E.; dos Santos, D. A.; Malagoli, M.; Lee, P. A.; Barlow, S.; Thayumanavan, S.; Marder, S. R.; Armstrong, N. R.; Bredas, J. L., Joint Experimental and Theoretical Characterization of the Electronic Structure of 4,4'-Bis(N-m-tolyl-N-phenylamino)biphenyl (TPD) and Substituted Derivatives. *J. Phys. Chem. A* **2001**, 105 (21), 5206-5211.
6. Holzer, W.; Penzkofer, A.; Hörhold, H. H., Travelling-Wave Lasing of TPD Solutions and Neat Films. *Synth. Met.* **2000**, 113 (3), 281-287.
7. Paci, B.; Andraud, C.; Anemian, R.; Nunzi, J.-M., One- and two-photon picosecond excitation dynamics of the singlet states of a tetraphenyl-diamine derivative in solution. *J. Phys. B: At., Mol. Opt. Phys.* **2004**, (8), 1581.
8. Holzer, W.; Penzkofer, A.; Hörhold, H. H.; Raabe, D.; Helbig, M., Photo-physical and lasing characterization of an aromatic diamine-xylylene copolymer. *Opt. Mater.* **2000**, 15 (3), 225-235.

9. Tsuboi, T.; Murayama, H.; Penzkofer, A., Photoluminescence characteristics of Ir(ppy)₃ and PtOEP doped in TPD host material. *Thin Solid Films* **2006**, *499* (1-2), 306-312.
10. Scholes, G. D., Long-range resonance energy transfer in molecular systems. *Annu. Rev. Phys. Chem.* **2003**, *54* (1), 57-87.
11. Dexter, D. L., A Theory of Sensitized Luminescence in Solids. *J. Chem. Phys.* **1953**, *21* (5), 836-850.
12. Bansal, A. K.; Penzkofer, A.; Holzer, W.; Tsuboi, T., Photodynamics of OLED Triplet Emitters Ir(ppy)₃ and PtOEP. *Mol. Cryst. Liq. Cryst.* **2007**, *467*, 21-31.
13. Veregin, R. P.; Harbour, J. R., Electron spin resonance spectroscopic study of electronic charge transport in an aromatic diamine. *J. Phys. Chem.* **1990**, *94* (16), 6231-6237.
14. Malicki, M. Electronic and Optical Properties of Hybrid Gold - Organic Dye Systems. Ph.D. Thesis, Georgia Institute of Technology, Atlanta, 2009.
15. Tsuboi, T.; Bansal, A. K.; Penzkofer, A., Temperature dependence of fluorescence and phosphorescence of the triphenylamine dimer 3-methyl-TPD. *Opt. Mater.* **2009**, *31* (6), 980-988.
16. Low, P. J.; Paterson, M. A. J.; Puschmann, H.; Goeta, A. E.; Howard, J. A. K.; Lambert, C.; Cherryman, J. C.; Tackley, D. R.; Leeming, S.; Brown, B., Crystal, Molecular and Electronic Structure of N,N'-Diphenyl-N,N'-bis(2,4-dimethylphenyl)-(1,1'-biphenyl)-4,4'-diamine and the corresponding Radical Cation. *Chem. - Eur. J.* **2004**, *10* (1), 83-91.
17. Vaidhyanathan, R.; Kirk, S., *Organic photochemistry and photophysics*. CRC press, Taylor and Francis Group: Boca Raton, 2006.
18. Lakowicz, J. R., *Principles of Fluorescence Spectroscopy*. Springer: New York, 2006; p 480.
19. Bredas, J.-L.; Beljonne, D.; Coropceanu, V.; Cornil, J., Charge-Transfer and Energy-Transfer Processes in Conjugated Oligomers and Polymers: A Molecular Picture. *Chem. Rev.* **2004**, *104* (11), 4971-5004.
20. Scholz, R.; Gissel, L.; Himcinschi, C.; Vragovic, I.; Calzado, E. M.; Louis, E.; San Fabia, Maroto, E.; Diáz-García, M. A., Asymmetry between Absorption and Photoluminescence Line Shapes of TPD: Spectroscopic Fingerprint of the Twisted Biphenyl Core. *J. Phys. Chem. A* **2008**, *113* (1), 315-324.

CHAPTER 5

ULTRAFAST SPECTROSCOPY OF SILVER NANOPARTICLES FUNCTIONALIZED WITH BIS(DIARYLAMINO)BIPHENYL LIGANDS

5.1. Introduction

Photophysical properties of chromophores in the proximity of metal nanostructures have fascinated scientists in recent years. The main focus in the studies of fluorescent chromophores adsorbed on metal surfaces is devoted to radiative and nonradiative decay rates of the chromophores.¹⁻³ The deactivation of the excited states of fluorescent chromophores in the proximity of metal surfaces has been studied for more than three decades.⁴⁻⁶ While the origin of the process is often assigned to energy^{2, 7} or electron transfer^{8,9} from the excited molecule to the metal, theoretical models describing such systems are still being investigated.^{3, 10, 11} Moreover, the effects associated with interactions between chromophoric ligands adsorbed onto metal surfaces, where the concentration of such ligands is usually much higher than in solution, are very often neglected. Recently, intermolecular interactions leading to excimer formation have been also proposed as a pathway for nonradiative depopulation of the excited states of chromophores attached to gold nanoparticles.^{1, 12}

In this chapter, the question of the effect of the Ag core on the photophysics of TPD, wherein the spectral overlap of the TPD emission and the AgNP plasmon absorption is substantial, and the role chromophore-chromophore interactions play in the

photophysics will be addressed. The results of femtosecond transient absorption experiments of a system composed of silver nanoparticles and bis(diarylamino)biphenyl (TPD) chromophores, which are chemically attached to the silver surface via a thiol group and an alkyl chain serving as a linker, will be detailed. The distance of the chromophores from the nanoparticle surface has been controlled by using $(\text{CH}_2)_3$, $(\text{CH}_2)_4$, $(\text{CH}_2)_8$ or $(\text{CH}_2)_{12}$ linkers. These silver nanoparticles functionalized with the TPD ligands have been characterized in chapter 3 by TEM, TGA, NMR, FTIR and UV-vis spectroscopy. The average sizes of the nanoparticles were determined to be in the range of 3.5-5.2 nm. Excited state lifetimes of the TPD chromophores attached to silver nanoparticles were measured to be within the range of 0.8-1.5 ps and it was determined that there is a distinct influence of the number of CH_2 groups in the linker on the lifetime. Furthermore, for the chromophores that are closest to the metal surface, the formation of a new species is observed following the initial chromophore photoexcitation. The new species resembles radical cation of TPDC12 spectrally and its formation is associated with intermolecular interaction in the TPD shell at high concentrations.

5.2. *Femtosecond Transient Absorption Spectroscopy in the NIR*

Due to the difficulties associated with desorption of the ligands from the nanoparticles and strong quenching of the fluorescence of the chromophores by the metallic core,^{4, 6, 13, 14} fluorescence-based dynamics are very difficult to interpret, since the signal can be dominated by the fluorescence from the desorbed chromophores. This point has been addressed in chapter 2 of this thesis. The fraction of desorbed chromophoric ligands has been estimated from ^1H NMR spectra in chapter 3. It has been

shown that less than 2% of the ligands are desorbed in all of the studied samples. Nonetheless, the small fraction of desorbed TPD ligands can significantly affect fluorescence decay measurements, if the fluorescence of the covalently attached chromophores is strongly quenched by metal nanoparticle. However, such a small fraction of desorbed ligands should not significantly affect transient absorption based studies. Kinetics of the TPD chromophores attached to silver nanoparticles reported herein was therefore studied by femtosecond transient absorption.

Transient absorption spectroscopy studies of the TPD excited state were focused on the NIR spectral region, since the excited state of the TPD in the visible region overlaps with the strong transient response of the AgNP plasmon absorption¹⁵⁻¹⁷. In this region, the transient absorption of silver nanoparticles shows very strong bleaching of plasmon resonance absorption with positive induced absorption bands on the wings of the plasmon bleach signal. The induced absorption bands are due to thermal heating of the nanoparticles¹⁸. Increased temperature of a nanoparticle can also increase its volume, which leads to lower density of electrons in the metal. As a consequence, the plasmon absorption band broadens and red shifts, increasing transient absorption in the plasmon wings. The positive transient signal in the plasmon wings decays as the particles cool down¹⁸. In the near IR, on the other hand, the transient response from silver nanoparticles is minimal while the TPD ligands have substantial excited state absorption in the range of 1000-1600 nm.

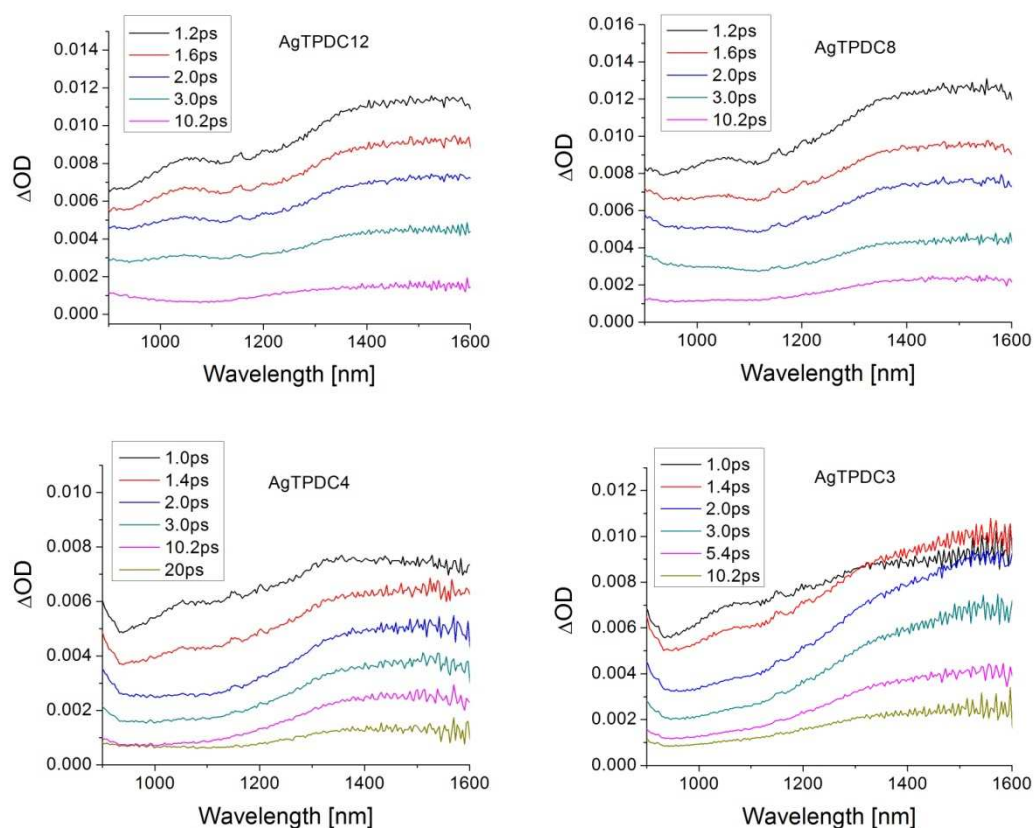


Figure 5.1. Time evolution of transient absorption spectra of: a) AgTPDC12-I, b) AgTPDC8-I, c) AgTPDC4-I and d) AgTPDC3-I in a mixture of 5:1 toluene:DMF. Samples were excited at 350 nm with pulse energy of 1.9 μJ . The delay times shown in the legends represent delay times from the initial onset of the transient signal. A delay time of 0.8 ps represents the time at which the transient signals reached their maxima.

Transient absorption spectra of TPD ligands attached to silver nanoparticles are shown in Figure 5.1. Overall the spectra resemble spectra of the excited state absorption of the TPD species in solution and in neat films. However, the decays are much faster for the chromophores attached to AgNP than for the samples of TPD moiety in solution or in films. The excited state absorption bands of AgTPDC12-I and AgTPDC8-I decay quite

uniformly throughout the spectrum, whereas transient spectra of AgTPDC4-I and AgTPDC3-I show rapid decay of the 1050 nm excited state absorption band and develop a new band at longer wavelengths, a few ps after the excitation pulse. It is also worth noting that the spectrum of the AgTPDC3-I sample at 1 ps shows a stronger signal at 1050 nm than at 1.4 ps, whereas the signal intensities at 1520 nm behave in the opposite way. This indicates that while the excited state absorption is decaying, there is growth of the absorption of some species with absorption at 1520 nm. Moreover, the shape and position of the growing band at 1520 nm resembles that observed for the neat film of the TPDC12 model compound, which was assigned to the formation of a cation-like form of TPDC12 (Chapter 4).

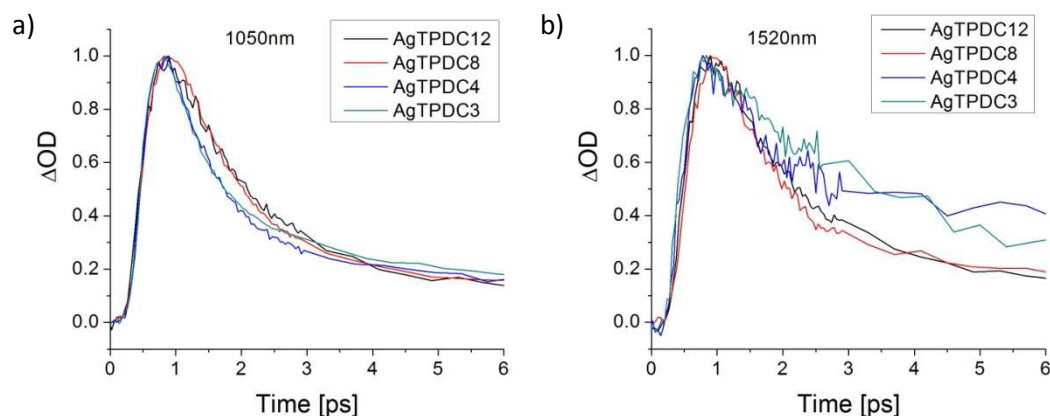


Figure 5.2. Normalized transient decay traces of AgTPDC_x-I (where x = 3, 4, 8 and 12) recorded at: a) 1050 nm and b) at 1520 nm. Samples were excited at 350 nm with pulse energy of 1.9 μ J.

The decay traces in Figure 5.2 depict the time evolution of the transient absorption at selected wavelengths in more detail. The plots show normalized decay traces of all four samples AgTPDC x -I (where $x = 3, 4, 8$ and 12) at 1050 nm (a) and 1520 nm (b). There are two sets of nearly overlapping decay curves at 1050 nm. The first set consists of the decays of AgTPDC12-I and AgTPDC8-I, and the second one belongs to AgTPDC4-I and AgTPDC3-I. The first set with longer linker lengths has an initially slower decay rate than the shorter linker set. While it is also evident that the decay curves of the first set are almost identical to each other, the decays of AgTPDC4-I and AgTPDC3-I are only similar to each other at very early time. After 2 ps the decay of AgTPDC4-I becomes slower than that of AgTPDC3-I.

The decay recorded at 1520 nm are very similar for AgTPDC12-I and AgTPDC8-I, while the decays of AgTPDC4-I and AgTPDC3-I are significantly slower. However, the latter two curves initially decay faster than the first two, only later becoming slower. It is also clear that the rate of decay of the AgTPDC4-I signal is generally greater than that of AgTPDC3-I, particularly at shorter times. The evolution of the transient spectra as well as the analysis of the decay traces, discussed below, indicate that there is a dominant fast decay of the excited state of the TPD moiety in AgTPDC12-I and AgTPDC8-I. The behavior of the other two samples however, resembles the behavior observed for the neat film where, during the decay of the excited state, a new species was being formed.

An analysis was conducted by using a global fitting routine on the transient decays at multiple wavelengths. Best fits were obtained with a sum of two exponentials:

$$\Delta OD(\lambda, t) = A_0(\lambda) + A_1(\lambda)e^{-(t-t_0)/\tau_1} + A_2(\lambda)e^{-(t-t_0)/\tau_2} \quad (5.1)$$

t_0 , τ_1 and τ_2 were all shared, and t was the time variable. The parameters varied independently for the fittings were the pre-exponential amplitudes, $A_1(\lambda)$ and $A_2(\lambda)$, and the offset parameter A_0 . τ_0 is an offset in time axis, which was fixed at the position of the maximum of decay curves.

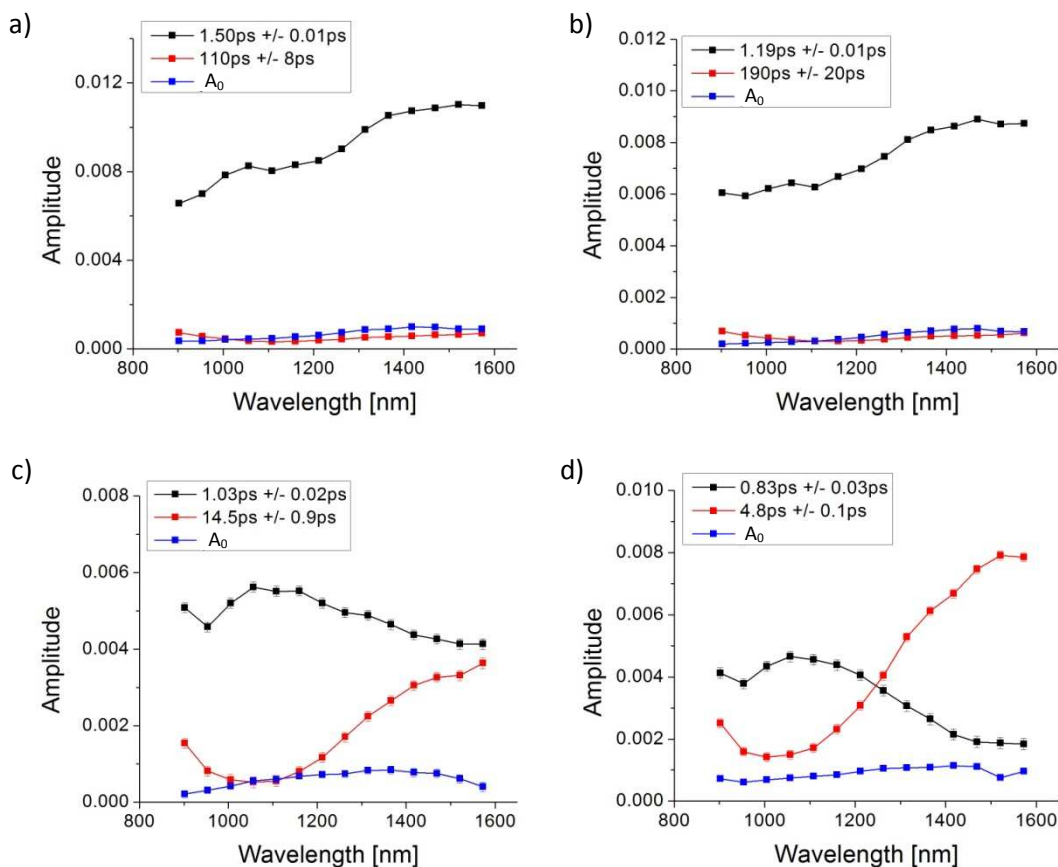


Figure 5.3. Spectral distribution of pre-exponential amplitudes from global fitting analysis ($A_1(\lambda)$ – black line, $A_2(\lambda)$ – red line) and the offset parameter ($A_0(\lambda)$ – blue line): a) AgTPDC12-I, b) AgTPDC8-I, c) AgTPDC4-I and d) AgTPDC3-I in a mixture of 5:1 toluene:DMF. Excitation wavelength was 350 nm, excitation energy per pulse was 1.9 μ J for AgTPDC8-I and 2.4 μ J for the rest of the samples.

Figure 5.3 shows the spectral distribution of pre-exponential amplitudes ($A_1(\lambda)$ and $A_2(\lambda)$) and the offset parameter $A_0(\lambda)$ obtained as a result of the global fitting analysis for AgTPDCx-I (where $x = 3, 4, 8$ and 12). Spectral profiles of the pre-exponential amplitudes for the samples AgTPDC12-I (Figure 5.3a) and AgTPDC8-I (Figure 5.3b) have only one significant component: $A_1(\lambda)$. These amplitudes correspond to the fastest decay times, which are 1.5 ps for AgTPDC12-I and 1.2 ps for AgTPDC8-I and their spectral profiles are consistent with the spectrum of the excited state of the TPD moiety in solution (Chapter 4).

Spectral profiles of the pre-exponential amplitudes of the samples AgTPDC4-I (Figure 5.3c) and AgTPDC3-I (Figure 5.3d) are significantly different from AgTPDC12-I and AgTPDC8-I, as expected from the analysis of the spectral evolution and decay traces described above. There are two significant decay amplitudes in the global fitting for AgTPDC4-I and AgTPDC3-I. The time constants, τ_1 , corresponding to the amplitudes, $A_1(\lambda)$, are 1.0 ps for AgTPDC4-I and 0.8 ps for AgTPDC3-I. The spectral profiles for these decay times are quite different from the transient absorption of the excited state of TPD in solution. The spectral amplitudes observed for AgTPDC4-I and AgTPDC3-I are very similar to spectral amplitudes of the fast decay component for the neat film of TPDC12. These results indicate that the TPD excited state properties for the AgTPDC4-I and AgTPDC3-I particles are quite similar to the neat film and that the chromophores in the shells are relatively densely packed as in the solid, which is consistent with the NMR T_2 data discussed in Chapter 3.

It should be emphasized that the peak position of the spectral amplitudes $A_1(\lambda)$ is distinctly different to that of $A_2(\lambda)$ and that each of these spectral components has a

distinct decay time. This suggests that the two spectral amplitudes are associated with two different species with different decay times and is consistent with the conclusion of the formation of a new species following excitation for AgTPDC4-I and AgTPDC3-I based on the transient absorption spectral data discussed above. The global fitting analysis provided the decay time constants τ_2 of 15 ps for AgTPDC4-I and of 5 ps for AgTPDC3-I, both of which are much longer than the excited state decay time constants.

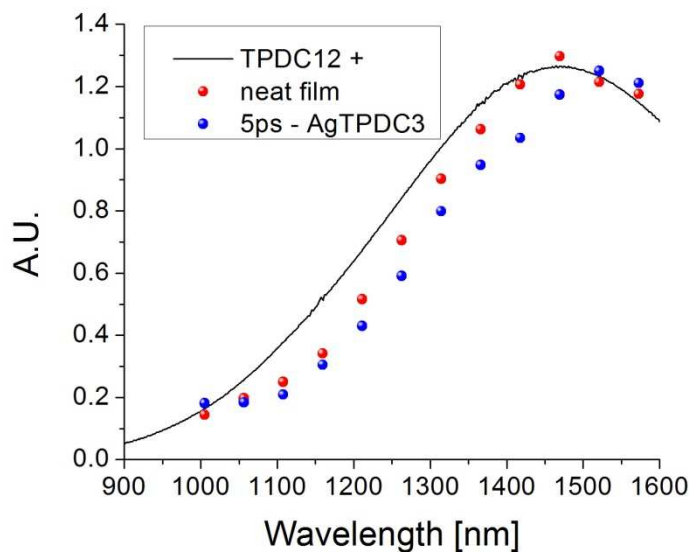


Figure 5.4. NIR absorption spectrum of radical cation of TPDC12 in DCM overlaid with spectral profiles of the offset ($A_0(\lambda)$) component obtained from global fitting analysis of neat film of TPDC12 and spectral profiles of pre-exponential amplitudes associated with time constant of 5 ps of the sample AgTPDC3-I.

The spectral profile of the pre-exponential amplitudes with time component of 5 ps of the sample AgTPDC3-I is consistent with both spectral profile of the offset $A_0(\lambda)$ of the neat film and the NIR absorption band on TPDC12 radical cation (Figure 5.4), suggesting a cation-like character of the new species formed after photoexcitation of the AgTPDC3-I.

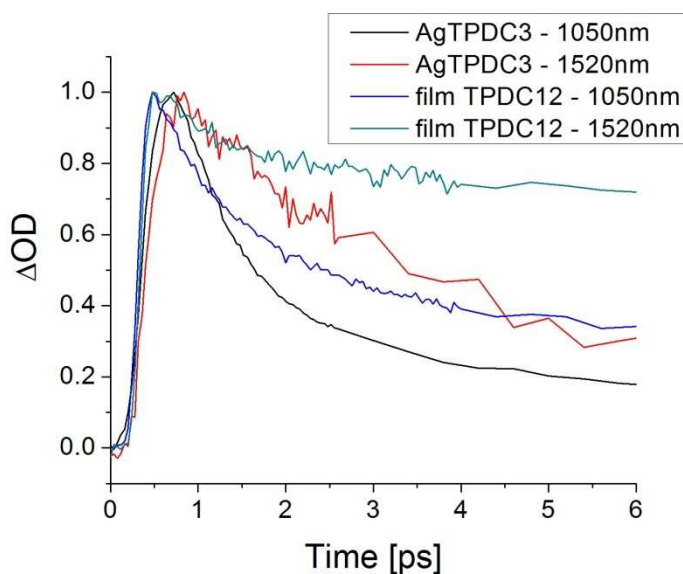


Figure 5.5. Normalized decay curves of transient absorption of AgTPDC3-I and the neat film of TPDC12, recorded at 1050 nm and 1520 nm. Excitation wavelength was 350 nm, excitation energy per pulse was 2.4 μ J for AgTPDC3-I and 0.48 μ J for the neat film.

Figure 5.5 shows the decay traces of AgTPDC3-I at 1050 nm and 1520 nm compared to the decays of the neat TPD film at the same wavelengths. Time traces associated with AgTPDC3-I decay faster than the ones corresponding to the neat film but overall the correlation between the decays at 1050 nm and at 1520 nm is quite good. At very early times, there is a shift in time between the transient maxima at 1050 nm and 1520 nm in the nanoparticle sample while no such shift is observed in the traces of the film. This temporal offset of the maxima is associated with a growth of the transient absorption and the formation of a species with absorption at 1520 nm. The estimated rise time for the C3 system is ~0.6-0.8 ps. On the other hand, the absence of a rising edge time shift in the neat film (which has a longer decay time constant) suggests a faster formation of the new species, which is not resolved in this experiment.

The above results and analysis of the transient absorption behavior of the silver nanoparticles with TPD ligands covalently attached reveals ultrafast relaxation of the excited state of the TPD moiety. The lifetimes obtained from fittings show a clear dependence on the length of the alkyl ligand spacer between the chromophoric end groups and the metal surface. The systems with C12 and C8 linkers undergo fast electronic relaxation with a simple single exponential decay and no evidence of formation of the TPD cation species formed. This suggests that a simple mechanism involving non-radiative relaxation due to energy transfer from the dye to the Ag nanoparticle core dominates the kinetics. For the C3 and C4 linker systems, the excited state spectrum and decay kinetics show solid-state like behavior consistent with a dense packing of the dyes in the chromophore shell. The photoexcitation of the shorter linker systems leads to a formation of a new species with an absorption peak at 1520 nm, with a surprisingly long

lifetime (5 – 15 ps) that has been assigned to a cation-like state that is spectrally very similar to the species observed following excitation of neat TPDC12 films. As a result, the excited states of the C3 and C4 linker systems can undergo nonradiative decay via energy transfer to the Ag nanoparticle core as well as a charge transfer process within the chromophore shell that leads to formation of a cation-like state.

5.3. Analysis of AgTPDC3 systems

In the following sub-sections AgTPDC3-x (where x = I, II and III) is discussed in terms of pulse energy dependence and coverage dependence in order to address the possible mechanisms of formation of the cation-like TPD in these systems. The other systems with longer alkyl linker are discussed in a separate section.

5.3.1. Excitation Energy Dependence

Photoexcitation of the TPD in close proximity to a silver nanoparticle surface may lead to the formation of a cation-like species either by excitation with one photon or potentially more than one photon. These different mechanisms can, in principle, be distinguished by pulse energy dependent studies. A one-photon excitation process is expected to show a linear energy dependence for the spectral amplitude of the cation-like species, while a process involving more than one photon should show a super-linear behavior.

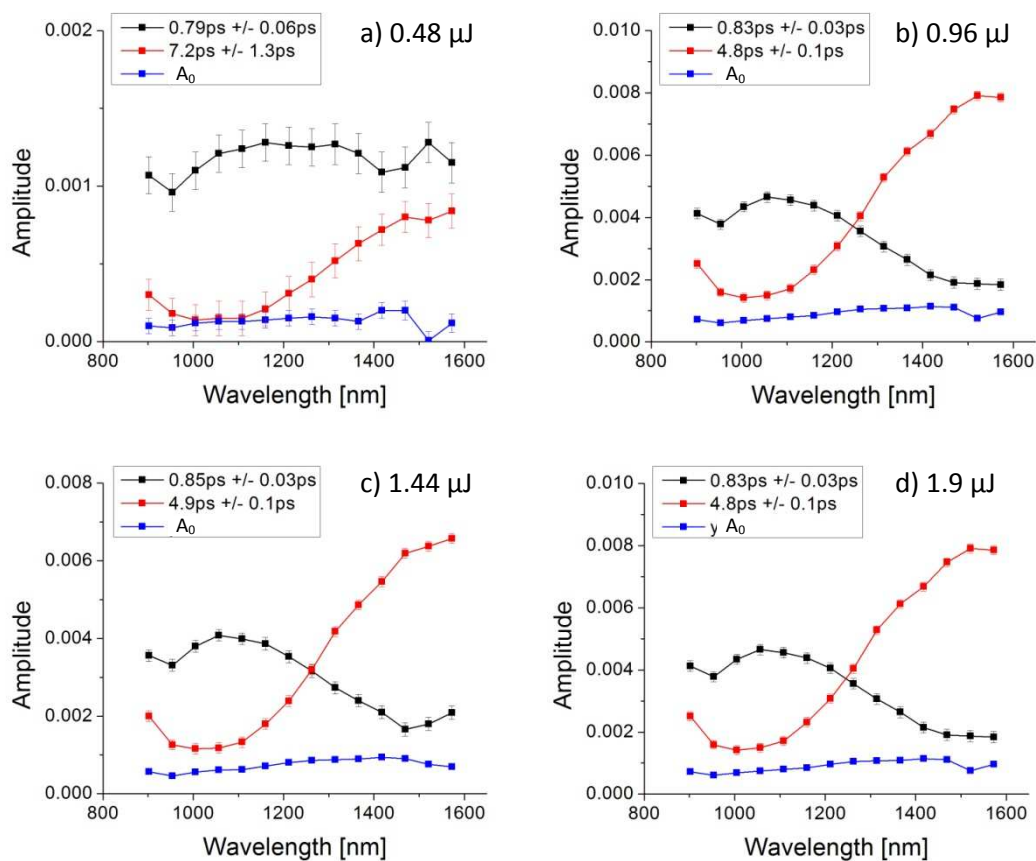


Figure 5.6. Spectral distribution of pre-exponential amplitudes ($A_1(\lambda)$ – black line, $A_2(\lambda)$ – red line) and the offset parameter ($A_0(\lambda)$ – blue line) obtained from fitting with sum of two exponentials of the decay traces of AgTPDC3-I in a mixture of 5:1 toluene:DMF at different excitation energies: a) 0.48 μ J, b) 0.96 μ J, c) 1.44 μ J, d) 1.9 μ J and e) 2.4 μ J. Time components are similar for all excitation energies: $\tau_1 \sim 0.8\text{ps}$ and $\tau_2 \sim 5\text{ps}$. The sample was excited at 350 nm.

In order to better understand the mechanism of formation of the TPD cation-like species in close proximity to the AgNP core, a set of pulse energy dependent experiments were conducted. Figure 5.6 shows the spectral amplitudes ($A_1(\lambda)$ and $A_2(\lambda)$) and the offset parameter $A_0(\lambda)$ obtained from global fitting analysis for AgTPDC3-I excited at five different excitation energies per pulse: a) 0.48 μJ , b) 0.96 μJ , c) 1.44 μJ , d) 1.9 μJ and e) 2.4 μJ . The exponential decay time constants obtained by fitting the decays at different excitation energies were found to be similar for all excitation energies: $t_1 \sim 0.8\text{ps}$ and $t_2 \sim 5\text{ps}$.

The spectral amplitudes for the samples excited at all the above energies have two significant components $A_1(\lambda)$ and $A_2(\lambda)$. At the lowest excitation energy, 0.48 μJ , (Figure 5.6a) the dominant component is $A_1(\lambda)$ and the amplitude $A_2(\lambda)$ is relatively weak but not negligible. The spectral profile of $A_1(\lambda)$ at low energy is rather broad, including absorption at $\sim 1500\text{ nm}$ but at increasing pulse energy the band tails off to longer wavelengths and the apparent absorption amplitudes decreases. At the same time the $A_2(\lambda)$ band shows an increase with pulse energy.

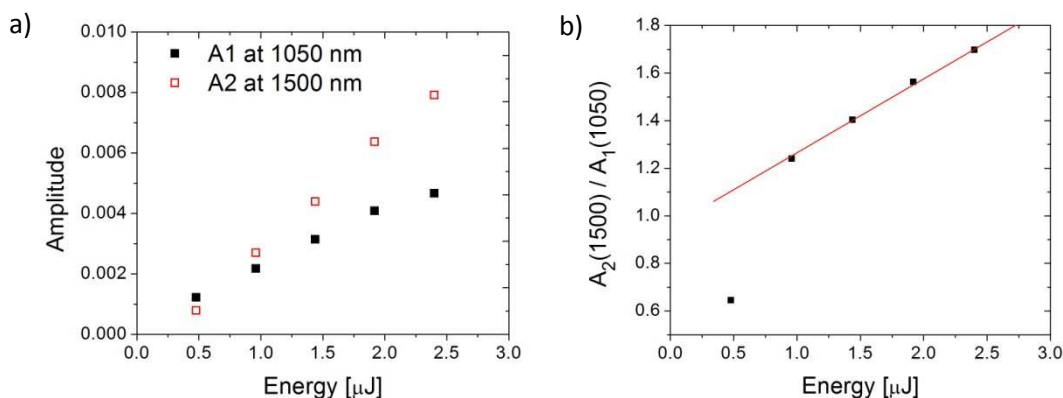


Figure 5.7. a) Pulse energy dependence of amplitudes A_1 at 1050 nm and A_2 at 1520 nm for AgTPDC3-I, b) ratio of amplitudes A_2 at 1520 nm to A_1 at 1050 nm plotted as a function of excitation energy.

The peak spectral amplitudes (A_1 at 1050 nm and A_2 at 1500 nm) are plotted as a function of excitation pulse energy in Figure 5.7a. $A_1(1050)$ appears nearly linearly-dependent on the excitation energy with a slight saturation at the higher energies, which is similar to the energy dependence for the 1050 nm band for all samples studied herein. This will be discussed later in the section on the results of the energy dependence of AgNP with TPD ligands with longer alkyl linkers. In order to assess power dependence of A_2 we examined the ratios of these two amplitudes (A_2/A_1), in order to compensate for potential saturation effects. Figure 5.7b shows ratios of pre-exponential amplitudes, $A_2(1500) / A_1(1050)$. The energy dependence of the amplitude ratio is linear, with an exception of the lowest energy point, which is well below the line. Although this point has a sizeable uncertainty as it is the ratios of small values, with error bars, its deviation from the line is also consistent with a threshold or nonlinearity for the process leading to the 1500 nm band.

The linear energy dependence of the amplitude ratio indicates a quadratic response of the amplitudes A_2 as a function of excitation energy, suggesting the involvement of two photons in the formation of the cation-like species, as will be discussed in detail in the following paragraphs. Possible mechanisms that could give rise to a quadratic intensity dependence are either two-photon (or sequential one-photon) absorption by TPD chromophores individually, or a bimolecular process, involving two excited state TPD molecules that may undergo exciton-exciton annihilation.

In order to explain the intensity dependent behavior described above, a kinetic analysis has been performed using three models: two that involve a two-photon induced charge separation (via instantaneous or sequential two-photon absorption) and another that involves annihilation of a pair of one-photon excited states that leads to charge separation. The schematic diagram shown in Figure 5.8 illustrates the relevant energy levels of TPD and TPD^{*+} (where TPD^{*+} refers to a cation-like TPD species) with instantaneous (2PA) or sequential (referred to as 1+1 excitation) two-photon excitation and exciton-exciton annihilation (EEA). In the 2PA model, the TPD molecules are directly excited from ground state $|g\rangle$ to the higher excited state $|n\rangle$, by instantaneous absorption of two photons. On the other hand, in the 1+1 excitation model, a TPD molecule is initially excited from its ground state $|g\rangle$ to the first excited state $|e\rangle$, from which it can be promoted to the higher excited state $|n\rangle$ by absorbing second photon with energy $h\nu$ or relax down to the ground state with decay rate k .

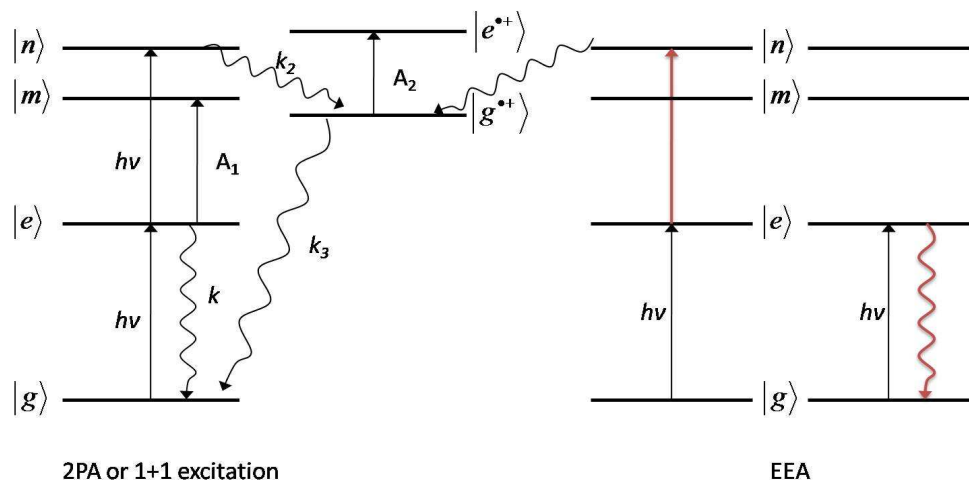


Figure 5.8. Schematic diagram describing energy levels of TPD and cation-like TPD (TPD^{•+}) and possible pathways for photoinduced charge separation. Straight arrows represent absorptions, whereas wavy arrows show spontaneous relaxation pathways. A_1 and A_2 are the excited state and cation-like absorptions associated with pre exponential amplitudes obtained from global fitting. The red arrows in EEA model represent energy exchange between two excited TPD molecules, where the wavy red line represents relaxation of one excited TPD molecule and the straight red line illustrates promotion of the second excited TPD molecule to higher excited state level via energy transfer.

Alternatively, the higher excited state $|n\rangle$ can be also reached by energy transfer between two excited molecules in the process of EEA. In this model, two TPD molecules in the first excited state $|e\rangle$ interact with each other by exchanging energy. One of the molecules relaxes to the ground state $|g\rangle$, which is represented in the Figure 5.8 by a wavy red line, and the energy of this transition is transferred to the second TPD in state $|e\rangle$, represented by straight red line in the Figure 5.8, which promotes the molecule to the higher excited state $|n\rangle$. Absorption of two photons with energy $h\nu$ provides enough energy to lead to charge separation, following which the system forms the TPD^{•+} ground state $|g^{*+}\rangle$.

It is possible that the molecule can reach state $|n\rangle$ either by simultaneous or sequential two-photon absorption (2PA) or by a bimolecular process such as exciton-exciton annihilation (EEA) as mentioned above. In the next section we examine kinetics of each of these mechanisms for the AgTPDC3 systems.

5.3.1.1. *Two-photon absorption*

The two-photon absorption process can result in promotion of a TPD molecule to the state $|n\rangle$ and the associated kinetic model can be expressed by the following equation:

$$\frac{dN_n(t)}{dt} = \delta\Phi^2[N_0 - N_n(t)] \quad (5.2)$$

the solution of which is:

$$N_n = N_0(1 - e^{-\delta\Phi^2 t}) \quad (5.3)$$

where N_0 is a total number of molecules and δ is the two-photon absorption cross-section. By applying a series expansion to the exponential function, equation (5.3) takes the following form:

$$N_n = N_0\delta\Phi^2 t \left(1 - \frac{\delta\Phi^2 t}{2!} + \frac{\delta^2\Phi^4 t^2}{3!} - \dots \right) \quad (5.4)$$

The first term in the expansion gives a quadratic dependence on flux Φ , with a saturation behavior due to second term at higher Φ . The rate of formation of the cation-like species is proportional to $N_n(t)*\eta(n \rightarrow g^{*+})$, where $\eta(n \rightarrow g^{*+})$ is the quantum efficiency of transition from state $|n\rangle$ to $|g^{*+}\rangle$.

5.3.1.2. Sequential One-Photon Absorption

The kinetics of the 1+1 excitation process can be described by the following pair of differential equations:

$$\frac{dN_e(t)}{dt} = \sigma_g \Phi (N_0 - N_e(t)) - (\sigma_e \Phi + k) N_e(t) \quad (5.5)$$

$$\frac{dN_n(t)}{dt} = \sigma_e \Phi N_e(t) \quad (5.6)$$

Assuming negligible population N_n compared to N_e and N_g the solution for $N_e(t)$ gives:

$$N_e(t) = \frac{\sigma_g N_0 \Phi}{a(\Phi)} (1 - e^{-a(\Phi)t}) \quad (5.7)$$

with $a(\Phi) = (\sigma_e + \sigma_g)\Phi + k$. By applying a series expansion to the exponential and rearranging, the above equation takes the following form:

$$N_e(t) = \sigma_g N_0 \Phi t \left(1 - \frac{a(\Phi)t}{2!} + \frac{a(\Phi)^2 t^2}{3!} - \dots \right) \quad (5.8)$$

At low photon flux the series expansion can be truncated at the first term, at which point $N_e(t)$ becomes linearly dependent on Φ . However, at high flux, the population of the molecules in the first excited state will also be diminished by the excited state absorption, leading to saturation behavior. In such a situation more terms of the series need to be included. The population of the molecules in the higher excited state, $N_n(t)$, is expressed by the following equation:

$$N_n(t) = \frac{\sigma_e \sigma_g N_0 \Phi^2}{a(\Phi)^2} (e^{-a(\Phi)t} + a(\Phi)t - 1) \quad (5.9)$$

Again applying a series expansion to the exponential term, the above equation takes the following form:

$$N_n(t) = \frac{1}{2} \sigma_e \sigma_g N_0 \Phi^2 t^2 \left(1 - \frac{2a(\Phi)t}{3!} + \frac{2a(\Phi)^2 t^2}{4!} - \dots \right) \quad (5.10)$$

The number of molecules in the state $|n\rangle$ is quadratically dependent on the photon flux at low excitation energy, whereas at higher energies it also shows saturation behavior.

5.3.1.3. *Exciton-Exciton Annihilation*

Before considering the kinetic model of the EEA process, the feasibility of this process needs to be assessed, as there needs to be more than one excited TPD per nanoparticles for EEA to occur. A assessment of this potential EEA process is provided by calculation of the fraction of the excited states of the TPD ligands to the number of the ligands in the ground state (N_e/N_0) throughout the excited volume of the sample.^{xxx} The calculation was done for sample AgTPDC3-I, where $OD(350 \text{ nm}) = 2.5$. The specific contributions to this absorbance from the TPD ligand and AgNP were determined based on the data provided in Table 3.5 of chapter 3: $OD_{\text{TPD}} = 2.0$ and $OD_{\text{AgNP}} = 0.5$. Under optical pumping, the concentration of the TPD excited states is highest at the front wall, since the beam intensity is the strongest there and falls off as it propagates through the highly absorbing solution. The average number of TPD ligands per one AgNP in AgTPDC3-I is ~ 250 (provided in Table 3.5 of chapter 3). Assuming a statistical distribution of the excited states for nanoparticles with an average of 250 chromophores, in order for one nanoparticle to have two TPD ligands in the excited state N_e/N_0 would need to be ≥ 0.008 .

^{xxx} Details of the calculations are provided in the section 2.6.7 of Chapter 2

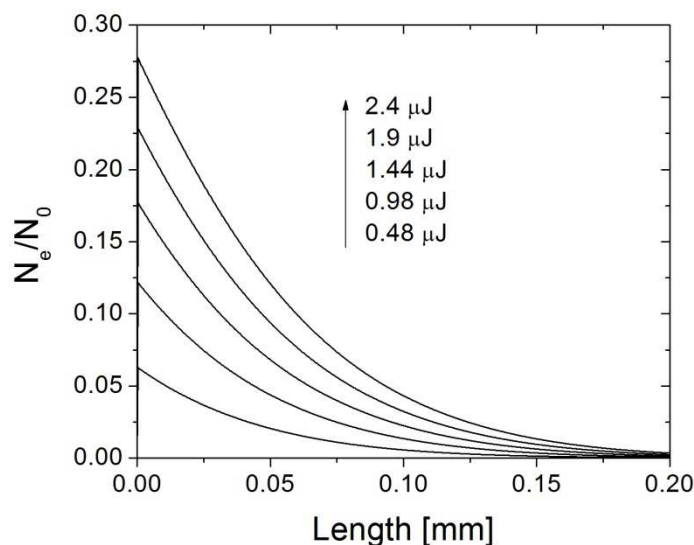


Figure 5.9. Fraction of TPD ligands in excited state to the molecules in ground state as a function of distance from the front wall of the cuvette (the wall through which the beam enters the cuvette) calculated for AgTPDC3-I for five excitation energies: 0.48 μJ , 0.98 μJ , 1.44 μJ , 1.9 μJ and 2.4 μJ . Calculations include pump beam depletion from both TPD ligand and AgNP.

Figure 5.9 shows the calculated dependence of N_e/N_0 as a function distance for the beam propagating through the solution. The threshold for two TPD ligands being in the excited state on the same nanoparticle is at $N_e/N_0 = 0.008$, which indicates that almost all nanoparticles have more than one TPD in the excited state for all excitation energies. This analysis indicates that the mechanism for formation of the cation-like species involving two excited TPD ligands is theoretically possible^{xxxi} at all excitation energies. Moreover, in order for this mechanism to be effective, excited state migration should be

^{xxxi} This argument assumes a statistical distribution of the excited states in the sample.

fast, since the lifetime of the excited states of these dyes on the nanoparticles is less than 1ps.

Here we consider a kinetic model for charge carrier generation via EEA, where the molecules in the first excited state $|e\rangle$, as depicted in Figure 5.8, are promoted to the higher excited state $|n\rangle$. In the following kinetic analysis we consider the EEA process after the laser pulse, which assumes that the number of annihilation events during the pulse can be neglected. Thus for the EEA kinetics we can assume initial number of excited states to be $N_e(0, \Phi) = \sigma_g N_0 \Phi t_p$. The kinetics of exciton-exciton annihilation leading to the formation of the cation-like species can be described by the following set of differential equations:

$$\frac{dN_e(t)}{dt} = -kN_e(t) - \gamma N_e(t)^2 \quad (5.11)$$

$$\frac{dN_n(t)}{dt} = \gamma N_e(t)^2 \quad (5.12)$$

where γ is EEA rate constant. The solution of the first equation for N_e gives:

$$N_e(t) = \frac{N_e(0, \Phi) e^{-kt}}{1 + B(0, \Phi)(1 - e^{-kt})} \quad (5.13)$$

where $B(0, \Phi) = N_e(0, \Phi)\gamma/k$. The total number of higher excited states that could generate cation-like species is:

$$N_n(t) = \frac{k}{\gamma} \{B(0, \Phi) - \ln[1 + B(0, \Phi)]\} \quad (5.14)$$

This equation can be expressed by the series expansion:

$$N_n(t) = \frac{kB(0, \Phi)^2}{2\gamma} \left(1 - \frac{2B(0, \Phi)}{3} + \frac{2B(0, \Phi)^2}{4} - \dots \right) \quad (5.15)$$

In conjugated polymers, e.g. MEH-PPV, γ is on the order of $10^{-8} \text{ cm}^3 \text{ s}^{-1}$. Under this condition $B(0, \Phi) \ll 1$, equation (5.15) can be approximated with the first term of the series, which makes the $N_n(t)$ quadratically dependent on excitation energy.

All the mechanisms discussed above show quadratic dependence on the excitation energy for low excitation intensities, with saturation occurring at high intensities. Due to the fact that the essential parameters δ , σ_e , and γ are not known, it is not possible to distinguish between the above mechanisms based on the pulse energy dependent behavior alone. However, the bimolecular process can be distinguished from the other mechanisms by studying the dependence of the formation of the cation-like species on the surface concentration of chromophores.

5.3.2. Coverage Dependence – AgTPDC3 Systems

The power dependent studies have revealed that the formation of the cation-like species upon excitation of the TPD in AgTPDC3-I is a nonlinear process with quadratic power dependence. The possible mechanisms discussed above are: absorption of two photons by one TPD molecule either simultaneously (2PA) or sequentially (1+1 excitation), and a bimolecular process (EEA). The bimolecular mechanism can be distinguished from the others by studying coverage dependence, since two molecules participate in the formation of the cation-like species, which is sensitive to the concentration of the chromophores on the surface of nanoparticles. This concentration was varied in a controlled manner by co-adsorption of dodecylthiol together with TPD ligands during the place exchange reaction. The effects of such dilutions on the transient

absorption response in these systems were studied and the results obtained from a global analysis are discussed below.

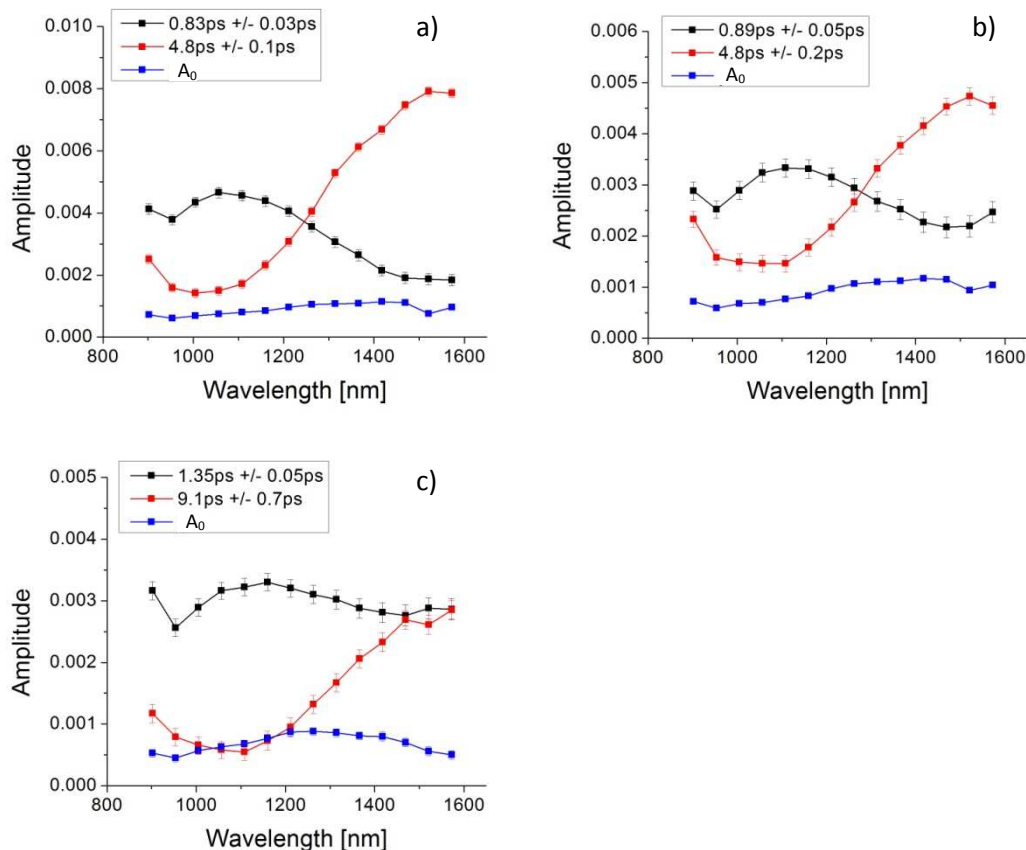


Figure 5.10. Spectral distribution of pre-exponential amplitudes for a) AgTPDC3-I, b) AgTPDC3-II and c) AgTPDC3-III in a mixture of 5:1 toluene:DMF. Spectral profiles $A_1(\lambda)$ – black line, $A_2(\lambda)$ – red line and the offset parameter $A_0(\lambda)$ – blue line are obtained from global fitting of the decay traces with a sum of two exponentials. The sample was excited at 350 nm, excitation energy was 2.4 μ J. Lifetimes of the components are shown in the plot legends.

Figures 5.10a, 5.10b and 5.10c show spectral amplitudes of AgTPDC3-I, AgTPDC3-II and AgTPDC3-III, respectively. The first sample was functionalized only

with TPDC3SH ligand and the latter two were prepared by co-adsorption of TPDC3SH with dodecylthiol (DDT) in the following molar ratios: 2:1 (TPD:DDT) for AgTPDC3-II and 1:2 for AgTPDC3-III. The dilution of the TPDs by incorporation of DDT leads to an increase in the average area per TPD ligand was determined to be 17.8\AA^2 , 18.4\AA^2 and 23.9\AA^2 for AgTPDC3-I, AgTPDC3-II and AgTPDC3-III, respectively.^{xxxii} With this larger average spacing of the TPD ligands upon dilution with DDT, if the process leading to the formation of the cation-like species is a bimolecular process, we would expect to see a significant reduction in the absorbance of the cation-like absorption band at 1500 nm, whereas no significant change would be expected if it were a monomolecular two-photon process.

It can be readily seen in Figure 5.10 that the peak pre-exponential amplitude of cation-like species relative that of to the excited state band ($A_2(1500) / A_I(1050)$) is diminished upon dilution with DDT. These results are summarized in Figure 5.11 where values of $A_2(1500) / A_I(1050)$ are shown as a function of area per one TPD ligand, for systems AgTPDC3-x (x = I, II, III). It is evident from this plot that efficiency of formation of the cation-like species is strongly dependent on the density of the TPD chromophores. This finding suggests that a bimolecular (or higher order) process, such as EEA, is responsible for the TPD cation-like species formation.

^{xxxii} The values of the average area per TPD ligand summarized in Table 3.5 of Chapter 3.

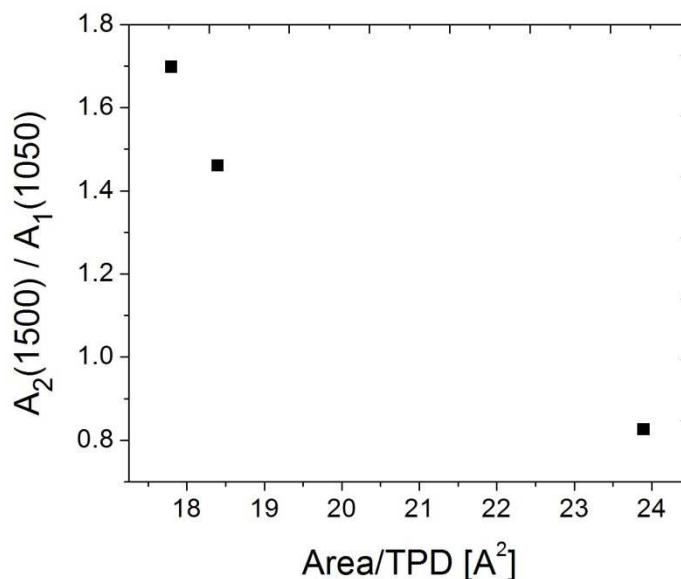


Figure 5.11. Ratio of pre-exponential amplitudes A_2 at 1500 nm to the amplitudes A_1 at 1050 nm as a function of the area per TPD ligand on the AgNP surface. The data are presented for AgTPDC3-I, AgTPDC3-II, AgTPDC3-III. Excitation energy used was 2.4 μJ and the excitation wavelength was 350 nm.

Interestingly, the lifetimes of the components are very similar for the particles with the higher TPD ligand concentration: for AgTPDC3-I $\tau_1 = 0.83$ ps, $\tau_2 = 4.8$ ps and for AgTPDC3-II $\tau_1 = 0.89$ ps, $\tau_2 = 4.8$ ps, whereas the time constants are substantially longer in AgTPDC3-III $\tau_1 = 1.35$ ps, $\tau_2 = 9.1$ ps. The decay time of the TPD excited state band (A_1 band) increases by about 50% on further dilution (AgTPDC3-III), which is consistent with a reduced quenching of the excited state via EEA. Thus, the dilution of the TPDs with the DDT ligands can either play the role of barriers¹⁹ to energy migration or merely act to reduce the population of adjacent TPD pairs or aggregates that are needed for the formation of cation-like species. The lengthening of the lifetime of the cation-like

transient species upon dilution with DDT implies a reduction in the recombination rate of the charge carriers. Perhaps the charges are able to get localized at larger separations upon dilution leading to slower recombination or there may be a destabilization of charged separated state upon dilution that slows the recombination.

5.4. *Analysis of AgTPDC4, AgTPDC8 and AgTPDC12 systems*

Systems with longer linker lengths (four, eight and twelve carbon alkyls), specifically, AgTPDC4-y (where y = I, II), AgTPDC8-x and AgTPDC12-x (where x = I, II and III) are discussed in this section in terms of pulse energy and dye coverage dependencies of the transient absorption bands. We examine these dependencies in order to contrast the photophysics of these systems relative to what was observed for the C3 linker system and to address the dependence of formation of the cation-like TPD species upon the distance of the dyes from the surface of silver nanoparticle. As will be shown below, the behavior appears to depend on the linker length along with the curvature of the particle, with the systems bearing longer linkers (C8 and C12) showing no evidence of formation of the cation like species.

5.4.1. *Excitation energy dependence*

Figure 5.12 shows spectral amplitudes ($A_1(\lambda)$ and $A_2(\lambda)$) and the offset parameter $A_0(\lambda)$ obtained from a global fitting analysis of AgTPDC4-I excited at four different pulse energies: a) 0.96 μJ , b) 1.44 μJ , c) 1.9 μJ and d) 2.4 μJ . Spectral amplitudes for the samples excited at the three highest energies have two significant components $A_1(\lambda)$ and

$A_2(\lambda)$. The spectral amplitudes of AgTPDC4-I have similar shapes to those of the sample AgTPDC3-I, but with a much weaker dependence on excitation energy. The cation-like band, represented by $A_2(\lambda)$, is not apparent at the lowest energy and only starts appearing at higher energies.

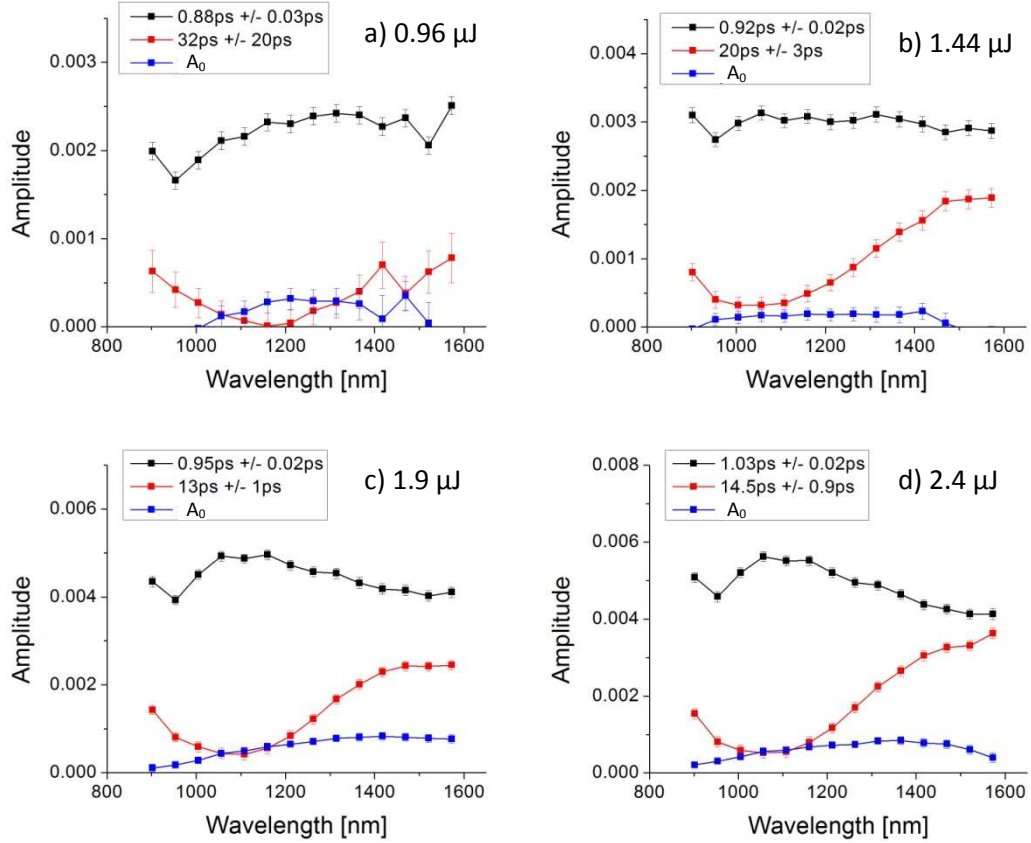


Figure 5.12. Spectral distribution of pre-exponential amplitudes for AgTPDC4-I in a mixture of 5:1 toluene:DMF at varied excitation energies: a) 0.96 μJ , b) 1.44 μJ , c) 1.9 μJ and d) 2.4 μJ . Spectral amplitudes $A_1(\lambda)$ – black line, $A_2(\lambda)$ – red line and the offset parameter $A_0(\lambda)$ – blue line are obtained from global fitting with sum of two exponentials. The samples were excited at 350 nm. Lifetimes of the components are shown in the plot legends.

It is evident from Figure 5.12 that the production of the cation-like species in the system AgTPDC4-I is not as favorable as in AgTPDC3-I system. The values of the amplitudes at 1050 nm for A_1 and at 1500 nm for A_2 are plotted as a function of energy per pulse in Figure 5.13. Due to the low number of data points^{xxxiii} and weak pulse energy dependence of the amplitudes A_2 , in this energy range, these data are discussed only qualitatively. The amplitudes $A_1(1050)$ and $A_2(1500)$ increase with increasing excitation energy. The trends of $A_2(1500)$ are consistent with a threshold behavior similar to the one observed in AgTPDC3-I system. However, intensity of the amplitude A_2 and its dependence on excitation energy is much weaker than in the case of AgTPDC3-I. This suggests that the formation of cation-like species upon photoexcitation is reduced even for a single carbon decrease in the number of carbon atoms in the aliphatic chain.

^{xxxiii} The low energy limit is due to low signal and the higher energy limit is due to the limitation of the excitation source.

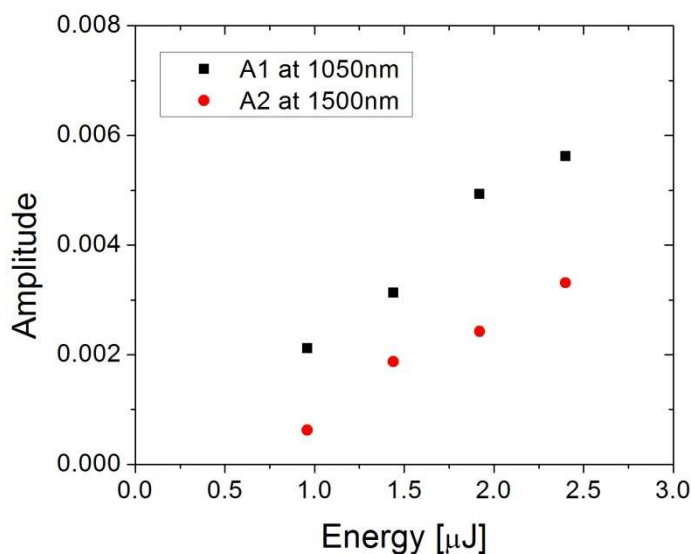


Figure 5.13. Changes in the amplitudes A_1 at 1050 nm and A_2 at 1520 nm plotted as a function of excitation energy in the sample AgTPDC4-I. The lowest plotted energy amplitude A_2 has a low value and large error, as shown in Figure 5.12.

The lifetime of the excited state for AgTPDC4-I is $\tau_1 \approx 1$ ps and that of the cation-like band is $\tau_2 \approx 14$ ps, both of which are longer than in the case of AgTPDC3-I. The longer lifetime of the species associated with τ_1 is consistent with reduction in the rate of energy transfer from the chromophore to the metal particle core as a result of being a little further away from the metal surface. As for the increase in lifetime of the cation like species, this indicates a slower recombination rate for the C4 vs. the C3 linker system. One possible explanation is that if the electron lost by a TPD molecule to form the cation-like species is transferred to the AgNP core, then the recombination rate would be expected to decrease as a result of the greater distance for the charge recombination. On the other hand, if the electron transfer happens between two TPD molecules, such a cation—anion pair could be stabilized by the formation of an image dipole in the metal.²⁰

However, if the image dipole stabilization is dominant, the charge recombination of the dye radical anion – radical cation system would be slower when the dye molecules are closer to the metal surface, which is contrary to our observations. The possible influence of length of alkyl chain on the generation of the cation-like species is discussed in the next section in conjunction with NMR results that offer information on the mobility and packing of the chromophores.

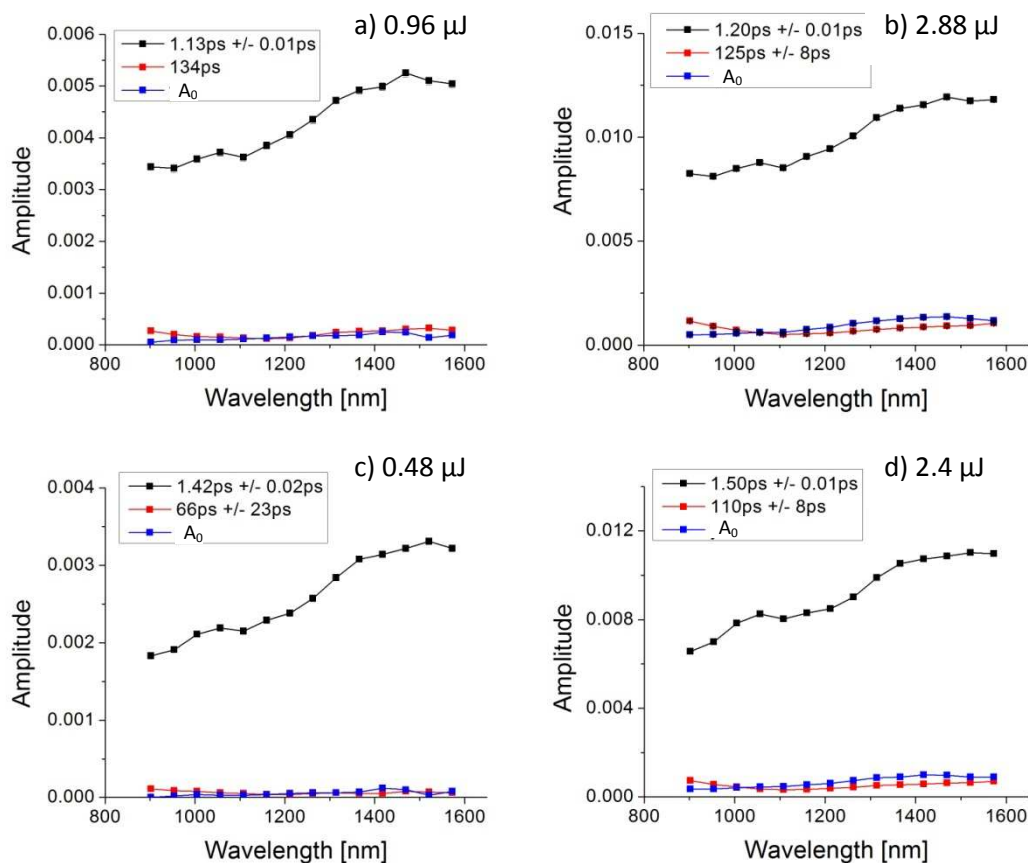


Figure 5.14. Spectral distribution of pre-exponential amplitudes for AgTPDC8-I and AgTPDC12-I in a mixture of 5:1 toluene:DMF at highest and lowest excitation energies. AgTPDC8-I: a) 0.96 μJ , b) 2.88 μJ , AgTPDC12-I: c) 0.48 μJ and d) 2.4 μJ . Spectral amplitudes $A_1(\lambda)$ – black line, $A_2(\lambda)$ – red line and the offset parameter $A_0(\lambda)$ – blue line are obtained from fitting with sum of two exponentials of the decay traces of the samples. The lifetimes are $\sim 1.2\text{ps}$ for AgTPDC8-I and $\sim 1.5\text{ps}$ for AgTPDC12-I. The samples were excited at 350 nm.

A different energy dependence of the spectral amplitudes was observed for AgTPDC8-I and AgTPDC12-I compared to AgTPDC3-I and AgTPDC4-I. The excitation energy dependencies of the transient absorption spectra of the systems AgTPDC8-I and AgTPDC12-I are shown in Figure 5.14. The pre-exponential amplitudes are only shown for the lowest and highest energies examined, as the spectral profiles and lifetimes remain

the same at all energies tested. This indicates that there is no generation of a cation-like species for the C8 and C12 linker systems. Indeed, the amplitudes have the same spectral distribution for both systems, AgTPDC8-I and AgTPDC12-I, which resemble the spectral profile of the excited state of TPD, as shown in Chapter 4. The absence of the cation-like species could be due to the following factors: 1) if the cation-like species is formed by electron transfer from TPD to AgNP, the distance from AgNP surface could significantly reduce electron transfer rate from dye to particle. 2) If the electron is transferred between TPD molecules, there should be a larger barrier to charge separation with larger distance from Ag surface, as there is less screening by the polarization of the Ag core. It should be noted that, the cation-like species is photogenerated in a neat TPD film with no metal particles so the barrier cannot be very large in any case. 3) The increased length of the linkers for the C8 and C12 systems and the curvature of the particle can lead to a lower packing density of dyes on the surface; this would lead to a lower average electronic coupling between adjacent molecules and a lower rate of charge separation which may not compete with quenching of the excited states by the Ag core. 4) Finally, there is a possibility of plasmon enhanced absorption by the TPD, which would depend on the distance from the nanoparticle surface. Plasmon enhanced absorption, for molecules at a closer distance from the surface can lead to a higher number of excited molecules, which would result in a greater production of cation-like species. However, this phenomenon should not be significant due to the small size of the nanoparticles and excitation wavelength being off-resonance with the plasmon.^{xxxiv} None of the above possibilities

^{xxxiv} Plasmon resonance absorption has its maximum at around 450 nm and the excitation wavelength is at 350 nm

can be excluded at this point and further discussion is provided below in conjunction with the coverage dependence and observations for the shorter alkyl chain linker systems.

The values of the peak amplitude A_I for AgTPDC8-I and AgTPDC12-I measured at 1050 nm are plotted against excitation energy in Figure 5.15. These amplitudes show somewhat linear behavior for the lower energies followed by some saturation. Therefore, the systems with 8 and 12 carbon linkers show evidence only for one photon excitation of the chromophores.

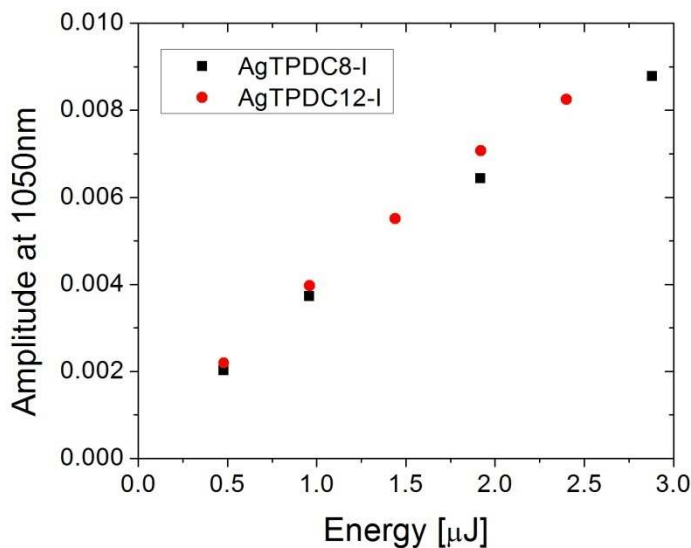


Figure 5.15. Peak spectral amplitude A_I at 1050 nm plotted as a function of excitation energy for samples AgTPDC8-I and AgTPDC12-I.

The results of the global fitting analysis show that TPD / AgNP systems with 8 and 12 carbon atoms in the alkyl linker have only one significant lifetime component with lifetimes of 1.2 and 1.5 ps respectively, which is three orders-of-magnitude shorter

than the lifetime of free TPD in solution. The presence of only one component suggests that the excited state of TPD undergoes relaxation to the ground state without formation of an intermediate species, suggesting that energy transfer from excited TPD to the metal nanoparticle is the dominant quenching mechanism for the longer alkyl linker ligands.

5.4.2. Coverage Dependence

Figure 5.16 shows spectral profiles of pre-exponential amplitudes of a) AgTPDC4-I, b) AgTPDC4-II and c) AgTPDC8-I and d) AgTPDC8-III, e) AgTPDC12-I and f) AgTPDC12-III. The first system a) is functionalized only with TPDC4SH ligands and the second one b) was prepared by co-adsorption of TPDC4SH with DDT in 1:1 ratio. The average area per TPD ligand on the surface of the nanoparticles was determined to be 13.2\AA^2 and 22.1\AA^2 for AgTPDC4-I and AgTPDC4-II respectively, as a result of the dilution of the TPD layer with DDT. The lifetimes associated with amplitudes A_1 and A_2 for case a) are $\tau_1 = 1.03$ ps, $\tau_2 = 14.5$ ps and for case b) are $\tau_1 = 1.07$ ps, $\tau_2 = 19$ ps.

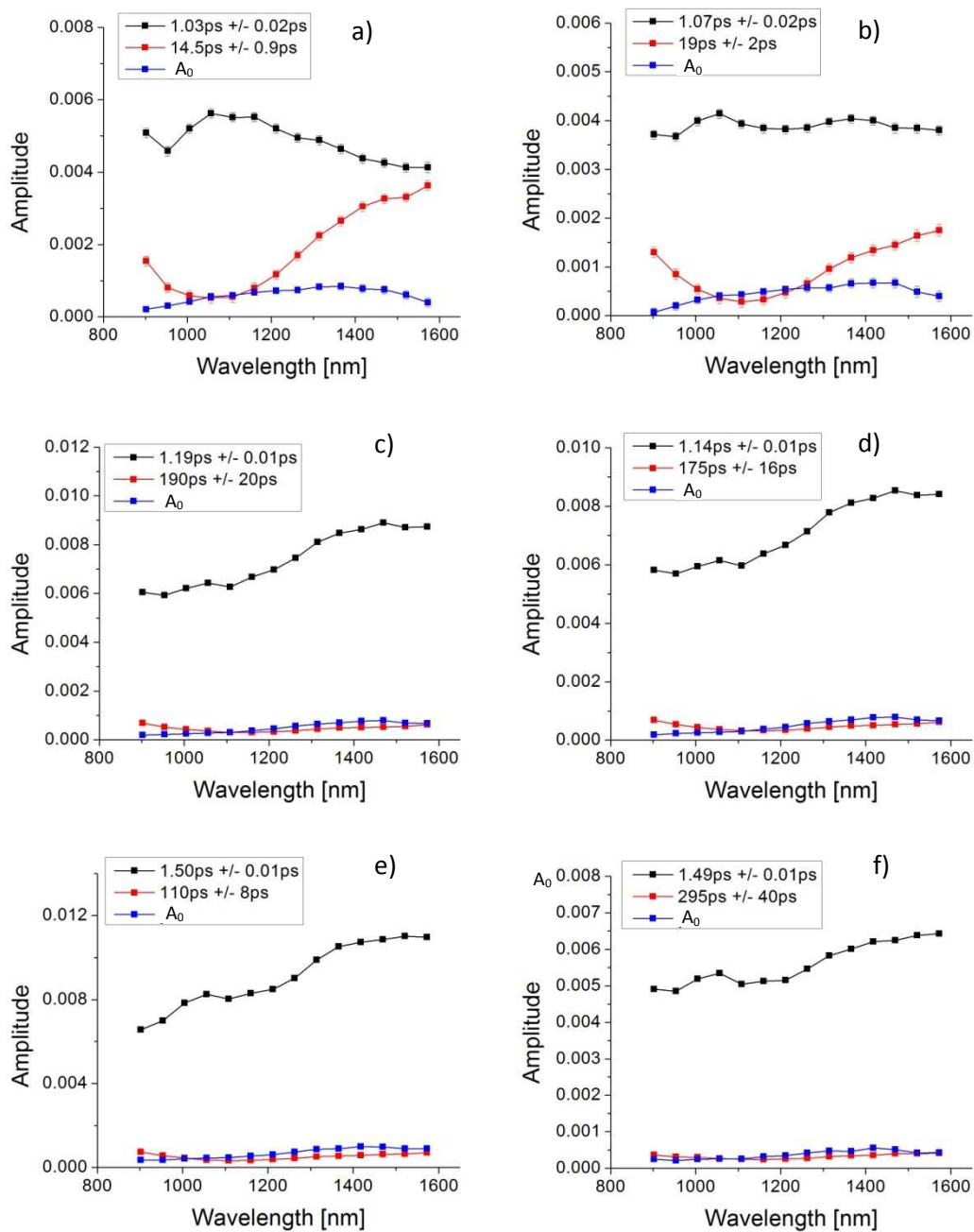


Figure 5.16. Spectral distribution of pre-exponential amplitudes ($A_1(\lambda)$ – black line, $A_2(\lambda)$ – red line) and the offset parameter $A_0(\lambda)$ – blue line obtained from fitting with sum of two exponentials of the decay traces of: a) AgTPDC4-I, b) AgTPDC4-II, c) AgTPDC8-I, d) AgTPDC8-III, e) AgTPDC12-I and f) AgTPDC12-III in a mixture of 5:1 toluene:DMF. The sample was excited at 350 nm, excitation energy was 2.4 μ J.

The systems AgTPDC8-I, AgTPDC8-III and AgTPDC12-I, AgTPDC12-III show no differences in the spectral distribution of amplitudes, despite large differences in the average area available to the TPD ligand (or the average distance between TPD ligands) on the nanoparticle surface: 14.1\AA^2 and 36.1\AA^2 for C8 and 14.0\AA^2 and 27.9\AA^2 for C12. The lifetimes associated with amplitudes A_I are very similar for AgTPDC8-I and AgTPDC8-III: $t_I = 1.19\text{ ps}$ and $t_I = 1.14\text{ ps}$, respectively, and for AgTPDC12-I and AgTPDC12-III: $t_I = 1.50\text{ ps}$ and $t_I = 1.49\text{ ps}$, respectively. It can be concluded at this point that for the samples AgTPDC8-I, AgTPDC8-III and AgTPDC12-I, AgTPDC12-III there is no significant surface concentration dependence of the transient absorption spectra and their lifetimes. This indicates that the energy transfer from the excited TPD to the AgNP is the dominant mechanism for quenching of the TPD excited state lifetime, and that charge separation between TPDs is insignificant. However, samples of AgNP functionalized with TPD ligands with C3 and C4 alkyl linker both show some, but different, dependencies of the transient spectroscopy on coverage as described below.

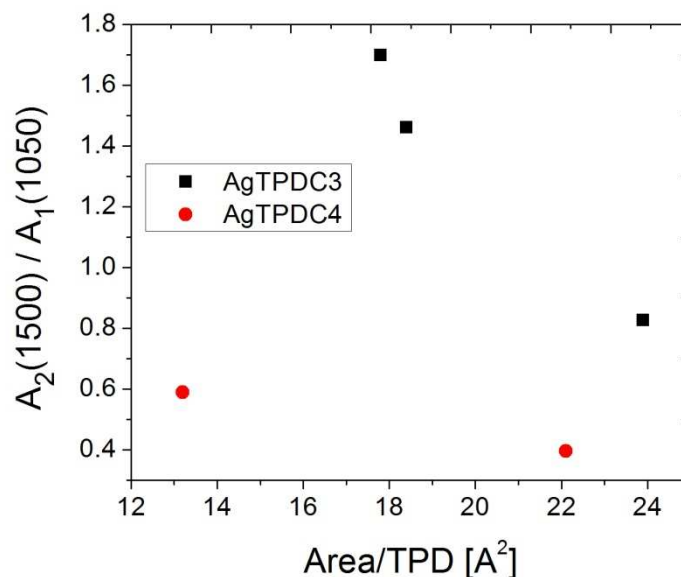


Figure 5.17. Pre-exponential amplitudes A_2 at 1500 nm normalized to the values of amplitudes A_1 at 1050 nm plotted as a function of the area available to a TPD ligand on the AgNP surface. The data is presented for systems AgTPDC3- x (where $x = \text{I, II, III}$) (black squares) and AgTPDC4- y (where $y = \text{I, II}$) (red dots). Excitation energy used was 2.4 μJ and the excitation wavelength was 350 nm.

Figure 5.17 shows the ratio of the spectral amplitudes for the cation-like band to that of the excited state band, $A_2(1500)/A_1(1050)$ a measure of the yield of the cation-like species, as a function of average area per TPD ligand in the mixed monolayers, for the systems AgTPDC3- x (where $x = \text{I, II, III}$) and AgTPDC4- y (where $y = \text{I, II}$). It is evident from this plot that efficiency of formation of the cation-like species is strongly dependent on the density of chromophores for systems AgTPDC3- x . The dependence, although only for 2 points, is less substantial for the samples AgTPDC4- y . These data suggest that the distance of the chromophores to the nanoparticle surface plays a significant role in the efficiency of formation of the cation-like species, although the difference in the linker

length is only one carbon. It is possible that whether the linker carbon number is even or odd (the so called even-odd effect²¹⁻²³) could also play a role here. The effect of having even or odd carbon numbers can result in different orientations of the chromophores with respect to the nanoparticle surface or with respect to each other, which can influence electronic couplings that control the rates of charge transfer.

Note that the footprint^{xxxv} of the TPDC4SH ligands is very similar to the footprints of the longer linker ligands and that all have even number of CH₂ groups in their linkers. Moreover, T₂ values of ¹H NMR indicate that the degree of packing of the chromophoric end groups is the highest for the smallest even number of CH₂ groups. This is consistent with the expected distance dependence of the free volume for the chromophoric end of the linker, discussed in Chapter 3. The footprint of TPDC3SH on the other hand is significantly larger than the footprint of the other ligands and the T₂ value indicates a smaller degree of packing between chromophoric end groups than in the case of AgTPDC4-I. These observations, together with transient absorption studies discussed above, indicate that the higher degree of packing of the chromophores is not the only factor controlling the efficiency of formation of the cation-like species. It has been shown above that the cation-like species is formed more effectively in the C3 linker systems than in the C4 linker systems and it is not formed in C8 and C12 linker systems, indicating strong dependence on the distance from the Ag core and/or an even-odd effect playing a role in this process. The packing geometry of the bulky TPD end groups may be affected by the alkyl chain being either even or odd in the number of carbons, such that the TPD chromophores are oriented favorably with respect to each other or to the

^{xxxv} Footprint refers to an area per TPD ligand in systems of AgNP functionalized with TPD ligands only.

metal surface, to facilitate charge separation. Another possibility that may affect the packing geometry of the chromophores is the fact that the short length of linker chains can result in higher degree of disorder^{xxxvi} within the monolayer on the nanoparticle surface, as is suggested by the IR data (Chapter 3). However, due to steric interactions between bulky chromophoric end groups and π -stacking interactions, the degree of disorder should be limited.²³ Thus, the formation of the cation-like species could be assisted by an appropriate arrangement of the chromophores with respect to each other or with respect to the metal surface, as a result of an even-odd effect or the disorder. Such an appropriate arrangement of the chromophores could be crucial for the energy migration within the chromophoric shell, which eventually could lead to the EEA. Moreover, the distance of the TPD chromophore from the surface of the silver nanoparticle can play a crucial role for the formation of a TPD cation-like species. The silver nanoparticle can play a role of either enhancing the charge separation between the TPD chromophores or provide additional pathway for charge separation via electron transfer to the AgNP.

Power dependent and coverage dependent studies of the yield of the cation-like species suggest that EEA leads to the formation of the cation-like species in the C3 alkyl linker systems. Such a process should be accompanied by migration of the excited state within the chromophoric shell, in order for the excited states to undergo EEA. Migration of excited states can be studied by anisotropy, which is the subject of the next section.

^{xxxvi} The degree of disorder within the alkylthiolate monolayer is defined by the introduction of *gauche* conformations within the predominantly *trans* alkyl chains.

5.5. *Anisotropy*

Interaction of two TPD chromophores in the excited state leading to formation of the cation-like species, through e.g. exciton-exciton annihilation (EEA), requires efficient energy migration within the chromophoric shell. In order to address possible energy migration between TPD chromophores in the shell, time-resolved absorption anisotropy measurements were performed. Energy migration between the chromophores should affect anisotropy decay rates since the chromophores are attached to the surface of a sphere-like particle so as energy moves from molecule to molecule the direction of the transient dipole will be averaged out. Another possibility is that energy transfer could occur between domains of chromophores that have different orientations and also lead to depolarization. In this section, the anisotropy of fs transient absorption is studied with a goal to determine whether efficient energy migration occurs between TPD chromophores. The anisotropy decay of the transient absorption in TPD / AgNP systems can be due to rotational diffusion or energy migration between the chromophores.

For chromophores in solution, the decay of anisotropy is usually associated with whole body rotational diffusion. The rotational rate of a molecule is often expressed by its rotational correlation time, which can be calculated from the Stokes-Einstein equation:²⁴

$$\theta = \frac{\eta V}{kT} \quad (5.15)$$

Where the correlation time, θ , is the time required for a molecule to rotate by 1 radian, η is viscosity of the solvent, V is volume of the molecule, k is Boltzmann constant and T is temperature.²⁵ The transient absorption anisotropy decay for TPDC12 model compound

in toluene has been reported to be around 320 ps.²⁶ However, given that the correlation time is proportional to the volume of the molecule, the rotational correlation time for systems of nanoparticles with more than 200 chromophores attached should be long compared to that for the free molecule. Additionally, it was shown above that the NMR T_2 times for TPD attached to Ag nanoparticles were on the order of 20 ms, such that the rotation time for chromophores on the particle is extremely long compared to that for the free molecule or the whole nanoparticle in solution.

Figure 5.17a shows transient absorption decay for TPDC3I with parallel pump and probe polarization, together with the anisotropy (r) at 1056 nm calculated using the following equation:

$$r = \frac{\Delta OD_{\parallel} - \Delta OD_{\perp}}{\Delta OD_{\parallel} + 2\Delta OD_{\perp}} \quad (5.16)$$

where ΔOD_{\parallel} and ΔOD_{\perp} are the change in absorption recorded following excitation with parallel and perpendicularly polarized pump and probe laser pulses, respectively. The anisotropies at 1056 nm, 1211 nm and at 1521 nm (Figure 5.17b) all show extremely rapid decay. Fitting these decays with a single exponential function gives time constants of about 0.6 ps for all three wavelengths. Recall that the shortest and longest wavelengths correspond to the positions of the TPD excited state absorption and the cation-like band, respectively. This ultrafast depolarization is orders of magnitude faster than the rotational correlation times discussed above, indicating that rotational diffusion cannot explain the ultrafast depolarization of the AgTPDC3-I system. The anisotropy decay of the excited state absorption is consistent with fast energy transfer between TPD molecules in AgTPDC3-I. It is somewhat surprising that the cation

absorption anisotropy is also very fast. This result suggests that hole hopping is as fast as energy hopping between chromophores in this system.

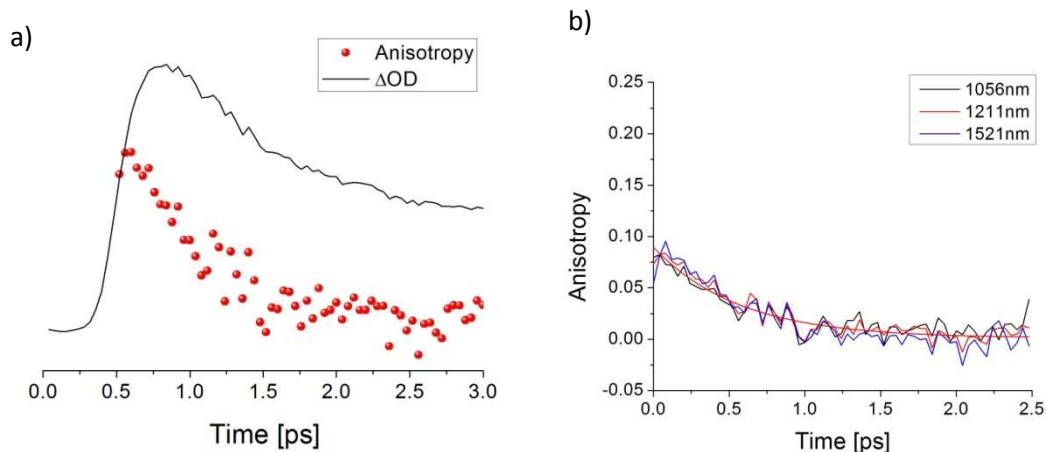


Figure 5.18. a) Anisotropy decay of AgTPDC3-I in solution of 5:1 mixture of toluene and DMF at 1211 nm (red dots) plotted together with transient decay at the same wavelength for sample (black line), b) anisotropy decay at three different wavelengths: 1056 nm, 1211 nm and 1521 nm plotted together with fitting lines. The decay lines were offset on time axis for fitting purpose. Excitation energy was 2.4 μ J, excitation wavelength was 350 nm.

The systems with longer alkyl chains exhibit somewhat different anisotropy decay behavior. Figure 5.19 shows anisotropy decays of a) AgTPDC3-I, b) AgTPDC4-I, c) AgTPDC8-I, and d) AgTPDC12-I. The decays were again fit to a single exponential function and the decay time constants obtained from these fittings are: 0.56 ± 0.04 ps for AgTPDC3-I, 0.30 ± 0.07 ps for AgTPDC4-I, 0.64 ± 0.15 ps for AgTPDC8-I and 0.66 ± 0.12 ps for AgTPDC12-I. The anisotropy decay times are similar in all the systems, however only the anisotropy of AgTPDC3-I decays to zero; in the other cases there is a residual anisotropy that has a much longer decay time. Ultrafast energy

migration between 4,4',-bis(di-n-butylamino)distyrylbenzene chromophores linked to silver nanoparticles via a C11 thiol linker has been previously reported based on time resolved fluorescence up-conversion measurements²⁷. The energy migration in that system results in depolarization with a decay rate of about 200 fs, which is of the same order of magnitude as observed for TPD coated nanoparticle systems reported here. Ultrafast depolarization has been attributed to very efficient dipole-dipole energy transfer between the densely packed chromophores.

The initial transient absorption anisotropy carries information about the relative orientation of the excited- , and probed- transition dipole moments, as indicated by the following equation:

$$r = \frac{3(\vec{\mu}_{ex}\vec{\mu}_{pr})^2 - 1}{5} \quad (5.17)$$

The initial anisotropy values measured for the different systems are: ~0.08 for AgTPDC3-I, ~0.15 for AgTPDC4-I, ~0.15 for AgTPDC8-I and ~0.20 for AgTPDC12-I, all much lower than the expected value of $r = 0.4$ for parallel ground-state and excited state transition moments. The initial anisotropy of the TPD transient absorption in the near-IR range has been determined to be ~0.3. This indicates that there is an angle of 30° between the ground and excited state transition moments. The initial anisotropy values for TPDC12 in polystyrene at 0.6 and 3.4 weight percent are ~0.2 indicating that there may be an effect of the surrounding TPDs or the dielectric environment on the angle between the transition dipole moments. Thus, the differences in the initial values of the anisotropy for the TPD coated Ag nanoparticles suggest that the transition dipoles are

significantly affected by the distance between the TPD chromophores in the monolayer and/or by the proximity to the silver nanoparticle.

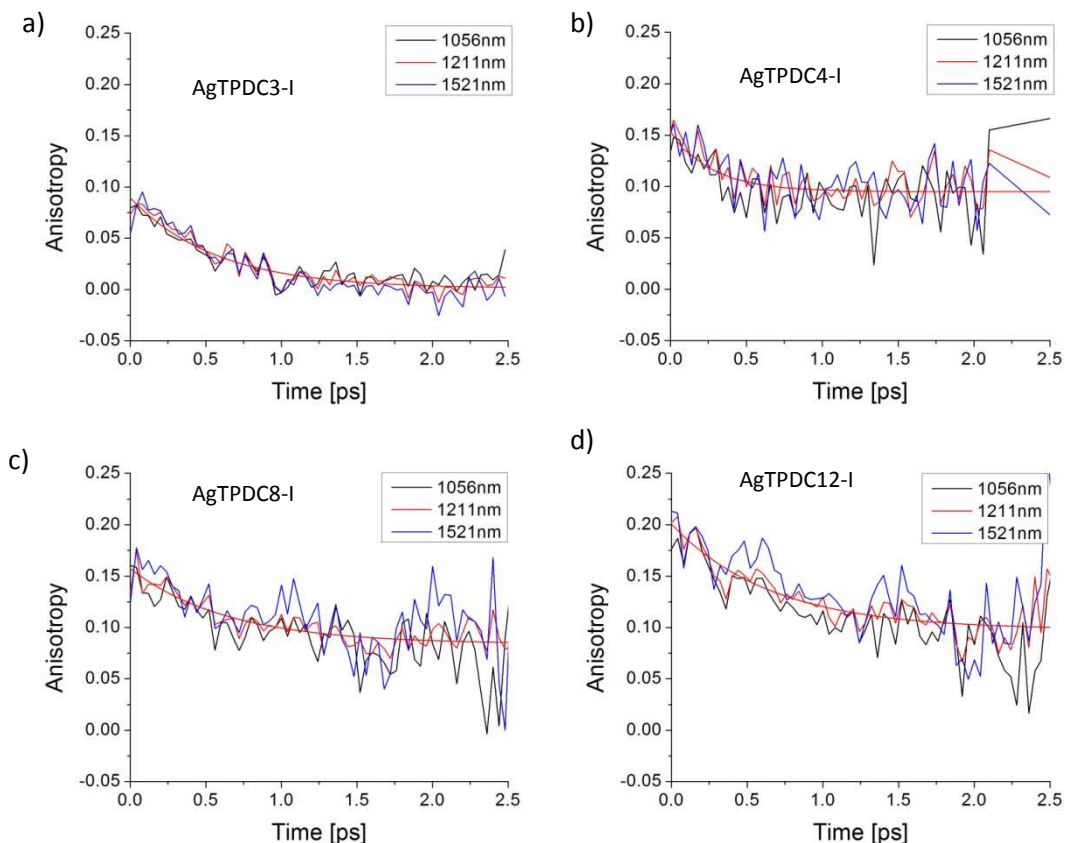


Figure 5.19. Anisotropy decays at 1056 nm, 1211 nm and 1521 nm measured for solutions in 5:1 mixture of toluene and DMF of: a) AgTPDC3-I, $\tau = 0.56 \pm 0.04$ ps, b) AgTPDC4-I, $\tau = 0.30 \pm 0.07$ ps, c) AgTPDC8-I, $\tau = 0.64 \pm 0.15$ ps, d) AgTPDC12-I, $\tau = 0.66 \pm 0.12$ ps.

The anisotropy measurements on the AgTPDC4, C8 and C12 systems differ from the C3 system in that the systems with the longer linkers show a residual anisotropy that must have a decay time of much greater than 2 ps. This indicates that a significant fraction of the TPD on the Ag nanoparticles do not undergo ultrafast energy migration.

This may be due to suppressed energy transfer between patches of chromophores on the surface in the C4, C8 and C12 systems that allows for greater retention of polarization over longer times.

5.6. *Conclusions*

Femtosecond transient absorption studies of TPD coated AgNP systems show ultrafast deactivation of the excited state of the TPD chromophore. The deactivation rates are three orders of magnitude larger than that of the free chromophore in solution. The quenching of the excited state was attributed to energy transfer from the dye to the Ag nanoparticle core for the samples with 8 and 12 CH₂ groups in the alkyl spacer. On the other hand, the deactivation of the excited states of the TPD moiety in samples with 3 and 4 CH₂ groups in the alkyl linker was shown to possess an additional channel leading to the formation of a new species, which we have attributed to a species that is spectroscopically very similar to the TPD cation.

The results from excitation energy and surface coverage dependence of the formation of the cation-like species are consistent with a model involving 1) 1PA excitation of multiple TPDs per particle, 2) exciton-exciton annihilation (EEA) of excited TPDs that is facilitated by ultrafast energy migration between TPDs on the surface, and 3) formation of a TPD cation like species from the higher excited state generated by EEA. It was suggested that either proximity of the chromophoric end groups of the ligands to the silver surface or the arrangement of the TPD chromophores with respect to each other or the metal surface, associated with an whether the linker has an even or odd number of carbons, plays a prominent role in this phenomenon. The arrangement of the

chromophores is expected to be crucial for the EEA process as ultrafast energy migration is needed for this to be competitive with energy transfer to the Ag nanoparticle core. Evidence for ultrafast energy transfer obtained using femtosecond absorption anisotropy measurements was presented and supports the EEA model for generation of the cation species. A short distance of the TPD chromophore from the surface of the silver nanoparticle appears to be critical for the formation of a TPD cation-like species, which may be due to an enhancement of the charge separation between two TPD chromophores by an image dipole generated in the Ag particle or by providing a pathway for the charge separation via electron transfer to the AgNP.

5.7. References

1. Thomas, K. G.; Kamat, P. V., Chromophore-Functionalized Gold Nanoparticles. *Acc. Chem. Res.* **2003**, *36* (12), 888-898.
2. Lakowicz, J. R.; Fu, Y., Modification of single molecule fluorescence near metallic nanostructures. *Laser Photonics Rev.* **2009**, *3* (1-2), 221-232.
3. Gersten, J.; Nitzan, A., Spectroscopic properties of molecules interacting with small dielectric particles. *J. Chem. Phys.* **1981**, *75* (3), 1139-1152.
4. Ruppin, R., Decay of an excited molecule near a small metal sphere. *J. Chem. Phys.* **1982**, *76* (4), 1681-1684.
5. Zhang, J.; Fu, Y.; Lakowicz, J. R., Enhanced Forster Resonance Energy Transfer (FRET) on a Single Metal Particle. *J. Phys. Chem. C* **2006**, *111* (1), 50-56.
6. Dulkeith, E.; Morteani, A. C.; Niedereichholz, T.; Klar, T. A.; Feldmann, J.; Levi, S. A.; van Veggel, F. C. J. M.; Reinhoudt, D. N.; Möller, M.; Gittins, D. I., Fluorescence Quenching of Dye Molecules near Gold Nanoparticles: Radiative and Nonradiative Effects. *Phys. Rev. Lett.* **2002**, *89* (20), 203002.

7. Malicka, J.; Gryczynski, I.; Lakowicz, J. R., Fluorescence spectral properties of labeled thiolated oligonucleotides bound to silver particles. *Biopolymers* **2004**, *74* (3), 263-271.
8. Kotiaho, A.; Lahtinen, R. M.; Tkachenko, N. V.; Efimov, A.; Kira, A.; Imahori, H.; Lemmetyinen, H., Gold Nanoparticle Enhanced Charge Transfer in Thin Film Assemblies of Porphyrin/Fullerene Dyads. *Langmuir* **2007**, *23* (26), 13117-13125.
9. Ipe, B. I.; Thomas, K. G.; Barazzouk, S.; Hotchandani, S.; Kamat, P. V., Photoinduced Charge Separation in a Fluorophore Gold Nanoassembly. *J. Phys. Chem. B* **2001**, *106* (1), 18-21.
10. Vielma, J.; Leung, P. T., Nonlocal optical effects on the fluorescence and decay rates for ad molecules at a metallic nanoparticle. *J. Chem. Phys.* **2007**, *126* (19), 194704.
11. Andreussi, O.; Corni, S.; Mennucci, B.; Tomasi, J., Radiative and nonradiative decay rates of a molecule close to a metal particle of complex shape. *J. Chem. Phys.* **2004**, *121* (20), 10190-10202.
12. Ipe, B. I.; Thomas, K. G., Investigations on Nanoparticle-Chromophore and Interchromophore Interactions in Pyrene-Capped Gold Nanoparticles. *J. Phys. Chem. B* **2004**, *108* (35), 13265-13272.
13. Horimoto, N. N.; Imura, K.; Okamoto, H., Dye fluorescence enhancement and quenching by gold nanoparticles: Direct near-field microscopic observation of shape dependence. *Chem. Phys. Lett.* **2008**, *467* (1-3), 105-109.
14. Bhowmick, S.; Saini, S.; Shenoy, V. B.; Bagchi, B., Resonance energy transfer from a fluorescent dye to a metal nanoparticle. *J. Chem. Phys.* **2006**, *125* (18), 181102.
15. Roberti, T. W.; Smith, B. A.; Zhang, J. Z., Ultrafast electron dynamics at the liquid-metal interface: Femtosecond studies using surface plasmons in aqueous silver colloid. *J. Chem. Phys.* **1995**, *102* (9), 3860-3866.
16. Link, S.; Burda, C.; Wang, Z. L.; El-Sayed, M. A., Electron dynamics in gold and gold-silver alloy nanoparticles: The influence of a nonequilibrium electron distribution and the size dependence of the electron-phonon relaxation. *J. Chem. Phys.* **1999**, *111* (3), 1255-1264.
17. Link, S.; El-Sayed, M. A., Spectral Properties and Relaxation Dynamics of Surface Plasmon Electronic Oscillations in Gold and Silver Nanodots and Nanorods. *J. Phys. Chem. B* **1999**, *103* (40), 8410-8426.
18. Link, S.; El-Sayed, M. A., Shape and Size Dependence of Radiative, Non-Radiative and Photothermal Properties of Gold Nanocrystals. *Int. Rev. Phys. Chem.* **2000**, *19*, 409-453.

19. Gong, X.; Ostrowski, J. C.; Moses, D.; Bazan, G. C.; Heeger, A. J., Electrophosphorescence from a Polymer Guest-Host System with an Iridium Complex as Guest: Förster Energy Transfer and Charge Trapping. *Adv. Funct. Mater.* **2003**, *13* (6), 439-444.
20. Chance, R. R.; Prock, A.; Silbey, R., Molecular Fluorescence and Energy Transfer Near Interfaces. *Adv. Chem. Phys.* **1978**, *37*, 1-65.
21. Gupta, V. K.; Abbott, N. L., Using Droplets of Nematic Liquid Crystal To Probe the Microscopic and Mesoscopic Structure of Organic Surfaces. *Langmuir* **1999**, *15* (21), 7213-7223.
22. Craievich, A.; Doucet, J.; Denicoló, I., Molecular disorder in even-numbered paraffins. *Phys. Rev. B* **1985**, *32* (6), 4164.
23. Barriet, D.; Lee, T. R., Fluorinated Self-Assembled Monolayers: Composition, Structure and Interfacial Properties. *Curr. Opin. Colloid Interface Sci.* **2003**, *8* (3), 236-242.
24. Lakowicz, J. R., *Principles of Fluorescence Spectroscopy*. Springer: New York, 2006; p 480.
25. Visser, N. V.; Hink, M. A.; van Hoek, A.; Visser, A. J. W. G., Comparison Between Fluorescence Correlation Spectroscopy and Time-Resolved Fluorescence Anisotropy as Illustrated with a Fluorescent Dextran Conjugate. *J. Fluoresc.* **1999**, *9* (3), 251-255.
26. Malicki, M. Electronic and Optical Properties of Hybrid Gold - Organic Dye Systems. Ph.D. Thesis, Georgia Institute of Technology, Atlanta, 2009.
27. Varnavski, O. P.; Ranasinghe, M.; Yan, X.; Bauer, C. A.; Chung, S.-J.; Perry, J. W.; Marder, S. R.; Goodson, T., Ultrafast Energy Migration in Chromophore Shell / Metal Nanoparticle Assemblies. *J. Am. Chem. Soc.* **2006**, *128* (34), 10988-10989.

CHAPTER 6

CONCLUSIONS

The ability to functionalize inorganic nanoparticles with organic ligands offers a means for synthesizing new hybrid systems with unique properties, which may substantially differ from the individual components. For instance, metal nanoparticles functionalized with organic chromophores can show enhanced fluorescence due to the concentrated electric field around the nanoparticles, which can find applications in imaging or as light harvesting materials for photovoltaics. Additionally, photophysics of organic chromophores at metal interfaces are of great interest in organoelectronics. However, literature on the subject of the photophysics of organic chromophore – metal nanoparticle systems is scarce, and often incomplete.

The objective of this dissertation was to investigate the photophysical properties of hybrid systems composed of bis(diarylamino) biphenyl (TPD) and silver nanoparticles (AgNP) with respect to the distance of the TPD from the nanoparticle surface as well as potential inter-chromophore interactions. The TPD chromophores were attached to the silver surface via an alkylthiol, where the distance between the chromophore and the nanoparticle surface is controlled by the length of the alkyl linker. The aspect of inter-chromophore interactions was addressed by synthesizing TPD / AgNP systems with varying coverage of the TPD chromophores. The coverage was controlled by co-adsorption of optically inert dodecylthiol (DDT) together with TPD ligands onto silver

nanoparticles. In order to attach the chromophores to the AgNP, while minimizing the possibility of chemical modification of the TPD ligand during synthesis, a very efficient ligand exchange reaction was utilized at room temperature without additional chemicals.

A detailed analytical characterization of the synthesized nanoparticles was performed in order to aid in the photophysical studies of these systems. The TPD / AgNP systems were characterized using TEM, absorption spectroscopy, FT-IR, NMR spectroscopy, ICP-ES and TGA. The following questions were addressed using these techniques: what are the sizes of the nanoparticles, are the ligands attached to the AgNP, do the alkyl linkers act as reliable spacers to control the TPD-AgNP distance, how are the TPD ligands packed and what are TPD ligand footprints in the studied systems?

The average diameters of the nanoparticles were measured by TEM, and the average sizes range from 3.5 to 5.4 nm. The presence of the TPD containing organic shells around silver nanoparticles was confirmed by UV-Vis, FT-IR and ^1H NMR spectroscopies. UV-Vis absorption and FT-IR spectra showed a clear dependence of the position of the surface plasmon resonance band on the length of the alkyl linker between the TPD end group and the nanoparticle surface, indicating that the alkyl linker controlled the TPD-AgNP distance. Insights into the density of packing of the TPD end groups in the AgNP systems were provided by T_2 relaxation times, which indicated an increase in the density of packing with decreasing alkyl linker-length for the systems with an even number of methylene groups. This trend is consistent with the concept of decreasing free volume when approaching the surface of a sphere, and the data were also consistent with an equivalent average area per TPD ligand at the surface of AgNP for the even number carbon linkers, $\sim 14 \text{ \AA}^2$. The system with the C3 linker possessed a larger value of T_2 than

for the C4 linker system, indicating a lower density of packing, both for the chromophoric end groups and the aliphatic linker. This was also consistent with an average area per TPD ligand at the nanoparticle surface of 17.9 \AA^2 . An odd number of carbon atoms in the alkyl linker may introduce a different orientation of the end groups of the ligands, compared to that for an even number of carbon atoms, affecting the way the ligands pack on the nanoparticle surface. Alternatively, disorder in the linker conformations may also lead to similar observations. The information about the degree of packing was deemed to be crucial in the discussion of the photophysics of the studied TPD / AgNP systems.

The photophysical properties of the TPD / AgNP systems were studied predominantly with the femtosecond transient absorption technique. This characterization showed ultrafast deactivation of the excited state of the TPD chromophore. The deactivation rates are three orders of magnitude larger than for that of the free chromophore in solution. The quenching of the excited state was attributed to energy transfer from the dye to the nanoparticle for the samples with 8 and 12 CH_2 groups in the alkyl spacer, as global fitting analysis showed only one significant component with its spectral profile of the pre-exponential amplitudes consistent with the excited state of TPD. On the other hand, the deactivation of the excited states of the TPD moiety in samples with 3 and 4 CH_2 groups in the alkyl linker was shown to possess an additional channel leading to the formation of a new species. A global fitting analysis showed that the spectral profile of the new species had characteristics similar to the cationic form of the TPD chromophore. Upon photoexcitation the cation-like species was also observed in the neat film of the TPD model compound but no signs of the species were present when the

chromophores were diluted either in liquid solution or in polystyrene films, indicating that interaction between TPD chromophores is needed to form the cationic species. The excitation energy dependence and the surface coverage dependence on the formation of the cation-like species were also studied. The population of the cation-like species was found to have a quadratic dependence on the excitation pulse energy, suggesting that either exciton-exciton annihilation (EEA), two-photon absorption or ground state absorption followed by excited state absorption are responsible for the formation of the cation-like species. However, the coverage dependent studies on the formation of the cation-like species indicate that EEA is most likely leading to the cation formation. The results of transient anisotropy measurements are also consistent with ultrafast energy migration, which is crucial in the EEA process. Moreover, despite the fact that AgTPDC4-I has a higher density of chromophores than AgTPDC3-I, the formation of the cation-like species is much more efficient for the systems with three carbon linker ligands. It was suggested that either the simple proximity of the chromophoric end groups to the silver surface or the arrangement of the TPD chromophores with respect to each other or the metal surface (the latter associated with an odd-even effect or a disorder), may play a prominent role in this phenomenon. Such chromophore arrangements could be crucial for energy migration within the chromophoric shell, which could eventually lead to EEA or may stimulate charge separation between chromophores or between TPD chromophores and AgNP after promotion of the TPD to a higher excited state via EEA. Moreover, the distance of the TPD chromophores from the surface of the silver nanoparticle can also be crucial for the formation of a TPD cation-like species. The AgNP core may play a role in

either enhancing the charge separation between the TPD chromophores or provide an additional pathway for the charge separation via electron transfer to the AgNP.

In future work, the possible impact of the odd-even effect on the formation of the cation-like species could be studied by synthesizing and characterizing AgNP / TPD ligands systems with an odd number of carbon atoms in the alkyl linker. Additionally, the potential influence of the arrangement of the chromophores with respect to each other could be addressed by photophysical studies of neat films of the TPD and the TPD model compound. The TPD model compound has an appended dodecanethiol group, which can make the neat film more amorphous than the TPD glass. The neat film of the model compound should have smaller crystalline domains and more disordered character than the TPD neat film. Thus, the packing of the TPD chromophores in the AgTPDC3 systems would likely more closely resemble packing in the film of the model compound, whereas the packing of the chromophores in the AgTPDC4 would resemble the packing in the TPD neat film.

The studies of the TPD ligands covalently attached to the silver nanoparticles, in the context of the chromophore packing and the chromophore-nanoparticle interactions, and the understanding of the photo-induced charge separation between TPD chromophores can be important in the design of TPD-like molecules exhibiting high charge mobility.

APPENDIX A

HIGH RESOLUTION 3-D MULTIPHOTON LITHOGRAPHY

The body of this chapter consists of a copy of a paper published in “Optics Express”.¹

“65 nm FEATURE SIZES USING VISIBLE WAVELENGTH 3-D MULTIPHOTON LITHOGRAPHY”¹

Wojciech Haske*, Vincent W. Chen*, Joel M. Hales, Wenting Dong, Stephen Barlow,
Seth R. Marder, Joseph W. Perry

**These authors contributed equally to this work*

School of Chemistry and Biochemistry and Center for Organic Photonics and Electronics,
Georgia Institute of Technology, Atlanta, GA 30332-0400

Abstract:

Nanoscale features with linewidths as small as 65 ± 5 nm have been formed reproducibly by using 520 nm, 100 fs, 1 kHz repetition rate pulsed excitation of a *bis*(di-*n*-butyl)aminobiphenyl chromophore to initiate crosslinking in a triacrylate blend. Thresholds for high probability formation of lines and minimum feature sizes were determined through power and scan speed dependent dosimetry studies for chromophores with sizable two-photon absorption cross sections at 520 and 730 nm. These studies show

that sub-diffraction limited linewidths are obtained in both cases and the lines written at 520 nm are smaller than those at 730 nm by a factor of 2.4 and the aspect ratio of the lines are 7:1 and 5:1, respectively. Three-dimensional multiphoton lithography at 520 nm has been used to fabricate polymeric woodpile photonic crystal structures with in-plane line spacings as small as 500 nm, which show stop bands in the near-infrared spectral region.

A.1. Introduction

Laser-excited two-photon or multiphoton photochemistry allows for the patterning of materials with true three-dimensional (3D) spatial resolution and provides a method for the direct laser writing of arbitrary three-dimensional structures. Three-dimensional multiphoton lithography (3D-MPL) has matured significantly as a 3D fabrication technology since its inception. Significant progress has been made in the development of photoactive materials systems for 3D-MPL, including negative² and positive³ tone polymer systems, inorganic-organic hybrid materials,⁴ and metal nanocomposites⁵, which provide means for 3D fabrication in a variety of material types. The development of chromophores with large two-photon absorption (2PA) cross-sections⁶ and sizable quantum yields for generation of reactive species has resulted in efficient materials, which can be patterned with low-power femtosecond lasers.⁷ 3D microstructures and devices fabricated using MPL include photonic crystals,⁸ mechanical structures with moveable⁹ or interlocking parts,⁷ microchannel and microfluidic devices,³ and biocompatible templates.¹⁰

There is considerable interest in the potential for the fabrication of 3D structures with nanoscale resolution using MPL. It has been shown that feature widths below the diffraction limit of one-photon processes can be obtained with MPL. Kuebler *et al.*⁷ have reported on the fabrication of woodpile structures with line widths of 200 nm using 730 nm laser excitation.⁷ Features with 120 nm¹¹ and later 100 nm resolution obtained through introduction of radical quenchers¹² have been reported by Kawata *et al.* and narrower features have been obtained through the use of controlled post-fabrication shrinkage.¹³ Misawa *et al.*¹⁴ have reported very narrow widths, which have been attributed to exposure based “baking” of features; however, the reproducibility of these features was limited. Although sub-diffraction-limited transverse feature sizes can be obtained, it is clear that the attainable resolution is controlled by the width of the nonlinear dose function at or above the dose threshold of the material and that this width is fundamentally related to the wavelength of the excitation radiation. While there are a few reports of 3D-MPL using visible excitation,^{15 16} the initiating systems used were typically un-optimized and the feature sizes produced were not exceedingly small (> 200 nm). Accordingly, we have investigated the resolution of MPL in a radical-initiated, crosslinkable acrylate resin system using a “donor- π -donor” chromophore designed for effective excitation at a shorter wavelength than has been typically utilized, and for good solubility in the resin.

In this paper, we report on the reliable fabrication of nanoscale polymeric features with a width as small as 65 nm using 520 nm femtosecond pulse excitation. We present studies of the scan speed and power dependence of the feature widths for 520 and 730 nm excitation to determine the dose dependence of the widths, which provide insight into the

order of the excitation process. We also demonstrate the fabrication of woodpile-type face-centered tetragonal photonic crystal (PC) structures with 65 nm line widths and lateral periodicity of 500 nm. These photonic bandgap (PBG) structures were found to have fundamental stop bands in the 700 – 1000 nm spectral region.

A.2. Experimental Details

A.2.1. Materials

The photosensitive resin used for the 3D-MPL consisted of a 50:50 wt% blend of triacrylate monomers (Sartomer SR9008 and SR368, used as received) along with 0.1 wt% photoinitiator consisting of either 4,4'-bis(di-*n*-butylamino)biphenyl (DABP) or *E,E*-1,4-bis[4-(di-*n*-butylamino)styryl]-2,5-dimethoxybenzene (DABSB). The chemical structures of the photoinitiators are shown in Figure A.1. DABSB has been shown to be an extremely effective two-photon absorbing radical photoinitiator² that exhibits a maximum 2PA cross-section at 730 nm of 900 GM ($1 \text{ GM} = 1 \times 10^{-50} \text{ cm}^4 \text{ sec photon}^{-1}$).⁶ DABP is a “donor- π -donor” chromophore with shorter conjugation length than DABSB that has been shown to possess a peak 2PA cross-section (~200 GM) at an excitation wavelength of 520 nm.¹⁷ It should be noted that for resin systems that excluded both of these photoinitiators, no photoinduced polymerization was observed.

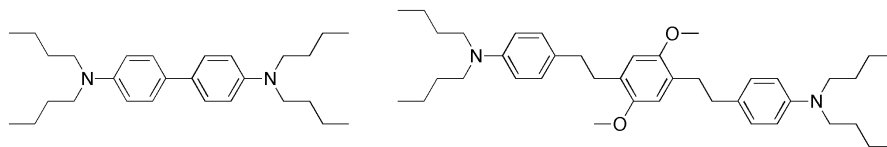


Figure A.1. Molecular structures of photoinitiators used in this work, DABP (left) and DABSB (right).

The liquid resin was sandwiched between a microscope slide and a coverslip substrate using a 100 μm thick Telfon ring as a spacer. The coverslip was treated with an adhesion promoter (trimethoxy[2-(7-oxabicyclo-[4.1.0]hept-3-yl)ethyl]silane). Following exposure, the sample was rinsed twice in methanol for a total of 15 minutes to remove the unexposed resin.

A.2.2. Dose-Dependent Photoinduced Polymerization Studies

Two different laser systems were used during the course of this work. The first system consisted of a tunable optical parametric amplifier (OPA-800CF, Spectra-Physics) pumped via a Ti:Sapphire regenerative amplifier (Spitfire, Spectra-Physics) providing ~ 100 fs pulses at a repetition rate of 1 kHz and tunable from 400 nm to 2100 nm. This system was employed for feature writing in the dose-dependent studies as well as for fabrication of the PCs and spectral characterization of the finished PBG structures. The second system was a Ti:Sapphire oscillator (Tsunami, Spectra-Physics) operating at 730

nm and a repetition rate of 82 MHz with 80 fs pulses. This system was used for the fabrication of support structures (see below) in the dose-dependent studies.

A dose-dependent photo-induced polymerization study was carried out with both DABP and DABSB to compare the feature sizes of the structures created using different excitation wavelengths. The wavelengths were chosen to coincide with the peak of the two-photon cross-section for each of the dyes, i.e. 730 nm for DABSB and 520 nm for DABP. The two excitation beams were delivered collinearly into the 3D-MPL set-up and the relevant wavelength was selected using appropriate bandpass filters. The 3D-MPL apparatus consisted of a 10X expansion telescope that was used to effectively overfill the objective (NA = 1.4) that focused the laser beam into the resin. Fabrication was performed by translating the sample using a computer-controlled 3D positioning stage (MP-285, Sutter Instruments). The incident laser power was controlled using a pair of calcite polarizers. Dosimetry studies were performed by laser writing of free-spanning lines that were written at various incident average laser powers and stage scan speeds. The range of laser powers was chosen to span the range from the threshold power for polymerization to the power at which damage to the sample occurred. For each excitation power, lines were fabricated at four different scan speeds: 60, 40, 20 and 10 $\mu\text{m}/\text{sec}$. The scan speed was limited on the high end by the repetition rate of laser used (1 kHz). Both the lateral and axial dimensions of the written lines were determined using scanning electron microscopy (1530, LEO).

The lines were written by scanning the focus of the laser beam between pre-fabricated support structures. Two different types of support structures were utilized. The first type of structure, as illustrated in Figure A.2a, consisted of parallel rectangular walls

(20 μm wide, 30 μm tall, 1 cm long) spaced by gaps that ranged from 2 to 5 μm . Due to the large dimensions of these structures, the 82 MHz repetition rate laser system was used in conjunction with a high-speed precision translation stage (XPS, Newport). These structures were written using the DABSB-triacrylate resin described above. The structures were developed and then backfilled with either the DABSB or DABP-triacrylate resin for line writing. The second type of support structure, shown in Figure A.2b, was a rectangular “stack of logs” structure (20 μm wide, 15 μm tall, 100 μm long, 5-10 μm spacing). These structures were fabricated in the same resin with the same laser source and excitation wavelength used for the dosimetry studies. Since using the lower repetition rate amplified system (Spitfire) required greater fabrication time, this porous structure was chosen over the more solid structure.

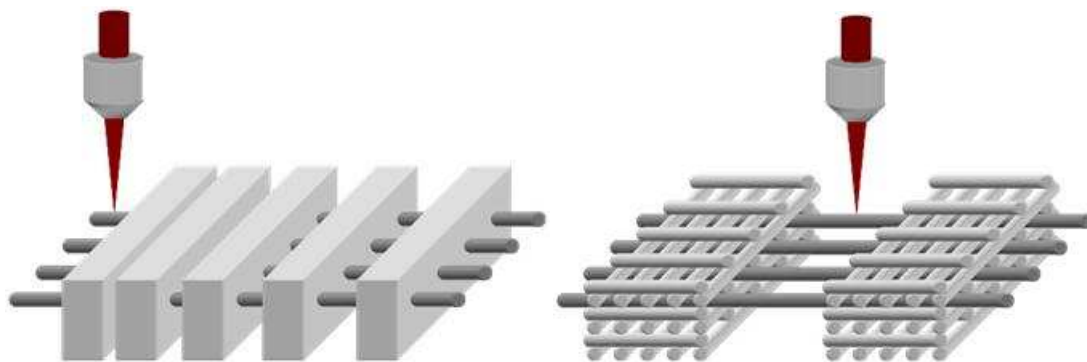


Figure A.2. Schematic illustrations of both types of support structures used for dosimetry studies: (a) rectangular solid walls and (b) rectangular “stack of logs” structure.

A.2.3. PC Fabrication and Stop-Band Characterization

Woodpile-type face-centered tetragonal photonic crystal structures⁸ were fabricated using the DABP-triacrylate resin to demonstrate the applicability of short wavelength 3D-MPL in the fabrication of free-standing microstructures. Woodpile structures were fabricated with lateral line-to-line spacings of 0.5 μm or 0.85 μm , vertical layer spacings of ~ 0.34 μm , and a height of 10 unit cell layers, with overall dimensions of 20 $\mu\text{m} \times 20$ μm . The wavelength-dependent transmission spectra were characterized using a white-light continuum (spectral bandwidth 450 - 1200 nm) that was generated by focusing 2-3 μJ of 1.3 μm excitation from the optical parametric amplifier into a 2 mm calcium fluoride window. This light was focused into the PC sample and the transmission spectrum was collected using a liquid nitrogen cooled CCD array (LN/CCD-1100-PB, Princeton Instruments) coupled to a spectrograph (SP150, Acton). The PC samples were mounted on a rotation stage and transmission spectra were collected for various angles of incidence.

A.3. Results and Discussion

A.3.1. Feature Sizes and Thresholds

Arrays of lines were written between supports, as discussed above, at various powers and scan speeds in order to establish both the threshold for multiphoton writing of polymeric lines and the minimum feature sizes that could be obtained reliably with laser wavelengths of 730 and 520 nm for the resin systems examined. In order to provide statistically meaningful data to support this analysis, between three and six lines have been analyzed for a given power and scan speed. Furthermore, multiple measurements

have been performed on any given line (made possible by their considerable lengths) thereby increasing the number of data points for analysis. The threshold power has been defined as the lowest average laser power at which the line survival probability (ratio of the number of lines that survived the developing or rinsing process to the total number of lines written) is more than 80%. This definition provides not only a statistical metric for the threshold power but also makes physical sense for the fabrication of reliable structures. Survival probabilities are expected to decrease at lower powers due to the reduction of feature size as well as crosslinking density both of which result in reduced mechanical strength of the polymerized structure. For this reason, the choice of support structure employed can have an effect on the threshold power. This will be addressed below.

A representative set of fabricated lines for each resin system is shown in Figure A.3. These sets of lines were written at their respective threshold powers at a scan speed of 60 $\mu\text{m}/\text{sec}$. Figure A.3a depicts lines written in the DABSB-triacrylate resin at 730 nm with a threshold power of about 0.9 μW (the power quoted is that at the sample). The resulting lines exhibit diameters of 200 ± 15 nm. This sub-diffraction limited resolution (the diffraction limited spot-size should be about 320 nm) is typical for 3D-MPL and results from the superlinear dependence of multiphoton absorption (MPA) on intensity coupled with the thresholding nature of the polymerization process.¹¹ This same resin system has been investigated for 3D-MPL at 730 nm⁷ using a similar optical layout but employing the same Ti:Sapphire oscillator system described above. The feature resolution determined at threshold using this laser oscillator system is consistent with the findings discussed in this work using the amplified laser system. Furthermore, when

taking into account the dependence of the absorbed excitation dose on repetition rate and pulsewidth, the average laser powers at threshold found using each source are also consistent with one another. However, the aspect ratios of the polymerized structures determined in the two works are somewhat different. Individual voxels fabricated by 3D-MPL are known to take the shape of ellipsoids of revolution where the height in the axial direction is greater than the widths in the lateral directions. This aspect ratio was determined to be roughly 3:1 using the high repetition rate laser system⁷ whereas a ratio of 5:1 was found in this work for the amplified kHz laser. Given the significantly larger peak powers used with the amplified system compared to the oscillator system (nearly 300 times greater), it is possible that the unusually high aspect ratios found here are due to self-focusing and self-trapping effects that can lead to polymerization beyond the typical Rayleigh range.¹⁸

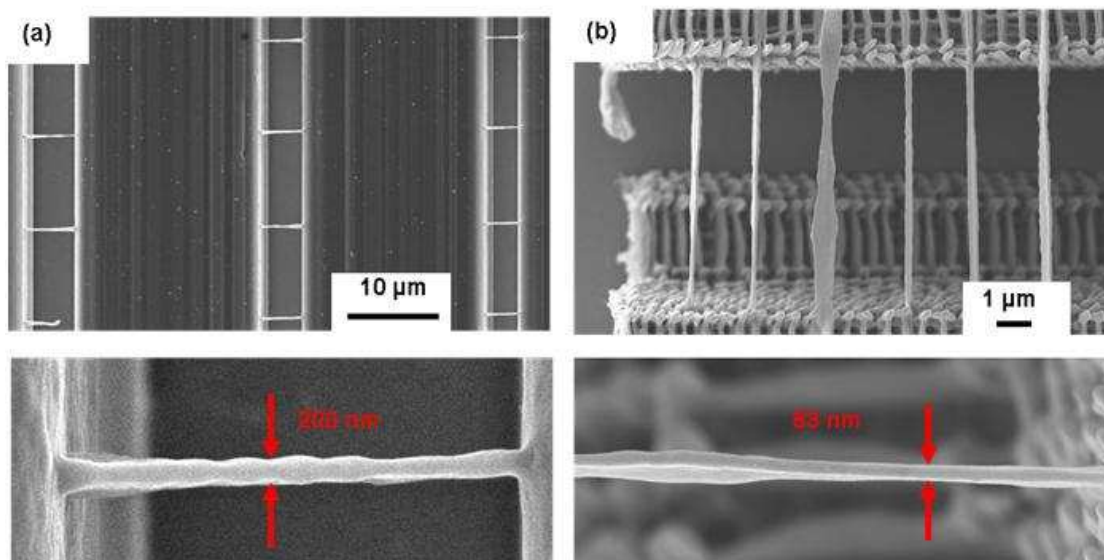


Figure A.3. SEM overview images of lines fabricated at threshold powers with (a) 730 nm excitation using DABSB-triacrylate resin and with (b) 520 nm excitation using DABP-triacrylate resin. Aerial views of support structures described in Figure B.2 are clearly visible in each image. Magnified images of a single line are shown below their respective overview images.

Figure A.3b shows lines written at 520 nm using the DABP-containing resin system. At the determined threshold power of about $0.7 \mu\text{W}$ (at the sample), the diameters of the resulting written lines are $80 \pm 5 \text{ nm}$. A number of observations can be made regarding 3D-MPL using the DABP-triacrylate resin. Firstly, as for the DABSB system, sub-diffraction-limited features are observed (the diffraction-limited spot-size is $\sim 225 \text{ nm}$ for 520 nm excitation). However, the roughly 2.4 times reduction in feature size compared to structures fabricated with 730 nm excitation illustrates that the resolution is fundamentally tied to the wavelength of the excitation. Secondly, not only are these feature sizes some of the smallest to be written by 3D-MPL, but the mechanical stability

of these free-spanning lines are evident by their high survival probability despite the large length-to-width ratios of the lines (nearly 100 to 1). Thirdly, the DABP initiator system exhibited a comparable power threshold to that of the DABSB system which itself has been shown to outperform a number of commercially available photoinitiators when used for two-photon microfabrication.⁷ Finally, the voxel aspect ratio (of height to width) was found to be 7:1. While self-focusing or self-trapping effects may again play a role here it is not clear why the ratio is higher than that of the DABSB system. However, this may be due to a linear dispersion effect resulting in a higher index change upon polymerization at 520 nm or a nonlinear dispersion effect that gives rise to a larger nonlinear refractive index at 520 nm. This large aspect ratio is evident in Figure A.3b where the lines have experienced some torsional forces, most likely during development, leading to some twisting of the lines. This torsion should be ameliorated for support structures providing smaller gaps (smaller length-to-width line ratios), and threshold powers should also decrease for such support structures. This will be elaborated on below.

A.3.2. Dosimetry and Order of Multiphoton Absorption Process

The results of the dose-dependent photo-induced polymerization study for the DABSB-triacrylate resin system are shown in Figure A.4. Figure A.4a plots line widths (or diameters) versus inverse scan speed (proportional to exposure or dwell time) for a number of different excitation powers. Clearly, line widths initially grow larger and then approach a constant value with increasing dwell time for a given power. The features also grow larger for increasing power at a particular inverse scan speed. The minimum feature size of 200 nm and the threshold power of 0.90 μW are clearly evident in the graph.

Assuming that a written voxel can be described as an ellipsoid of revolution with equivalent widths in both lateral directions (given by the data in Figure A.4a) and a height dictated by the 5:1 aspect ratio described above, the voxel volume versus dwell time (or inverse scan speed) can be plotted. This is shown in Figure A.4b.

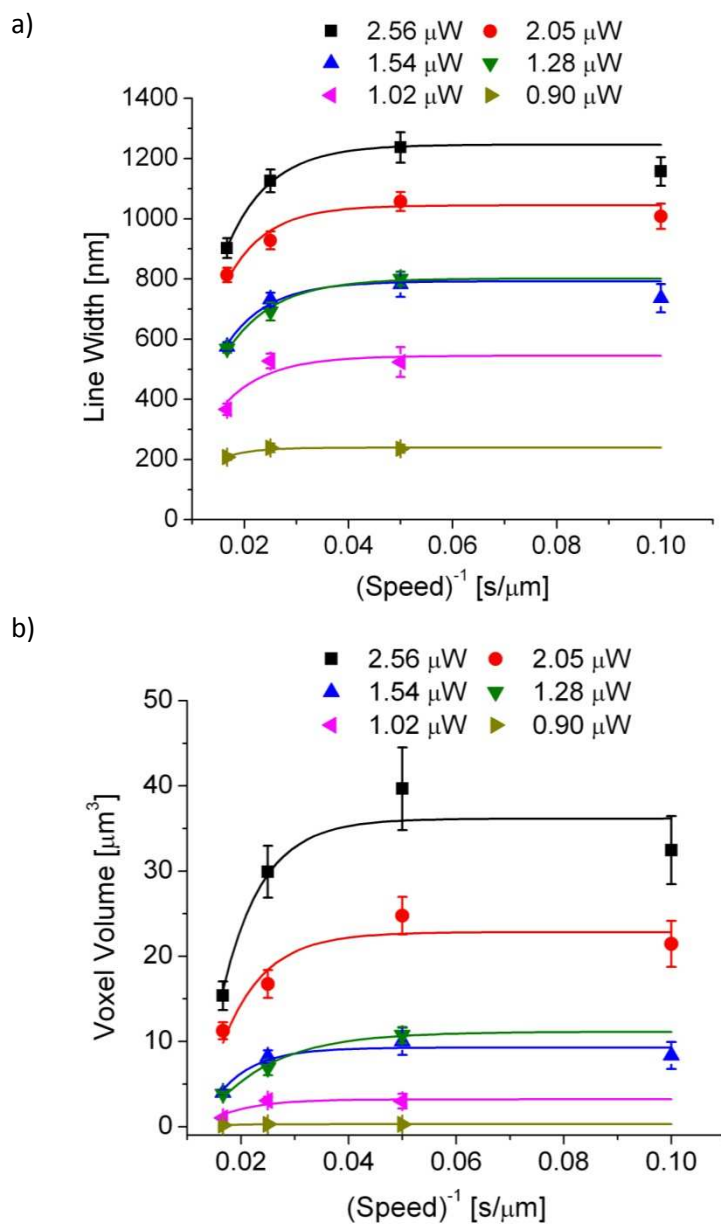


Figure A.4. Dosimetry studies on lines fabricated with 730 nm excitation using DABSB-triacrylate resin. Measured (a) line widths and (b) calculated voxel volumes (see text) as a function of inverse scan speed for different excitation powers. Error bars are given by standard deviations of experimentally measured line widths. The solid lines in (a) are guides for the eye whereas in (b) they represent fittings according to Eq. (1) as described in the text.

The data in Figure A.4b can be fitted to the following equation,⁷

$$V = A[1 - \exp(-B \cdot t)] \quad (1)$$

where V is the volume of the polymerized voxel, t is the exposure time (proportional to the inverse scan speed) and A and B are fitting parameters. The polymer growth rate is then given by the product of these two parameters, i.e. $R_p = A \times B$. The growth rates determined from the fitting curves in Figure A.4b are plotted versus the corresponding average laser power in Figure A.5. It has been shown that the rate of polymer growth is proportional to $(I)^{N/2}$ ¹⁹ where I is the intensity of the laser source (linearly proportional to the average laser power) and N is the order of the MPA process involved in the polymerization process. Therefore, by fitting the data in Figure A.5 to a power law function of the form

$$R_p = C \cdot |P - P_{th}|^{N/2}, \quad (2)$$

where C is a constant, P is the average power, and P_{th} is the threshold power, the order of the MPA process can be determined. The fit to the data in Figure A.5 reveals a power law dependence of $N \approx 3.1$ suggesting that an effective three-photon process correctly describes the MPA process involved in the photoinduced polymerization. Thus, while it is clear that the DABSB chromophore exhibits a strong two-photon resonance at 730 nm, absorption of at least one additional photon is involved in the photoinitiation process. As such, the process can be thought of as a 2PA event followed by one-photon absorption, or a 2+1 MPA event. It should be noted that the determination of the order of this process may be affected by non-local effects such as diffusion, which have not been taken into

account in this analysis. The threshold power is identified as $0.66 \mu\text{W}$ by the fitting curve in Figure A.5. The discrepancy between this value of P_{th} and the value of $0.90 \mu\text{W}$ found in the dosimetry studies discussed above stems from the influence of the developing process. A larger threshold power ensures greater crosslinking of the polymer resulting in the requisite survival probability.

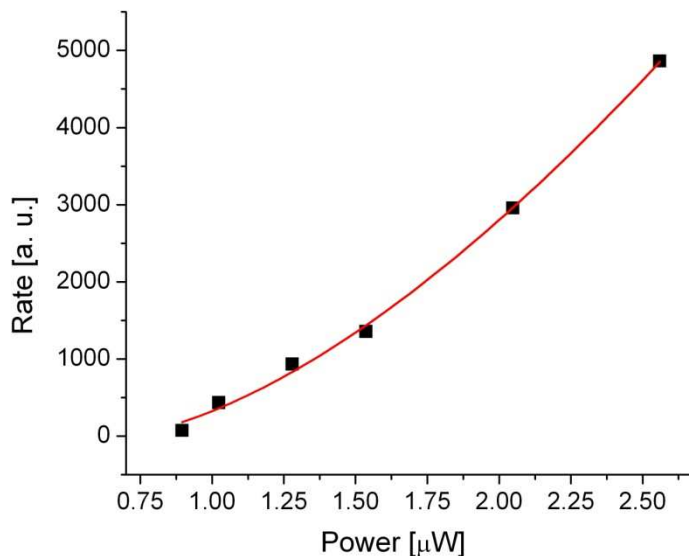


Figure A.5. Polymer growth rates (as determined in text) derived from the dosimetry studies shown in Figure A.4b as a function of excitation power. The experimentally determined values are given as filled black squares and the red solid line indicates a fitting according to Eq. 2. The fitting parameters are: $C = 1770$, $P_{\text{th}} = 0.66$, and $N = 3.14$.

Figure A.6 shows the dosimetry results for the DABP-triacrylate resin system. Once again, the trends of the line widths as a function of dwell time and the power are

consistent with the results found for the DABSB-triacrylate resin system described above. Furthermore, a threshold power of $0.70\ \mu\text{W}$ along with the corresponding 80 nm minimum feature size is also evident in the graph. However, a reliable study of the polymerization kinetics, similar to the one performed above for the DABSB-triacrylate resin, was not possible due to the larger errors associated with these line width measurements. This was mainly attributed to the smallness of the feature sizes and their tight grouping (the difference between the smallest and largest feature size measured was a mere 35 nm, as opposed to nearly 1000 nm for the DABSB data using 730 nm excitation). More detailed work on these polymerization kinetics studies will be conducted in the future using a more stable source of visible wavelength, high repetition rate, femtosecond pulse excitation to accurately determine the order of the MPA process involved.

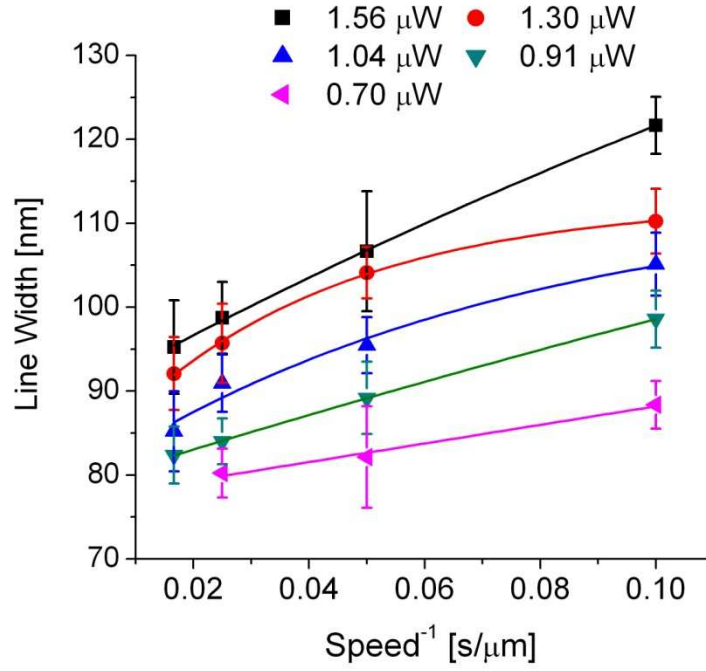


Figure A.6. Dosimetry studies on lines fabricated with 520 nm excitation using the DABP-triacrylate resin. Error bars are given by standard deviations of experimentally measured line widths. The solid lines are guides for the eye.

A.3.3. PC Structures and Stop-Band Spectra

Using the DABP-triacrylate resin system, woodpile-type face-centered tetragonal PC structures were fabricated. Compared to the previous lines fabricated between supporting walls separated by 5-10 μm , these PC structures provide smaller separation between anchoring points and therefore more structural support for the lines written by 3D-MPL. Consequently, since these structures enhance the survival probability of the line features, even smaller features than the 80 nm diameter lines reported above have

been achieved in these structures. Figure A.7 shows two typical PC structures written at 520 nm with the DABP-triacrylate resin. In all, three sets of PCs were fabricated with powers of 0.75, 0.60 and 0.45 μW at a scan speed of 60 $\mu\text{m}/\text{sec}$ with lateral spacings of either 0.50 μm or 0.85 μm . Average widths of the measured lines were 81 ± 7 nm, 75 ± 5 nm, and 63 ± 5 nm, respectively. It is immediately apparent that this more mechanically supportive structure lowers the threshold power for polymerization and thereby allows for finer resolution structures to survive.

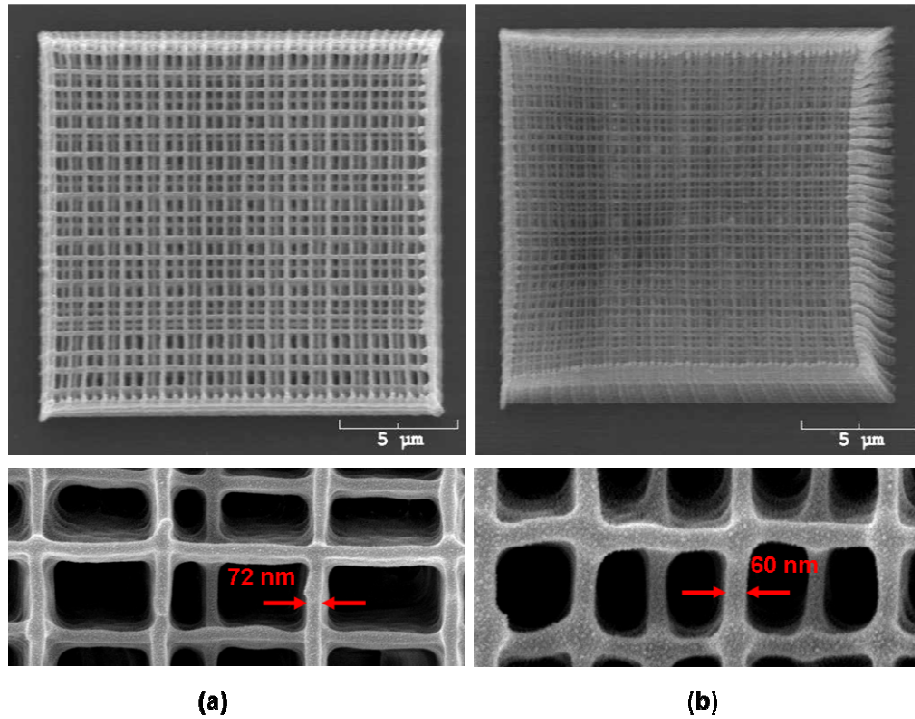


Figure A.7. SEM overview images of woodpile-type PC structures fabricated with 520 nm excitation at (a) 0.60 μW and at (b) 0.45 μW using the DABP-triacrylate resin. Fabrication parameters of PCs were: lateral line-to-line spacings of (a) 0.85 μm and (b) 0.5 μm , axial layer-to-layer spacings of ~ 0.34 μm , and scan speeds of 60 $\mu\text{m}/\text{sec}$. Magnified images of the PC structures are shown below their respective overview images.

Transmission spectra for several of the PC structures described above were collected according to the procedures detailed in Section 2.3. The spectra for different angles of incidence for one of these structures are shown in Figure A.8. Fringes are observed at longer wavelengths (> 900 nm) and the period corresponds to a film thickness of ~ 14 μm consistent with the height of the PC structure. Stop bands have been observed and are indicated by arrows and appear at 717 nm, 810 nm, 890 nm, and 986 nm for incident angles of 0, 10, 20, and 30 degrees, respectively. This trend of the red-shifting of PBG stop bands with increasing angle of incidence has been observed previously.²⁰ It is apparent that the ability to fabricate PBGs with high-resolution mechanically stable lines permits the design of structures possessing fundamental stop bands in the short-wavelength portion of the near-infrared spectral region. In fact, the spectral position of the stop band is primarily dictated by the axial layer-to-layer spacing of the PBG. The large aspect ratio of the lines written at 520 nm using the DABP-triacrylate resin gave rise to large line heights (~ 0.34 μm) and therefore placed a lower limit on the axial spacing that could be achieved with these PBGs. Stop bands in the visible portion of the spectrum could, therefore, be achieved by reducing this line height resulting in smaller axial layer-to-layer spacings. The contrast in the observed stop bands can be enhanced by improving the fidelity of the fabricated PBG structures and by utilizing higher index materials.

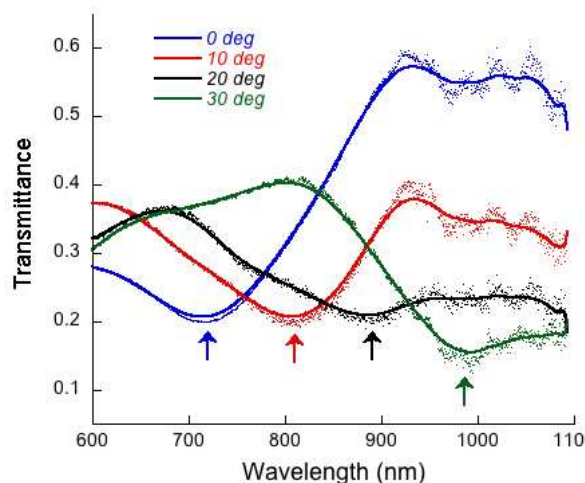


Figure A.8. Transmission spectra of PBG structure fabricated with 520 nm excitation at 0.60 μW using the DABP-triacrylate resin. The dotted lines indicate experimentally observed spectra while the solid lines are merely guides for the eye. Observed stop bands have been indicated by appropriately colored arrows. Fabrication parameters of PBG were: average line width of 75 nm, lateral line-to-line spacing of 0.5 μm , axial layer-to-layer spacing of $\sim 0.34 \mu\text{m}$, scan speed of 60 $\mu\text{m}/\text{sec}$.

A.4. Conclusion

The use of laser-induced polymerization using a photoinitiator with a sizable two-photon absorption cross-section in the visible wavelength region (520 nm) has allowed for multiphoton 3D lithography with nanoscale lateral feature resolution: line widths of 80 nm for long, free-spanning lines and 65 nm line widths in woodpile photonic crystal structures. Comparative studies with two-photon absorbing initiators at 730 and 520 nm show that the minimum lateral feature sizes are below the diffraction limit for the resin

systems examined at both excitation wavelengths, while the height to width aspect ratio for the features written with high intensity pulses at a 1kHz repetition rate is two to three times greater than typically observed for writing with high repetition rate sources. The fabrication of nanoscale lines via visible wavelength 3D-MPL has been utilized to fabricate initial polymeric photonic crystal structures with lateral periods of 500 nm, which gave stop bands in the near infrared spectral region. The capability for reliable formation of nanoscale features using 3D-MPL should have a substantial impact on the fabrication of photonic, electronic and MEMS devices, among others.

Acknowledgments

Support of this work by the Office of Naval Research APEX Consortium (N00014-05-0303) and the National Science Foundation, through the Science and Technology Center for Materials and Devices for Information Technology Research (DMR-0120967), is gratefully acknowledged. We wish to thank Dr. Mariacristina Rumi for supplying preliminary two-photon absorption data on the DABP photoinitiator compound. We also thank Greg Walker for a sample of the DABSB compound.

A.5. References

1. Haske, W.; Chen, V. W.; Hales, J. M.; Dong, W.; Barlow, S.; Marder, S. R.; Perry, J. W., 65 nm feature sizes using visible wavelength 3-D multiphoton lithography. *Opt. Express* **2007**, *15* (6), 3426-3436.
2. Cumpston, B. H.; Ananthavel, S. P.; Barlow, S.; Dyer, D. L.; Ehrlich, J. E.; Erskine, L. L.; Heikal, A. A.; Kuebler, S. M.; Lee, I. Y. S.; McCord-Maughon, D.; Qin, J.; Rockel, H.; Rumi, M.; Wu, X.-L.; Marder, S. R.; Perry, J. W., Two-photon polymerization initiators for three-dimensional optical data storage and microfabrication. *Nature* **1999**, *398* (6722), 51-54.
3. Zhou, W.; Kuebler, S. M.; Braun, K. L.; Yu, T.; Cammack, J. K.; Ober, C. K.; Perry, J. W.; Marder, S. R., An Efficient Two-Photon-Generated Photoacid Applied to Positive-Tone 3D Microfabrication. *Science* **2002**, *296* (5570), 1106-1109.
4. Serbin, J.; Egbert, A.; Ostendorf, A.; Chichkov, B. N.; Houbertz, R.; Domann, G.; Schulz, J.; Cronauer, C.; Fröhlich, L.; Popall, M., Femtosecond laser-induced two-photon polymerization of inorganic-organic hybrid materials for applications in photonics. *Optics. Lett.* **2003** *28* (5), 301-303.
5. Stellacci, F.; Bauer, C. A.; Meyer-Friedrichsen, T.; Wenseleers, W.; Alain, V.; Kuebler, S. M.; Pond, S. J. K.; Zhang, Y.; Marder, S. R.; Perry, J. W., Laser and Electron-Beam Induced Growth of Nanoparticles for 2D and 3D Metal Patterning. *Adv. Mater.* **2002**, *14* (3), 194-198.
6. Rumi, M.; Ehrlich, J. E.; Heikal, A. A.; Perry, J. W.; Barlow, S.; Hu, Z.; McCord-Maughon, D.; Parker, T. C.; Rockel, H.; Thayumanavan, S.; Marder, S. R.; Beljonne, D.; Bredas, J. L., Structure-Property Relationships for Two-Photon Absorbing Chromophores: Bis-Donor Diphenylpolyene and Bis(styryl)benzene Derivatives. 2000; Vol. 122, pp 9500-9510.
7. Kuebler, S. M.; Rumi, M.; Watanabe, T.; Braun, K.; Cumpston, B. H.; Heikal, A. A.; Erskine, L. L.; Thayumanavan, S.; Barlow, S.; Marder, S. R.; Perry, J. W., Optimizing Two-Photon Initiators and Exposure Conditions for Three-Dimensional Lithographic Microfabrication. *J. Photopolym. Sci. and Tech.* **2001**, *14*, 657-668.
8. Deubel, M.; von Freymann, G.; Wegener, M.; Pereira, S.; Busch, K.; Soukoulis, C. M., Direct laser writing of three-dimensional photonic-crystal templates for telecommunications. *Nat. Mater.* **2004**, *3* (7), 444-447.
9. Galajda, P.; Ormos, P., Complex micromachines produced and driven by light. *Appl. Phys. Lett.* **2001**, *78* (2), 249-251.

10. Pitts, J. D.; Campagnola, P. J.; Epling, G. A.; Goodman, S. L., Submicron Multiphoton Free-Form Fabrication of Proteins and Polymers: Studies of Reaction Efficiencies and Applications in Sustained Release. 2000; Vol. 33, pp 1514-1523.
11. Kawata, S.; Sun, H.-B.; Tanaka, T.; Takada, K., Finer features for functional microdevices. *Nature* **2001**, *412* (6848), 697-698.
12. Takada, K.; Sun, H.-B.; Kawata, S., Improved spatial resolution and surface roughness in photopolymerizationbased laser nanowriting. *Appl. Phys. Lett.* **2005**, *86*, 071122-1.
13. Takada, K.; Sun, H.-B.; Kawata, S. In *The study on spatial resolution in two-photon induced polymerization*, Eric, G. J.; Gregory, P. N.; Thomas, J. S., Eds. SPIE: 2006; p 61100A.
14. Juodkazis, S.; Mizeikis, V.; Seet, K. K.; Miwa, M.; Misawa, H., Two-photon lithography of nanorods in SU-8 photoresist. 2005; Vol. 16, p 846.
15. Straub, M.; Gu, M., Near-infrared photonic crystals with higher-order bandgaps generated by two-photon photopolymerization. *Opt. Lett.* **2002**, *27* (20), 1824-1826.
16. Lemerrier, G.; Mulatier, J.-C.; Martineau, C.; Anémian, R.; Andraud, C.; Wang, I.; Stéphan, O.; Amari, N.; Baldeck, P., Two-photon absorption: from optical power limiting to 3D microfabrication. *C. R. Chim.* **2005**, *8* (8), 1308-1316.
17. Rumi, M., *School of Chemistry and Biochemistry and Center for Organic Photonics and Electronics, Georgia Institute of Technology, Atlanta, Georgia 30332-0400 (unpublish results, 2006)*.
18. Kewitsch, A. S.; Yariv, A., Self-focusing and self-trapping of optical beams upon photopolymerization. *Opt. Lett.* **1996**, *21* (1), 24-26.
19. Kuebler, S. M.; Cumpston, B. H.; Ananthavel, S.; Barlow, S.; Ehrlich, J. E.; Erskine, L. L.; Heikal, A. A.; McCord-Maughon, D.; Qin, J.; Roeckel, H.; Rumi, M. C.; Marder, S. R.; Perry, J. W. In *Three-dimensional microfabrication using two-photon-activated chemistry*, Joseph, W. P.; Axel, S., Eds. SPIE: 2000; pp 97-105.
20. Lin, S. Y.; Fleming, J. G.; Hetherington, D. L.; Smith, B. K.; Biswas, R.; Ho, K. M.; Sigalas, M. M.; Zubrzycki, W.; Kurtz, S. R.; Bur, J., A three-dimensional photonic crystal operating at infrared wavelengths. *Nature* **1998**, *394* (6690), 251-253.